Investigation of GHz and THz Frequency Dynamics of Thin Films and Micro- and Nanostructures

Thesis submitted for the degree of
Doctor of Philosophy (Science)
In
Physics (Experimental)

By
Pratap Kumar Pal

Department of Physics
Jadavpur University
2024

To be submitted as per this format

CERTIFICATE FROM THE SUPERVISOR(S)

This is to certify that the thesis entitled "**Investigation of GHz and THz Frequency Dynamics of Thin Films and Micro- and Nanostructures**" Submitted by Sri / Smt. **Pratap Kumar Pal** who got his / her name registered on **16th October 2020** for the award of Ph. D. (Science) Degree of Jadavpur University, is absolutely based upon his own work under the supervision of **Prof. Anjan Barman** and that neither this thesis nor any part of it has been submitted for either any degree / diploma or any other academic award anywhere before.

Anjan Barman 25/06/24

.....

(Signature of the Supervisor(s) date with official seal)

Dr. Anjan Barman, FASc, FInstP
Senior Professor & Dean (Faculty)
Department of Condensed Matter and Materials Physics
S.N. Bose National Centre for Basic Sciences
Block-JD, Sector-III, Salt Lake City, Kolkata-700106, India

Dedicated to my father and mother...

Abstract

In the era of escalating demands for computational power, traditional electronic circuits are nearing their limits with respect to miniaturization, performance, and energy efficiency. Among others, spintronic and magnonic devices present a promising alternative by utilizing spin waves (SWs) instead of electric charges to carry information, potentially revolutionizing future spin-based technologies. This thesis explores the dynamic magnetization phenomena in various ferromagnetic nanostructures, emphasizing the control and reconfigurability of SW properties within magnonic crystals (MCs)—periodically structured metamaterials that exhibit unique magnetic characteristics, paving the way for the next generation of highly efficient and miniaturized microwave devices.

This thesis explores several innovative approaches to the control and application of SWs in ferromagnetic thin film heterostructures and nanostructures. Initially, the reconfigurable nature of SW dynamics in 1D MCs in the form of ferromagnetic nanostripe arrays was investigated through a combination of experiments and micromagnetic simulations. This study revealed the potential to manipulate SW propagation by varying nanostripe thickness and external magnetic field geometry, paving the way for reconfigurable magnonic circuit components. Such a remarkable variation of SW spectra may inspire the development of SW waveguides with wedge-shaped thickness profile which may accommodate different parallel frequency channels lying adjacent in the same waveguide structure without the need for additional nanopatterning.

The research focus then shifts from conventional magnonics to hybrid magnonics, utilizing ferromagnetic nanocross elements as magnonic cavities. The study demonstrated that those nanocross elements act as magnonic cavity and dipole-exchange interaction within the array results in the observed magnon-magnon coupling in the form of an anticrossing phenomenon. The strength of magnon-magnon coupling has been tuned by adjusting microwave excitation power and external magnetic field orientation. Further work focused on controlling the anticrossing phenomenon in nanocross structures by varying the nanocross dimensions and using the same broadband ferromagnetic resonance technique, achieving significant enhancements in coupling strengths. These results will have significant implications for on-chip magnonic devices for quantum information processing and communication.

Furthermore, the amplification of SWs in cobalt-based nanomagnet systems using alternating current spin-orbit torque (ac SOT) has been investigated. Employing time-resolved magneto-optical Kerr effect (TR-MOKE) under bias field-free conditions, we have achieved resonance with intrinsic SW modes by applying radio frequency (rf) currents with different frequencies. The amplitude of these SWs increased up to ten-fold with varying rf power. Our findings highlight significant SW amplification and enhanced signal-to-noise ratios across various frequencies. This establishes ac SOT as a pivotal tool for tailoring SW dynamics in nanoscale devices, promising advancements in spintronic applications by enabling efficient information transmission and optimized SW characteristics.

The focus of the thesis then shifts to the investigation of spin pumping, spin-mixing conductance, interfacial spin transparency and spin diffusion in topological insulator (TI)/ferromagnet FM heterostructures using TR-MOKE techniques, revealing efficient spin current injection and high interfacial spin transparency. The role of topological surface states and high spin-orbit coupling of the TI on the spin pumping and the ensuing modulation of Gilbert damping have been extensively studied.

Finally, we investigated the THz polarization efficiency of metallic wire grid (MWG) structures and demonstrated the enhancement of polarization efficiency by reducing the pitch of the wire grid structures using THz time-domain spectroscopy. The achievement of high polarization efficiency over a relatively broadband THz frequency promotes their application potential in various THz applications including THz spintronics. These findings collectively advance the understanding and technological potential of THz spectroscopy.

সারসংক্ষেপ

ক্রমবর্ধমান গণনামূলক শক্তির চাহিদার যুগে, প্রচলিত ইলেকট্রনিক সার্কিটগুলি সঙ্কোচন, কর্মক্ষমতা এবং শক্তি দক্ষতার ক্ষেত্রে তাদের সীমার কাছাকাছি চলে আসছে। অন্যান্যদের মধ্যে, স্পিনট্রনিক এবং ম্যাগননিক ডিভাইসগুলি বৈদ্যুতিক চার্জের পরিবর্তে তথ্য বহন করতে স্পিন ওয়েভ (SW) ব্যবহার করে একটি প্রতিশ্রুতিশীল বিকল্প প্রস্তাব করে, যা ভবিষ্যতের স্পিন-ভিত্তিক প্রযুক্তিতে বিপ্লব ঘটাতে পারে। এই থিসিসটি বিভিন্ন ফেরোম্যাগনেটিক ন্যানোস্ট্রাকচারে গতিশীল চৌম্বকীয় ঘটনাগুলি অন্বেষণ করে, ম্যাগননিক ক্রিস্টালগুলির (MCs) মধ্যে SW বৈশিষ্ট্যের নিয়ন্ত্রণ এবং পুনর্গঠনের উপর জোর দেয়—যেগুলি অনন্য চৌম্বক বৈশিষ্ট্য প্রদর্শন করে, যা উচ্চ দক্ষ এবং ক্ষুদ্রাকৃতির মাইক্রোওয়েভ ডিভাইসগুলির পরবর্তী প্রজন্মের পথ প্রশস্ত করে।

এই থিসিসটি ফেরোম্যাগনেটিক থিন ফিল্ম হেটারোস্ট্রাকচার এবং ন্যানোস্ট্রাকচারে SW নিয়ন্ত্রণ এবং প্রয়োগের জন্য বেশ কয়েকটি উদ্ভাবনী পদ্ধতির অনুসন্ধান করে। প্রাথমিকভাবে, পরীক্ষামূলক এবং মাইক্রোম্যাগনেটিক সিমুলেশনের সমন্বয়ের মাধ্যমে ফেরোম্যাগনেটিক ন্যানোস্ট্রাইপ অ্যারে আকারে 1D MCs-এ SW গতিশীলতার পুনর্গঠনযোগ্য প্রকৃতির তদন্ত করা হয়েছিল। এই গবেষণায় দেখা গেছে যে ন্যানোস্ট্রাইপের পুরুত্ব এবং বাহ্যিক চৌম্বক ক্ষেত্রের জ্যামিতি পরিবর্তন করে SW প্রচারকে নিয়ন্ত্রণ করার সম্ভাবনা রয়েছে, যা পুনর্গঠনযোগ্য ম্যাগননিক সার্কিট উপাদানগুলির পথ প্রশস্ত করে। SW বর্ণালীতে এই ধরনের অসাধারণ পরিবর্তন SW ওয়েভগাইডগুলির বিকাশকে অনুপ্রাণিত করতে পারে যা অতিরিক্ত ন্যানোপ্যাটার্নিংয়ের প্রয়োজন ছাড়াই একই ওয়েভগাইড কাঠামোর সাথে সংলগ্ন থাকা বিভিন্ন সমান্তরাল ফ্রিকোয়েন্সি চ্যানেলকে সামঞ্জস্য করতে পারে।

গবেষণার ফোকাস তখন প্রচলিত ম্যাগননিক্স থেকে হাইব্রিড ম্যাগননিক্সে স্থানান্তরিত হয়, ফেরোম্যাগনেটিক ন্যানোক্রস উপাদানগুলি ম্যাগননিক গহ্বর হিসাবে ব্যবহার করা হয়। গবেষণায় দেখানো হয়েছে যে এই ন্যানোক্রস উপাদানগুলি ম্যাগননিক গহ্বর হিসাবে কাজ করে এবং অ্যারেতে ডাইপোল-এক্সচেঞ্জ মিথস্ক্রিয়া একটি অ্যান্টিক্রসিং ঘটনাটির আকারে পর্যবেক্ষিত ম্যাগনন-ম্যাগনন কাপলিংয়ের ফলে ঘটে। মাইক্রোওয়েভ উত্তেজনার শক্তি এবং বাহ্যিক চৌম্বক ক্ষেত্রের অভিমুখ সমন্বয় করে ম্যাগনন-ম্যাগনন কাপলিংয়ের শক্তি সামঞ্জস্য করা হয়েছে। একই ব্রডব্যান্ড ফেরোম্যাগনেটিক রেজোন্যান্স কৌশল ব্যবহার করে ন্যানোক্রস গঠনগুলিতে অ্যান্টিক্রসিং ঘটনাটিকে নিয়ন্ত্রণ করার জন্য আরও কাজ করা হয়েছে, কাপলিং শক্তিতে উল্লেখযোগ্য উন্নতি অর্জন করা হয়েছে। এই ফলাফলগুলি কোয়ান্টাম তথ্য প্রক্রিয়াকরণ এবং যোগাযোগের জন্য অন-চিপ ম্যাগননিক ডিভাইসগুলির উপর উল্লেখযোগ্য প্রভাব ফেলবে।

এছাড়াও, বিকল্প বর্তমান স্পিন-অরবিট টর্ক (ac SOT) ব্যবহার করে কোবাল্ট-ভিত্তিক ন্যানোম্যাগনেট সিস্টেমগুলিতে SW-এর পরিবর্ধনের তদন্ত করা হয়েছে। বায়াস ফিল্ড-মুক্ত অবস্থায় টাইম-রেজোলভড ম্যাগনেটো-অপটিক্যাল কের ইফেক্ট (TR-MOKE) ব্যবহার করে, বিভিন্ন ফ্রিকোয়েন্সির রেডিও ফ্রিকোয়েন্সি (rf) কারেন্ট প্রয়োগ করে অন্তর্নিহিত SW মোডগুলির সাথে অনুরণন অর্জিত হয়েছে। এই SWগুলির প্রশস্ততা বিভিন্ন rf পাওয়ারের সাথে দশগুণ পর্যন্ত বৃদ্ধি পেয়েছে। আমাদের অনুসন্ধানে উল্লেখযোগ্য SW পরিবর্ধন এবং বিভিন্ন ফ্রিকোয়েন্সি জুড়ে উন্নত সংকেত-থেকে-শব্দ অনুপাত হাইলাইট করা হয়েছে। এটি ন্যানোস্কেল ডিভাইসগুলিতে SW গতিশীলতাকে সামঞ্জস্য করার জন্য একটি গুরুত্বপূর্ণ সরঞ্জাম হিসাবে ac SOT প্রতিষ্ঠা করে, দক্ষ তথ্য সংক্রমণ এবং অপ্টিমাইজড SW বৈশিষ্ট্যগুলিকে সক্ষম করে স্পিনট্রনিক অ্যাপ্লিকেশনগুলিতে উন্নতি প্রতিশ্রুত করে।

তারপর থিসিসের ফোকাস TR-MOKE কৌশল ব্যবহার করে টপোলজিকাল ইনসুলেটর (TI)/ফেরোম্যাগনেট (FM) হেটারোস্ট্রাকচারে স্পিন পাম্পিং, স্পিন-মিক্সিং কন্ডাকট্যান্স, আন্তঃপৃষ্ঠ ট্রান্সপারেন্সি এবং স্পিন ডিফিউশন তদন্তে স্থানান্তরিত হয়, দক্ষ স্পিন কারেন্ট ইনজেকশন এবং উচ্চ আন্তঃপৃষ্ঠ ট্রান্সপারেন্সি প্রকাশ করে। স্পিন পাম্পিং এবং পরবর্তীকালের গিলবার্ট ড্যাম্পিংয়ের সংযমের উপর TI-এর টপোলজিকাল পৃষ্ঠের অবস্থা এবং উচ্চ স্পিন-অরবিট কাপলিংয়ের ভূমিকা ব্যাপকভাবে অধ্যয়ন করা হয়েছে।

অবশেষে, মেটালিক ওয়্যার গ্রিড (MWG) স্ট্রাকচারের THz পোলারাইজেশন দক্ষতার তদন্ত করা হয়েছে এবং THz টাইম-ডোমেইন স্পেকট্রোস্কপি ব্যবহার করে ওয়্যার গ্রিড স্ট্রাকচারের পিচ কমিয়ে পোলারাইজেশন দক্ষতার উন্নতি প্রদর্শন করা হয়েছে। অপেক্ষাকৃত ব্রডব্যান্ড THz ফ্রিকোয়েন্সি জুড়ে উচ্চ পোলারাইজেশন দক্ষতার অর্জন তাদের বিভিন্ন THz অ্যাপ্লিকেশনগুলিতে, সহ THz স্পিনট্রনিক্সে, প্রয়োগের সম্ভাবনাকে উন্নীত করে। এই অনুসন্ধানগুলি THz স্পেকট্রোস্কপির বোঝাপড়া এবং প্রযুক্তিগত সম্ভাবনাকে সম্মিলিতভাবে এগিয়ে নিয়ে যায়।

List of Publications

Included in the thesis:

1. "Thickness Dependent Reconfigurable Spin-Wave Dynamics in Ni80Fe20 Nanostripe Arrays", **P. K. Pal**, S. Sahoo, K. Dutta, S. Barman, Y. Otani and A. Barman, Advanced Materials Interfaces 9, 2201333 (2022).

2. "Bias-Field Tunable Magnon-Magnon Coupling in Ni80Fe20 Nanocross Array", **P. K. Pal**, S. Majumder, Y. Otani and A. Barman, Advanced Quantum Technologies 6, 2300003 (2023).

3. "Control of Magnon-Magnon Coupling in Ni80Fe20 Nanocross Arrays through System Dimensions", **P. K. Pal**, A. Barman, Journal of Magnetism and Magnetic Materials, 588 (B), 171431 (2023).

4. "Resonant Amplification of Spin Waves by GHz-Frequency Spin-Orbit Torque in Cobalt Nanomagnets", **P. K. Pal** et. al. (Manuscript to be submitted)

5. "Exploring Spin Pumping Effect and Giant Spin Transparency in (Bi0.3Sb0.7)2Te3/Co20Fe60B20 Heterostructures via an All-Optical Method", **P. K. Pal** et. al. (Manuscript to be submitted)

6. "Optimizing the Polarization and Antireflection Characteristics of Metallic Wire Grid Structures in the Terahertz Frequency Range", **P. K. Pal**, S. Chakraborty, R. K. Mitra, and A. Barman, Optical Materials 146, 114553 (2023).

Not included in the thesis:

7. "Extreme sub-wavelength magnetoelastic electromagnetic antenna implemented with multiferroic nanomagnets", J. L. Drobitch, A. De, K. Dutta, **P. K. Pal**, A. Adhikari, A. Barman and S. Bandyopadhyay, Advanced Materials Technologies 5, 2000316 (2020).

8. "Acousto-Plasmo-Magnonics: Coupling Spin Waves with Hybridized Phonon-Plasmon Waves in a 2D Artificial Magnonic Crystal Deposited on a Plasmonic Material", S. Pal, **P. K. Pal**, R. Fabiha, S. Bandhyopadhyay, and A. Barman, Advanced Functional Materials 33, 2304127 (2023).

9. "All-Optical Observation of Giant Spin Transparency at the Topological Insulator BiSbTe1.5Se1.5/Co20Fe60B20 Interface", S. Mukhopadhyay, **P. K. Pal**, S. Manna, C. Mitra and A. Barman, NPG Asia Materials 15, 57 (2023).

10. "Laser Fluence-Tunable Spin Transport and Ultrafast Demagnetization in Topological Insulator BiSbTe1.5Se1.5/Co20Fe60B20 Bilayers", S. Mukhopadhyay, **P. K. Pal**, S. Manna, C. Mitra, A. Barman, Physical Review B 109, 024437 (2024).

11. "Spin-Wave Mode Reversal and Anisotropy in Bi-component Magnonic Crystals", C. Kumar, **P. K. Pal** and A. Barman, Physical Review B 109, 075407 (2024).

12. "Enhancement of spin to charge conversion efficiency at the topological surface state by inserting normal metal spacer layer in the topological insulator based

heterostructure", S. Pal, A. Nandi, S. G. Nath, **P. K. Pal**, K. Sharma, S. Manna, S. Aon, A. Barman and C. Mitra, Applied Physics Letters 124, 112416 (2024).

13. "Using Magnons as a Quantum Technology Platform: A Perspective", **P. K. Pal**, A. K. Mondal and A. Barman (Accepted for publication)

14. "Tripartite Phonon-Magnon-Plasmon Coupling, Parametric Amplification, and Formation of a Phonon-Magnon-Plasmon Polariton in a Two-Dimensional Periodic Array of Magnetostrictive/Plasmonic Bilayered Nanodots", S. Pal, **P. K. Pal**, R. Fabiha, S. Bandyopadhyay, and A. Barman. (Manuscript under Review).

15. "Hot Carrier Cooling Mechanism in 2D perovskite and MoS2 Heterostructure", S. Parveen, **P. K. Pal**, S. Mukhopadhyay, S. Majumder, A. Rahman and A. Barman. (Manuscript under Review).

Acknowledgments

Finally, my doctoral journey of over five years has reached its destination. Along this long path, I've been incredibly fortunate to receive support and encouragement from many people. First and foremost, I want to express my deepest gratitude to my supervisor, Prof. (Dr.) Anjan Barman, for giving me the opportunity to work in his world-class laboratory as part of his esteemed research group. His guidance in developing my scientific temperament, from planning and conducting challenging experiments to rigorously analyzing data and discussing findings, has been invaluable. His tireless efforts in maintaining state-of-the-art research facilities, meticulous attitude, and incredible multitasking ability have profoundly inspired me.

I am deeply thankful to our collaborators: Prof. Rajib Kumar Mitra from SN Bose Centre, Prof. YoshiChika Otani from Japan, Prof. Supriyo Bandyopadhyay from the USA, and Prof. Chiranjib Mitra from IISER Kolkata for providing us with interesting samples to explore exciting physics. Special thanks to Prof. Chiranjib Mitra for allowing me to use and learn their PLD system and to Mr. Subhadip Manna for his constant help with the PLD system at IISER Kolkata. The insightful advice and deep understanding of physics from Prof. Supriyo Bandyopadhyay left me in awe. Besides, I am profoundly grateful to Dr. Jaivardhan Sinha for his valuable insights during the early days of my doctoral journey, especially related to depositions. I would also like to acknowledge Dr. Arabinda Halder for recommending me for the IEEE Summer School in Italy and Dr. Saswati Barman for her useful advice a number of times.

A huge thanks to all our current and past group members. Working with seniors like Dr. Sushmita Saha, Dr. Avinash Kumar Chaurasiya, Dr. Sucheta Mondal, Dr. Samiran Choudhury, Dr. Santanu Pan, Dr. Kartik Adhikari, Dr. Sandeep Agarwal, Dr. Arpan Bhattacharya, Dr. Ajit Sahoo and Dr. Sumaiya Parveen has been invaluable due to their help, suggestions, and valuable discussions. I also liked spending time discussing various topics with Dr. Anup Ghosh. I learned so much from amazing seniors like Anulekha di, Sourav da, Surya Panda da, Amrit da, Koustuv da, Sudip da, and Arundhati di—from rigorous alignment processes and experiments to analyzing data and learning depositions. Apart from sharing lab space and working on projects, we also had numerous professional discussions and shared joyful moments, discussing both academic and non-

academic issues in a friendly atmosphere. The off-topic discussions over a cup of tea with Koustuv da will be cherished forever.

I am thankful to my juniors—Payal, Sreya, Soma, Suchetana, Chandan, Bikram, Sayan, Sayanti, and Swapnil—for maintaining a friendly lab environment. Special memories include working with Suchetana at IISER and conducting smooth experiments with Sreya, for which I am very grateful. Additionally, I like to acknowledge some junior and project students during my PhD tenure including Daisy, Abhilash, Kajal, Subhojit, Shubham, Gaurav Patel, Rajdeep, Gaurav Kanu, Riya (Ashoka University), Prapti, Prerak, Adwitiya, Dimple, Najrul, Sourav, Keshav, Shuvoshree and Meghashree for maintaining a healthy atmosphere in the lab. I would also like to acknowledge Dr. Dheeraj Kumar for developing the Dotmag code, which has made our lives easier. Beyond my lab, I express sincere thanks to senior researchers like Sumana, Subhrasish da, Pabi da, Rafiqul da, Shubhadip da, Jayanta Da, Anupam da, Swarnali di, and junior Riju, from whom I learned so much.

I would like to thank every member of the SNB Cricket, Football, Badminton, and Table Tennis teams. I always cherished spending time in sports, especially cricket. Special thanks to Biswajit Panda, Shubham Purwar, Panda da, Amrit da, Premasish da, Anirban, Animesh, Dhananjay, and Kapil for their competitiveness and sportsmanship.

I am especially grateful for sharing the same timeline with my batchmate, Shivam Mishra.

I want to convey my sincere thanks to DST for supporting my doctoral journey through CSIR, Jadavpur University for PhD registration, and IEEE Magnetics Society for the travel grant to attend the summer school in Italy—truly a dream come true. Thanks to S.N. Bose Centre for providing excellent research facilities and financial support for various national and international conferences. I also acknowledge the support from the academic, accounts, purchase, engineering, and electrical sections, and I am thankful to the cooking (both canteen and mess), cleaning, and gardening staff who ensured a beautiful campus environment and made our daily lives easier. Special thanks to the SNB security staff for keeping us safe.

Lastly, I extend my deepest gratitude to my family and friends who have been my rock. I couldn't have done this without the unconditional love, support, and sacrifices of my father, Mr. Prafulla Kumar Pal, and my mother, Mrs. Latika Pal. They supported my career decisions despite all adversities, and I convey my deepest gratitude and respect to them.

I am grateful for their love and blessings for me. I also express my sincere care and sorrow to my late sister, Smritikana Pal—I deeply regret for not being there during her crisis. I also gratefully admire my loving nephew, Abhirup Das. My heartfelt thanks go to my maternal aunt, Mrs. Archana Pal, and my cousins Anushree and Tanmoy for their support and care for my family while I was away. I also extend my gratitude towards aunt, Parbati Pal and their family for their support to my family.

To my close friends, Abhi (Soham), Soumya, Pritam, Mantu, Subrata, and many more, your support has meant the world to me. I am also grateful to Bhargab, Kalyan, Swadesh, Rashmoni, Snigdha, Sourav, and Ratnesh for their unwavering support. Special thanks to Mouli Chattoraj for teaching me important life lessons during my teenage years and Priyanka for showing unwavering care towards me. I want to extend a heartfelt thank you to Ananya Chakraborty for her endless love and for bringing warmth and humanity into my robotic life. Her constant support and the important lessons she taught me have greatly enriched my life. I will always cherish these lessons, which remind me of the value of compassion and connection.

Finally, I am indebted to my school teachers and professors from my school, college, and university days—Suvendu da, Nabin Sir, Kamruzzaman Sir, Sujit Sir, Arghya Sir, Shyamal Sir, Manash Sir, Bappa Sir, Jibon Sir, Jahir Sir, Abhijit Sir, Partha Sir, SKP Sir, Tanmoy Sir, Bishnu Sir, AR Sir, and many more—who inspired me to become an avid learner of physics and, moreover, a good human being. Heartfelt thanks to Kamruzzaman Sir for improving my English at crucial stage and for his immense faith in me. Nevertheless, I extend my gratitude towards Jathu and Jathima from Burdwan for their loving and caring attitude towards me. It never felt like away from home during my 5-year stay in Burdwan.

List of Abbreviations

1D	: One-dimensional
2D	: Two-dimensional
3D	: Three-dimensional
AFM	: Atomic force microscopy
AOM	: Acousto-optic modulator
AR	: Antireflection
ASI	: Artificial spin ice
BBO	: β-barium borate
BLS	: Brillouin light scattering
BV	: Backward-volume
CVD	: Chemical vapor deposition
CW	: Continuous wave
DE	: Damon-Eshbach
(i)DMI	: (Interfacial) Dzyloshinskii Moriya interaction
DOP	: Degree of polarization
DUT	: Device under test
EA	: Easy axis
EBE	: Electron-beam evaporation
EBL	: Electron-beam lithography
EDX	: Energy dispersive X-ray
EM	: Edge mode
ER	: Extinction ratio
EY	: Elliott-Yafet
FFT	: Fast Fourier transform
FM	: Ferromagnet
FMR	: Ferromagnetic resonance
FP	: Fabry-Pérot
fs	: Femtosecond
GHz	: Gigahertz
GMR	: Giant magnetoresistance
GSG	: Ground-signal-ground

GVD : Group velocity dispersion
HA : Hard axis
HDD : Hard disk drive
HM : Heavy-metal
HR : High resistive
InP : In-plane
IR : Infrared
LD : Linear dichroism
LD^r : Reduced linear dichroism
LLG : Landau-Lifshitz-Gilbert
MFM : Magnetic force microscopy
MO : Microscope objective
MOD : Modulation of damping
MOKE : Magneto-optical Kerr effect
MRAM : Magnetic random-access memory
MTJ : Magnetic tunnel junction
mW : Milliwatt
MWG : Metallic wire grid
NA : Numerical aperture
NC : Nanocross
NM : Nanomagnet
ns : Nanosecond
NS : Nanostripe
OBD : Optical bridge detector
OOP : Out-of-plane
(P)BS : (Polarized) beam splitter
PLD : Pulsed laser deposition
PMA : Perpendicular magnetic anisotropy
ps : Picosecond
PVD : Physical vapour deposition
PSSW : Perpendicular standing spin wave

PWM : Plane wave method
QM : Quantized mode
RR : Retro-reflector
rf : Radio-frequency
SAW : Surface acoustic wave
SEM : Scanning electron microscopy
SHE : Spin Hall effect
(i)SHE : (Inverse) spin Hall effect
SHG : Second harmonic generator
SML : Spin memory loss
SOC : Spin-orbit coupling
SOI : Spin-orbit interaction
SOT : Spin-orbit torque
SP : Spin Pumping
ST-FMR : Spin-torque ferromagnetic resonance
STNO : Spin-torque nano oscillator
STT : Spin-transfer torque
SW : Spin wave
TDS : Time-domain spectroscopy
TI : Topological insulator
TMR : Tunnelling magnetoresistance
TMS : Two-magnon scattering
TR-MOKE : Time-resolved magneto-optical Kerr effect
UM : Uniform mode
UV : Ultraviolet
VNA : Vector network analyzer
XRD : X-ray diffraction
XRR : X-ray reflectivity
μs : Microsecond

Contents

List of Figures

Chapter 1

Introduction

The captivating force of magnetism, a fundamental interaction governing the behavior of certain class of materials, has engrossed humankind for millennia. From the lodestone compass guiding courageous ancient mariners to the powerful electromagnets propelling modern particle accelerators, magnetism has demonstrably revolutionized technological advancements. Yet, the narrative extends beyond the simple attraction of objects. The intrinsic property of an electron, its spin, has emerged as a transformative paradigm for information processing and storage, ushering in the exciting realm of spintronics [1–3]. Spintronics capitalizes on the electron's spin, alongside its well-established charge counterpart, to encode and manipulate information. This approach offers compelling advantages over conventional electronics that rely solely on charge manipulation. Spin currents can be generated and manipulated with lower energy consumption, paving the way for a new generation of energy-efficient devices [4]. Additionally, spin information exhibits a remarkable resilience to external noise compared to its charge-based counterpart, fostering robust and reliable information processing capabilities [5]. Nestled within the engrossing world of spintronics lies a fascinating property known as spin waves or magnons. These waves represent low lying collective excitations of electron spins within magnetic materials. Imagine a vast ensemble of synchronized electron spins in a magnetic material. When a wave of excitation ripples through this ensemble, causing them to precess in harmony, that synchronized motion is analogous to a spin wave [6].

The continuous miniaturization of electronic devices has closely followed Moore's Law, which forecasts that the number of transistors on a microchip approximately doubles every two years. [3,7]. However, as we near the significant physical constraints of miniaturization, this exponential growth trajectory nears its inevitable conclusion. This critical juncture presents a phenomenal opportunity for magnonics to emerge as a promising alternative for future information technologies [2,8,9]. The field of magnonics explores the compelling potential of harnessing spin waves, the magnons, for information processing and storage, marking a significant departure from traditional charge-based electronics. These spin waves offer many advantages that make them highly promising for future technologies. One key advantage stem from the weak interaction of magnons with the lattice structure of materials. This unique property allows magnons to propagate over longer distances with minimal energy loss compared to the electron charge transport in conventional electronics [10]. As a result,

magnonic devices have the potential to significantly reduce energy consumption, making them a compelling alternative for sustainable and energy-efficient technologies[2,11].

Moreover, magnons can be manipulated at significantly higher frequencies than electrons. This attribute paves the way for the creation of significantly faster devices capable of processing information at unprecedented speeds [12]. The ability to operate at higher frequencies not only enhances the performance of magnonic devices but also contributes to their potential scalability, paving the way for the integration of magnonics into diverse technological applications. The paramount significance of magnonics lies in its capacity to tackle the formidable challenges encountered by conventional electronics as we reach the boundaries of miniaturization. The miniaturization of electronic components, as predicted by Moore's Law, has driven technological advancements for decades. However, the diminishing returns of traditional scaling approaches highlight the need for alternative strategies, and magnonics emerges as a promising solution. Magnon-based devices hold the convincing promise of being faster, more energy-efficient, and potentially even more scalable technology than its established charge-based counterparts. This transformative potential extends across various technological sectors, including but not limited to data storage, logic devices, biomedicine, and the development of magnon-based neuromorphic computing architectures[13–15]. The versatility and efficiency of magnonic devices position them as key players in shaping the future of information technology, offering novel solutions to the challenges faced by the rapidly evolving digital landscape.

1.1. Thin Films

Miniaturization and ultrafast magnetization switching are paramount considerations in the relentless pursuit of enhanced data storage capacity and information processing speeds within the realm of magnetic recording technologies. This endeavor demonstrably parallels the significant advancements witnessed in spintronics, particularly since the discovery of Giant Magnetoresistance (GMR) [16,17]. However, conventional magnetic storage media face limitations arising from superparamagnetic effects, where thermal fluctuations destabilize the magnetization of miniscule magnetic bits, and inter-bit coupling, often referred to as crosstalk[18]. These challenges have fuelled research efforts into alternative solutions, culminating in the exploration of materials exhibiting perpendicular magnetic anisotropy (PMA). Thin films of Cobalt (Co)[19], Cobalt Platinum (CoPt)[20], and Cobalt Chromium Platinum (CoCrPt)[21] with PMA characteristics have emerged as promising candidates due to their inherent advantages. PMA films boast superior data density and thermal stability when compared to traditional materials exhibiting in-plane anisotropy[22–25]. This

discovery has ignited a surge in research focused on PMA-based systems, multilayers and heterostructures, aiming to further optimize magnetic recording capabilities through a deeper understanding of magnetization dynamics at the nanoscale. Magnetic thin films exhibit intriguing dynamic phenomena beyond their well-characterized static properties. The formation of stripe domains, spatially modulated regions of alternating magnetization, offers an exciting example[26,27]. These striped structures and their response to external stimuli, such as spin waves in metallic multilayers, provide valuable insights into the material's magnetization dynamics and potential for manipulating spin information. A significant challenge lies in overcoming the high magnetic fields required to switch the magnetization state in PMA systems. This has spurred the exploration of innovative techniques such as heat-assisted magnetic recording (HAMR)[28] and microwave-assisted magnetic recording (MAMR)[29,30]. These approaches exploit thermal or microwave energy to reduce the necessary applied field during the switching process. Another promising avenue lies in spin-transfer-torque (STT) induced switching mechanisms, a cornerstone of magnetic random-access memory (MRAM) technology[31]. Here, a spin-polarized current directly manipulates the magnetization state of a storage element. While STT offers advantages like fast switching times, thermal dissipation during operation presents a significant hurdle for widespread adoption of this technology.

In the realm of spintronics, minimizing Gilbert damping – a crucial parameter quantifying energy dissipation within a precessing spin system – is of paramount importance. Yttrium iron garnet (YIG) thin films hold the record for the lowest observed Gilbert damping coefficient, rendering them exceptionally attractive for magnonic applications due to their efficient spin wave propagation characteristics[32]. However, the intricate crystallographic structure of YIG thin films presents significant challenges for seamless integration into practical spintronic devices. Half-metallic Heusler alloy (HA) compounds[33,34], on the other hand, are rapidly emerging as a compelling alternative material class. Their exceptionally low damping, coupled with a unique spin-dependent band structure, positions them favourably for magnonic applications. Additionally, the inherent compatibility of HAs with diverse spintronic device architectures offers a significant advantage for device development.

Recent advancements in spintronics research have highlighted the intriguing potential of topological insulators (TIs)[35–37]. These materials possess a remarkable property: insulating bulk interiors contrasted with conducting surface states. This unique characteristic grants them immunity to backscattering by non-magnetic impurities, a significant obstacle in conventional spintronic devices. The peculiar properties of TIs make them particularly

attractive for spintronics applications. Their surface states exhibit a unique "helical spin texture" and a strong interplay between spin and momentum (spin-momentum locking)[38,39]. These intriguing features have spurred significant interest in heterostructures combining TIs with ferromagnets (FMs) for spintronic and spin-orbitronic functionalities. TI/FM heterostructures hold immense promise for future spintronic devices due to their exceptional charge-to-spin conversion efficiency[40]. Theoretical predictions suggest that TIs can achieve conversion efficiencies exceeding those of conventional heavy metals by an order of magnitude. This remarkable enhancement in efficiency positions TI/FM heterostructures at the forefront of advancements in spin-based technologies.

Thin magnetic films have emerged as a cornerstone for breakthroughs in spintronics. Their tailored properties, including PMA and tunable spin-orbit coupling, have demonstrably surpassed the limitations of conventional magnetic recording media. These films facilitate the development of innovative devices like MRAM, enabling significant advancements in information storage density and manipulation efficiency. The ongoing quest for materials with intrinsically low magnetization damping and the exploration of novel classes like TIs epitomizes the relentless pursuit of innovation within the dynamic field of spintronics.

1.2. Magnonic Crystals

Magnetic crystals (MCs) represent a class of materials with profoundly structured arrangements of magnetic components, designed meticulously to harness specific properties for diverse applications in the realm of magnetic devices[41]. These materials, with their periodicity and tailored magnetic characteristics, offer a rich ground for exploring advanced functionalities at the micro and nanometer length scale. Spin waves, serve as the carrier of information within MC-based systems. The intriguing feature of MCs lies in their static and dynamic attributes, which have garnered substantial attention and research interest in recent decades. Researchers have delved deeply into understanding how the arrangement and composition of MCs influence the behavior of spin waves. This exploration spans across one-dimensional (1D)[42,43], two-dimensional (2D)[44,45], and three-dimensional (3D) configurations[46,47], each offering unique insights into spin wave localization, propagation, and manipulation characteristics. The materials chosen for constructing MCs play a pivotal role in shaping their functionality and suitability for different applications. YIG stands out prominently in this domain, due to its exceptionally low damping properties that make it ideal for spin wave propagation over long distances with minimal energy loss[32]. However, the intricate patterning required for MCs with YIG can pose challenges, leading researchers to explore alternative materials and structures. Among the alternatives, metallic ferromagnets

such as $Ni_{80}Fe_{20}$ (permalloy)[48], cobalt (Co)[49], and cobalt iron boron (CoFeB)[50] have emerged as promising candidates for micro and nanostructured magnonic devices. These materials offer advantages such as lower magnetocrystalline anisotropy, which enhances their responsiveness to external magnetic fields and facilitates easier patterning processes. This combination of favorable properties positions them as key contenders for realizing efficient and compact magnonic devices with tailored functionalities. In addition to material selection, the design and fabrication of MC-based devices involve intricate considerations of geometry, magnetic field configurations, and interface engineering. These aspects, along with advancements in characterization techniques and computational modeling, contribute to the holistic understanding and optimization of MCs for various applications ranging from spin wave-based computing[51] to magnetic memory and beyond[31,52].

One of their defining characteristics is their ability to manipulate magnetic properties through precise modulation techniques. Researchers achieve this by carefully controlling the composition or structure of these composites, leading to significant changes in key parameters such as coercivity, switching field, and the induction of anisotropies[53]. These modifications not only impact the material's magnetization reversal behavior but also play a crucial role in shaping the localization and propagation of spin waves within the MC. One of the most intriguing aspects of MCs is their ability to tailor the band structure of these spin waves[54]. This phenomenon is achieved through a combination of coherent scattering, Bragg reflection and dynamic dipolar interactions within the composite material[55]. As a result, MCs can exhibit partial or complete bandgaps within the spin wave spectrum, leading to the formation of dispersive energy bands reminiscent of electronic band structures[55]. This intricate band engineering offers a rich playground for exploring novel magnonic phenomena. The domain of 1D MCs encompasses a wide array of sophisticated structures. These include arrays of magnetic stripes[56], bicomponent MCs with tailored properties[57], single magnetic stripes[58] with modulated parameters, and waveguide structures crafted from chains of magnetic dots or periodic arrays of holes etched into a ferromagnetic stripe. Each of these structures is meticulously designed to offer unique opportunities for manipulating and controlling the propagation of spin waves. In recent years, advancements in lithography and deposition techniques have revolutionized the field of 2D MCs. These advancements have enabled the practical realization of highly intricate structures with unprecedented precision and control[5]. For example, researchers can fabricate magnetic dot arrays, where nanoscale magnetic dots are arranged in a regular pattern. Antidot arrays[48,49], featuring periodic absences of material within the composite, are another

intriguing development. Additionally, arrays of magnetic rings exhibit complex magnetic interactions and behaviors. These complex 2D MC structures boast tunable magnonic band structures that can be finely tuned and engineered for specific applications. Moreover, they often exhibit unique magnetic ground states, such as the vortex and onion states, which have garnered significant interest due to their potential for novel device functionalities. The interplay between structure, composition, and magnetic properties in MCs continues to fuel research efforts aimed at unlocking new frontiers in magnonics and spintronics.The potential applications of MCs extend well beyond fundamental investigations into spin wave behavior. Researchers anticipate a diverse array of novel spin wave-based devices leveraging these materials and their properties. Magnonic waveguides, filters, splitters, emitters, amplifiers, multiplexers, interferometers, and logic gates represent a subset of envisioned futuristic devices. Moreover, MCs offer promise for the development of innovative converters seamlessly interfacing with spintronic and electronic environments, ushering in an era of integrated functionalities. Techniques such as inductive microwave excitation[3], spin-transfer torque (STT)[59], and spin Hall effect (SHE)[60]-based magnon injection present compelling avenues for generating and manipulating spin waves within these intriguing materials. In essence, MCs signify a substantial advancement in spin wave manipulation and control. Through precise customization of material composition and structure, researchers can craft MCs with distinctive band structures and functionalities. As research in this captivating field progresses, MCs stand poised to revolutionize the landscape of magnonic devices, paving the way for a new era of spin wave-based information processing[11].

1.3. Hybrid Magnonics

Despite the distinct advantages offered by magnons compared to conventional charge-based electronics, including efficient propagation across long distances with minimal energy dissipation attributed to their weak lattice interaction, as well as the potential for manipulation at higher frequencies, certain challenges persist. The direct manipulation of individual magnons and their sustained confinement present significant hurdles, thus driving the investigation of novel hybrid systems.

Hybrid magnonics, an evolving field at the intersection of magnonics and diverse physical platforms, offers a pioneering strategy to overcome these hurdles and unlock magnons' full potential for quantum information processing[61–63]. This strategy involves integrating magnons with other quantum systems, fostering synergistic interactions that enhance the functionalities of both components. A captivating avenue in hybrid magnonics is the coupling of magnons with photons, the quanta of light. Known as cavity opto-magnonics, this coupling

exploits the interaction between magnons in a magnetic material and photons confined within an optical cavity[64]. This strategic coupling facilitates the conversion between magnons and photons, enabling efficient magnon manipulation and detection using established photonic techniques[65–67]. Another exciting avenue in hybrid magnonics lies in the integration of magnons with superconducting qubits[63,68,69], the fundamental units of information in superconducting quantum computers. This magnon-superconducting qubit coupling offers the potential for the creation of robust quantum memories and long-distance entanglement, a critical ingredient for realizing scalable quantum computation[70,71]. The long coherence times of superconducting qubits combined with the efficient information storage capabilities of magnons hold immense promise for overcoming limitations in current quantum information processing architectures. The burgeoning field of hybrid magnonics extends beyond these two prominent examples. Researchers are actively exploring the integration of magnons with other quantum systems, such as phonons (quantized lattice vibrations) and plasmons (collective oscillations of electrons in a conductor). Each of these hybrid configurations offers unique advantages and paves the way for the development of novel functionalities.

Magnon-magnon coupling, a fundamental aspect of hybrid magnonics, presents distinct advantages in quantum information processing compared to other forms of coupling phenomena[50,72–78]. Unlike electron-electron coupling, which often experiences significant decoherence due to interactions with phonons and impurities, magnon-magnon coupling exhibits considerably weaker intrinsic damping[79]. This characteristic results in longer coherence times for magnons, allowing them to preserve quantum information over extended periods with minimal degradation[80,81]. Moreover, magnons can be manipulated at frequencies substantially higher than those achievable with electron spins, leading to enhanced processing capabilities. Additionally, the inherent spatial coherence of magnons facilitates efficient long-range interactions within magnetic materials, enabling the creation of entangled magnon states—an essential component for establishing robust quantum networks. Magnon-magnon coupling offers a unique combination of low decoherence, high manipulation frequencies, and effective long-range interactions, making it an exceptionally appealing platform for developing scalable and reliable quantum devices in the field of hybrid magnonics[82].

The potential applications of hybrid magnonics are vast and encompass a wide range of technological advancements. Some of the most promising applications include:

Scalable Quantum Information Processing: Hybrid magnonic systems offer the potential for the development of robust, scalable quantum computers capable of tackling complex problems beyond the reach of classical computers[82].

Quantum Communication: The ability to efficiently manipulate and transmit quantum information using hybrid magnonic systems could revolutionize secure on-chip communication protocols[11].

High-Sensitivity Magnetic Sensors: By harnessing the unique properties of hybrid magnonic systems, researchers envision the development of ultra-sensitive sensors capable of detecting subtle magnetic fields with unprecedented accuracy[83].

In conclusion, hybrid magnonics represents a paradigm shift in the field of magnonics, unlocking unparalleled capabilities for manipulating and harnessing magnons for quantum information processing. By strategically integrating magnons with other quantum systems, researchers are paving the way for a new era of technological advancements, propelling us towards the realization of robust quantum devices and revolutionizing the landscape of information processing.

1.4. Spin-orbit Torque Driven Magnonics

Spin-orbit torque (SOT)-driven magnonics stands as a burgeoning field within spintronics, poised to revolutionize information processing technologies[84]. This fascinating paradigm leverages the intricate interplay between spin currents and magnons. By strategically manipulating these interactions, SOT-driven magnonics offers a plethora of advantages, paving the way for transformative applications in the domain of information storage, logic, and communication. One of the most compelling advantages of SOT-driven magnonics lies in its potential for low-energy information processing[85,86]. Unlike conventional charge-based devices that rely solely on the physical movement of electrons, spin currents employed in SOT-driven magnonics offer a more energy-efficient approach. The efficient manipulation of magnons through spin currents translates to significantly lower power consumption, a critical factor in the ever-growing demand for sustainable and energy-efficient electronics. SOT-driven magnonics not only excels in energy efficiency but also boasts the potential for high-speed operation. Magnons exhibit inherently fast dynamics, characterized by precession frequencies in the GHz regime. Spin-orbit torque offers a powerful tool to effectively control the propagation and behavior of these magnons. This precise control over magnon dynamics lays the foundation for the development of high-speed magnonic devices capable of rapid information processing and data transfer, exceeding the capabilities of conventional

electronics. Another absorbing advantage is its non-volatile nature. Unlike charge-based devices that lose their information once power is interrupted, magnons are inherently non-volatile. This unique characteristic allows magnonic devices to retain information without a continuous power supply. The non-volatile nature of magnons makes them highly attractive for designing energy-efficient and robust memory and logic devices, particularly for applications requiring low-power standby operation.

The scalability potential towards nanoscale dimensions represents a pivotal aspect in the advancement of SOT-driven magnonics. In contrast to charge-based mechanisms, which encounter impediments such as heightened resistance and increased power dissipation as dimensions shrink, magnonic systems offer distinctive advantages. The proficient manipulation of magnons at nanoscale levels introduces compelling prospects for densely integrated and miniaturized magnonic devices. This scalability assumes paramount importance in the evolution of forthcoming ultra-compact and high-density electronic systems. Moreover, SOT-driven magnonics embodies a versatile methodology applicable across a wide spectrum of magnetic frameworks. SOT can be adaptly utilized in diverse materials, encompassing ferromagnetic, antiferromagnetic, and magnetic insulator categories. This adaptability empowers researchers to explore an array of material combinations and device architectures, thereby significantly broadening the horizons of magnonics research and unleashing potential avenues for innovative functionalities.

However, realizing the crucial potential of SOT-driven magnonics requires a multidisciplinary approach encompassing several key steps:

Material Selection: Choosing suitable magnetic materials with strong spin-orbit coupling and favourable magnon properties is paramount. Heavy metals like platinum (Pt) and tantalum (Ta), tungsten (W), Iridium (Ir) are often employed due to their strong spin-orbit interactions. Additionally, magnetic layers such as ferromagnetic thin films (CoFeB/Co/$Ni_{80}Fe_{20}$) are strategically selected based on their magnon characteristics to optimize the device performance.

Device Fabrication: Fabricating functional devices for SOT-driven magnonics necessitates precise deposition and patterning techniques. Methods like sputtering, electron-beam evaporation, optical, electron beam and ion beam lithography, and etching are meticulously employed to create high-quality structures that combine spintronic and magnonic functionalities within a single device.

Spin-Orbit Torque Generation: The efficient generation of spin-orbit torque is crucial for manipulating magnons. Techniques such as the spin Hall effect[60] or the Rashba-Edelstein effect[87] are employed to inject spin currents into the magnetic layers. These spin currents apply a torque to the spins within the material, ultimately influencing the behavior of magnons through phenomena like spin-wave excitation or propagation control.

Characterization and Optimization: To ensure optimal performance, thorough characterization of device functionalities and optimization of critical parameters are essential steps. Techniques like magneto-optical Kerr effect (MOKE), ferromagnetic resonance (FMR), and spin transport measurements come into play for comprehensive characterization. By analyzing these measurements, researchers can refine parameters like current density, magnetic field strength, and thickness of the film to achieve the desired magnonic behavior.

1.5. Introduction to THz spectroscopy and THz polarizers

Terahertz (THz) radiation occupies a distinctive segment within the electromagnetic spectrum, situated between microwaves and infrared waves. This spectral region harbors unique characteristics that hold significant potential for scientific inquiry and technological advancement. Historically, the progress of THz technologies was hindered by limited availability of cost-effective sources, detectors, and operational systems, leading to what became known as the "THz Gap"[88]. However, recent breakthroughs have substantially mitigated these challenges, resulting in a surge of research activities and a plethora of promising applications in the THz domain. One of the primary merits of THz radiation is its relatively low energy compared to neighboring spectral regions. This attribute renders THz waves suitable for applications where high-energy radiation, which may be disruptive or hazardous, is unsuitable. Consequently, THz technologies contribute to the development of more energy-efficient systems across diverse domains[89,90]. The versatility of THz radiation is a key asset, particularly evident in THz spectroscopy—a technique exploiting the interaction between THz waves and matter. This approach has found utility across an extensive range of disciplines, including solid-state physics, semiconductor research, nanoscience, molecular biology, pharmaceuticals[90], security[91], and art conservation[92]. THz spectroscopy provides a unique avenue for investigating materials and phenomena with exceptional sensitivity. Furthermore, THz radiation acts as a bridge between quantum mechanical and classical descriptions of electromagnetic waves and their interactions with materials.. This bridging position makes THz radiation highly appealing for fundamental research, enabling the exploration of novel phenomena at the intersection of these paradigms.

Recent strides in THz technology, particularly in generators, detectors[93], and manipulation techniques, have empowered researchers to surmount previous limitations. These advancements have catalyzed groundbreaking discoveries and applications in THz science and technology, steering this field towards a promising future characterized by continued innovation and exploration. Among the assortment of high-fidelity quasi-optical components such as phase shifters[94], filters[95], and polarizers operating in the THz range, THz polarizers[34,35,101–105,42,43,93,96–100] exhibit remarkable versatility, particularly in applications such as THz ellipsometry[106,107]. These polarizers, functioning as straightforward devices, selectively transmit a specific polarization component of THz radiation while attenuating others. They are broadly classified into two groups: free-standing polarizers (without a supporting substrate)[108] and substrate-backed polarizers[102,109]. While free-standing polarizers demonstrate notable polarization efficiency, their intricate fabrication process necessitates a preference for substrate-backed alternatives in many applications due to ease of production. Among the various substrate-backed polarizers, metallic wire grid polarizers emerge as highly adaptable devices, boasting exceptional performance and tunability across a broad frequency spectrum[109].

1.6. Objectives of the Thesis

This thesis undertakes an extensive exploration, both experimentally and numerically, into the static and dynamic magnetization behaviors across a range of materials, particularly focusing on emerging 1D ferromagnetic nanostripes, ferromagnetic nanocross structures, and topological insulator-based ferromagnetic heterostructures. Employing advanced techniques such as time domain (time-resolved MOKE or TRMOKE) and frequency domain (broadband FMR) methods, the study aims to delve into the intricate magnetic properties and spin wave characteristics of these materials. Central to the research are investigations into how various geometrical factors, external magnetic field strengths, and orientations influence the magnetic parameters and spin wave behaviors within these complex systems. This work not only seeks to unravel fundamental aspects of magnetism in these materials but also lays the groundwork for potential applications in advanced magnetic devices and technologies. Each work is precisely outlined in the following:

Chapter 4[110] investigates the impact of variations in stripe thickness and external magnetic fields on spin-wave dynamics within arrays of ferromagnetic nanostripes. Through our investigation, we elucidate various spin wave mode types and their alterations by varying these parameters, notably observing the mode-merging phenomenon. Leveraging simulations, we discern anisotropic spin wave propagation within the nanostripes, This

underscores its importance for magnonic circuit elements like reconfigurable waveguides and spin-wave emitters..

Chapter 5[111] delves into the study of magnon-magnon coupling in a $Ni_{80}Fe_{20}$ nanocross array, characterized by a reduced spin number of approximately $\approx 10^{12}$. The investigation reveals the effective modulation of coupling strength by external factors, including the power of microwave excitation and orientation of the bias field. In-depth simulations clarify the roles of both static and dynamic dipolar couplings in the observed anticrossing phenomenon. Moreover, the softening of spin wave modes, influenced by slight adjustments in bias-field orientation, is comprehensively demonstrated.

Building upon the groundwork laid in Chapter 5, **Chapter 6**[112] delves into the investigation of $Ni_{80}Fe_{20}$ nanocross arrays' dynamics. This exploration entailed meticulous adjustments of the external bias magnetic field strength through the utilization of a broadband FMR technique. The study encompassed varied arm lengths in the samples, facilitating the examination and subsequent analysis of magnon-magnon coupling within the nanocross system. Moreover, the research demonstrated the capability to control the occurrence of the anticrossing phenomenon by adjusting sample dimensions through engineering techniques. Notably, the research demonstrated the achievement of robust coupling strengths reaching up to 0.52 GHz, and cooperativity factor of 1.5 achieved through the external modulation of microwave excitation power amplitudes.

Chapter 7 delves into the amplification of spin waves within cobalt-based nanomagnet systems through the utilization of alternating current spin-orbit torque. Through the application of radio frequency (RF) current at precise frequencies, resonance conditions are established with intrinsic spin wave modes, leading to a substantial augmentation in spin wave amplitudes. This investigation uncovers remarkable spin wave amplification, which not only improves information transmission efficiency but also presents auspicious opportunities for spintronics applications.

Chapter 8 employs an all-optical methodology to illustrate effective spin pumping at ambient temperature within BST/CoFeB thin films. Through the examination of Gilbert damping modulation and spin-mixing conductances, we ascertain a significant spin transparency at the BST/CoFeB interface. This observation implies promising prospects for utilizing these systems in spin-orbitronic devices.

Chapter 9[109] introduces a novel approach to enhance the efficiency of gold-based metallic wire grid polarizers in the THz frequency regime through the modulation of the wire grid structure's periodicity. This method yields remarkable results, achieving a polarization degree of ~94.3% and an extinction ratio of ~22.1 dB over a wide frequency spectrum spanning from 0.2 to 2.5 THz. Additionally, these structures demonstrate proficiency as anti-reflection coatings, underscoring their multifunctional utility.

Chapter 10 briefly summarizes the thesis and offers insights into future directions.

Chapter 2

Theoretical Backgrounds

2.1. The necessity of studying magnetization dynamics

Unveiling the dynamic nature of magnetism, magnetization dynamics offers a multifaceted lens to explore and manipulate magnetic phenomena[113]. By delving into the time-dependent behavior of a material's magnetization, one can gain insights into its fundamental properties like saturation magnetization, magnetic anisotropy, and internal magnetic fields. This knowledge extends to the material's interaction with electromagnetic radiation, influencing aspects like wavelength, phase, and absorption, critical for applications in electromagnetic shielding and magneto-optics. Furthermore, studying magnetization dynamics acts as a window into material's phase transitions by analyzing specific magnetic excitations, and provides valuable characterization tools like ferromagnetic resonance experiments to assess magnetic microstate quality. Finally, understanding these dynamics is essential for designing and optimizing signal processing devices like phase shifters and filters, whose operational frequencies hinge on the manipulation of magnetization within the materials. In essence, magnetization dynamics stands as a cornerstone, unlocking a deeper understanding of magnetism's dynamic nature and paving the way for advancements across diverse fields[114].

2.2. The Dynamics of Magnetism: A Micromagnetic Approach

Ferromagnetic materials possess an intriguing characteristic – the alignment of atomic spins in a parallel manner, resulting in a collective macroscopic magnetic moment. The complex interactions among these atomic spins within ferromagnets exhibit dynamic behaviors that underpin diverse technological applications. To investigate this captivating domain, physicists employ micromagnetism as a potent analytical tool, which provides a simplified yet highly effective means to characterize the dynamic processes within ferromagnetic materials. It employs a continuous vector field denoted as 'M' to represent magnetization, signifying the magnetic moment per unit volume (V) within the material and facilitating a convenient quantification of the overall magnetic state:

$$M = \frac{\sum_{\delta V} \mu}{V} \tag{2.1}$$

Crucially, micromagnetism assumes a constant magnitude of the magnetization vector M, equivalent to the material's saturation magnetization, Ms. This assumption implies that while individual atomic spins within the ferromagnet can change direction, they cannot alter their

magnitude. The essence of micromagnetism lies in its continuous representation of magnetization, which circumvents the discrete nature of atomic spins, thereby simplifying the intricate atomic interactions within a ferromagnet. By adopting this continuum framework, micromagnetism provides a robust tool for analyzing and predicting the dynamic behavior of magnetization in diverse ferromagnetic materials. Nevertheless, it is imperative to recognize the limitations inherent in the micromagnetic approach. Its applicability is primarily confined to dynamic processes characterized by length scales significantly larger than the interatomic distances within the material. This constraint stems from the continuous nature of the magnetization vector, which does not accurately capture the atomic-level intricacies of magnetic interactions. Furthermore, micromagnetism is applicable only at temperatures significantly lower than the Curie temperature (T_C) of the ferromagnetic material. As the temperature approaches T_C, thermal fluctuations become more pronounced, disrupting the long-range magnetic order crucial for ferromagnetism. Consequently, micromagnetic theory becomes inadequate for describing behaviors beyond the Curie point[115].

For this thesis, our focus is on magnetic materials such as permalloy with a Curie temperature (T_C) around 750 K[116,117], CoFeB with T_C approximately 1000 K[118], and Co with T_C roughly 1200 K[119]. These materials exhibit stability at room temperature and possess T_C well above room temperature (approximately 300 K). The characteristic length scales governing dynamic processes significantly exceed interatomic distances, thereby validating the application of micromagnetic theory. These dual criteria - sufficiently high characteristic length scale and sufficiently high T_C—form the basis for employing the micromagnetic approach. This methodology involves treating the system as a macrospin model rather than considering individual atomic moments, thereby enhancing its practical utility and effectiveness.

2.3. Magnetization Dynamics

There are primarily two mechanisms for magnetization switching: precessional motion (faster) and domain wall motion (slower). Depending upon various external stimuli and choice of materials, one out of those two mechanisms dominates. In systems with the incorporation of an external magnetic field, precessional motion dominates while the domain wall motion dominates related to the phenomena of domain wall motions or ac SOT-driven dynamics.

2.3.1. Precessional dynamics

When subjected to an external magnetic field, magnetic moments within a magnetic material experience a torque effect, causing them to undergo a precessional motion around the direction of the field. At the same time, these moments strive to align themselves with the external field in order to minimize the Zeeman energy, leading to a damped spiral motion known as precessional magnetization dynamics. This dynamic phenomenon is described by the Landau-Lifshitz-Gilbert (LLG) equation of motion[120,121]. This equation, initially derived from quantum mechanical principles to represent torque, incorporates a damping term to refine its accuracy as given by:

$$\frac{dM}{dt} = -\gamma\left(M \times H_{eff}\right) + \frac{\alpha}{M_S}\left(M \times \frac{dM}{dt}\right) \tag{2.2}$$

Here, α is called the Gilbert damping parameter and H_{eff} is the sum of all possible magnetic field components present in the system, given by:

$$H_{eff} = H_{ext} + H_{ex} + H_{demag} + H_k + h(t) + \cdots \tag{2.3}$$

2.3.2. Domain wall dynamics

In ferromagnetic materials, the motion of boundaries between regions with aligned magnetic moments, known as domain walls, is a critical aspect governed by dynamic processes. These walls can be influenced by external magnetic fields[122], spin currents[123], or temperature gradients[124], resulting in translation, expansion/contraction, or annihilation depending upon factors such as wall type, material characteristics, and the strength of the driving force. The induction of domain wall motion through a magnetic field was first achieved by J. Galt during 1951–52[122], and this motion was detected using the giant magnetoresistance (GMR)[16,17] technique. Spin-orbit torque (SOT)-driven dynamics of domain walls[125,126] offers energy-efficient and rapid motion compared to other external stimuli. The dynamics of domain walls are also mathematically described by the LLG equation[120,121], as discussed previously. Understanding domain wall dynamics is essential for various applications due to their impact on electrical conductivity, magnetic recording processes, and the development of advanced devices such as domain-wall racetrack memory[127].

2.4. Spin waves

As depicted in Figure 1(a), when a ferromagnetic sample is placed under the influence of an external bias magnetic field, all the spins get oriented along the field direction. But immediately upon a small perturbation field is applied perpendicularly to the sample, instead

of flipping one spin (that would eventually increase the Heisenberg exchange interaction in the system; Figure 1(b)), the phase of disturbances propagates in the form of a wave to minimize the exchange interaction, this wave is popularly called as spin waves and the quanta of which is called magnons (Figure 1(c)). Originally predicted in 1930 by Bloch, spin waves gained significant research interest in the mid-20th century for their potential in signal-processing devices. Interest in spin waves remains robust and continues to grow within both the scientific community and industry, showing no signs of diminishing over time (Figure 1(d)). The advantages include the capability to encode information in both the amplitude and phase of the wave, enabling non-Boolean logic operations, exceptionally high operating

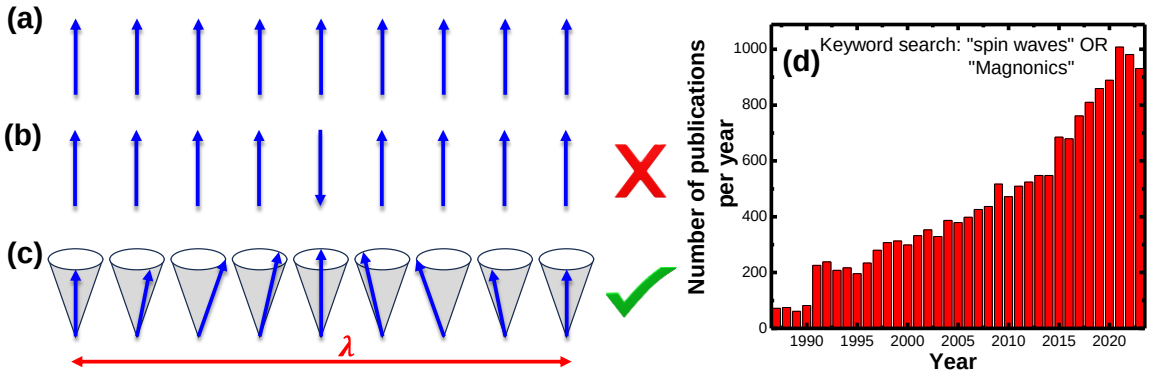

[1]Figure 2.1. (a) The magnetic moments of all atoms align in parallel with each other at the ground state of a ferromagnet, resulting in a state of maximum magnetic order. (b) Higher-energy excitations, when one of these aligned spins abruptly flips, creating an energetically unfavorable state due to the disruption of magnetic alignment. (c) Spin waves represent the lowest-energy excitations above the ground state. (d) The graph illustrates the evolutionary trend of the number of publications per year related to the research keywords "spin waves" OR "magnonics", indicating the growing interest and exploration in this field over time.

frequencies reaching terahertz ranges, and short wavelengths at the nanoscale, facilitating the creation of miniaturized devices. Currently, spin-wave electronics are undergoing a resurgence in interest owing to the distinctive benefits offered by spin waves in advancing computing technologies. This enthusiasm is further fueled by the integration of magnons with various quasi-particles in different systems, leading to the development of highly efficient technological devices by opening up new domains like hybrid quantum systems.

Uniform Precession and Ferromagnetic Resonance (FMR) (k = 0):

A special case of spin wave excitation occurs under a uniform applied magnetic field (H_{ext}). In this scenario, all the magnetic moments precess together at the same frequency and in the same phase (i.e., $\lambda \rightarrow \infty$), a phenomenon termed as uniform precessional motion. This collective precession can be detected using an oscillating magnetic field. When the frequency of the oscillating field aligns with the natural precession frequency of the spins, it causes a

resonant absorption of energy known as FMR. This phenomenon can be understood further by solving the LLG equation, $\frac{dM}{dt} = 0$, the FMR frequency can be evaluated[128]:

$$f = \frac{\gamma}{2\pi}\sqrt{[H + H_k + (N_y - N_z)M_s][H + H_k + (N_x - N_z)M_s]} \quad (2.4)$$

This is the solution for a general ellipsoid for the applied field along z-direction and N_i's are the demagnetizing factors along three coordinate axes. For thin magnetic film ($N_x = N_z = 0, N_y = 4\pi$, the solution takes the following form:

$$f = \frac{\gamma}{2\pi}\sqrt{[H + H_k][H + H_k + 4\pi M_s]} \quad (2.5)$$

Non-uniform Precession and the Spin Wave Dispersion ($k \neq 0$):

2.4.1. Exchange spin waves

Exchange spin waves, collective excitations of electron spins arising from the exchange interaction, are fundamental to spintronics. These short-wavelength, isotropic excitations propagate efficiently due to their reliance on the strong exchange force between neighboring spins. The exchange spin waves dominate for the wavelength approximately equal to the exchange length of the material, which are highly beneficial for various spintronic applications, including information transfer and manipulation in magnetic tunnel junctions (MTJs)[129–131] and spin valves[132]. Notably, they form the foundation of spin wave logic devices[133,134], where information is carried and processed by exchange spin waves[135–137], offering potential advantages include low power consumption and high-speed operation[138–141].

The dispersion relation for dipole-exchange spin wave[142–144] is given by:

$$f_{Dip-Ex} = \frac{\gamma}{2\pi}\sqrt{[H - 2\pi M_s kt * sin^2\theta_k + \frac{2Ak^2}{M_s}][H + 4\pi M_s - 2\pi M_s kt + \frac{2Ak^2}{M_s}]} \quad (2.6)$$

θ_k is the angle between H and k.

Besides exciting k, it is also feasible to stimulate spin waves that travel perpendicular to the plane of the film, resulting in perpendicular standing spin wave (PSSW) modes[145]. The dispersion relation of PSSW mode is given by:

$$f_{PSSW} = \frac{\gamma}{2\pi}\sqrt{[H + \frac{2Aq^2}{M_s}][H + \frac{2Aq^2}{M_s} + 4\pi M_{eff}]} \quad (2.7)$$

where $q = \frac{n\pi}{t}$ and M_{eff} is the effective magnetization of the sample.

2.4.2. Dipolar spin waves

Dipole-dominated spin waves, arising from dipole-dipole interactions, exhibit longer wavelengths and anisotropic behavior in comparison to exchange-dominated spin waves [2]. This anisotropy arises from the magnetostatic interactions between localized spins within the material [1]. Dipole-dominated spin waves offer valuable insights into long-range spin dynamics and interactions [2].

Several types of dipole-dominated spin waves exist, each with distinct characteristics and applications in spintronic devices:

Magnetostatic backward volume spin wave mode (MBVM): *M* and *k* are coplanar and parallel to each other within the sample plane. The dispersion relation[135] is:

$$f_{MBVM} = \frac{\gamma}{2\pi}\sqrt{H\left(H + 4\pi M_s * \frac{1-e^{-2kt}}{kt}\right)} \tag{2.8}$$

Damon-Eshbach (DE) mode/ Magnetostatic surface spin wave mode (MSSW): *M* and *k* are situated within the sample plane and are orthogonal (perpendicular) to each other. The dispersion relation without any exchange energy contributions is[146]:

$$f_{DE\ or\ MSSW} = \frac{\gamma}{2\pi}\sqrt{H(H + M_s) + 2\pi {M_s}^2(1 - e^{-2kt})} \tag{2.9}$$

Magnetostatic forward volume mode (MFVM): Here, the magnetic field is oriented perpendicular to the plane of the film, while the spin wave propagates parallel to the surface. The dispersion relation of this mode takes the following form[147]:

$$f_{MFVM} = \frac{\gamma}{2\pi}\sqrt{(H - 4\pi M_s)\left(H - 4\pi M_s * \frac{1-e^{-2kt}}{kt}\right)} \tag{2.10}$$

2.5. Spin waves in confined magnetic structures

In thin magnetic films, the demagnetization field is typically negligible owing to the distinct magnetic charges that form at their boundaries, which are widely spaced. However, in confined magnetic structures[148,149] characterized by dimensions in the sub-micron or nanometer scale, the demagnetization field becomes noteworthy due to the close proximity of magnetic poles situated at the edges. This phenomenon is intricately influenced by the imposed boundary conditions, thereby impacting the response of spin waves across diverse modes within the system. Examples of such confined systems encompass magnetic dots[150–152], interconnected dots[153,154], antidots[150,151,155–157], rings[158,159], bi-component magnetic structures[160–162], among others. The count of spin wave modes

within these systems notably increases, primarily influenced by parameters such as shape[163,164], size[113], arrangement of structures[165–169], as well as the magnitude and orientation of external bias magnetic fields[163,170]. These combined factors intricately determine the behavior and distinct characteristics exhibited by spin waves within the confined magnetic systems. Based on the observation of various kinds of spin wave modes, some of them are discussed in the following[113]:

Centre mode: This particular type of spin wave mode typically spans a significant portion of the patterned structures, often concentrated around the central region. The intensity and frequencies of this centre mode typically exhibit a Kittel-like variation with slight decrease in the effective magnetization as opposed to the saturation magnetization[171].

Edge mode: Edge modes refer to the localized spin wave modes that occur in regions with reduced effective fields, i.e., at the edges of the patterned structures. Consequently, the typical frequency associated with edge mode is much lower compared to that of the centre mode[171].

Quantized mode: Depending on the specific shape and geometry of magnetic structures, standing spin wave modes can form within laterally confined magnetic structures due to reflection of the spin waves at the boundaries and the subsequent superposition. Each of these modes is characterized by a quantization number, which corresponds to the number of nodal planes present within the structure in a particular direction[111].

Figure 2.2(a) illustrates the power and phase distribution of three discrete spin wave modes within a 2D elliptical dot structure (at H = 1 kOe along the x-axis). Conversely, Figures 2.2(b) and (c) depict the schematic representation of the effective field distribution for these modes and the varying quantization numbers associated with the quantized PSSW mode within the system, respectively.

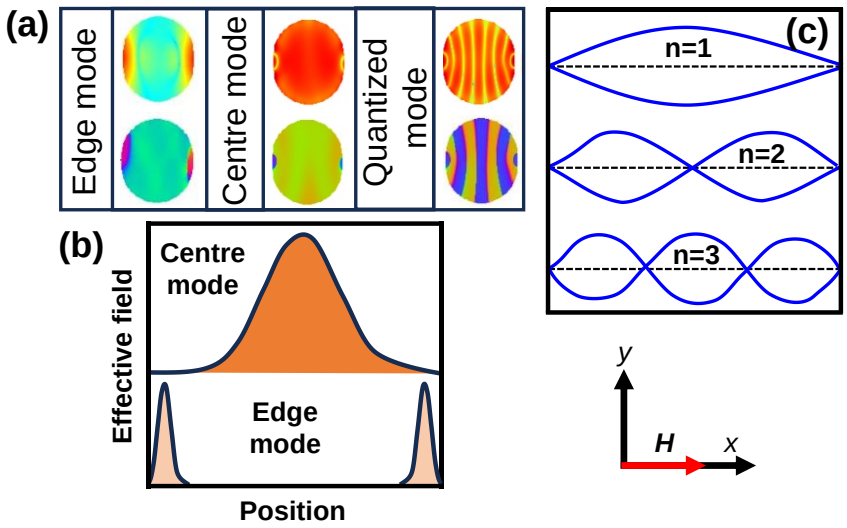

[2]**Figure 2.2.** (a) Simulation results depicting the power and phase profiles of three different types of spin-wave modes observed in permalloy elliptical dot structures. (b) Visualization showing the distribution of the effective field within the sample for two specific spin wave modes. (c) Calculation method for determining the quantization number associated with perpendicular standing spin wave modes, (e.g., PSSW mode).

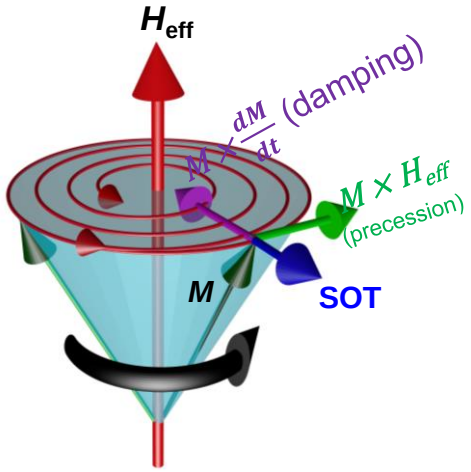

[3]**Figure 2.3.** The illustration provides a visual understanding of how various torque terms (precessional, damping and SOT term) interact within the LLG equation under the influence of the effective field (H_{eff}).

2.6. Magnetic Damping

Magnetic damping encompasses the intricate energy dissipation mechanisms responsible for the gradual loss of magnetization within a magnetic system over time to reach equilibrium. This phenomenon holds high significance in various technological domains due to its key role

in determining how rapidly a magnet stabilizes following alterations in its magnetic field. Notably, magnetic recording technologies heavily rely on a comprehensive understanding and precise control of damping effects. Within the domain of MRAM, for instance, heightened damping in memory pixels facilitates expeditious data-writing processes. Damping manifests in two primary categories: intrinsic and extrinsic damping[172]. Intrinsic damping emanates from inherent material attributes and ensues from electron interactions with the crystal lattice[173]. Conversely, extrinsic damping arises from external influences such as two-magnon scattering[174,175] and magnetic inhomogeneity due to defect states and rough sample surfaces. Through sophisticated methodologies like optical heating or meticulous interface engineering, researchers can manipulate these variables to tailor magnetic material damping properties, effectively customizing them to suit specific applications within diverse technological landscapes. In spintronics, both low and high-damping materials have unique advantages. Low damping materials are useful in applications requiring long spin coherence times for devices like spin logic gates where spin information needs to travel long distances without degradation[176,177]. Conversely, high-damping materials offer rapid spin relaxation, making them suitable for memory and storage applications where fast switching of magnetization states is necessary for efficient data writing[178]. By strategically choosing materials with the appropriate damping properties, spintronic/magnonic devices can achieve optimal performance for their specific function.

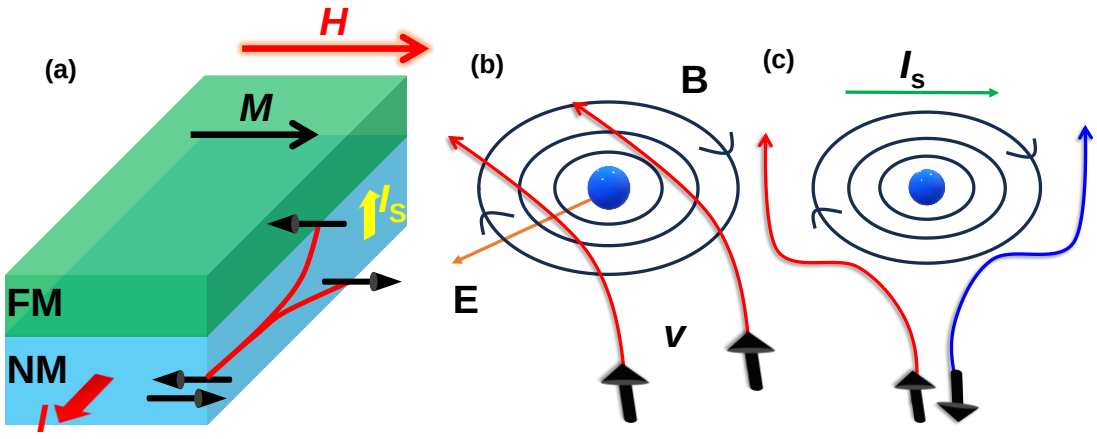

[4]**Figure 2.4.** (a) Diagram illustrating the injection of a pure spin current Is into a ferromagnetic layer, generated as a result of the spin Hall effect (SHE) occurring in a heavy metal (HM). (b) Schematic depicting the skew scattering mechanism, wherein spin-up (↑) electrons are scattered consistently in one direction regardless of their approach side, encountering an impurity characterized by a scattering potential V(x,y,z). This scattering process induces an effective magnetic field (B) due to spin-orbit interaction (SOI). (c) Pictorial representation demonstrating the side-jump mechanism within the context of spin transport phenomena.

2.7. Spin Hall Effect (SHE)

The spin Hall effect (SHE)[60] offers a powerful tool for manipulating spin currents in spintronics, a field that explores the use of electron's "spin" degrees of freedom for information processing and storage. This effect arises in materials with strong spin-orbit interaction (SOI), like platinum (Pt), tantalum (Ta), or tungsten (W). SOI describes the coupling between an electron's spin and its orbital angular momentum. The generation of pure spin current is shown schematically in Figure 2.4 (a).

The Core Mechanism:

(a) Skew Scattering Mechanism: The key to SHE lies in SOI. When a free electron travels past a negatively charged ion within the material, the electron experiences an effective magnetic field that arises from the Lorentz transformation of the ion's electric field ($B \propto (v \times E)$). This effective magnetic field interacts with the electron's spin angular momentum, resulting in a Zeeman energy – an energy difference based on the relative orientation of the spin and the magnetic field. The effective magnetic field generated by the SOI is not uniform across the material. This non-uniformity exerts a force on the electron's magnetic moment ($F \propto \nabla(\sigma.B)$). Electrons with their spins oriented "down" (opposite to the effective magnetic field) are pushed towards regions with stronger magnetic fields, while electrons with "up" spins experience the opposite force. This spin-dependent scattering process separates electrons with different spin orientations, resulting in the generation of a pure spin current perpendicular to the direction of the applied electrical current[179,180]. In simpler terms, the electrical current acts as a pump, and SOI acts as a separator, creating a current consisting solely of electrons with a specific spin orientation (Figure 4(b)).

(b) Side Jump Mechanism: Because of the low symmetry due to SOI in the system, the electrons with opposite spins deviate either spatially or by a certain angle. This quantum mechanical mechanism results in a side-wise "jump" of opposite spins and results SHE in the system[181] (Figure 4(c)).

Significance for Spintronics:

The capacity to create and control spin currents is essential for spintronic devices. Traditional electronics rely on the flow of charge, but spintronics leverages the electron's spin as an additional information carrier. The SHE provides a mechanism to efficiently convert an electric current into a pure spin current, opening doors for novel spintronic applications. Pure spin current offers several advantages over traditional charge current or spin polarized current, including reduced energy dissipation due to the absence of Joule heating ($as\ E.J_S =$

0) and the potential for non-volatile memory due to the inherent stability of electron spin states.

Control and Applications:

By manipulating the material properties that influence SOI strength, researchers can tailor the characteristics of the generated spin current. Furthermore, the direction of the spin current can be controlled by reversing the direction of the applied electrical current. This tunability makes SHE a versatile tool for various spintronic applications, including spin logic gates[182], spin-based transistors[183], and MRAM[184].

2.8. Spin Pumping

Spin pumping, an important and well-studied phenomenon in spintronics facilitates the transfer of spin angular momentum from a FM layer to an adjacent NM layer due to the spin chemical potential difference between those two layers. This transfer manifests as a pure spin current, playing a vital role in various spintronic devices. Pioneered in 1988 by Hurquint et al.[185], spin pumping arises from the precession of magnetization within the FM layer induced by an external excitation. They proposed that this precessing magnetization generates a nonequilibrium spin accumulation at the interface between the FM and NM layers. This spin accumulation diffuses into the NM layer and eventually dissipates through spin-flip processes (Figure 4(a)). Berger et al. (1996) showed damping enhancement in NM/FM/NM spin-valve structures[186]. They observed that the damping parameter (α), which characterizes the decay rate of the precession amplitude, increases due to spin pumping. This enhancement depends on the thickness and material properties of different layers. Tserkovnyak and Brataas (2002) provided a theoretical foundation using time-dependent adiabatic scattering theory[187]. Their work predicted the pumping of a spin current (I_{Spump}) from the FM layer into the NM layer. This spin current magnitude can be expressed using the spin-mixing conductance and the rate of magnetization precession. The spin accumulation at the NM/FM interface plays a crucial role in damping enhancement. This accumulation is influenced by the spin backflow factor (β), which describes the fraction of spin current reflected into the FM layer[188]. A higher damping enhancement is observed when β approaches zero, indicating minimal spin backflow. For efficient spin pumping, the thickness of the NM layer needs to be greater than the spin diffusion length. This ensures the NM layer acts as an effective spin sink, allowing the spin current to propagate and dissipate within it. Heavier metals like W, Ta, Pt, or Pd are preferred choices for the NM layer due to their higher spin-flip relaxation rate (r):

$$r \propto Z^4; \text{ Z: atomic number} \quad (2.11)$$

2.9. Spin-Orbit Torque (SOT)

SOT[189,190] is a groundbreaking phenomenon in spintronics, offering a new avenue for manipulating the magnetization of materials. Unlike spin-transfer torque (STT)[191,192], which relies on the direct transfer of angular momentum between different magnetic layers, SOT utilizes the intriguing interplay between an electron's spin and its orbital motion, known as spin-orbit coupling (SOC). This unique coupling gives rise to various mechanisms that generate torque on the magnetic moments within a material or heterostructure.

2.9.1. Mechanisms of SOT

Several mechanisms contribute to SOT, each with its unique characteristics. Here are some prominent examples:

Spin Hall Effect (SHE): As described earlier, SHE provides a powerful method for generating a pure spin current perpendicular to an electric current[60]. In an SOT context, this spin current can exert a torque on the magnetization of a adjacent ferromagnetic layer.

Rashba-Edelstein Effect: This effect arises in materials with broken inversion symmetry, leading to a spin splitting of electron energy bands[87]. When an electric current passes through such a material, the spin-orbit interaction acts to deflect electrons with different spins, resulting in a net spin current that can exert torque on a ferromagnetic layer.

Orbital Hall Effect: Similar to the SHE, this effect creates a transverse charge current due to the spin-orbit interaction[193,194]. However, in this case, the deflection is based on the orbital character of the electrons, which can indirectly influence the magnetization through various mechanisms.

Beyond these fundamental mechanisms, research is exploring other avenues for generating SOT, including thermally or phonon-driven spin torque and magnon-driven spin torque. These emerging mechanisms offer a broader toolbox for manipulating magnetic states through various stimuli.

2.9.2. Field-like SOT and damping-like SOT

SOT can be further categorized into two key components based on their effect on magnetization: field-like and damping-like. Field-like SOT[195,196] acts akin to an external magnetic field, exerting a torque that preferentially aligns the magnetization with a specific current-dependent direction. This directional influence makes it suitable for switching the magnetic state. Damping-like SOT[197], on the other hand, resembles the intrinsic damping

mechanism but does not directly reduce magnetization. Instead, it influences the precession dynamics, acting as a current-controlled "acceleration" or "deceleration" for the magnetization precession depending on the material properties. The damping-like and field-like terms are given by the following equations[198–200]:

$$\tau_{DL} \propto J_e \, \hat{m} \times (\hat{\sigma} \times \hat{m}) \tag{2.12}$$

$$\tau_{FL} \propto -J_e \, (\hat{\sigma} \times \hat{m}) \tag{2.13}$$

2.9.3. Efficiency and Advantages of SOT

One of the most exciting aspects of SOT lies in its potential for energy-efficient spin manipulation[190]. Unlike STT, where the angular momentum transfer per electron is limited to a value of one, some SOT mechanisms can achieve an efficiency exceeding one. This translates to lower switching currents needed in SOT-based devices compared to STT devices. This not only reduces energy consumption but also minimizes heating effects, which can be detrimental to device performance and reliability.

Furthermore, SOT offers several advantages over STT[201]:

Separate Read and Write Paths: In SOT devices, the current path for reading the magnetic state can be separated from the writing path. This enhances reliability by avoiding the need for large write currents that could damage the ultrathin tunnel dielectric layers used in STT-MRAM.

Simplified Device Structure: Some SOT mechanisms do not require a second magnetic layer, simplifying device fabrication and potentially leading to more compact and efficient spintronic devices.

2.9.4. Applications of SOT

The diverse advantages of SOT propel its exploration in a wide range of spintronics applications, including faster-switching and potentially lower-power MRAM[202], neuromorphic circuits mimicking biological neurons[203], race-track memory for high-density storage[204], nano-oscillators generating terahertz waves for communication and imaging, and more[205].

2.10. Magneto-optical Kerr effect (MOKE)

When linearly polarized light is reflected from the surface of a magnetized sample, the plane of polarization of the reflected light gets rotated and the light becomes elliptically polarized. This effect is popularly recognized as the magneto-optical Kerr effect (MOKE) and the corresponding rotation of the plane of polarization is called the Kerr rotation (θ_k). If ε_k

represents the ellipticity and r, k denotes the parallel and perpendicular component of the electric field vectors (concerning the incident light), then[206]:

$$\theta_k + i\varepsilon_k = \frac{k}{r} \tag{2.14}$$

2.10.1. Origin of MOKE

Macroscopic viewpoint: Electrons in a magnetic medium respond to circularly polarized light with circular motion, but linearly polarized light (containing both left and right circular components) averages this motion out. When a magnetic field is present, the Lorentz force acts differently on these circular motions due to their opposing directions. This alters the electrons' precession and modifies the material's response to each polarization-state (described by the dielectric tensor). Consequently, upon reflection from a magnetized surface, the originally equal left and right circular components of the incident light experience different phase shifts, transforming the reflected light from linearly to elliptically polarized. Analyzing this change in

Microscopic viewpoint: The MOKE stems from SOC, where an electron's motion under light's electric field (represented by $S \times \nabla V$, where S is spin and ∇V is the electric field) alters its spin. While present in both FM and NM materials, MOKE is stronger in FM materials. Here's the key: the inherent imbalance of up-spin and down-spin electrons in FM materials polarization allows MOKE to probe the magnetic properties of the material[206,207]. makes

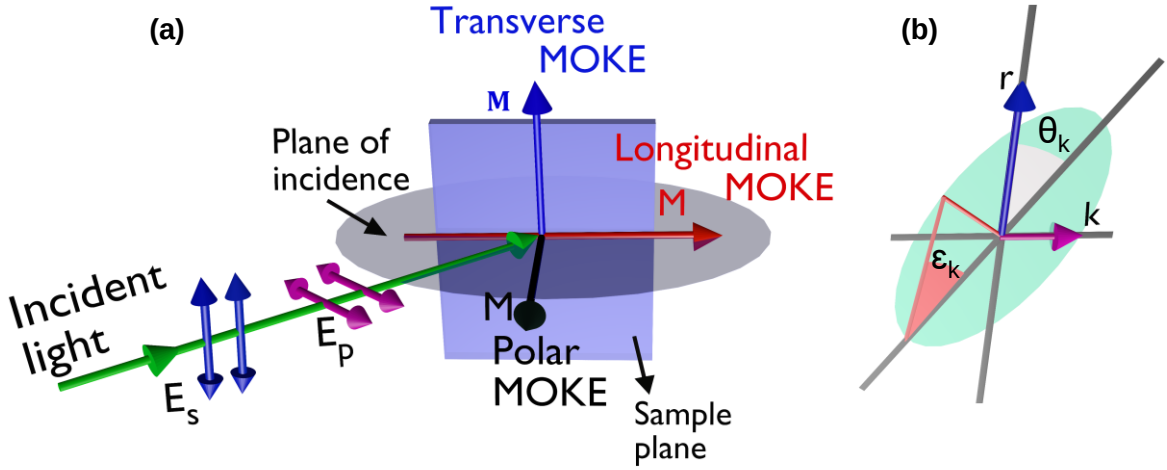

[5]**Figure 2.5.** (a) Depiction of the polar, longitudinal, and transverse configurations of the magneto-optical Kerr effect (MOKE) applied to a sample exhibiting magnetization (M). (b) Illustration of the geometric arrangement governing Kerr rotation (θ_k) and Kerr ellipticity (ε_k) within the framework of the MOKE.

SOC more sensitive to the electron's spin direction under light's influence. This sensitivity translates to a more pronounced difference in how the material responds to left and right

circularly polarized light, ultimately resulting in the characteristic change of reflected light polarization observed in MOKE and used to probe magnetic properties[208–213].

2.10.2. Different MOKE geometries

The MOKE exhibits distinct characteristics depending on the relative orientation of the magnetization vector within the sample, the sample surface, and the plane of light incidence. This distinction leads to three main geometries (Figure 5 (a)) used in MOKE measurements:

Polar MOKE: In this geometry[214], the magnetization is oriented perpendicular to the sample surface yet lies parallel to the plane of light incidence.

Longitudinal MOKE: In this geometry[215], the magnetization lies within the plane of the sample and is parallel to the plane of light incidence. Here, the magnetization vector is parallel to the surface and points in the same direction as the light wave propagation.

Transverse MOKE: The magnetization lies within the plane of the sample but is perpendicular to the plane of light incidence. This geometry[216] is exclusive to p-polarized light and offers advantages for studying anisotropic materials where the magnetic properties vary depending on direction.

Chapter 3

Methodologies

In this chapter, I will begin with a brief summary of the nanofabrication processes for both non-magnetic and ferromagnetic materials, followed by an exploration of various thin film deposition techniques. The chapter then presents a range of experimental setups used to measure GHz-THz dynamics pertinent to this PhD research. Key physical theories that form the basis of these experimental tools are briefly outlined. Detailed descriptions of the instrumentation, including their operational procedures and detection mechanisms—crucial components of any experimental tool—are provided. Finally, the chapter concludes with an in-depth discussion of various commercially available simulation packages and custom-built simulation tools, offering comprehensive insights into the subjects under study.

Experimental Techniques

The experimental techniques cover the sample fabrication and growth, characterization and measurement techniques used for the work done in this thesis as described below.

3.1. Lithography Techniques

Lithography is a fundamental process in the fabrication of integrated circuits (ICs). It involves transferring well-defined patterns onto a semiconductor substrate, typically silicon, to create the tiny transistors and interconnects vital for modern electronics. The term "lithography" derives from Greek roots, with "lithos" referring to stone, and "graphia" to writing[217]. While ancient lithography indeed involved engraving patterns onto stone, modern electron-beam, ion-beam and optical lithography utilize electron-beam, ion-beam or photon/light to define patterns on substrates such as silicon, quartz, or corning glass.

3.1.1. Electron-beam lithography

Electron-beam lithography (EBL)[218,219] is an advanced nanofabrication technique that employs a focused beam of electrons to intricately pattern custom designs onto a thin resist layer positioned atop a substrate. This technology stands out for its exceptional resolution capabilities, capable of achieving feature sizes below 10 nm, which is crucial for applications in nanotechnology and cutting-edge electronics. Unlike traditional photolithography methods, EBL does not rely on pre-patterned masks, granting designers greater flexibility in creating complex structures and allowing compatibility with a wide range of materials and resist chemistries. The process of EBL begins with a precisely controlled electron beam emitted from an electron gun. This beam is then focused and directed onto the resist-coated

substrate, where it selectively exposes areas according to the desired pattern. The exposed regions undergo chemical or physical changes, enabling subsequent development steps to transfer the pattern onto the substrate.

One of the primary advantages of EBL lies in its ability to create ultra-fine features with unparalleled accuracy and detail. This capability is particularly valuable in the development of next-generation electronic devices, micro electromechanical systems (MEMS), high-resolution photomasks for semiconductor manufacturing, and the fabrication of novel nanostructures with tailored properties. However, despite its remarkable resolution and versatility, EBL is inherently a slow and serial process compared to photolithography techniques. This limitation restricts its widespread use in high-volume manufacturing where speed and throughput are critical considerations. Nonetheless, EBL remains indispensable in research and development environments, where the focus is on pushing the boundaries of miniaturization and precision.

3.1.2. Photolithography

Photolithography[220,221], in contrast to EBL, relies on the use of light, typically ultraviolet (UV) light, to transfer patterns onto a substrate. This technique involves exposing a photosensitive resist layer to light through a mask, which contains the desired pattern.

The core process of both lithography relies on the following steps (Figure 3.1):

Substrate cleaning: The substrate where the pattern will be drawn undergoes a thorough cleaning process to ensure its purity and suitability for the desired application. Initially, it is ultrasonicated in acetone to eliminate inorganic impurities, and then ultrasonicated in isopropyl alcohol (IPA) to remove organic residues. Subsequently, the substrate is dried using dry nitrogen to prepare it for the patterning process.

Electron-beam resist/Photoresist coating: During the process, a layer of electron-beam/photoresist is applied using spin coating, wherein the substrate spins rapidly to ensure uniform distribution and achieve the desired thickness of the resist layer. The speed of rotation plays a defining role in determining both the uniformity and thickness of the resist,

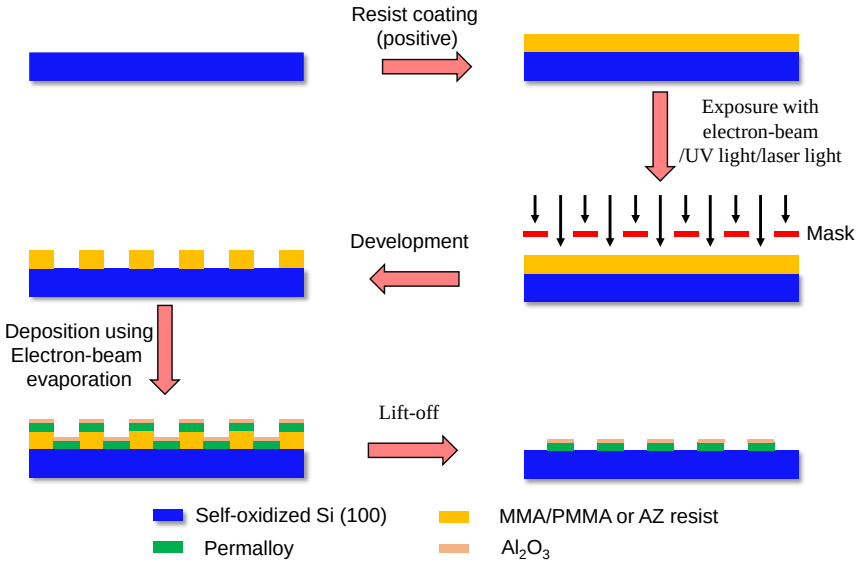

[6]**Figure 3.1:** Schematic representation of the steps involved in the electron-beam (photo) lithography using positive resist.

which are essential factors for obtaining the desired resolution of the pattern. For the preparation of gold wire structures, a positive resist AZ-1512[222] is used. On the other hand, for the preparation of Py (permalloy) and Co (cobalt) dot structures, a PMMA/MMA bilayer resist is utilized (thesis work).

Soft bake: The coated substrate undergoes a low-temperature heating process, typically around 100°C. This step serves multiple purposes: first, it evaporates the excess coating solvent, ensuring a uniform and dry resist layer. Second, it compacts and hardens the resist, enhancing its adhesion to the substrate. This improved adhesion makes the film less susceptible to contamination and ensures its stability during subsequent processing steps, ultimately contributing to the overall quality and durability of the patterned structures.

Mask alignment: A meticulously designed mask or digital pattern created using software such as CAD, showcasing the desired layout or structure, is carefully aligned over the resist-coated substrate. This alignment process ensures that the pattern on the mask corresponds accurately to the intended location on the substrate. It is a crucial step in photolithography or electron beam lithography processes, where the mask acts as a template for transferring the pattern onto the resist-coated surface with high precision and accuracy.

Electron-beam exposure/laser exposure: During the photolithography process, intense UV or laser light passes through the mask, or an electron beam falls during EBL. This exposure varies depending on the type of resist used—positive or negative. For positive resist, the

exposed region becomes more soluble in the developer solution, while for negative resist, the exposed region becomes less soluble. The fundamental mechanism at play here is the chemical reaction triggered by the interaction of light or electron-beam with the resist material. In this thesis work, positive resist has been employed, meaning that the areas exposed to light or electron-beam become more soluble. This differential solubility allows for the targeted removal of either the exposed or unexposed regions of the resist during the development stage, thereby creating the desired pattern on the substrate.

Development: After exposure to light or an electron beam, a chemical solution is used to remove either the exposed regions (in the case of positive resist) or the unexposed regions (for negative resist) of the resist layer. This process results in a patterned layer on the substrate that mirrors the design on the mask.

Post-exposure bake: Optionally, after the development process, a post-exposure bake may be conducted to further solidify the remaining photoresist pattern. This additional step helps improve the durability and stability of the patterned resist, making it more resistant to damage during subsequent processing steps or handling.

Depostion of thin film: Thin layers of the required films are deposited using various physical vapor deposition (PVD)[223] techniques. These techniques include processes such as thermal evaporation, sputtering, and electron beam evaporation. We have mostly utilized the electron-beam evaporation technique for the deposition of various films in the thesis works.

Lift-off process: In the final step of the process, a lift-off technique is employed to remove the undesired portion of the pattern. This method involves a chemical reaction to dissolve the "more soluble" areas of the resist, resulting in the desired pattern remaining on the substrate. We used acetone for this purpose. Additionally, plasma etching is performed to eliminate any residual resist material that may remain after the lift-off process using inductively-coupled plasma reactive ion etching (ICPRIE) system. Plasma etching is a highly controlled process that uses reactive ions to selectively remove materials, ensuring precise and clean removal of the resist residues without affecting the underlying substrate or patterned layers.

3.2. Thin Film Deposition Techniques

3.2.1. Sputtering

Sputtering, an important technique within PVD[223], stands out for its exceptional control and precision in the creation of high-quality thin films, multilayers and heterostructures. This method relies on the interaction between a plasma, typically generated from an inert gas like

Argon[224] within a vacuum chamber, and a target material. The target, serving as the cathode, is bombarded by accelerated positive ions (Ar+) formed through collisions between free electrons and gas atoms. This energetic bombardment ejects atoms from the target material, which subsequently condenses on a precisely positioned substrate, growing the desired thin film with atomic-level precision, as illustrated in Figure 3.2. An optimally

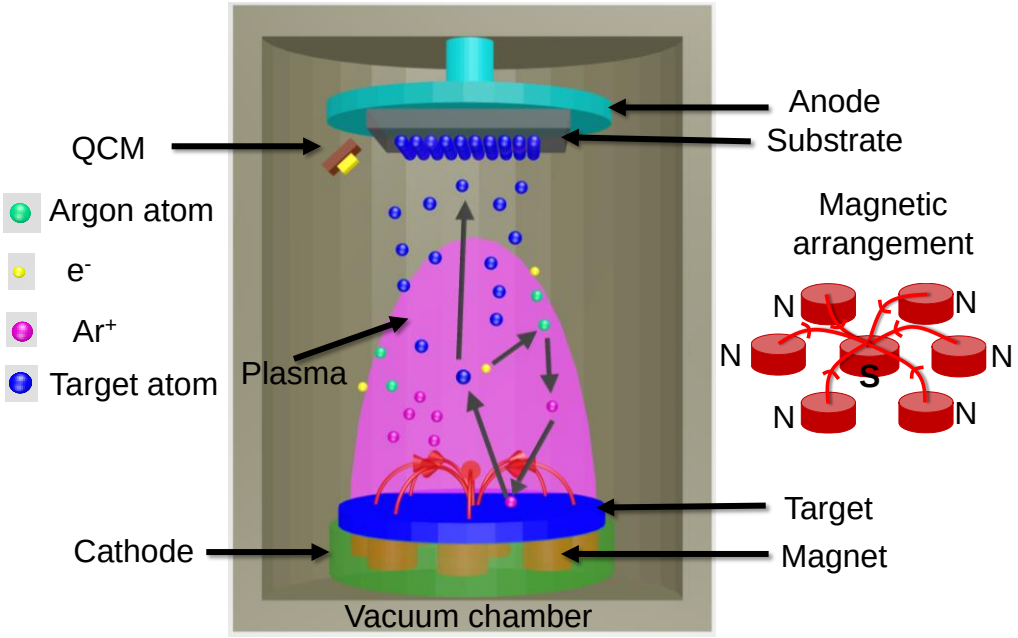

[7]**Figure 3.2:** A pictorial illustration of the magnetron sputtering system. The inset shows the magnetic arrangement behind the cathode.

positioned quartz crystal microbalance (QCM)[222], consisting of a thin quartz crystal oscillator, is used to measure the rate of deposition and thickness of the film. It works based on the principle that when an alternating voltage is applied to the crystal, it oscillates at its resonant frequency. The resonant frequency of the crystal depends on its mass. Now, when a film is deposited on the crystal surface during sputtering, the mass of the crystal changes, causing a shift in its resonant frequency.

While the conventional DC sputtering method provides a cost-effective solution for conductive target materials, its limitations include sluggish deposition rates and excessive target heating due to sustained electron bombardment. Magnetron sputtering, a revolutionary variant, addresses these drawbacks through the strategic placement of magnets behind the cathode (as shown in the inset of Figure 3.2). These magnets confine electrons in a looped path (following a cosine trajectory), significantly increasing the probability of ionization and enhancing deposition rates. Additionally, this magnetic

configuration reduces electron velocity near the target, minimizing substrate heating. This paves the way for faster deposition and the creation of intricate layered structures critical for advanced device functionalities.

The selection between DC and RF sputtering hinges on the target's electrical conductivity[225]. The cost-effective DC sputtering is ideal for conductive materials due to its straightforward implementation. However, for insulating targets, DC sputtering encounters significant challenges. The inability to dissipate charge buildup effectively can lead to arcing and non-uniform deposition. RF sputtering, with its constantly alternating current, elegantly overcomes these hurdles. The rapid polarity reversal prevents charge accumulation, minimizes phenomena like "race-track erosion"[226,227] (non-uniform target wear), and ultimately fosters uniform deposition across insulating target materials. RF sputtering can sustain a stable plasma at lower gas pressures translates to a more efficient deposition process. This translates to a significant reduction in wasted target material due to minimized re-sputtering (re-deposition of ejected atoms) and a more economical use of expensive target materials like platinum or iridium. Furthermore, RF sputtering offers superior uniformity across large-scale substrates, making it an essential technique for high-volume thin film production in industries like photovoltaics and microelectronics.

On the other hand, reactive sputtering[228] is a variant of conventional sputtering that involves introducing a reactive gas (such as oxygen or nitrogen) into the sputtering chamber along with the inert gas (Argon). This reactive gas interacts with the sputtered material, leading to the formation of a compound film on the substrate. Reactive sputtering's primary advantage is its capability to deposit compound films. with controlled stoichiometry and tailored properties. By adjusting the ratio of reactive gas to inert gas, the deposited film's composition can be accurately controlled, making it particularly useful for applications requiring specific chemical characteristics or compound formation (such as Ta-N[229], TaO_x[230], etc).

3.2.2. Electron-beam evaporation

Electron-beam evaporation (EBE)[231], another important technique within PVD[223], stands out for its versatility and ability to deposit thin films of high quality of a wide range of materials. This method leverages the power of a focused electron beam to precisely heat and evaporate the target material within a chamber of high-vacuum ($\sim 10^{-7} - 10^{-8}$ Torr). The electrons, thermionically emitted from a heated tungsten filament, are accelerated and precisely directed using magnets. Due to thermionic emission[232] electrons of the target

materials gain enough energy to overcome the work function and overcome the attractive forces. Upon impact with the target material (typically held in a water-cooled crucible), the electron beam transfers its kinetic energy, converting it into thermal energy. This localized heating efficiently elevates the target's temperature to its boiling point, inducing evaporation and the creation of a vapor flux, as shown in Figure 3.3. The emission of electrons, or electron evaporation, occurs at varying voltages depending on the material's work function[233].

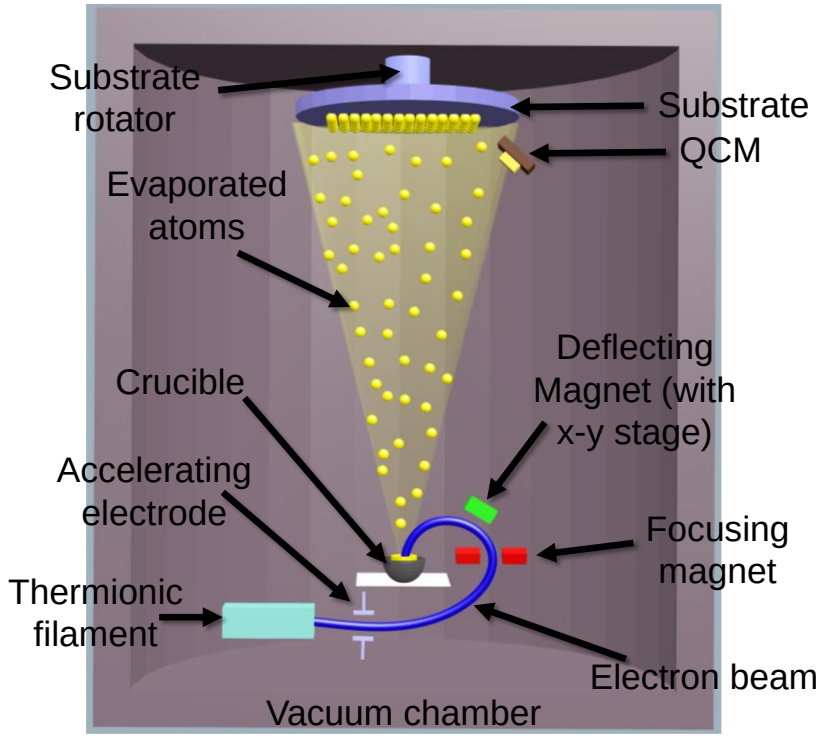

[8]**Figure 3.3:** Pictorial illustration depicting the electron beam evaporation (EBE) system.

The essence of EBE lies in the precise control over the electron beam. Unlike thermal evaporation[234], where the entire crucible is heated, EBE concentrates the energy onto a specific area of the target material. This focused heating minimizes thermal diffusion within the target, leading to a much purer vapor source for film deposition. The evaporated material then travels almost in a straight line due to the high vacuum environment, reaching the precisely positioned substrate. To ensure uniformity of the film, the substrate holder is frequently rotated at a uniform speed during deposition., especially for films deposited on micro or nanostructures where precise control over sidewall coverage is crucial. A significant advantage of EBE is its ability to deposit a broad spectrum of materials, encompassing both non-magnetic elements like gold (Au), titanium (Ti), insulating oxides like aluminum oxide (Al_2O_3) and silicon dioxide (SiO_2), as well as ferromagnetic elements like nickel (Ni), iron (Fe), cobalt (Co), $Ni_{80}Fe_{20}$ etc. This versatility stems from the precise control over the electron

beam's energy density, allowing for the controlled evaporation of even high melting point materials. Additionally, the load-locked chamber system within an EBE setup minimizes contamination by allowing sample introduction and removal without compromising the high vacuum environment within the main deposition chamber. This ensures a clean and controlled environment for the creation of high-purity thin films, a critical requirement for many advanced material systems and device functionalities.

3.2.3. Pulsed-laser deposition

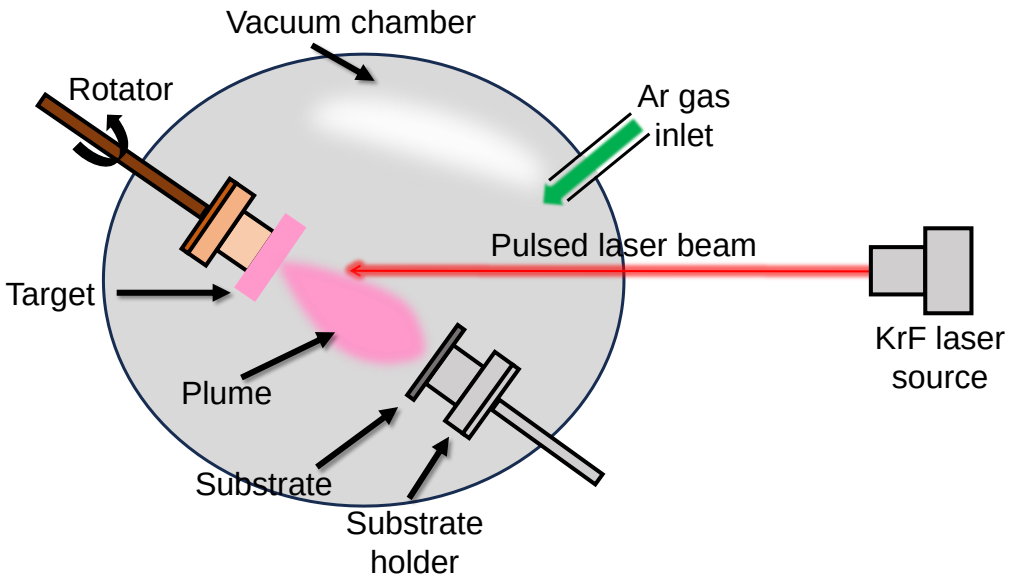

[9]**Figure 3.4:** A schematic illustration of the pulsed laser deposition (PLD) system.

Pulsed laser deposition (PLD)[235] stands out as a revolutionary technique within PVD for its ability to create thin films with exceptional control and near-perfect transfer of material properties. Unlike thermal evaporation methods that rely on controlled heating, PLD harnesses the power of pulsed laser beam to achieve material ablation with atomic-level precision. At the heart of PLD lies the dynamic interplay between the high-powered laser and the target material. Here fast laser beam acts as a microscopic hammer, delivering a concentrated surge of energy onto a confined area of the target's surface. KrF/ArF excimer lasers (wavelength 248 nm, and 193 nm, respectively) are generally used for their ability to deliver high-energy pulses of UV light, which are well-suited for ablating a wide variety of target materials including metals, ceramics, and polymers. This impulsive energy transfer far exceeds the vaporization point of the material, triggering a miniature explosion on the target, which results in the creation of a plume composed of atoms, ions, and even electrons that

erupts from the impact zone, propelled outwards by the sheer force of the ablation phenomenon.

This transient plume acts as the source material for film deposition. The energetic species within the plume travel ballistically across the vacuum, propelled toward the precisely positioned substrate. Upon reaching the substrate, these energetic species condense to its surface, meticulously building the desired thin film one atom at a time (Figure 3.4). A key advantage of PLD lies in its ability to directly transfer complex materials, including stoichiometric compounds,

from the target to the growing film[236,237]. Unlike other PVD techniques where the source material might decompose during the deposition process, PLD's laser ablation preserves the target's original composition. This allows for the creation of intricate thin films with properties that closely mirror the target material, a feat particularly valuable for replicating the functionalities of novel materials in device applications. Additionally, PLD offers the potential for depositing films that are not readily achievable through other methods, such as those containing metastable phases or exotic material combinations.

The precise nature of laser ablation in PLD also translates to excellent control over film thickness and composition. By carefully manipulating the laser parameters like pulse fluence (energy density) and repetition rate, and deposition pressure of Ar, one can fine-tune the ablation process and achieve precise control over the amount of material ejected with each pulse. For our topological insulator samples, we have optimized its growth at deposition temperature at a high temperature using a heater attached to the sample holder within the chamber.

3.3. Characterization Techniques

The routine characterization techniques like SEM, AFM/MFM, XRD, VSM, Static MOKE, etc. can be found elsewhere[238].

3.4. Measurement Techniques

3.4.1. Time-resolved magneto-optical Kerr effect (TR-MOKE) microscopy and magnetometer:

3.4.1.1. Need of optical pump-probe technique

Numerous natural phenomena, including atomic movements, molecular oscillations, and interactions between light and matter, occur within exceedingly brief intervals, often measured in picoseconds or even femtoseconds. To effectively capture these ultrafast events, we need measurement methodologies with temporal resolutions approaching the

femtosecond scale. Initial efforts in time-resolved spectroscopy utilized techniques such as stopped-flow[239,240] and flash photolysis[241], achieving resolutions limited to milliseconds or microseconds. However, these methods were constrained by the capabilities of detectors available during the mid-20th century, resulting in temporal resolutions around nanoseconds. This constraint significantly impeded advancements in studying ultrafast dynamics. A pivotal breakthrough arose with the introduction of pump-probe spectroscopy[242–244]. This innovative approach involves utilizing two pulses: a "pump" pulse initiates the desired process within the sample, followed by a "probe" pulse that examines the system after a precisely controlled time delay. By analyzing how the probe pulse interacts with the sample post-pump pulse excitation, one can indirectly observe ultrafast dynamics occurring at femtosecond timescales. This indirect methodology overcomes detector response time limitations, allowing pump-probe spectroscopy to achieve groundbreaking temporal resolutions. The emergence of pump-probe spectroscopy has revolutionized time-resolved investigations across various scientific domains. This powerful technique has empowered researchers to unveil intricate details of dynamic phenomena in materials, chemical reactions, and biological processes, providing unprecedented insights into the ultrafast realm that underpins a significant portion of our universe.

3.4.1.2. Different mechanisms to create ultrafast laser pulse

Mode-locking[245–247] is a technique used to produce ultra-short pulses in lasers by synchronizing the phases of the optical resonator modes. The mechanism entails establishing a consistent phase relationship among the longitudinal modes of the laser cavity. This synchronization leads to the constructive interference of the modes, resulting in the generation of an extremely short, high-intensity pulse. Actively mode-locked lasers offer a versatile approach to generating ultrashort optical pulses ahead of passive-mode locking mechanism. One technique within this domain utilizes acousto-optic modulators (AOMs)[248,249] to achieve mode-locking. The core component is a quartz crystal with a piezoelectric transducer bonded to one side. It induces vibrations (acoustic waves) within the crystal with the application of an RF signal to the transducer. These acoustic waves modulate the refractive index of the crystal through the acousto-optic effect. The crystal is strategically positioned at one end of the laser cavity, close to a laser mirror. To minimize reflection losses from the crystal surfaces, the crystal faces are precisely oriented at the Brewster angle. The applied RF signal, typically ranging from 25 to 50 MHz, launches acoustic waves propagating through the crystal. These acoustic waves create a periodic variation in the refractive index, resulting in Bragg reflection for light traveling at specific wavelengths (Figure 3.9(a)).

Importantly, the Bragg reflection occurs at a frequency twice the RF driving frequency. This effectively creates a dynamic shutter within the cavity, with the transmission properties dependent on the RF signal strength. At the peak of the RF cycle, the acoustic wave intensity is strongest, leading to significant Bragg reflection and high intra-cavity loss for the light. Conversely, when the RF signal reaches zero, the acoustic wave ceases, and the Bragg reflection vanishes. This translates to a clear window for light transmission, effectively opening the shutter. The key to mode-locking lies in the synchronization between the RF modulation period and the laser cavity round-trip time. When these periods are harmonically related, a specific mode with the correct phase relationship experiences minimal loss during each cavity round trip. This preferential treatment allows the favored mode to amplify and dominate the laser output. As the pulse propagates through the cavity, it experiences a phase shift due to the acousto-optic interaction. This periodic phase shift, coupled with the inherent nonlinearities of the gain medium, leads to the formation of short, stable pulses. This mode-locking mechanism is superior for creating ultrafast laser pulses (below ns time-scale) which is significantly different from the well-known Q-switching[250,251] mechanism in the following way:

Aspect	**Q-Switching**	**Mode-Locking**
Principle	Q-switching operates on the principle of manipulating the population inversion within the gain medium of a laser system. This is achieved through controlled pumping of the gain medium until it reaches a steady-state population inversion. The key idea is to store energy in the gain medium and then rapidly release it, leading to the generation of short, high-energy pulses.	Mode-locking, in contrast, is based on synchronizing the phases of different longitudinal modes within the laser cavity. This synchronization is accomplished either actively, using external modulators like acousto-optic (in our case) or electro-optic devices, or passively through techniques such as saturable absorbers. The synchronized phases result in the constructive interference of modes, producing ultrashort pulses.
Energy Release	Rapid release of stored energy in the gain medium	No rapid energy release; emphasis on phase synchronization

Pulse Duration	Typically generates nanosecond pulses or below	Typically generates femtosecond or picosecond pulses
Timing Control	Key principle is timing control: opening the Q-switch at the right moment relative to population inversion buildup	Key principle is phase control: ensuring constructive interference among modes in the cavity
Key Components	Q-switch (rapid switch or modulator)	Active or passive elements for phase synchronization (modulators, saturable absorbers, etc.)
Applications	Suitable for applications requiring high peak powers in short bursts (e.g., laser machining, range finding)	Suitable for applications needing ultrafast processes (e.g., ultrafast spectroscopy, telecommunications)
Output Characteristics	Produces high-energy pulses with relatively longer durations	Produces pulses with extremely short durations and high peak powers

3.4.1.3. Specialties of TR-MOKE technique

In our TR-MOKE microscope-based set-up, the femtosecond oscillator used typically has a pulse width of approximately 80 fs and operates at a repetition rate of 80 MHz. This translates to a single pulse being emitted every 12.5 ns, with subsequent pulses following at intervals of 12.5 ns (e.g., pulse 1 at 12.5 ns, pulse 2 at 25 ns, pulse 3 at 37.5 ns, and so forth). Unlike a streak camera[252] setup, TR-MOKE does not function as a single-shot measurement system; instead, its measurement process unfolds over time, typically spanning several seconds. During this time, the lock-in integration period, which ranges between 1 to 3 seconds, captures the desired signal, while the wait time, ranging from 1 to 2 seconds, allows for system stabilization, background correction and data acquisition as well. Importantly, TR-MOKE operates stroboscopically[253], meaning it records an average response over millions of laser pulses. Despite this averaging, the system's response remains exceptionally stable and consistent across millions of pulses. Consequently, TR-MOKE enables the observation of stable dynamics spanning from femtoseconds to nanoseconds with high precision and reliability.

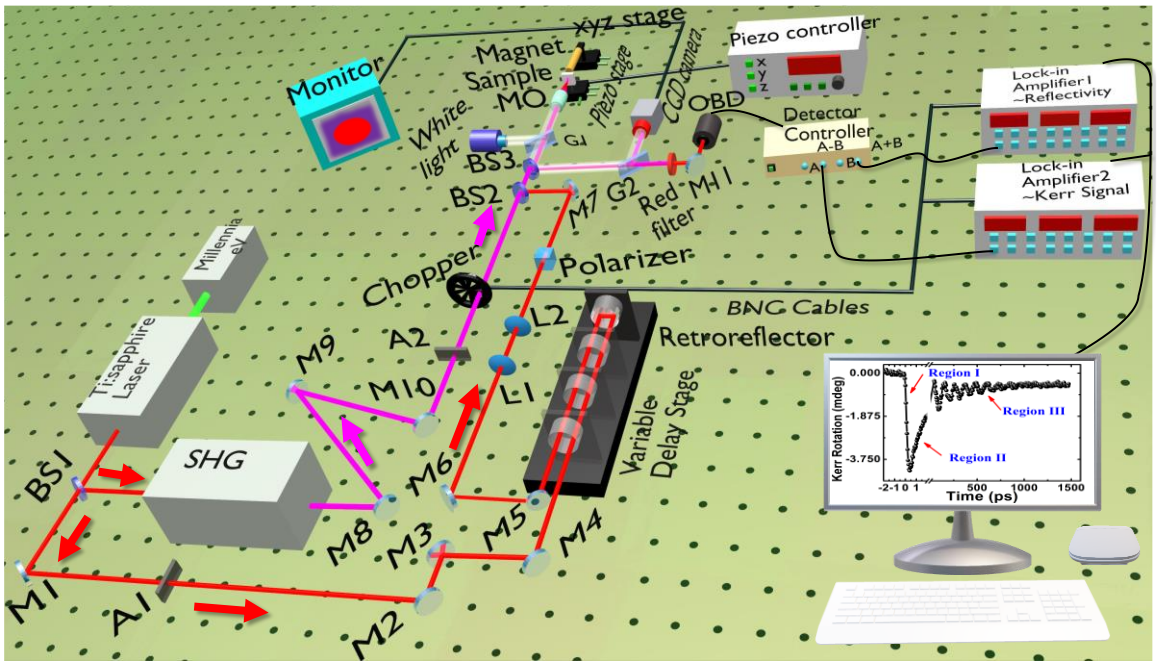

[10]**Figure 3.5:** A schematic diagram of a custom-built colinear microscope-based TR-MOKE set-up.

3.4.1.4. Experimental set-up of TRMOKE microscopy

The TR-MOKE microscope setup described herein employs a Tsunami laser (oscillator with Ti:sapphire as the gain medium) where its fundamental component to produce both a pump beam and a probe beam, as shown in Figure 3.5. Although the output wavelength can be tuned between 680 nm and 1080 nm, we maintain it at a constant 800 nm because Si-based detectors exhibit the highest sensitivity in this range. The initial S-polarized fundamental beam is bifurcated by an optical beam splitter, with the majority of its intensity (70%) directed towards a second harmonic generator (SHG) unit to achieve frequency doubling, thereby creating the pump beam. Here the non-linear crystal, barium beta-borate acts as the frequency-doubler based on the principle of non-linearity. The remaining portion (30%) is utilized as the probe beam. It is made to pass through a series of mirrors followed by a retro-reflector fitted on a motorized scanning stage, which acts as a variable delay generator between the pump and probe beam. It is noteworthy here to mention that our experimental set-up is limited to offer a maximum time-delay of 3.33 ns due to the limited length (L) of the delay stage of approximately 50 cm [$2L = ct; 2 \times 50\ cm = 3 \times 10^{10}\ cm/s\ \times t; t\ \approx 3.33\ ns$; where, "2" factor is due to back and forth motion within the delay stage. Following that, the probe beam passes through a combination of lenses, L1 and L2, which act as a telescopic arrangement, helping in beam collimation and expansion. Next, it passes through the Glan-Thompson polarizer, which confirms the polarization-state of the probe beam and then directed towards the sample surface through the combination of mirrors and beam-

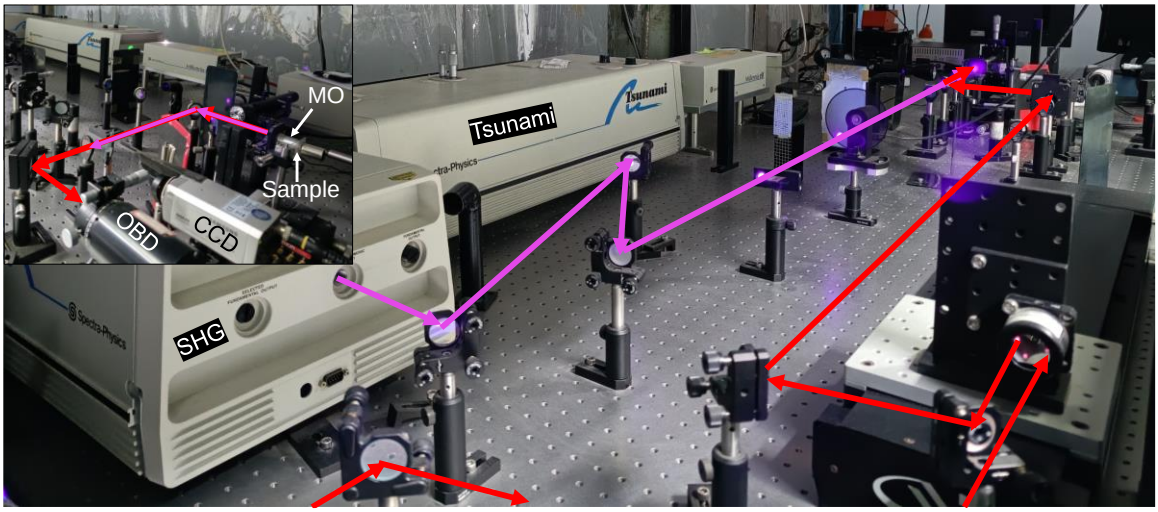

[11]**Figure 3.6:** A photo of the TR-MOKE microscope set-up in Prof. Anjan Barman's laboratory at the S.N. Bose National Centre for Basic Sciences in Kolkata, India.

combiners for eventual coalescence with the pump beam. The pump beam, having undergone similar intensity attenuation and fundamental beam component removal, also converges at the beam combiner. Here, the collinear combination of the probe and pump beams is facilitated. A chopper modulates the probe beam's frequency at approximately 2 kHz, enhancing compatibility with lock-in detection methodologies. The probe beam, tightly focused onto the sample surface using a microscope objective (MO) with 40× magnification and a numerical aperture of 0.65, achieves a diffraction-limited spot size of approximately 800 nm. Spatial overlap with the pump beam occurs at the sample point, albeit with slight defocusing due to chromatic aberration. The incorporation of a white light illumination system allows for sample visualization, complemented by a CCD camera for precise tracking of the pump and probe beams' relative positions on the sample. Upon reflection, a portion of the beams retraces its path through the MO, with a fraction directed towards the monitoring CCD camera, while the remainder is incident on a balanced photodetector known as optical bridge detector (OBD).

3.4.1.5. Experimental set-up of non-collinear TRMOKE magnetometer

As illustrated in Figure 3.7, the vertically polarized output beam (pulse width = 35 fs, repetition rate = 1 kHz, power = 4 W) emanating from the Libra amplifier laser passes through a beam splitter, effectively dividing the beam into two distinct paths. One portion is directed towards the SHG for frequency doubling. The remaining portion of the original beam traverses a variable attenuator, significantly reducing its power, and establishes itself as the probe beam for subsequent detection. The probe beam then undergoes meticulous preparation to optimize its characteristics for sensitive magneto-optical detection. A series of

plano-convex lenses, each possessing precisely chosen focal lengths (10 cm and 15 cm), are employed to collimate the probe beam. This collimation ensures a well-defined and uniform beam profile, crucial for accurate measurements. Furthermore, a motorized delay stage equipped with a retro-reflector is incorporated into the probe beam path. Such precise control over temporal overlap is paramount for TR-MOKE measurements, where the dynamic response of the sample is investigated. Following collimation and temporal manipulation, the probe beam encounters a Glan-Thompson polarizer. This high-performance polarizer serves a critical function, ensuring a remarkably high degree of linear polarization (extinction ratio of 100000:1) within the probe beam. This enhanced level of polarization is essential for the sensitive detection of the magneto-optical response in the sample, as even minute changes in the polarization state can be readily measured. Additionally, variable attenuators are strategically positioned within both the pump and probe beam paths. These attenuators enable independent power control, allowing for the fine-tuning of signal levels and the optimization of the experiment.

The sample under investigation is mounted on a specialized holder integrated with a x-y-z

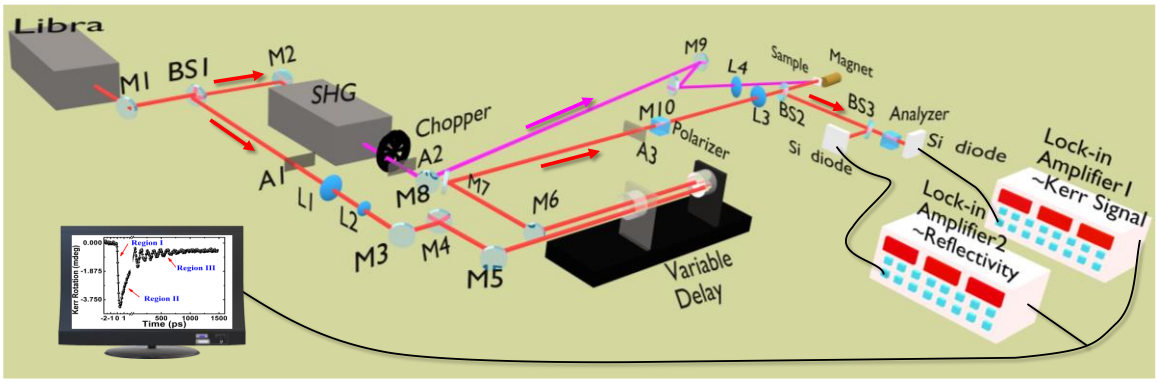

[12]**Figure 3.7:** A schematic diagram of a non-collinear TR-MOKE magnetometer.

translational stage. This stage grants the ability to precisely position the sample within the precisely defined beam paths, ensuring optimal interaction between the laser beams and the sample. The pump beam, possessing higher energy due to frequency doubling, is directed to fall upon the sample at an oblique angle. Conversely, the probe beam interacts with the sample at a normal incidence. Both the pump and probe beams are slightly defocused to create beam spot sizes of approximately 200 µm (pump) and 100 µm (probe). This slight defocusing serves a dual purpose: firstly, it optimizes the signal-to-noise ratio within the detected signal, and secondly, it minimizes the risk of potential damage to delicate metallic thin film samples. The reflected probe beam, containing the crucial magneto-optical information encoded within its polarization state, encounters another beam splitter. This splitter divides the reflected probe

beam into two distinct paths. One path directs the light towards a silicon photodetector, which measures the total reflectivity of the sample. The other path directs the light through an analyzer, which in this instance is another Glan-Thompson polarizer. This analyzer isolates the Kerr rotation signal, a minute change in the polarization state of the probe beam induced by the interaction with the magnetized sample. The Kerr rotation signal is then measured by a separate silicon photodetector.

To achieve the highest level of sensitivity and eliminate potential noise contributions, lock-in amplifiers are employed for the detection of both time-resolved reflectivity and Kerr rotation. These sophisticated instruments require a reference signal for optimal performance. This reference signal is provided by an optical chopper at 373 Hz, a device that modulates the intensity of the light beam at a specific frequency. The lock-in amplifiers synchronize with the reference signal from the optical chopper, effectively filtering out background noise and enabling the detection of even the faintest magneto-optical signals. Applying an external magnetic field is crucial for inducing the Kerr effect within the sample. In this setup, a permanent magnet is positioned to generate a well-defined magnetic field onto the sample. The interaction between the magnetic field and the sample's intrinsic magnetic properties results in the observed magneto-optical response, which is subsequently measured through the Kerr rotation signal.

3.4.1.6. Data Acquisition and Detection

The experimental setup involves the utilization of a permanent magnet oriented at an angle, which generates a magnetic field along with a precisely controlled demagnetization field that acts upon the sample. This sample is securely positioned using a piezoelectric scanning x-y-z stage, enabling scanning at nanometer scales. The experimental process is initiated by directing a high-intensity pump beam towards the sample, which disrupts its magnetization, leading to the initiation of precession around the effective magnetic field. To analyze the behavior of the precessing magnetization, particularly focusing on its z-component, an OBD is employed at regular time intervals. The OBD output is subjected to simultaneous measurements using two lock-in amplifiers, capturing data on Kerr rotation (A-B) and reflectivity (A+B) from the OBD signal, where A and B are equally amplified outputs from two photodiodes after the reflected probe beam from the sample is split into two orthogonally polarized lights using a polarized beam splitter placed at the entrance of the OBD. A mechanical chopper is integrated into the setup to modulate the pump beam at a frequency of 373 Hz, providing a stable reference signal. For precise quantification of Kerr rotation, the OBD undergoes calibration, ensuring accurate measurement of the dynamic magnetization

behavior. Before interaction with the pump beam, the (A-B) signal is nullified (balanced condition) to enhance sensitivity during detection. This intricate experimental arrangement facilitates a detailed spatial investigation into the dynamic characteristics of magnetization within the sample, offering insights into its behavior under varying magnetic fields and demagnetization forces.

3.4.1.7. Data Analysis and extraction of spin wave frequency

The raw data is acquired from the sample at a specific resolution. Figure 3.8(a) illustrates the raw time-resolved data obtained from a $Ni_{80}Fe_{20}$ thin film with a thickness of 20 nm under an external bias field of H = 1850 Oe. The bi-exponential background, attributed to the slow remagnetization mechanism, is subtracted to isolate the precessional data, as depicted in Figure 3.8(b). Conversion to the frequency domain is accomplished using a fast Fourier

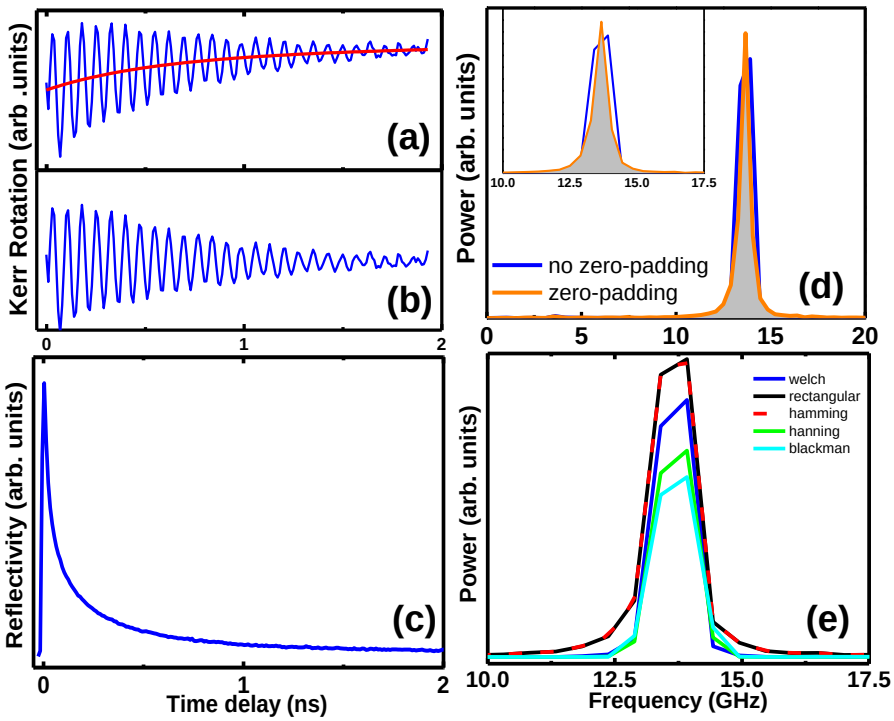

[13]**Figure 3.8:** (a) Time-resolved precessional data, (b) background-subtracted precessional data, and (c) reflectivity data are representative datasets obtained from a Ni80Fe20 thin film (at H = 1.85 kOe). (d) The FFT of the precessional data from (b) is presented alongside the FFT performed after zero-padding. An inset provides a magnified view of the SW spectra for enhanced clarity. Additionally, (e) illustrates the FFT analysis performed using various window functions, highlighting their impact on the frequency domain representation of the data.

transform (FFT) procedure of the time-domain data. FFT is an algorithmic method utilized for computing the discrete Fourier transform, thereby transforming the time-domain data into the frequency domain data. This process decomposes the time-domain signal into its constituent frequencies, revealing details about their amplitudes and phases. It is essential to

emphasize that obtaining an accurate frequency spectrum necessitates uniform sampling and an adequate number of data points.

$$F(w) = \int_{-\infty}^{+\infty} f(t)e^{-i\omega t}dt \tag{3.1}$$

Figure 3.8(d) represents the FFT power spectra which specifies that it consists of a single magnetic mode with 13.7 GHz frequency. In certain cases, zero-padding is performed to enhance the resolution and accuracy of the spectrum.

Zero-padding in FFT: Zero-padding[253] is a computational method applied in FFT procedures to artificially increase the number of data points and the total time window of a time domain signal. This technique involves adding zeros to the end of the original data, effectively extending the length of the signal. Zero-padding serves advantageous roles in specific scenarios, such as enhancing frequency resolution during FFT analysis or mitigating spectral leakage phenomena. Various techniques for zero-padding exist, with the Cooley-Tukey algorithm[254] being notably popular. In this algorithm, the total requisite data points for performing FFT is 2^N (N is a real positive and non-fractional number). In our experimental context, the dataset initially comprised 200 points, which is not a power of 2. Consequently, 56 data points of value 0 were incorporated to yield 256 data points, the nearest higher power of 2. This addition of zero-padding is discernible in Figure 3.8(d) as illustrated by the inset, demonstrating enhanced data quality in comparison to the non-zero-padded data.

Window function in FFT: In the context of FFT analysis, a window function refers to a mathematical function applied to a time-domain signal before conducting the FFT computation[255]. The primary objective behind employing a window function lies in mitigating spectral leakage and related artifacts inherent in the analysis of finite-duration signals using FFT. The FFT operation assumes an infinite extension of the input signal, which can lead to spectral leakage, a phenomenon where energy from a specific frequency spills over into neighboring frequency bins, distorting the frequency domain representation. By employing a window function, these issues can be solved. A window function essentially modifies the time-domain signal before subjecting it to FFT analysis, primarily by tapering the signal's edges. This tapering minimizes abrupt discontinuities that contribute significantly to spectral leakage. Among the various types of window functions, the rectangular window function is widely used, although it tends to exhibit more spectral leakage as it leaves the signal mostly unchanged. On the other hand, hamming and hanning window functions are effective in reducing spectral leakage by tapering the signal's edges with different coefficients. Blackman window function offers superior side-lobe suppression

compared to hamming and hanning windows but results in a wider main lobe. The FFT results, when different window functions are applied, are illustrated in Figure 3.8(e). While the frequency values generally remain consistent across different window functions, it is crucial to note that for systems with a single frequency, the impact of windowing is less significant. However, in multi-modal systems, proper windowing is imperative to obtain accurate FFT spectra (preferably avoiding rectangular function), as it helps mitigate spectral leakage and enhances the fidelity of frequency domain representations.

Reflectivity dynamics: In Figure 3.8(c), the reflectivity signal from the silicon substrate exhibits a sharp increase shortly after the pulse, followed by an exponential decay before stabilizing at the equilibrium level[256]. This rapid increase in reflectivity is indicative of the generation of free carriers (electrons and holes) within the silicon, resulting from the absorption of energy from the pump pulse. This energy absorption leads to an augmentation in the material's optical response. The subsequent relaxation process is attributed to electron-electron and electron-phonon scattering mechanisms, following an exponential decay pattern.

3.4.2. Ferromagnetic resonance

Ferromagnetic resonance (FMR) is a phenomenon observed in magnetic materials with strong exchange coupling among their electron spins. It involves the resonant absorption of electromagnetic radiation, typically in the microwave range, caused by the precession of magnetic moments within the material when exposed to an external magnetic field. This precession occurs at a specific frequency known as the FMR frequency. Several factors influence the FMR frequency, including the magnetic properties of the material, its crystal structure, and the magnitude of the external magnetic field. When the frequency of the external magnetic field matches the FMR frequency of the material, a resonance condition is achieved. During resonance, the material absorbs maximum energy from the electromagnetic radiation, leading to noticeable changes in its magnetic properties. These changes are crucial for various kinds of applications such as magnetic data storage and spintronic and magnonic devices, where controlling the magnetic behavior of materials is essential.

3.4.2.1. Vector Network Analyzer

In this experimental approach, the behavior of magnetization dynamics is studied through a frequency-domain analysis achieved by systematically varying the frequency across a wide range within a constant magnetic field setting or by varying magnetic field within a constant frequency. This process allows for the measurement and recording of spin wave absorption

spectra in terms of scattering parameters denoted as S-parameters[257]. The utilization of a Vector Network Analyzer-based FMR (VNA-FMR)[258] setup offers distinct advantages as it enables the extraction of both the amplitude and phase information embedded in the signal through the capabilities of the VNA instrument. However, it is crucial to note that this methodology requires meticulous calibration procedures and the accurate subtraction of reference signals to ensure the attainment of precise and reliable results.

Network analyzers are sophisticated electronic instruments to measure and analyze the behavior of electrical networks, components, and systems across a wide range of frequencies. Vector network analyzers have become a cornerstone for researchers investigating the dynamical magnetic properties of materials. Unlike microwave transition analyzers (MTAs) or large signal network analyzers (LSNAs) that focus on the magnitude of fundamental and harmonic responses, VNAs offer a more nuanced characterization by measuring both the amplitude and phase of electromagnetic waves. This comprehensive capability makes VNAs highly valuable in network analysis[259], allowing researchers to delve deeper into the behavior of electrical networks, including crucial reflection and transmission properties. This specialized setup harnesses the VNA's ability to measure the complex ratio of the reflected and transmitted signals' amplitude and phase. This detailed information provides an intricate fingerprint of the magnetic resonance behavior within the material under study.

3.4.2.2. Conventional FMR vs Broadband FMR

In conventional FMR technique, a resonant cavity is utilized where the sample is positioned, and this cavity possesses its unique resonance frequency denoted as f_c. Consequently, conventional FMR is limited to measuring solely at f_c and cannot capture other frequencies. However, the resonant frequency of a material is modifiable by an external magnetic field, allowing for adjustments to match the sample's resonance with f_c. Through a magnetic field scan, frequency measurement becomes feasible. Nonetheless, numerous magnetic systems exhibit multiple eigenmodes, leading to a sequential measurement approach with conventional FMR—each eigenmode must be measured individually by adjusting the field accordingly. To overcome this cumbersome process, a more efficient method termed broadband FMR has been developed. Unlike traditional methods, broadband FMR utilizes a non-resonant cavity distinguished by a broad and flat Q-factor. As a result, this setup enables the simultaneous measurement of all eigenmodes present within the system, significantly enhancing measurement efficiency and accuracy.

Compared to conventional FMR setups, VNA-based spectrometers offer several advantages[260,261]. The broad operating range of VNAs, typically spanning from MHz to high GHz frequencies, allows researchers to explore a wider variety of magnetic materials with diverse resonant characteristics. This is particularly beneficial for investigating patterned structures, which can exhibit multiple resonant spin wave modes. Additionally, VNAs can be integrated with non-resonant cavities. Unlike their resonant counterparts, non-resonant cavities provide a flat Q-factor response across a broad frequency band. This flat response minimizes distortions in the measured data, leading to more accurate characterization of complex magnetic materials. The combination of broad frequency range and non-resonant cavity design makes VNA-based FMR spectrometers ideal for studying various magnetic phenomena. This includes magnetic heterostructures where the interplay of magnetic properties and the applied magnetic field strength can induce transitions between in-plane and out-of-plane magnetization states.

3.4.2.3. Scattering (S) parameters

The rationale behind employing S-parameters[257] in this high RF/MW regime stems from several practical limitations associated with directly measuring admittance (Y), impedance (Z), or hybrid (h) parameters. At these high frequencies, equipment capable of accurately measuring total current and voltage becomes scarce. Additionally, achieving perfect open or short circuit conditions for these measurements prove challenging. Furthermore, some active devices, like the samples under investigation, might exhibit unstable behavior under such extreme open/short conditions or at high frequencies. S-parameters offer a compelling alternative, being:

- Relatively easy to measure even in the high-frequency regime using VNAs.
- Lack of suitable equipment for measuring total current and voltage in the RF/MW range.
- Directly relatable to familiar and easily interpretable quantities like gain, loss, reflection coefficients, and transmission coefficients.
- Convertible to Y, Z, or h-parameters if needed for further analysis, providing a bridge between these traditional parameters and the more convenient S-parameters in the high RF/MW domain.

If a_1 and a_2 represent the incident signals from the two ports while b_1 and b_2 are the acquired signals, then according to the S-parameter formalism (Figure 3.9(b)):

$$\begin{bmatrix} b_1 \\ b_2 \end{bmatrix} = \begin{bmatrix} S_{11} & S_{12} \\ S_{21} & S_{22} \end{bmatrix} \begin{bmatrix} a_1 \\ a_2 \end{bmatrix} \tag{3.2}$$

Hence S-parameters are defined as:

$$S_{11} = \frac{b_1}{a_1}|_{a_2=0} \tag{3.3}$$

$$S_{12} = \frac{b_1}{a_2}|_{a_1=0} \tag{3.4}$$

$$S_{21} = \frac{b_2}{a_1}|_{a_2=0} \tag{3.5}$$

$$S_{22} = \frac{b_2}{a_2}|_{a_1=0} \tag{3.6}$$

We generally express S-parameters in terms of dB as $20\log_{10}|S_{ij}|$ where, i, j = 1, 2 respectively. We have measured S_{11} parameters only, while performing all the works in this thesis.

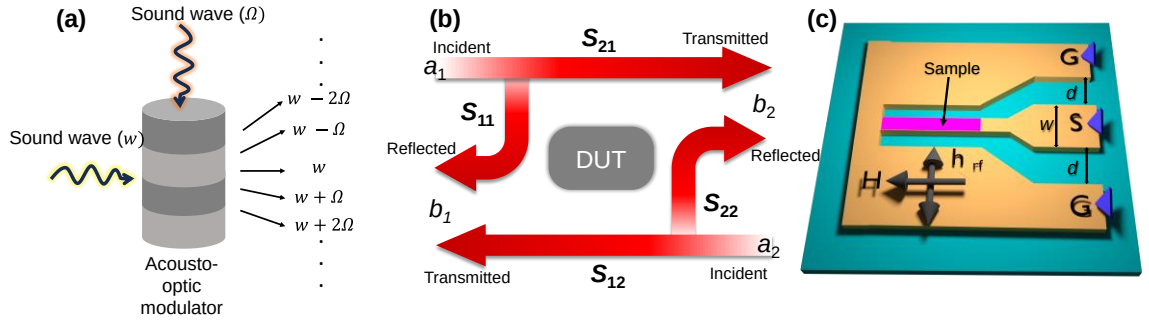

[14]**Figure 3.9:** (a) The fundamental operational concept of an acousto-optic modulator. (b) A schematic representation of the S-parameters for the device under test (DUT). (c) A diagram illustrating how RF excitation is achieved using a ground-signal-ground (GSG) type antenna within a CPW structure.

3.4.2.4. Coplanar waveguide (CPW)

Coplanar waveguides (CPWs)[262] represent a type of electrical transmission line frequently utilized for conveying RF/MW frequency signals. These waveguides are created using photo-lithography techniques. A CPW typically comprises a single signal line alongside two return conductors, commonly referred to as ground lines. The signal line is positioned between the ground lines on the same plane of the dielectric substrate, signifying the term 'coplanar'. The separation between the signal line and the ground lines denoted as gap width (d) and the width (w) of the signal line determines the system's impedance. This impedance matching is crucial for efficient signal transfer with maximum attainable power from co-axial cable to CPW structure. Depending on the measurement setup, CPWs can be configured in either reflection or transmission geometry. In reflection geometry, the three lines are typically shorted at one end. In all the works performed for this thesis, reflection geometry is utilized,

as shown schematically in Figure 3.9(c). It is important to highlight that the decreased signal line and increased ground line widths in a linear fashion are crucial to minimize impedance mismatch. In this configuration, FM samples are positioned either above or below the central signal line, separated by a sufficiently thick insulating layer to prevent damage from high-frequency RF currents. The RF current induces a perturbation field, h_{rf} which induces precessional dynamics of the system under external field H.

3.4.2.5. Calibration: requirements and procedure

Calibration plays a vital role in ensuring the accuracy, reliability, and error-free FMR measurements, which are crucial for studying magnetic materials and phenomena effectively.

There are mainly 3 different kinds of errors:

Systematic errors: These errors are characterized by their reproducibility, predictability, and lack of variation over time. They arise from non-ideal components within the measurement setup, such as impedance mismatches and cable losses in a VNA setup. Systematic errors[263] are inherent and consistent, affecting measurements consistently in a specific direction (either underestimating or overestimating the true value). They are fundamental to the measurement system and can significantly impact the accuracy of results.

Drift error: Drift errors[264] result from changes in the measurement environment that occur after calibration. These changes could include fluctuations in temperature, humidity, or other external factors. Drift can lead to inaccuracies over time, especially in long-duration measurements. Minimizing drift requires maintaining a stable and controlled test environment or allowing instruments to stabilize (warm-up) before measurements.

Random errors: Random errors[264] stem from various sources such as instrument noise, imperfect measurement practices, or issues with cables and connectors. Unlike systematic errors, random errors are not consistent or predictable; they fluctuate over time and do not follow a specific pattern. High-quality equipment and meticulous measurement techniques can help minimize random errors, but they cannot be entirely eliminated due to their inherent variability.

The calibration procedure in electrical measurements serves to enhance accuracy by eliminating unwanted signals (especially systematic errors) originating from internal or external noise sources. In the conducted thesis, the CS-5 calibration kit from GGB Industries Inc. was utilized as the standard for electrical measurements, ensuring precise calibration parameters. The calibration process was executed by establishing contact between the

picoprobe and patterned pads, following the established short-open-load-through (SOLT) calibration method[265–267]. Incorporating "open" pads in the calibration structure was crucial to mitigate errors stemming from fringing electric fields at the probe tip, thereby enhancing measurement accuracy. Furthermore, the inclusion of "short" and "load" structures within the calibration framework facilitated the attainment of specific electrical characteristics essential for accurate measurements. Notably, the "load" structure was designed to accommodate small shunt capacitance or series inductance at high frequencies, meticulously compensated to maintain resistive characteristics and further refine the calibration process.

3.4.2.6. Experimental set-up of VNA-FMR

A broadband FMR spectrometer based on a VNA from Agilent [currently Keysight] Technologies, (PNA-L with model N5230C) is employed to measure frequency domain spin wave dynamics as shown in Figure 3.10. A customized probe station is utilized, featuring an electromagnet powered by a bipolar power supply (KEPCO, INC. model BOP 36-6D) to generate a bias magnetic field within the plane of the FM sample, aligning its magnetization. A high-precision rotation stage with an angular resolution of 1° allows variation of the

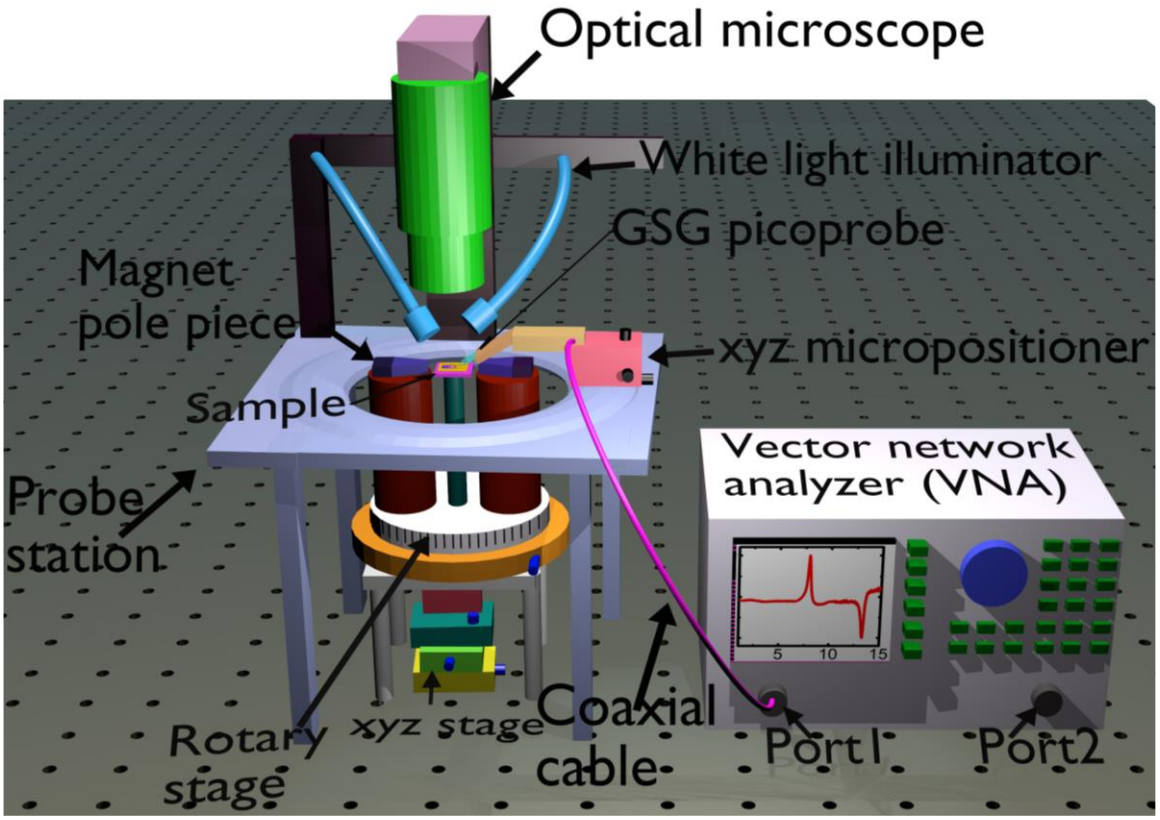

[15]**Figure 3.10:** Schematic representation of a broadband FMR spectrometer system integrated with a VNA, illustrating the setup used for measuring magnetic properties.

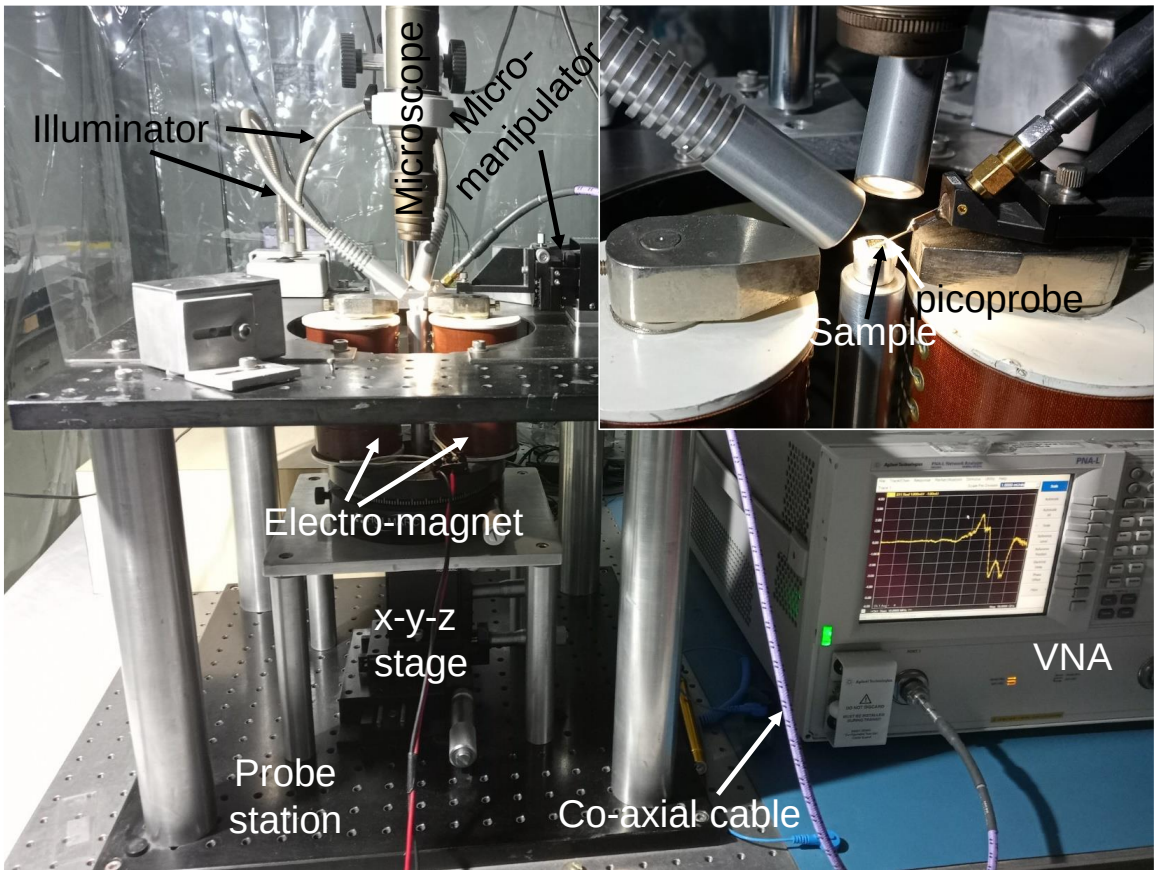

[16]**Figure 3.11:** A photograph of the broadband FMR spectrometer, which is equipped with a VNA and a probe station, located in Prof. Anjan Barman's laboratory at the S.N. Bose National Centre for Basic Sciences in Kolkata, India. Inset shows a closer view of the sample and the picoprobe mounted on the probe station.

magnetic field's azimuthal orientation within the sample plane over a full 360° range. Precise positioning of a microscale picoprobe on the sample is achieved using a microscope (Shodensha Inc.) with an illumination system, facilitating visual inspection and connection adjustments. A microwave current (I_{rf}) with a variable frequency range of 10 MHz to 50 GHz is introduced into a CPW via a non-magnetic ground-signal-ground (G-S-G) picoprobe (40 GHz bandwidth, model 40A-GSG-150-EDP, GGB Industries). The picoprobe is connected using a coaxial cable (model N1501A-203) and a precise micro-positioner (NPS, model 800MRF-L). The oscillating current I_{rf} generates a perpendicular microwave field, h_{rf}, and the setup operates in reflection geometry. The CPW is shorted at one end, enabling reflection mode operation for investigation of the forward scattering parameter (S_{11}) collected by the picoprobe. The collected data is then analyzed by the VNA. The FMR spectrum is obtained by sweeping the microwave signal frequencies while monitoring the power absorbed by the sample at various magnetic field strengths and azimuthal orientations. This reveals the presence of different spin wave modes within the magnetic structures. To minimize background contributions, a reference spectrum acquired at the highest bias field value is

subtracted from the measured signal. However, some residual background noise might still be present in the final FMR spectrum. This experimental setup provides a versatile platform for investigating frequency domain spin wave dynamics in various magnetic materials by offering precise control over the magnetic field, microwave excitation, and signal detection. The careful background reduction step further enhances the quality of the acquired FMR spectra, facilitating the analysis of spin wave characteristics.

3.4.3. THz-Time-Domain Spectroscopy

History of THz technology: The terahertz (THz) region of the electromagnetic spectrum resides between the microwave and infrared regimes, encompassing frequencies from 0.1 THz to 10 THz (wavelengths of 3000 μm to 30 μm)[268,269]. This unique regime offers distinct advantages for scientific exploration. At 1 THz, the energy content corresponds to a modest 4.1 meV, aligning with a timescale of 1 ps. This specific energy range is particularly intriguing as it falls between the quantized thermal unit and higher energy photons, bridging the gap between the classical and quantum mechanical descriptions of electromagnetic waves. Historically, the "THz gap"[88,270] presented a significant challenge. The lack of readily available, cost-effective sources, detectors, and operational systems within this frequency range hindered its scientific potential. Detection posed a particular hurdle. Electronics-based sources struggled beyond 0.3 THz, while semiconductor detectors faced limitations below 10 THz due to inherent band-gap restrictions. However, the past 15 years have witnessed a surge in THz research, leading to significant advancements. Novel THz generation and detection strategies are continuously being developed, paving the way for a

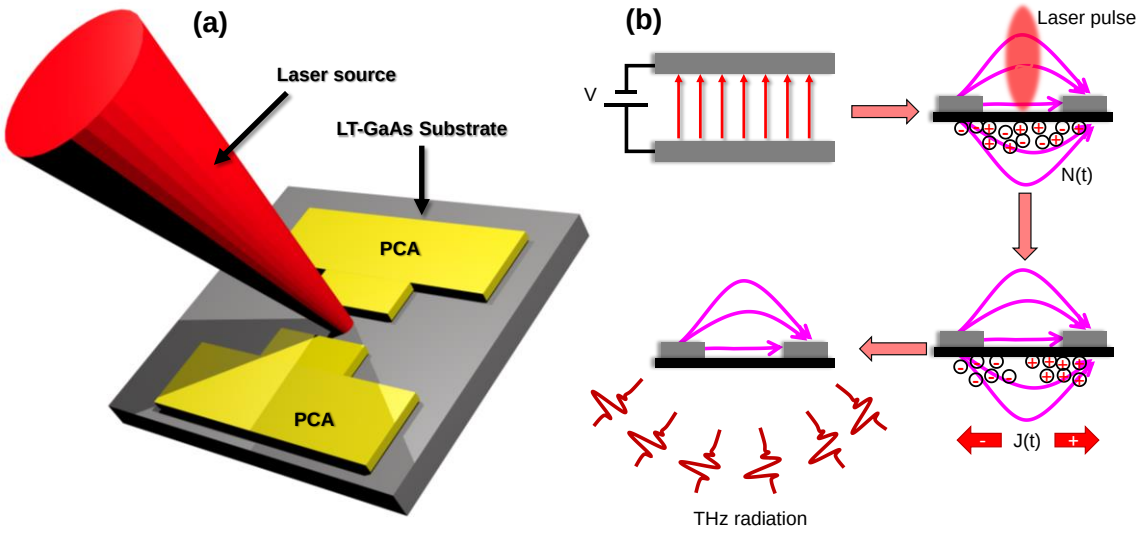

[17]**Figure 3.12:** (a) The diagram and operational concept of a photoconductive antenna illustrate its integration with a THz antenna. (b) The schematic of THz generation via a photoconductive antenna demonstrates how optical signals are converted into THz radiation.

multitude of groundbreaking applications. The unique properties of THz radiation have opened doors for scientific exploration across diverse fields. Solid-state physics, semiconductors, and nanoscience, all benefit from THz spectroscopy, which allows for the investigation of material properties at the atomic and molecular levels. Similarly, THz waves prove invaluable in the realm of biology and pharmaceuticals, enabling the characterization of biomolecules and potential drug interactions. Beyond the realm of fundamental science, THz technology finds practical applications in security and imaging systems. Its ability to penetrate certain non-conducting materials like clothing and paper makes it ideal for non-invasive security screening[91]. Additionally, THz imaging holds promise in healthcare diagnostics, offering the potential for early-stage cancer detection and improved medical imaging techniques[90]. The exciting world of THz astronomy also stands to gain tremendously. THz observations can potentially pierce through dust clouds, revealing previously obscured celestial objects and furthering our understanding of star and planet formation. Furthermore, the prospect of ultrafast data storage utilizing THz waves presents a revolutionary leap in information storage capacity. Current research efforts in the field of THz technology are heavily focused on application-driven studies. This includes the development of devices capable of manipulating THz radiation, exploring materials that exhibit GMR for enhanced THz functionalities, and investigating the potential of spintronics and ultrafast data storage within this frequency range.

Generation of THz Radiation: THz generation in photoconductive antennas (PCAs)[271,272] exploits the ultrafast modulation of semiconductor conductivity by light as shown in Figure 3.12. Femtosecond optical pulses induce resonant inter-band transitions within the semiconductor material. These transitions promote electrons to the conduction band, creating electron-hole pairs and a dramatic increase in conductivity. However, disentangling the exact contribution of resonant and non-resonant interactions, such as free-carrier absorption and heating, to THz generation remains a challenge. To achieve efficient THz generation, PCAs typically utilize low-temperature-grown gallium arsenide (LT-GaAs)[271] due to its suitable bandgap and carrier mobility. Coplanar metallic electrodes, often gold (Au), are fabricated on the LT-GaAs substrate. When a DC bias voltage is applied, these electrodes establish a strong electric field near the air breakdown threshold. The THz generation process can be then described in three key stages:

Excitation (timescale ~ fs): The incident femtosecond optical pulse excites the semiconductor, creating electron-hole pair within a few hundred femtoseconds. This rapid change significantly alters the material's conductivity.

Charge transport and transient current (timescale ~ fs-ps): The evolution of the photoexcited carrier density is governed by complex time-dependent transport equations, accounting for both short-term (fs's) and long-term (ps's) changes due to scattering and recombination. The presence of these free carriers significantly influences the conductivity, leading to the generation of a transient current within the PCA.

THz pulse radiation and equilibrium (~ps and beyond): The transient current, driven by the applied electric field, acts as the source for THz radiation. As the carriers are accelerated within the electric field, they radiate electromagnetic waves in the THz range. The specific characteristics of the THz pulse depend on the dynamics of carrier acceleration and scattering within the semiconductor. Finally, after a few ps, various scattering and recombination processes restore the system to a state of thermal equilibrium, terminating THz pulse generation.

3.4.3.1. Experimental set-up of THz-TDS

The THz time-domain spectrometer (THz-TDS)[273] leverages the Auston switch principle for both its emitter and detector antennas. This section details the THz radiation generation and detection mechanisms within this setup (Figure 3.13).

Emitter antenna: The emitter antenna is a biased semiconductor structure, typically fabricated from materials like InGaAs/InAlAs. In its unbiased state, the antenna remains inactive. Upon excitation by an ultrafast laser pulse, electron-hole pairs (carriers) are generated within the semiconductor. The applied bias voltage accelerates these carriers, initiating a photocurrent within the antenna. This transient current produces an electromagnetic field via the principle of photoconduction. Importantly, the rate of change of the photocurrent is proportionate to the amount of THz radiation emitted. Notably, the femtosecond duration of the optical pulse leads to the generation of a THz pulse in the picosecond range, significantly longer than the optical pulse itself.

Detector antenna: The detector antenna adopts a dipole design featuring a small gap. When excited by the femtosecond laser pulse, this gap region acts as a photoconductive switch, similar to the emitter. However, in the detector, an incoming THz pulse induces a small current within the antenna. This key aspect differentiates the detector from the emitter, where the current originates from the laser excitation.

Stroboscopic sampling and temporal resolution: A crucial feature of the THz-TDS setup is stroboscopic sampling. The detector antenna remains essentially blind without illumination from the synchronized laser pulse. This allows for the selective detection of the THz pulse arriving precisely when the detector is "gated on" by the laser pulse. This stroboscopic approach offers significant advantages, enabling the isolation of the desired THz signal amidst potential background noise. The temporal resolution of the THz-TDS system hinges on two critical factors: the short carrier lifetime within the semiconductor antennas and the ultrashort duration of the laser pulses. Short carrier lifetimes ensure a rapid decay of the photocurrent, leading to a well-defined temporal profile of the emitted THz pulse. Additionally, the femtosecond nature of the laser pulse translates to a high-fidelity replica of the THz pulse during the detection process. This interplay between carrier lifetime and laser pulse duration is fundamental for achieving high temporal resolution measurements in the THz-TDS system. By employing these principles, the THz-TDS setup facilitates the measurement of the electric field (E(t)) as a function of time. Having access to time-domain information is crucial for obtaining a thorough grasp of the dynamics of THz waves and their interactions with materials.

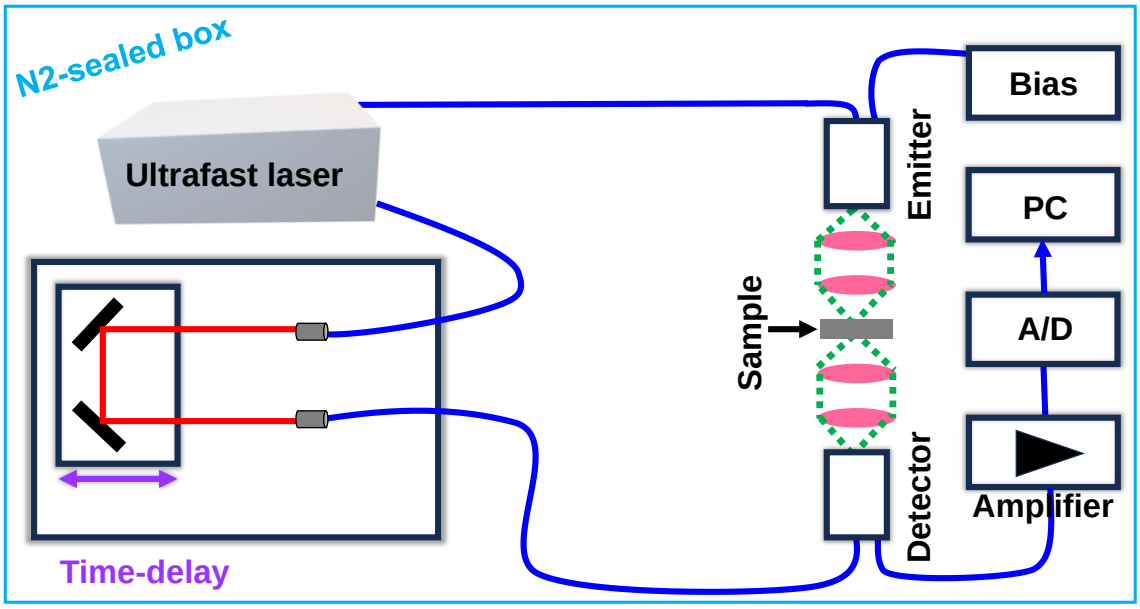

[18]**Figure 3.13:** Schematic illustration of a THz-TDS set-up.

3.4.3.2. Data acquisition and analysis

THz-TDS in our setup involves meticulous control over time delay via a high-resolution stepper motor (0.82 ps step size) for sub-picosecond sampling of the THz electric field (E(t)). The laser path length is optimized to ensure a well-defined reference peak from the air at 10 ps for accurate temporal calibration with maximum attainable delay time of 850 ps. The data points are selected as a power of 2 (e.g., 512, 1024), balances spectral resolution and acquisition speed through the FFT for frequency domain analysis by incorporating Blackman window function (by default). To enhance signal-to-noise ratio, a longer time constant (300 ms) is used in the lock-in amplifier compared to the stepper motor (100 ms) for improved data averaging. A square wave bias voltage of 30 V at a frequency of 10 kHz is used to stimulate the THz emitter antenna. Acquired data is meticulously recorded with time domain data, processed THz electric field, and relative delay line position for post-processing. Minimizing errors involves acquiring reference and sample spectra multiple times at different sample positions to account for potential inconsistencies and inhomogeneity. This rigorous approach ensures the collection of high-fidelity THz data, revealing the intricate spectral characteristics of the samples under investigation. Fabry-Pérot (FP) oscillations, caused by multiple THz pulse reflections within a sample, introduce challenges in THz-TDS data analysis. These reflections manifest as additional peaks in the THz waveform, potentially obscuring the true material response. The impact is particularly pronounced for thin, low-

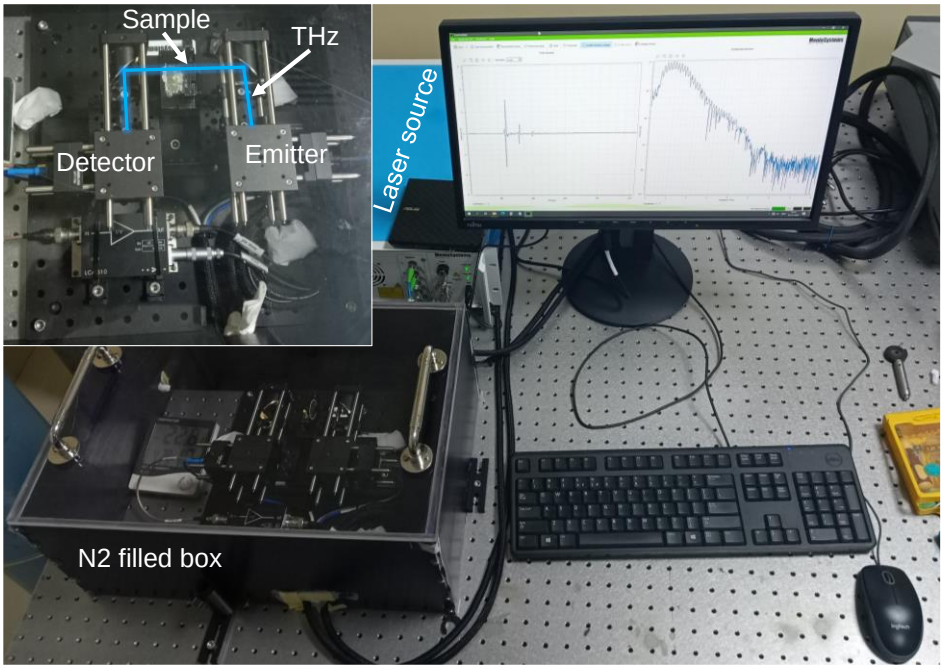

[19]**Figure 3.14:** Photograph of the compact THz-TDS set-up present in the labrarotory of Prof. Rajib Kumar Mitra in SNBNCBS.

absorption samples where FP oscillation peaks can overlap with the main transmitted pulse. Accurate determination of sample thickness and the use of techniques like angular dispersion or electromagnetic simulations can aid in differentiating the intrinsic material response from the FP oscillations. By mitigating these effects, researchers can achieve a more accurate and reliable characterization of the sample's optical constants using THz-TDS.

3.5. Numerical Methods

In simulating the quasistatic and dynamic magnetic processes of magnetic thin films and engineered structures, solving the LLG equation, which is an ordinary differential equation, is essential. However, obtaining exact solutions faces challenges such as defining boundaries and initial conditions. A common numerical approach involves using either the finite-difference method (FDM) or the finite-element method (FEM)[274] to solve the LLG equation. Both methods divide the sample under study into numerous cells, each representing a single spin or average magnetization. FDM employs a uniform grid of small cells, suitable for simpler geometries but can struggle with complex shapes due to stair-like approximations of curved edges. On the other hand, FEM divides the material into a mesh of flexible elements like triangles or tetrahedrons, offering more versatility with complex geometries owing to its adaptable mesh structure. Popular FDM-based simulators include Object Oriented Micromagnetic Frameworks (OOMMF)[275], LLG micromagnetic simulator[276], MicroMagus[277], MuMax3[278], Boris[279], among others. Meanwhile, FEM-based simulators like NMAG[280], MAGPAR[281], MicroMagnum[282], TetraMag[283], etc. provide solutions for simulations involving more intricate geometries.

3.5.1. OOMMF

The OOMMF[275], developed by the National Institute of Standards and Technology (NIST), is a robust, open-source software tool specifically engineered to simulate the intricate behaviors of magnetic materials at the microscopic scale. Leveraging a combination of C++ programming and Tcl scripting, OOMMF facilitates highly efficient micromagnetic simulations. Central to OOMMF's methodology is the solution of the LLG equation, which serves as the fundamental model for tracking the temporal and spatial evolution of magnetization within materials, assuming a temperature of absolute zero (T = 0 K). The magnetic material is identified by parameters such as saturation magnetization (M_s) and exchange stiffness constant (A_{ex}). Additionally, OOMMF integrates sample structure through image (bmp) files. In its operational sequence, OOMMF initiates by discretizing the entire sample space into numerous parallelepiped cells, each with dimensions smaller than the

material's exchange length[284] ($l = \sqrt{\frac{A}{\mu_0 {M_S}^2}}$). This discretization is vital for accurately capturing the exchange interaction within the system. Before dynamic simulations, OOMMF ensures an equilibrium state, achieved by applying a sufficiently large static bias magnetic field. The simulation process within OOMMF is driven by evolvers, with a prominent example being the fourth-order Runge-Kutta evolver utilized for solving the LLG equation. This process involves a staged approach where the system is first fully magnetized under a high bias magnetic field, allowed to relax extensively, and then gradually brought to the desired bias magnetic field while continuing relaxation, all while stabilizing the system with a damping value below unity. Control over simulation stages is managed through drivers and stopping criteria. At each iteration, the magnetization configuration undergoes updates from two types of evolvers: a time evolver that tracks LLG dynamics and an energy minimization evolver seeking local energy minima. The simulation halts when the maximum torque, expressed as (m × H), converges below a pre-determined threshold, typically around 10^{-6} A/m. The culmination of these processes yields a time-dependent magnetization trace, from which SW frequency and amplitude can be extracted through FFT analysis. This comprehensive approach within OOMMF provides a robust toolkit for investigating and comprehending the intricate dynamics of magnetic materials at the microscopic scale.

3.5.2. LLG micromagnetic simulator

The LLG micromagnetic simulator[276], developed and licensed by M. R. Scheinfein, serves as a comprehensive tool for micromagnetic simulations, offering a customizable platform where parameters are given as inputs to tailor simulations. It also employs finite differences for exchange energies and fields, alongside boundary elements for handling magnetostatic self-energies and fields within the LLG equation framework. Operating within a grid structure defined by rectangular pixels on a cartesian grid, the simulator initializes arrays and computes demagnetization field coupling tensors, accommodating diverse boundary conditions. Key advantages encompass graphical animations depicting magnetic domain or magnetostatic field profiles in simulated ferromagnetic samples in 2D and 3D, temperature-dependent simulations, multilayer system analysis with customizable material parameters, dynamics of domain walls in magnetic heterostructures, simulation of spin valve or magnetic tunnel junction nanostructures with injected spin-polarized current, and visualization of effective magnetic field strengths to interpret inter-element interactions and magnetic profiles.

3.5.3. Dotmag

Studying how magnetization changes over time and understanding the distinct nature of spin wave mode require carefully analyzing power and phase patterns within nanostructures is highly essential. This analysis helps reveal the strengths and phases of different spin wave modes and how they spread across the system. Many simulation tools available today do not directly calculate these mode profiles, which limits our grasp of these phenomena. To fill this void, DotMag, a specialized MATLAB-based code[285,286], is designed to explore these aspects in detail. The time-domain magnetization data is arranged in the form of a 3D matrix in the form of (m(x, y, z, t)). To identify individual resonant modes, we apply a Fourier transform to the time-resolved, spatially averaged magnetization curve. This process produces a frequency spectrum that reveals well-resolved resonant modes. DotMag simplifies this by performing a discrete Fourier transform of the time-dependent magnetization while keeping one spatial coordinate fixed concerning time. Usually, simulations that overlook discretization along the z-dimension consider an average demagnetizing effect and other potential spatial impacts on the distribution of spin waves across the entire cell. However, when discretization along the z-direction is introduced, fixing a specific z-coordinate ($z = z_m$) allows for a discrete Fourier transform of $|m(x, y, z, t)|$ to ascertain the spatial distribution. The chosen z-coordinate can vary from the top to the bottom surface of the system. DotMag then generates plots illustrating the spatial distribution of power and phase of spin waves at selected frequencies using the following equations:

$$P_{z0}(x, y) = 20 \log_{10} \mathrm{FFT}|m_{z0}(x, y, f_n)| \tag{3.7}$$

$$\varphi_{z0}(x, y) = \tan^{-1} \left| \frac{Im\,(m_{z0}(x,y,f_n))}{Re\,(m_{z0}(x,y,f_n))} \right| \tag{3.8}$$

where f_n represents the frequency of a resonant mode, power is typically represented in decibels (dB), while the phase is measured in radians. The code is developed using MATLAB, ensuring efficient execution and control. The outputs consist of plots that illustrate the spatially dependent power and phase at specific frequencies. The frequency resolution is dictated by the overall simulation time, while the spatial resolution of power and phase maps is contingent on the sample's discretization or the number of cells used during micromagnetic simulation.

Chapter 4

4. Thickness Dependent Reconfigurable Spin-Wave Dynamics in $Ni_{80}Fe_{20}$ Nanostripe Arrays

Ferromagnetic nanostripes have gained massive attention due to their intriguing magnetic properties associated with dimensional confinements and shape anisotropy leading towards potential applications in magnetic storage, memory and spin-wave-based devices. Consequently, reconfiguration of their static and dynamic magnetic properties by the geometric parameters and external field is imperative. Here, we present a combined experimental and numerical study of the reconfigurable spin-wave dynamics in arrays of ferromagnetic nanostripes by the stripe thickness and external magnetic field strength and orientation. We have observed different uniform, localized and standing spin waves in the nanostripes and their monotonic and non-monotonic variation, including mode merging with these parameters. The observed variations are interpreted with the aid of simulated spin configurations, magnetostatic field maps and spin-wave mode profiles. Further numerical study reveals anisotropic spin-wave propagation in nanostripes for different thicknesses and in different bias-field geometry opening potential applications in magnonic circuit components such as reconfigurable magnonic waveguides and omnidirectional spin-wave emitters.

4.1. Introduction

Dimensionality plays an important role in determining the static and dynamic magnetic properties of ferromagnetic materials due to the different avenues of electronic and magnetic interactions in three-dimensional (3-D), two-dimensional (2-D), and one-dimensional (1-D) nanomaterials[287–290]. The 1-D elements of ferromagnetic nanostructures, i.e., nanorods[291], nanotubes[292], nanopillars[293], nanowires[294,295] and nanostripes (NSs)[296] have attracted intense attention to the research community over the last few decades owing to their fascinating electronic, optical, and magnetic properties manifested by its shape anisotropy[297], increased surface to volume ratio[298], and quantum confinement effect (QCE)[299]. In case of ferromagnetic NSs, the shape anisotropy depends upon the aspect ratio creating an easy axis of magnetization along its length which affects the demagnetization fields. A collection of periodically coupled NSs form a 1-D magnonic crystal (MC)[300,301] where spin waves (SWs) act as information carrier. They provide further opportunities of tailoring the magnetic properties and the corresponding SW dynamics due to the modification of inter-stripe interaction field. Consequently, there are a plethora of

theoretical[296,299,302] as well as experimental[303–306] reports exploring the static and dynamical magnetic response in isolated NS and their 1-D arrays by varying the NS width, inter-stripe separation, etc. Those prompted the findings of different novel phenomena such as quantization[297,307], localization[308–310], interference and self-focussing[311] of surface SW due to the finite width, inhomogeneity of internal field distribution, etc. By precise control of various geometric parameters[312,313] (e.g., length, width) and magnetic properties[304,314–317] (e.g., magnetic anisotropy, saturation magnetization, strength and orientation of external bias magnetic field, etc.), magnonic band-structure[318] can be reconfigured which also modulates the dynamical magnetic response in the pico- and nanosecond timescale (i.e., the precessional motion). Owing to the reconfigurable magnonic band structure, these 1-D MCs[303,312] can find potential applications in magnonic waveguides[319–321] which can channel, split and manipulate SWs. Such systems can also act as an information propagating media avoiding any crosstalk in various microwave[322,323] magnetic storage and memory devices[324,325]. Development of electric-field controlled on-demand spin-wave nanochannels in the form of switchable NS-like regions with different magnetic properties using the voltage controlled magnetic anisotropy (VCMA) showed great potential for reconfigurable magnonics and parallel processing of information[5]. Additionally, ferromagnetic NSs can be utilized in developing numerous domain wall-based recording and logic devices[326,327]. Recently, ferromagnetic NSs have seen burgeoning interest as they can be used as a guiding "track" of magnetic skyrmions acting as a data bit carrier, which is the building block of skyrmion-based racetrack memory devices[328,329]. Therefore, the fundamental study of SW dynamics of ferromagnetic NSs is crucial not only from the scientific point of view but also from the engineering standpoint.

However, no studies have been reported so far in the literature focusing on the role of confinement along the direction perpendicular to the sample plane, i.e., exploring the role of thickness of NSs in modulating the SW dynamics. Here, we report a large tunability of SW dynamics in a 1-D arrays of $Ni_{80}Fe_{20}$ (Permalloy: Py hereafter) NS of constant width (w) and inter-stripe separation (s) by simply manipulating the confinement along the z-axis and the associated demagnetizing field. In order to study the SW dynamics, we have exploited a custom-built time-resolved magneto-optical Kerr effect (TR-MOKE) microscopy technique. A remarkable variation of SW spectra has been observed for the two different systems under investigation for applied bias magnetic fields along the easy and hard axis of magnetization. In addition, a clear signature of SW mode merging beyond a certain bias field strength has

been observed for the thinner NS, entangled with a stark variation of SW mode frequency with the bias field. All the experimental findings are qualitatively reproduced using micromagnetic simulations. Subsequently, the power and phase profiles of different SW frequencies underpin the observed behaviour aided by the numerically calculated internal and stray magnetostatic field profiles. Further numerical calculations demonstrated the difference in SW propagation characteristics through the two different systems for varying bias field orientations, promoting these NSs for reconfigurable magnonics devices.

4.2. Experimental and Simulation Methods

4.2.1. Sample fabrication

Py NS arrays having width (w) of the individual NS of 220 nm, separation (s) between consecutive NSs of 280 nm and two different thicknesses (t) of 10 nm (T1) and 30 nm (T2) were prepared using a combination of electron-beam lithography (EBL) and electron-beam evaporation (EBE) techniques[297]. The scanning electron micrograph (SEM) images of the samples are shown in Figure 4.1(a).

4.2.2. Measurement technique

The details of the measurement procedure using the custom-built TR-MOKE microscope have been explained in Section 3.4.1.4. in Chapter 3. In the experimental set-up, we have varied H at two different in-plane (azimuthal; φ, as defined in Figure 4.1(b)) angles (φ = 0° and φ = 90°) during the measurement. The experimental time window of 2 ns is found to be sufficient to resolve the SW peaks from the fast Fourier transform (FFT) of the time-resolved traces. The whole measurement has been carried out under ambient conditions.

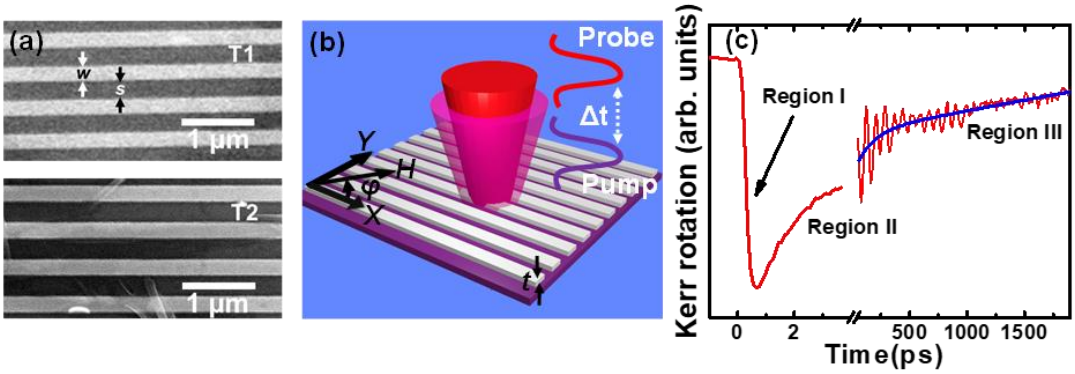

[20]**Figure 4.1.** (a) SEM images of Py NS arrays of constant width w ~ 220 nm and inter-stripe separation s ~ 280 nm having two different thicknesses of t ~ 10 nm (T1) and 30 nm (T2). (b) A schematic of experimental geometry for the TR-MOKE measurement and (c) typical time-resolved Kerr rotation data obtained from the sample T1, at H = 1.72 kOe applied along the HA (φ = 90°).

4.2.3. Micromagnetic simulation

The details of the simulation are discussed in section 3.5.1. in chapter 3. Here, we have taken 5 NSs of length 4 μm and applied 2-D periodic boundary condition (PBC) to mimic the large sample area used in the experiment. The entire array has been discretized into identical parallelepiped-shaped cells with volume 4×4×10 nm^3 (T1) and 4×4×30 nm^3 (T2). The lateral cell size is intentionally kept well below the exchange length of Py (~ 5.2 nm), to incorporate the exchange interaction in the system. The material parameters that are used in the simulation are: gyromagnetic ratio, γ = 17.6 MHz/Oe, saturation magnetization, M_S = 860 emu/cc, anisotropy field, H_K = 0, exchange stiffness constant, A = 1.3×10^{-6} erg/cm[330] and damping coefficient α = 0.008[331] for dynamic simulation. The value of M_S is taken from the bias field-dependent precessional frequency of a Py thin film (shown in Figure 4.5(c)). The FFT of the simulated time-resolved out-of-plane magnetization component (m_z) is shown in Figure 4.2(c), revealing the corresponding SW spectra.

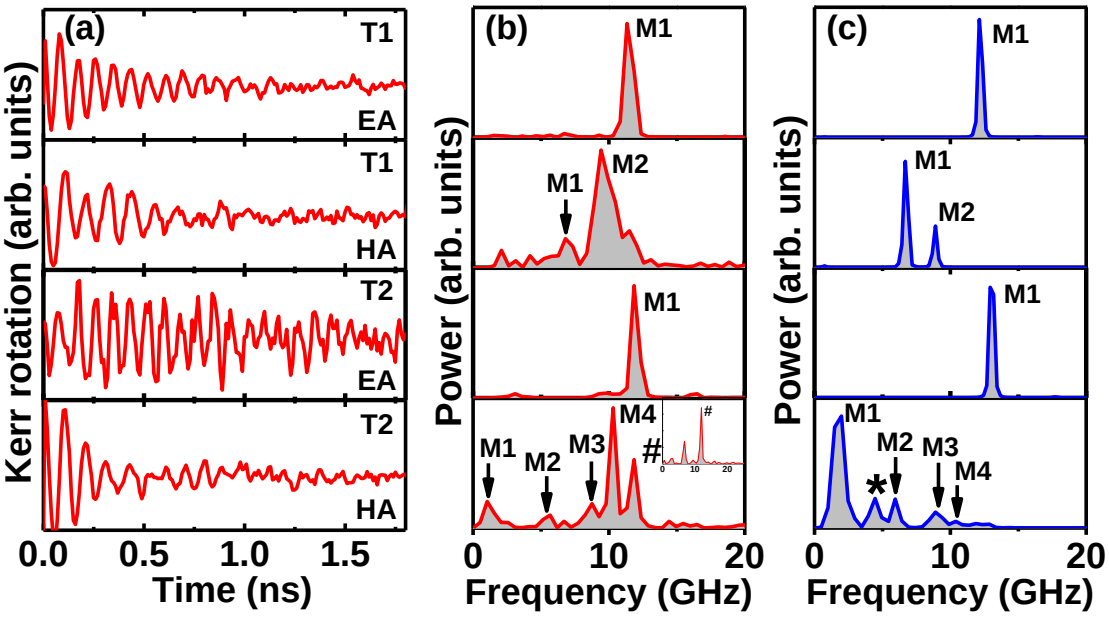

[21]**Figure 4.2.** (a) Background subtracted time-resolved Kerr rotation and (b) corresponding FFT power spectra for the samples T1 and T2 for H = 1.13 kOe applied along the EA (φ = 0°) and the HA (φ = 90°) of the NS. (c) FFT power spectra of simulated time domain magnetization (m_z component) at the corresponding experimental configurations. SW Modes are numbered as M1-M4 in ascending orders of their frequency values and identified by downward arrows wherever needed in both experimental and simulated power spectra. FFT power spectra of the time-resolved reflectivity of T2 at φ = 90° is shown at the inset in the bottom panel of (b) for comparison.

4.3. Results and discussion

4.3.1. Evolution of spin wave modes with strength and orientation of external bias field

The experimental measurement geometry is schematically depicted in Figure 4.1(b), where the sample lies in the *x*-*y* plane and the bias magnetic field is applied at an angle φ with respect to the length of the NS (*x*-axis). In this particular measurement, *H* has been applied along two different orientations as mentioned above, i.e., $\varphi = 0°$, which corresponds to the easy axis (EA) and $\varphi = 90°$, which corresponds to the hard axis (HA) of magnetization of the NS. Figure 4.1(c) displays a representative time-resolved Kerr rotation trace consisting of different temporal regimes from the sample T1 at *H* = 1.72 kOe applied along the HA. Here, the ultrafast demagnetization (region l) occurs within 230 ± 10 fs from the zero-delay due to the rise of the spin temperature (following the rise of electronic temperature) of the system, followed by fast remagnetization (region II) due to the energy dissipation from the electron and spin baths to the lattice bath. Region III is the slow recovery of magnetization, i.e., slow remagnetization region, occurring due to the diffusion of lattice heat to the surroundings. The region III also includes the precession of magnetization around the effective magnetic field, which eventually damps out in ns timescale. A more detailed discussion about underlying mechanism can be found elsewhere[332].

Figure 4.2(a) shows the experimentally measured background-subtracted Kerr rotation data obtained from the samples T1 and T2, for *H* = 1.13 kOe applied along the EA ($\varphi = 0°$) and HA ($\varphi = 90°$) of the NSs. The FFT of the time-resolved data gives rise to the associated SW frequencies as shown in Figure 4.2(b). For $\varphi = 0°$, a single dominant magnetic mode is found for both the samples T1 and T2. However, the SW frequency is slightly higher for the thicker

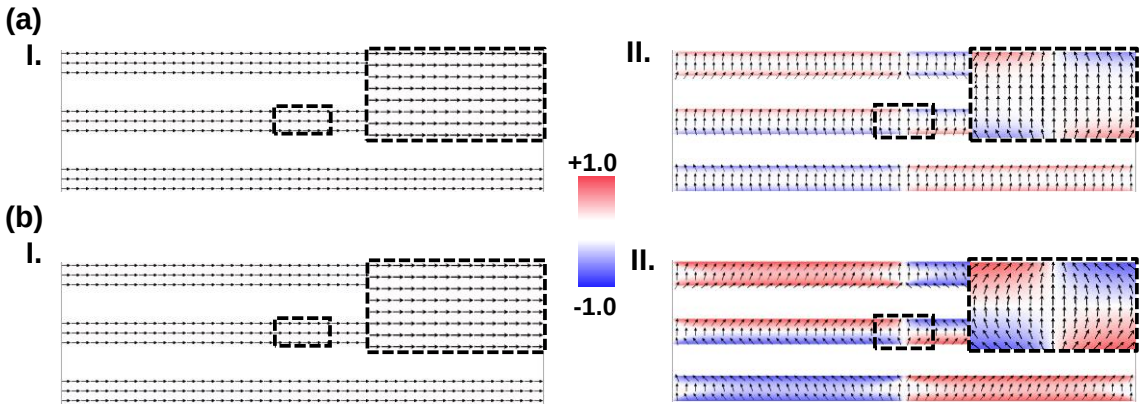

[22]**Figure 4.3.** Simulated static magnetic configurations of sample (a) T1 and (b) T2 for *H* = 1.13 kOe applied along (I) easy axis ($\varphi = 0°$) and (II) hard axis ($\varphi = 90°$). The magnetization (m_z component) is represented by blue-white-red colour map. Sizes of stripes are not to scale.

sample (T2). This can be explained by considering the shape anisotropy contribution in the system arising from demagnetization fields. The demagnetization factors along the length (N_l) and width (N_w) of the NSs are given as[333]: $N_l = \frac{2t}{\pi l}$ and $N_w = \frac{2t}{\pi w}$, respectively. The shape anisotropy field (H_{sh}) is proportional to the difference in the demagnetization fields along two orthogonal directions[334], which is given by $H_{sh} = M_s \times (N_l - N_w) = M_s \times \frac{2t}{\pi w} \times (\frac{w}{l} - 1) \approx -M_s \times \frac{2t}{\pi w}$, as $\frac{w}{l} \ll 1$. As the shape anisotropy is proportional to the aspect ratio (t/w) of the NS, the effective field is enhanced, and hence, the SW frequency is higher for thicker sample (T2). For φ = 90°, more complex and richer SW dynamics has been observed as the number of SW modes increase. For sample T1, two SW modes appear in the system at 7.1 GHz (M1) and 9.7 GHz (M2), while four SW modes appear at 1.2 GHz (M1), 5.6 GHz (M2), 8.7 GHz (M3) and 10.3 GHz (M4) for T2. M4 is the most intense magnetic mode and there also exist another mode at 12 GHz marked as #, which is also present in the FFT spectra of the time-resolved reflectivity as shown in the inset of the bottom panel of Figure 4.2(b). Mode # turns out to be nonmagnetic in nature as it does not show any magnetic field dispersion and it also does not interact with the magnetic branch of the SW spectra. We have primarily focused on the SW modes here, and detailed discussion about nonmagnetic modes is beyond the scope of this manuscript. Figure 4.2(c) represents corresponding simulated SW spectra. There is also one additional mode in the simulated SW spectra (marked as '*' for sample T2 at φ = 90°), which is not present in the experimental FFT power spectra. This could be either due to the line broadening of the spectral modes and/or lack of sensitivity due to its insignificant power in the experimental mode as mentioned in the literature[46]. The intensities of different SW modes are nontrivial to reproduce precisely in FDM-based micromagnetic simulations. There are several reasons behind it, which include the fact that the simulations were done at T = 0 K as opposed to the experiments performed at room temperature and difficulties in incorporating the precise edge roughness and deformation as well as the surface properties in the simulation.

However, since we are more concerned about the frequencies and spatial profiles of the SW modes, the mismatch of intensities does not alter the results and the conclusion. Roughness in magnetic structures (both the edge and the surface roughness) significantly modifies the physical behaviour of magnetic systems such as changes in coercivity, formation of pinning potential at the surface etc. eventually causing stark modification in the dynamical response of the system[335,336]. The observed difference in the SW spectra of T1 and T2 between two

different bias-field orientations can be explained from their difference in the ground-state spin configurations. For φ = 0°, all spins orient towards the field direction resulting in a uniform precessional motion, whereas for φ = 90°, there is formation of coupled-C magnetic states which results in multiple SW modes. Figure 4.3(a), (b) shows the static magnetic configurations from the simulated arrays of NSs T1 and T2 for H applied along φ = 0° (I) and φ = 90° (II). The magnified views of the central portion of the array have been shown at the inset for convenience. For Figure 4.3 (a, b) I, when H is applied along the easy axis (φ = 0°), all the spins are oriented along the field direction, resulting in uniform precessional motion of all spins in phase, which in turn, gives a single resonant mode in the SW spectra. However, in Figure 4.3 (a, b) II, when H is applied along the hard axis (φ = 90°), due to the competition between exchange and magnetostatic energy, a complex magnetic state is formed, consisting of two C-states (clock-wise and anti-clock-wise) around the centre of each stripe in the array. As the demagnetizing field is enhanced in T2 (higher thickness) as opposed to T1 (lower thickness), the contrast of this nonuniform distribution is also increased (Figure 4.3(b) II in T2), leading towards more complex SW dynamics including the number of SW modes. To elucidate the effects of dimensional confinement along the nanostripe thickness, we have presented systematic numerical simulation results in Figure 4.4 with thickness varying

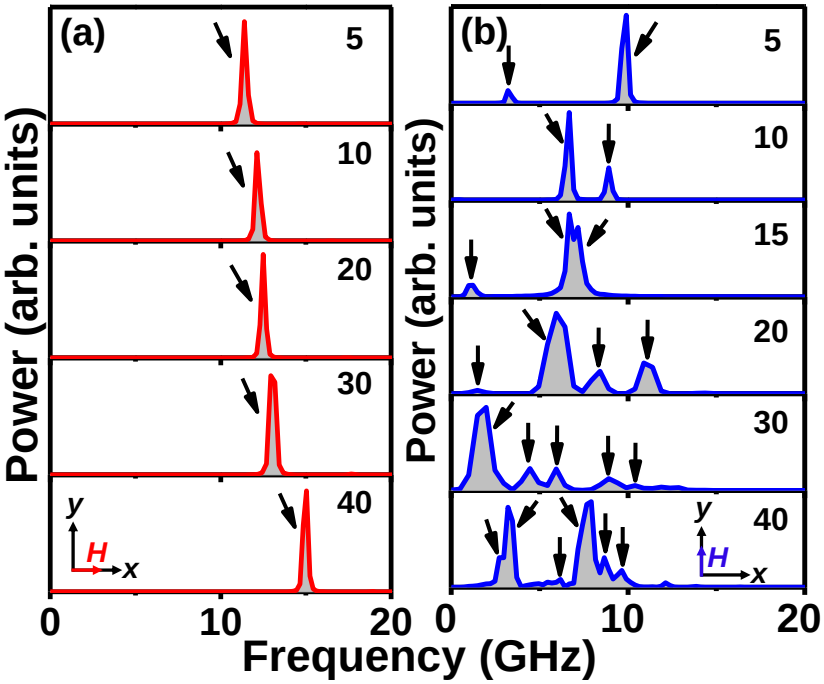

[23]**Figure 4.4.** Simulated SW spectra of NS having different thicknesses with in-plane bias magnetic field (H = 1.13 kOe) applied along (a) φ = 0° and (b) φ = 90°. The schematic of the orientation of H is presented in the lowest panel of (a) and (b). The number in each panel represents the corresponding thickness value in nm. The arrows represent different SW modes in the system.

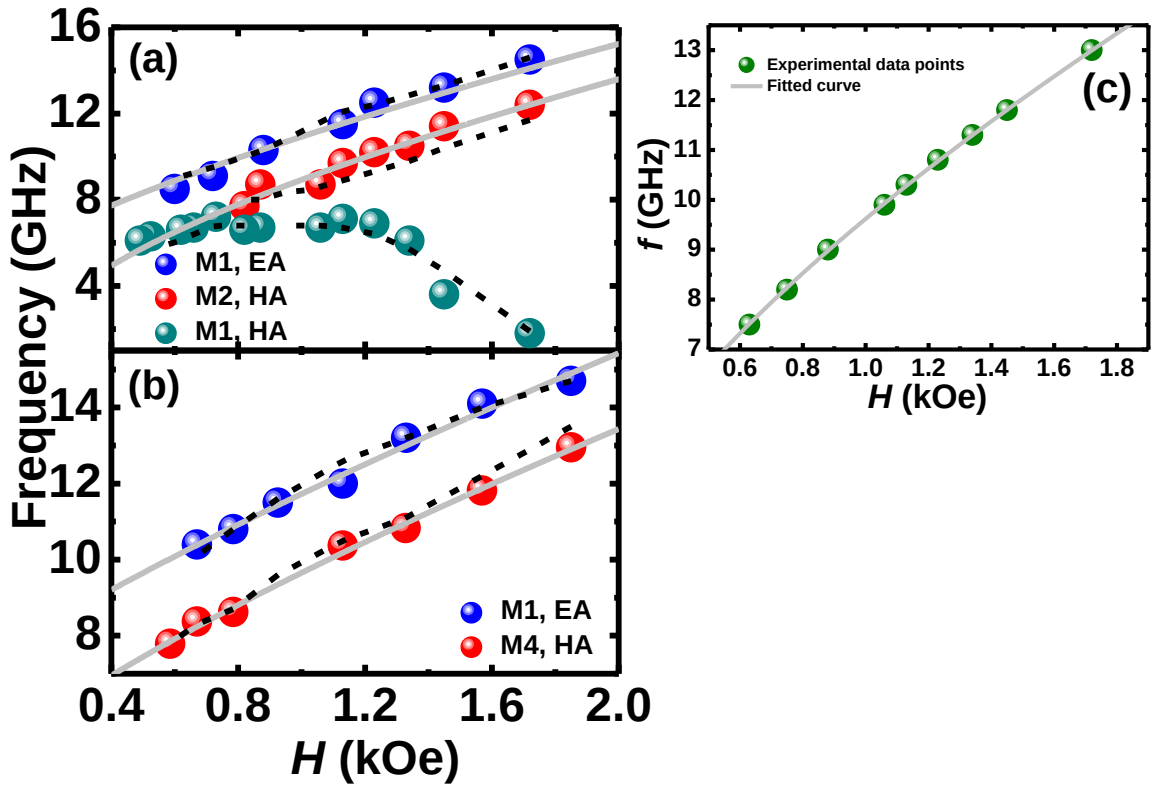

[24]**Figure 4.5.** Bias field dependent SW frequencies of Py NS arrays: (a) T1, (b) T2 are plotted as a function of H applied along φ = 0° (EA) and φ = 90° (HA). (c) Bias-field dispersion of unpatterned thin Py film. Filled circular symbols: experimental data points, dashed lines: micromagnetic simulation results, solid lines: Kittel fit.

between 5 and 40 nm. The results clearly shows that even a subtle variation in thickness can cause a significant shift in the SW frequency for φ = 0° (Figure 4.4(a)) and a drastic change in the number and frequency of the SW modes for φ = 90° (Figure 4.4(b)). Such a remarkable variation of SW spectra may inspire the development of SW waveguides with wedge shaped thickness profile which may accommodate different frequency channels lying adjacent in the same waveguide structure without the need of additional nanopatterning. In the experimental work, we have carefully chosen two particular thicknesses 10 nm (T1) and 30 nm (T2) from the simulated thickness series to clearly showcase the rapid variation in the number of modes and mode frequencies.

Figure 4.5(a), (b) represents the experimental and simulated bias magnetic field-dependent SW frequencies from the samples T1 and T2, respectively. For H = 1.72 kOe applied along HA in sample T1, one high-intensity mode (M2) at 12.4 GHz is accompanied by another low-intensity mode (M1) at 1.8 GHz. With the decrease of H, the frequency of mode M2 shows a redshift along with a reduction in intensity whereas the mode M1 is found to vary following a reverse trend both in terms of frequency and intensity. Eventually, those two modes coalesce together to form a single mode for $H \leq 0.82$ kOe. This phenomenon is referred to as mode

merging. However, M1 for EA in both the samples T1 and T2 follows the usual bias field dispersion of SW frequencies[128]. There is a clear frequency difference between SW modes along EA and HA of around 1.8 GHz for T1 and 2.2 GHz for T2 due to the presence of shape anisotropy in the system. The mode M1 for EA and the highest intense mode M4 along HA show Kittel-like behaviour for sample T2 as shown in Figure 4.5(b). The simulated frequencies slightly differ from the experimental frequencies, possibly due to the rough edges of the NSs that could not be incorporated in the FDM-based simulation as described in the literature[337]. Furthermore, the experimental data have been fitted with the modified Kittel formula[338] given by Equation 4.1.

$$f = \frac{\gamma}{2\pi}\sqrt{[H + H_{int} + H_k + (N_t - N_l)M_s][H + H_{int} + H_k + (N_w - N_l)M_s]} \qquad (4.1)$$

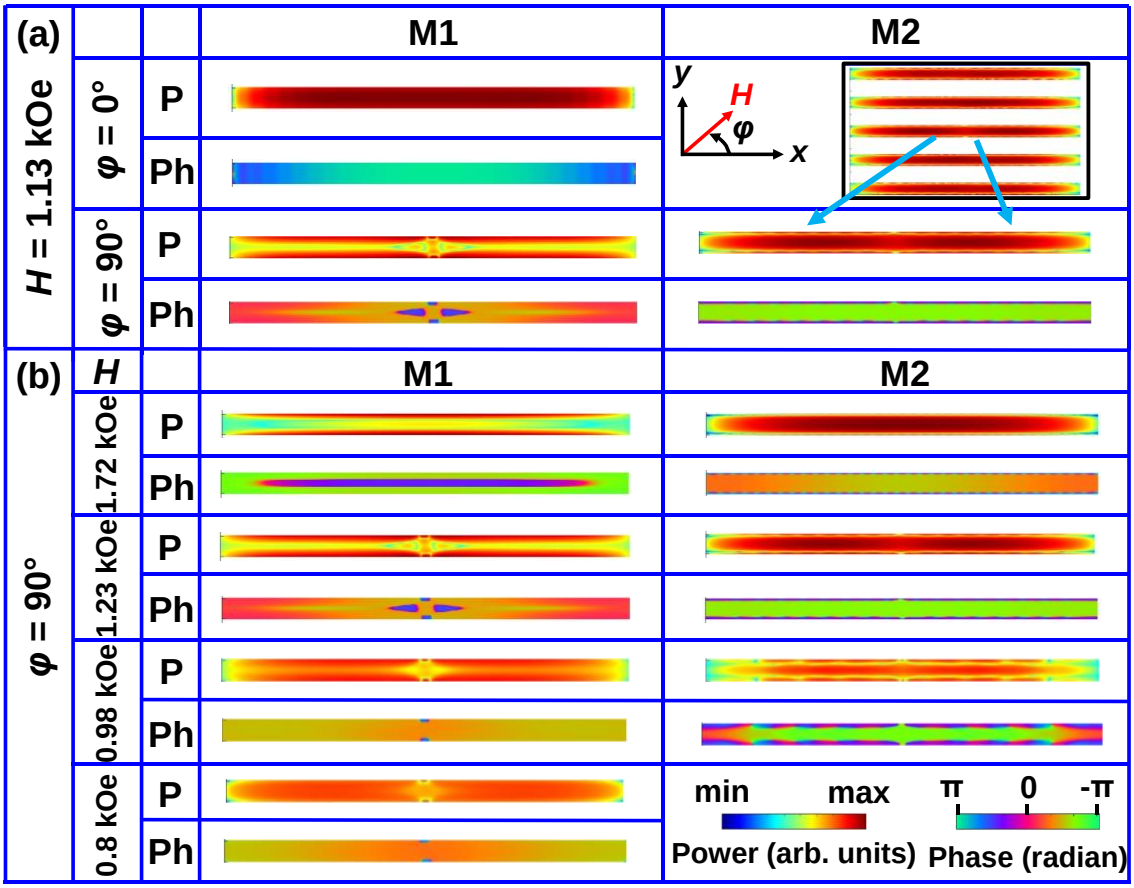

[25]**Figure 4.6.** (a) The power (P) and phase (Ph) maps of different SW modes for the sample T1 at H = 1.13 kOe along two orientations (φ = 0° and 90°). (b) The power (P) and phase (Ph) maps at different H values along the HA (φ = 90°). The schematic of the orientation of H is shown at top right corner and the colour maps for power and phase distributions are shown on the bottom right corner. Only the central NS from the array is shown for clarity in visualization of the mode profiles. However, the entire array is shown at the inset for a particular frequency. Sizes of the NSs are not to scale.

where, f is the precessional frequency, H, $H_{int,}$ and H_k are the external field, inter-stripe interaction field, and magnetocrystalline anisotropy field, respectively, M_s is the saturation magnetization and N_l, N_w, N_t are demagnetization factors along the length (l), width (w) and thickness (t), respectively. From Equation 4.1, we extract N_l, N_w, $N_{t,}$ and H_{int} as the fitting parameters which are presented in Table 4.1. The obtained values of N_t are much higher than those of N_l and N_w, which support their definition as discussed earlier. As both N_l and N_w are proportional to t, the obtained values of N_l and N_w increase for T2 as opposed to T1. The values of N_l and N_w increase for φ = 90° in comparison with those at φ = 0°, as the demagnetization fields (M_s multiplied by N_l or N_w) increase at φ = 90°. A more detailed discussion has been presented in the simulated magnetostatic field distribution section based on Figure 4.8(a) and (c). While to hold the relation $N_l + N_w + N_t = 4\pi$[339], N_t decreases in both the cases. While H_{int} is somewhat negligible at φ = 0° for both T1 and T2, it has significant values of ~170 Oe and ~420 Oe along HA for T1 and T2, respectively. This plays an important role in modifying the SW spectra along that direction.

Table 4.1: Parameters obtained from the Kittel fit of the bias magnetic field dependent SW frequencies.

Thickness (nm)	φ (degree)	M_S (emu/cc)	H_{int} (Oe)	N_l	N_w	N_t
10 (T1)	0	860	19	0.11	0.34	12.11
	90	860	170	0.20	0.53	11.83
30 (T2)	0	860	7	0.38	1.24	10.94
	90	860	420	1.28	1.36	9.92

4.3.2. Micromagnetic analysis of collective SW dynamics

4.3.2.1. Mode profiles analysis

To unlock the nature of the resonant magnonic modes, the spatial profiles of the corresponding dynamic magnetization components obtained from OOMMF simulations are analyzed using a home-built code[285]. The output files of the dynamic simulations containing information about the magnetization distribution as a function of space and time, i.e., $M(r, t)$, which is then arranged into 4-D matrices. Thereafter a discrete Fourier transform with respect to time is performed for each elemental cell and the power value of the FFT spectrum corresponding to the desired frequency is extracted. The plot of power value of all the cells gives the power profile of the system at that frequency. Similarly, phase plots have been extracted by taking the phase information from complex dynamic magnetization

distribution. Power and phase maps of different SW modes for the sample T1 are shown in Figure 4.6(a) for H = 1.13 kOe. It is quite clear from the power profile of M1 at φ = 0° that the SW power is uniformly distributed over the entire length of the NS resembling the uniform precessional mode or the centre mode (CM). On the other hand, for φ = 90°, the power of M1 is concentrated at the edges along the length of the NSs, which is the so-called edge mode

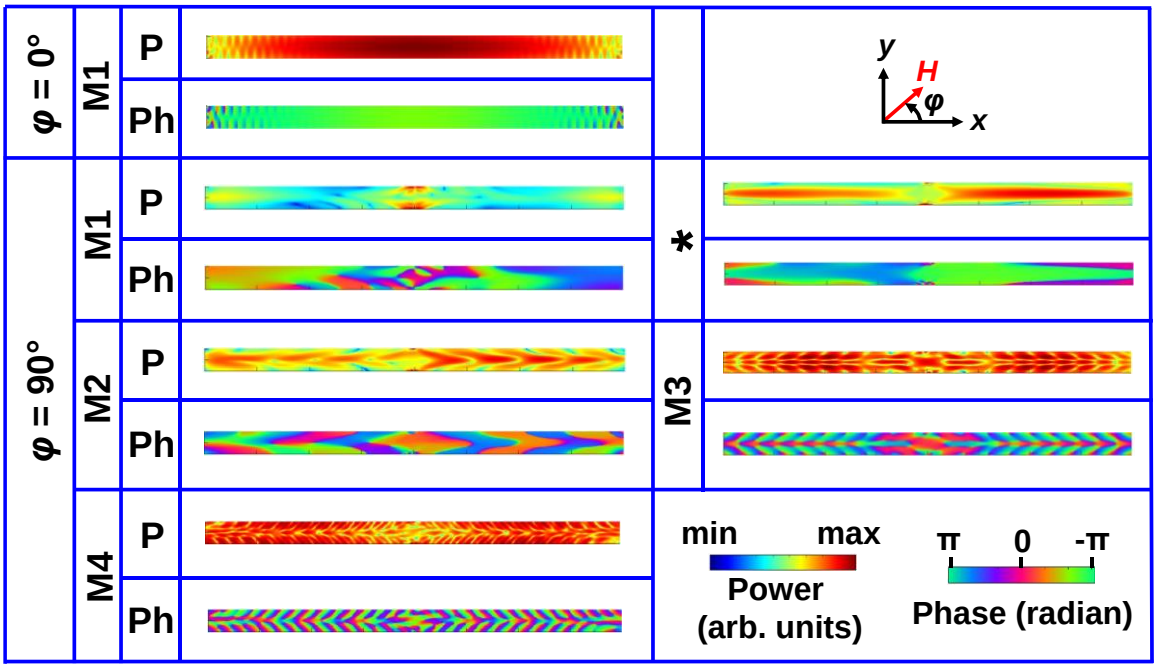

[26]**Figure 4.7.** The power and phase maps of different SW modes for the sample T2 for H = 1.13 kOe at two perpendicular orientations (φ = 0° and 90°) are shown. The schematic of the orientation of H is shown on the top right corner and the colour maps for power and phase profiles are shown at the bottom right-hand side. Only the central stripe from the array is shown for visual clarity. Sizes of the NSs are not to scale.

(EM). Here, the SW extends through the potential well, formed due to the edge demagnetized regions of the NSs. On the other hand, M2 shows a quantized behaviour in the backward-volume (BV) geometry with quantization axis parallel to the bias magnetic field direction having mode quantization number, n = 3. To understand the reverse trend of the bias field dependent frequency of M1 for T1 at φ = 90°, the corresponding power and phase profiles at four different bias field values near and away from the mode merging regime (H_m ~ 0.82 kOe) are presented in Figure 4.6(b). At H = 1.72 kOe, i.e., well above H_m, M1 and M2 clearly reveal EM and CM, respectively. However, with a decrease in H, M1 starts to extend towards the centre, while M2 gradually narrows down. At H = 0.98 kOe, M2 possess both the EM and CM characters before complete merging of the two to form a single CM for $H \leq$ 0.82 kOe. This drastic variation of the nature of M1 is responsible for the observed variation of SW mode frequencies with H as observed in Figure 4.5(a). Here, we have presented the power and phase maps from a single stripe from the centre of the array for clarity of visualization of the

mode profiles. The power map from the entire simulated array for a particular frequency (M2) at a particular orientation (φ = 90° at H = 1.13 kOe) is presented at the inset Figure 4.6(a), which reveals that the observed nature of modes in the central stripe is uniformly distributed over the entire array. This is true for all other SW modes as well. Figure 4.7 represents the power and phase profiles of different SW modes for the sample T2 calculated for H = 1.13 kOe applied along two in-plane orientations. For φ = 0°, M1 is a combination of

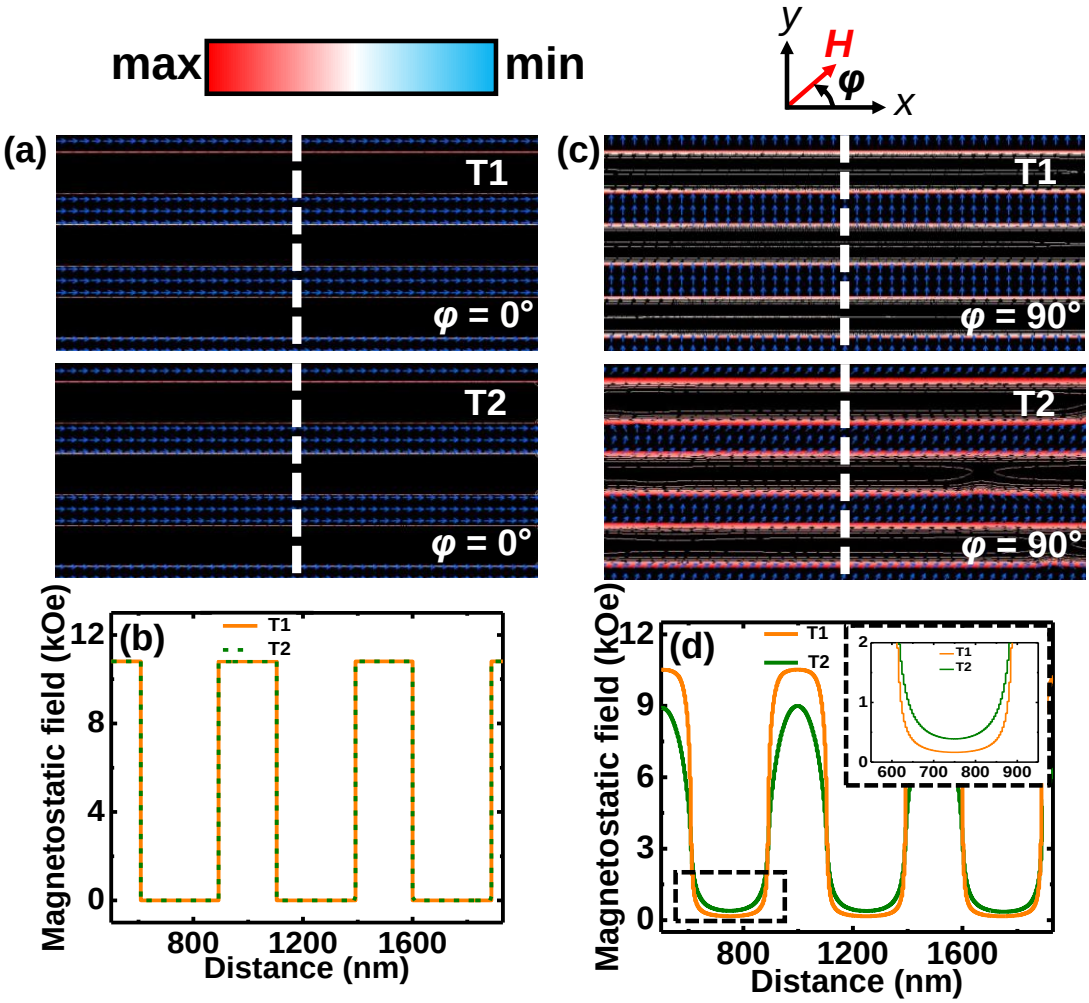

[27]**Figure 4.8.** The contour maps of simulated magnetostatic field distribution are shown for Py NS arrays of sample T1 and T2 for H = 1.13 kOe applied along (a) φ = 0° and (c) φ = 90°. The arrows inside the stripes represent the magnetization states. The schematic of the orientation of H and the colour bar of the strength of magnetostatic field are represented at the top of the figure. Sizes of the stripes are not in scale. Line scans of simulated magnetostatic field distributions from the arrays for bias field along (b) φ = 0° and (d) φ = 90°, taken along the white dotted lines as shown in (a) and (c), respectively. The magnified view of the magnetostatic field for φ = 90°, is shown at the inset of 4.8 (d).

the CM and quantized mode near the ends of the NS in the BV geometry. However, for φ = 90°, we observe the formation of different kinds of quantized SW modes due to the confining

potentials by the demagnetizing field. Due to quantization both along the length and the width of the stripe, an arrow like quantized mode with increased quantization number (n) along the length of the stripe is observed with increased mode number (SW frequency). Despite the

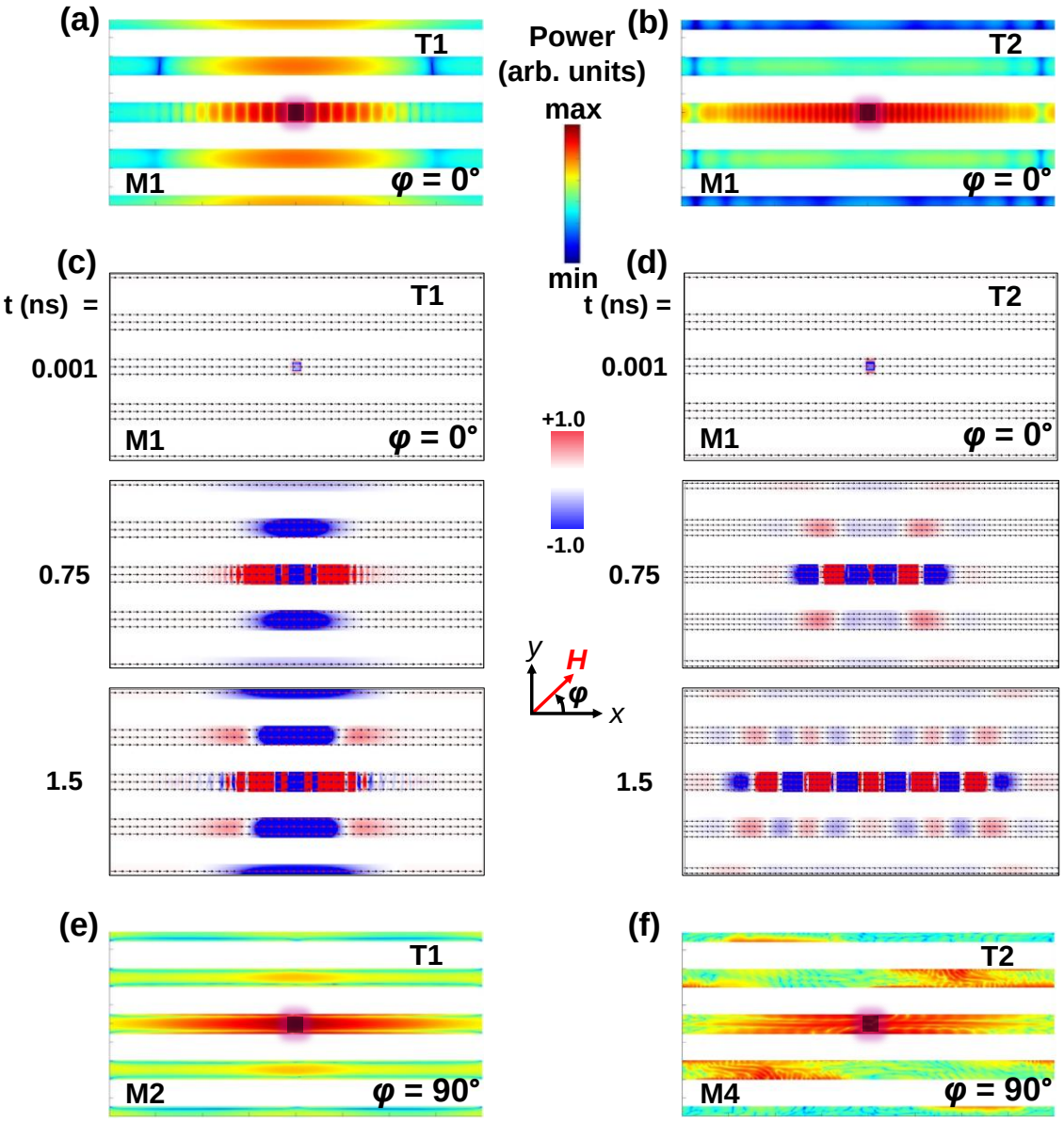

[28]**Figure 4.9.** Simulated power profiles of M1 for H = 1.13 kOe applied along φ = 0° in the samples (a) T1 and (b) T2 after local excitation at the centre of the NS represented by blue square region. Simulated SW propagation at different times (t in ns) in (c) T1 and (d) T2 at H = 1.13 kOe applied along the length of the NSs considered in the simulation. The power profiles of most intense SW mode (M2 for T1 and M4 for T2) for H applied along φ = 90° for the sample (e) T1 and (f) T2 due to the local excitation at the center of the array (highlighted by blue square region). The excitation field is applied at the centre of the NS array in a direction perpendicular (z-direction) to the sample plane. The schematic of the orientation of H, the colour map for z-component of magnetization vector of the propagating SWs and the colour map of power profile are shown at the centre of the figure.

complexity of the mode profiles, we could assign mode quantization number, n = 7, 13 and 41

for M2, M3 and M4, respectively. The mode "*" does not appear in the experiment as discussed earlier.

4.3.2.2. Simulated magnetostatic field distribution

We have further numerically simulated the magnetostatic field distribution in the NS array to underpin the origin of the collective SW modes by employing LLG micromagnetic simulator[340]. The contour maps of the simulated magnetostatic fields of samples T1, T2 for H = 1.13 kOe applied along $\varphi = 0°$ and $\varphi = 90°$ are shown in Figure 4.8(a) and (c), respectively. A careful observation reveals that there is a drastic variation of stray field distribution for H applied along $\varphi = 90°$ compared to that for $\varphi = 0°$ for the two samples. It is evident that the magnetic stray-field lines penetrate deeper inside the NSs in sample T2 as opposed to T1 for $\varphi = 90°$ as depicted in Figure 4.8(c). This is likely due to the increase in uncompensated magnetic poles in the NS structures at the boundaries for T2 at $\varphi = 90°$. On the contrary, almost negligible stray-field penetration occurs at $\varphi = 0°$ for both samples as observed in Figure 4.8(a). The magnetostatic field distribution, as shown in Figure 4.8(b) and (d), are calculated by taking the line scans along the white dashed lines as marked in Figure 4.8(a) and (c), respectively. Due to the negligible interaction between the NSs for both the samples for H along $\varphi = 0°$, as observed in Figure 4.8(a), the magnetostatic fields of the two coincide as manifested in Figure 4.8(b). For $\varphi = 90°$, the internal field strength of sample T1 is much greater than that of T2 as shown in Figure 4.8(d), which indicates modification of the demagnetization field. The higher demagnetizing field for sample T2 than T1 is responsible for the higher complexity of ground-state spin configurations (as shown in Figure 4.3), resulting in rich SW dynamics in the system. Consequently, the number of SW modes present in sample T2 at $\varphi = 90°$ is higher than T1 as observed from Figure 4.2(b). The magnified view of the magnetostatic field outside the NSs for both the samples are shown in the inset of Figure 4.8(d) (black dotted box), from where the stray field or the demagnetizing field are calculated as ~160 Oe for T1 and ~390 Oe for T2. This shows good agreement with the obtained values from the Kittel fit of the bias field dependent SW frequencies (as presented in Table 4. l).

4.3.2.3. Simulated spin-wave propagation

We have further numerically explored the propagation of the characteristic SW modes in the NS array and the role of NS thickness in determining the SW propagation. For this study, we have launched a sinusoidal excitation (a sinc excitation has given similar result but due to visual clarity of SW mode profile a sine excitation is preferred here) of the desired frequency corresponding to the SW mode frequency applied locally at the centre of the NS array over

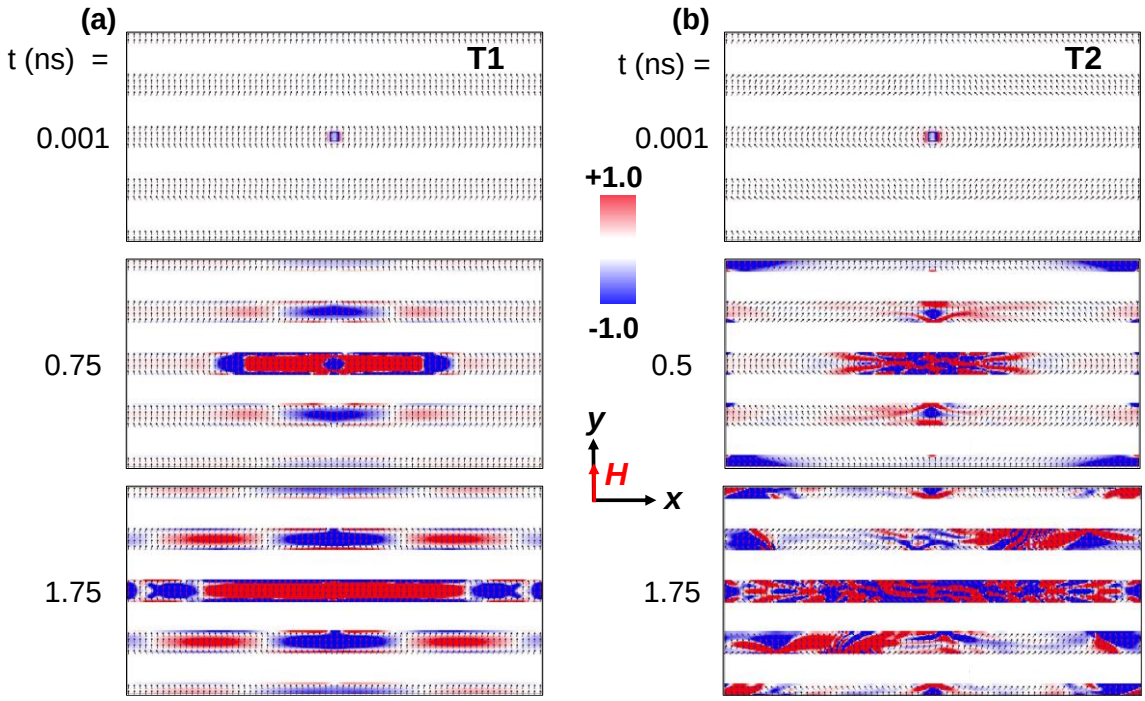

[29]**Figure 4.10.** Simulated SW propagation at different times (t in ns) in sample (a) T1 and (b) T2 for H = 1.13 kOe applied along the width of the NSs (φ = 90°) considered in the simulation. The excitation field is applied at the centre of the NSs in a direction perpendicular (z-direction) to the sample plane. The schematic of the orientation of H and the colour map for z-component of magnetization vector of the propagating SWs are shown at the centre of the figure.

100 nm × 100 nm area (highlighted by blue square region in Figure 4.9) to stimulate the SW in OOMMF. An external bias field H = 1.13 kOe is applied along the desired in-plane orientation. Figure 4.9(a) and (b) reveal that for H applied along φ = 0°, the SW mode M1 propagates uniformly in all possible directions for the sample T1, whereas for T2, M1 propagates primarily along the bias-field direction but ceases to propagate in other directions. This is due to much lower interaction fields between the NSs in T2 as opposed to T1 as shown in Table 4.1. Furthermore, Figure 4.9(c) and (d) illustrate the propagating nature of mode M1 with time. The spatial maps of SW reveal that the SWs travelled longer distance (along the bias-field direction) in sample T2 than T1 as evident from snapshots at t = 0.75 ns and t = 1.5 ns. This clearly indicates, the velocity of SW is much higher in T2 (approximately 2.3 km/s) as opposed to T1 (approximately 0.9 km/s). A careful observation will also reveal that the SW intensity along the direction perpendicular to the bias field is appreciable in T1, while it fades away quickly in T2. This asserts a possible application of T1 (lower thickness) as an omnidirectional emitter of SW while T2 (higher thickness) can be considered for application in SW waveguide with faster SW propagation. Finally, Figure 4.9(e) and (f) reveal the power distribution of the most intense SW mode for sample T1 (mode M2) and T2 (mode M4), respectively, for H applied along φ = 90° following a local excitation as described above.

For T1, due to the symmetric distribution of internal field as confirmed from the contour plots of magnetostatic field distribution in Figure 4.8(c), the power of mode M2 is distributed uniformly across the stripe-length as well as propagating across the array by virtue of the inter-stripe interaction field. On the contrary, the non-uniform distribution of inter-stripe stray field comes into play in T2 to distribute the SW power of mode M4 non-uniformly from the centre of the local excitation to the associated stripes. The spatial maps at different timescales for H applied along φ = 90° are presented in Figure 4.10 to explain the SW propagation across the array via the stray field distribution. These clearly divulge that only by subtle tuning of the aspect ratio and external bias-field direction, one can efficiently tune the SW propagation direction as well as velocity of propagation which can have significant impact in designing various components for magnonic circuits leading towards on-chip microwave communication devices.

4.4. Conclusion

In summary, we have studied the SW dynamics of $Ni_{80}Fe_{20}$ (Py) nanostripe (NS) arrays of 220 nm width, 280 nm inter-NS separation having two different thicknesses of 10 (T1) and 30 nm (T2) by controlling the strength (H) and orientation (φ) of the external bias magnetic field using an all-optical TR-MOKE microscopy. While both samples showed single mode with slight variation in frequency due to a difference in the demagnetizing field for φ = 0°, far more complex behaviour is observed for φ = 90° resulting in different but rich SW spectra in both the samples. The bias field dependences of SW frequencies for φ = 0° and 90° have been studied and an unusual variation of mode M1 of sample T1 at φ = 90° is observed, whose frequency increases non-monotonically with the decrease in bias field before merging with the mode M2 at ~ 0.82 kOe. The other modes were fitted with Kittel formula to extract the demagnetizing factors and inter-NS interaction fields, both of which are found to play significant roles in modifying the SW dynamics for different bias-field orientations. The primary features of the experimental findings have been qualitatively reproduced by micromagnetic simulations and the directional dependences of the SW spectra have been examined based on the ground state spin configurations and magnetostatic field distribution. The simulated power and phase profiles of the SW modes at different bias fields revealed an extension of M1 from the edges towards the centre and gradually narrowing down of M2 with the decrease in bias field before a complete merging of the two to form a single uniform mode for $H \leq 0.82$ kOe for the sample T1. Simulated magnetostatic field distributions threw further insights into the observed variation of SW modes due to changes in the internal magnetic field and inter-stripe interaction fields for the array. Further simulations using local excitations of

specific SW mode frequencies in different bias-field geometry opened up possible control over SW propagation by tuning the thickness of the NS. In essence, by subtle control of the dimensions and external magnetic field direction, rich and tunable SW properties can be obtained in ferromagnetic NS arrays which can be utilized to construct advanced frequency-selective components for magnonic circuits for allowing parallel data communication and processing[341].

Chapter 5

5. Bias-Field Tunable Magnon-Magnon Coupling in $Ni_{80}Fe_{20}$ Nanocross Array

Hybrid dynamical systems have gained huge momentum not only due to their exotic physical properties but also their compelling engineering standpoint, particularly owing to their potential for coherent information processing. Remarkably, we experimentally identify magnon–magnon coupling in $Ni_{80}Fe_{20}$ nanocross array with number of spins reaching a very low value of $\sim 10^{12}$. Moreover, we are able to effectively tune the coupling strength via different external parameters, viz. microwave excitation power and the bias-field orientation. Extensive simulations reveal that both the static and dynamical dipolar coupling contribute to the observed anticrossing phenomenon. Simultaneously, we also observe mode-softening of spin wave tunable by subtle changes of bias-field orientation. Our findings could greatly enrich various hybrid phenomena with a magnonic platform.

5.1. Introduction

When the interaction between an electromagnetic wave and a collective excitation in a matter is reinforced to a large extent by a cavity, the energy is exchanged between them. The combined system is termed as hybrid quantum system which will act as quantum nodes of the future quantum computing.[342] Such hybrid systems showcase huge versatility for combining platforms and devices based on strong coupling between different quasiparticles and allow for tailoring the response of the system in one degree of freedom via regulating the excitations in the other. Over the last few years, the coherent interaction between magnons and other quasiparticles of matter, e.g., phonons, photons, magnons, superconducting qubits, etc. has attracted intense attention of the research community owing to the advantage of quantum transduction and coherent information transfer in quantum information processing,[82] storage,[343] and sensing.[83] It all started from the discovery of spin ensembles coupled to microwave photons as reported in the literature,[69,344] where the spin-photon coupling strength (g) was stated to be triggered by the Dicke's size-scaling law,[345] $g \propto \sqrt{N}$, where N is the total number of spins in the system. So, in order to achieve high coupling strengths, the dimensions of the magnonic cavity require to be of the order of millimetres. Considering that, numerous experimental works[63,66,67,346–350] have been done in the field of microwave cavity enhanced magnon coupling in various systems with YIG acting as the preferred material for cavity magnetics[2,32] in most of the cases due to its low damping and very high spin density.[351] Recently, magnon-magnon coupling in different

kinds of systems have also been reported, including compensated ferrimagnet,[76] 2D antiferromagnetic $CrCl_3$ material[72] as well as in synthetic antiferromagnetic systems,[79,352,353] which offers wide versatility of parameter spaces to tailor the coupling phenomena. In addition, magnon-magnon interactions were observed in magnetic metal/insulator hybrid structures,[354] YIG/Co heterostructures,[355] and YIG/Py bilayer[356] systems predominantly demonstrating the role of interlayer exchange interaction as well as dynamic dipolar interaction in the observed phenomena. But, most of the works demonstrating hybrid interactions with magnon as one of the quasiparticles are in bulky materials, i.e., in the form of large-sized spheres or infinite thin films, which pose limitations in device miniaturization and on-chip integration for scalable information processing.[357] More recently, few breakthrough works[358–360] have demonstrated significant magnon-magnon coupling in ferromagnetic nanoelements which is tunable by material and geometric parameters of nanomagnets as well as microwave power. However,

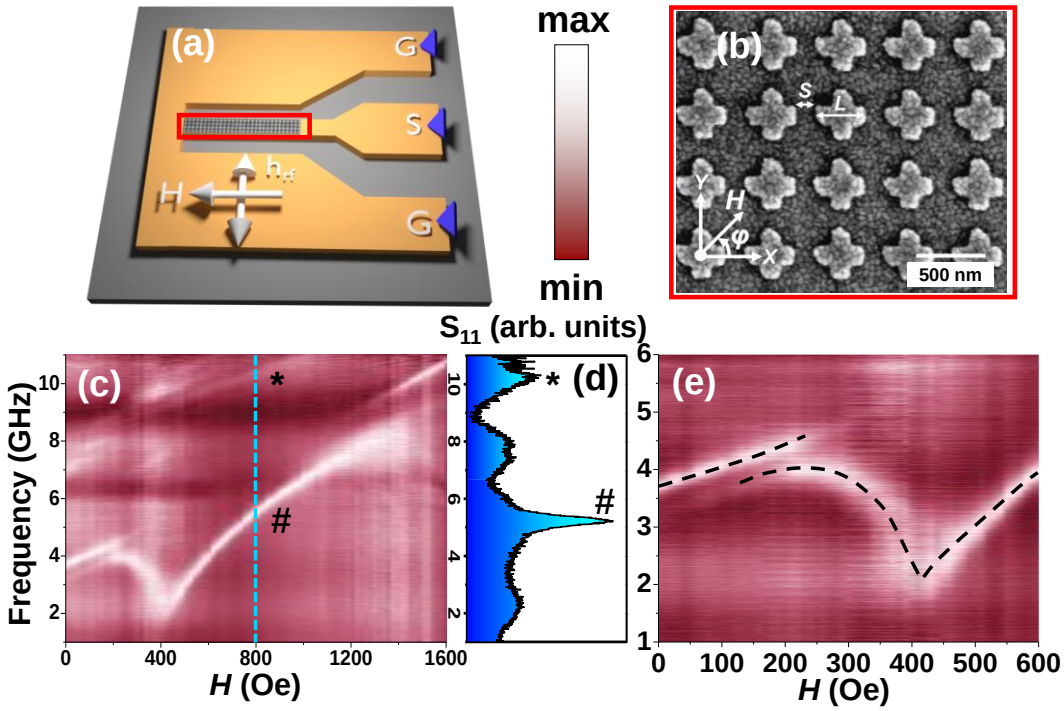

[30]**Figure 5.1.** (a) A schematic of experimental geometry for the broadband FMR measurement, where the sample lies in the red boxed region and (b) SEM image of Py NC array of arm length $L \sim 330 \pm 20$ nm, inter-NC separation $S \sim 170 \pm 10$ nm and thickness $t \sim 20$ nm. Orientation of bias field is shown for convenience. (c) Surface plot of bias-field-dependent SW mode frequencies for NC array for $\varphi = 0°$ at $P = -15$ dBm, where the real part of S_{11} parameter showing the raw FMR spectra at the blue dotted point of $H = 800$ Oe is shown in (d). The two SW modes are marked as * and #, respectively. The magnified view of the anticrossing region is shown in (e), where the black dotted line is a guide to eye. The color map of the surface plot is shown at the top central portion of the figures.

such studies in nanoscale ferromagnets is still at a nascent stage. This includes, ferromagnetic nanocross elements[358] which possess complex ground-state spin configurations[361–363] as well as rich spin wave (SW) properties[170,364,365] showing various rich phenomena such as magnonic mode softening, mode crossover, mode splitting, mode merging and nonlinear ferromagnetic resonance shift in their dynamical response. Interestingly this system also exhibited two avoided crossing in the magnetic field dispersion of spin-wave frequencies characteristic of magnon-magnon coupling of spin-wave modes confined inside the individual elements acting as a magnonic cavity.[358] The coupling strength increased with increased microwave excitation power and detailed analyses revealed that increased dipolar coupling between the nanocross played a major role in enhancing the magnon-magnon coupling. However, the lateral dimensions of the studied nanocross were about 600 nm, which is substantially large for on-chip integration of hybrid systems and significantly large magnon-magnon coupling with further downscaling of ferromagnetic element will be necessary.

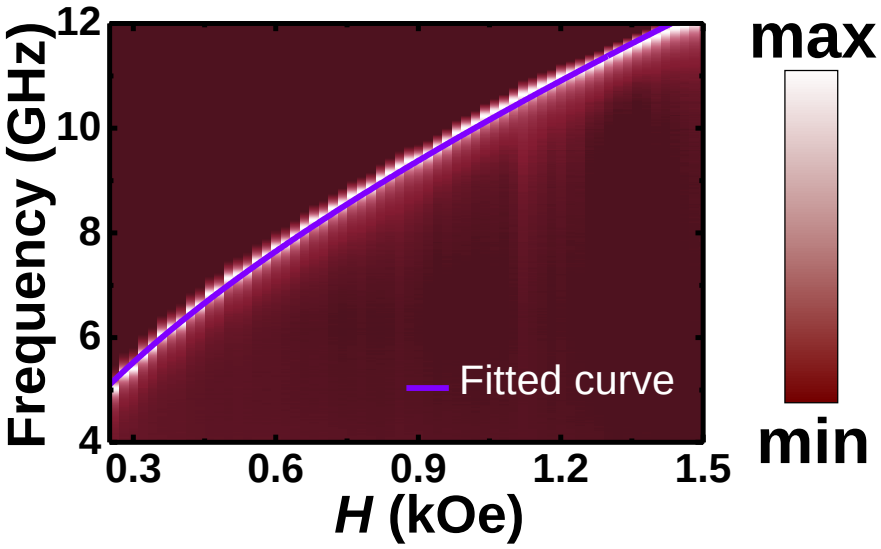

[31]**Figure 5.2.** Experimental results of bias magnetic field dependent precessional frequency of an unpatterned Py thin film is shown as a surface plot. The solid line represents theoretical fit using the Kittel formula.

Here, we have downscaled the nanocross dimensions by about a factor of two (number of spins reduced by an order of magnitude) and demonstrated tunable magnon-magnon coupling in a $Ni_{80}Fe_{20}$ (Permalloy: Py hereafter) nanocross array by using a custom-built broadband ferromagnetic resonance (FMR) technique. The magnon-magnon coupling is found to be tunable over a wide range of microwave excitation power and we have decoded the observed phenomenon from the simulated magnetic field distribution. Eventually, the

power and phase profiles of the interacting SW modes at and away from the anticrossing region substantiate the observed phenomenon. Moreover, we have examined the crucial role of subtle variation of bias-field angle to further tune the coupling strength via magnetic microstate tuning and supported our experimental observations by micromagnetic simulations. We have also detected a mode-softening of SW, due to different magnetic microstate of the nanocross structure, which could also be controlled by subtle tuning of bias-field angle. Finally, we anticipate this system can serve as a testbed for future quantum communication devices.

5.2. Experimental and Simulation Methods

5.2.1. Sample fabrication

A 25 μm × 250 μm array of ferromagnetic nanocross structures having arm length (L) ~ 330 ± 20 nm, edge-to-edge separation (S) ~ 170 ± 10 nm, and thickness (t) ~ 20 nm was fabricated using a combination of electron beam lithography (EBL) and electron beam evaporation (EBE) technique followed by lift-off processes.[365] The scanning electron micrograph (SEM) image of the sample is illustrated in Figure 5.1(b). A bilayer PMMA/MMA (polymethyl methacrylate/methyl methacrylate) resist pattern was first developed on self-oxidized Si (100) substrate using EBL followed by deposition of a 20-nm-thick Py layer at a base pressure of 2×10^{-8} Torr. A 60-nm-thick insulating layer of Al_2O_3 was subsequently deposited on top of the Py layer to avoid any damage to the samples due to high radio frequency (rf) current. A coplanar waveguide (CPW) structure made up of Au with a nominal thickness of 150 nm was deposited on top of the array structures for the broadband FMR measurement in such a way that the entire array remains beneath the signal conducting line of the CPW. The width and length of the central conducting line of this CPW are 30 μm and 300 μm, respectively, having a nominal characteristic impedance (Z_0) of 50 Ω, which ensures maximum power handling capacity as well as minimum attenuation loss of the FMR measurement.

5.2.2. Measurement technique

The broadband FMR measurements were performed using a vector network analyzer (VNA; Agilent, PNA-L N5230C, frequency range: 10 MHz - 50 GHz) and a custom-built high-frequency probe station with a non-magnetic G-S-G type probe[165] (GGB Industries, Model No. 40A-GSG-150-EDP). The external bias magnetic field with strength (H) up to ±1.8 kOe was applied by virtue of an in-built electromagnet. The electromagnet is mounted on a high-precision rotary mount, which can be rotated over 360° angles within the sample-plane. Variable frequency microwave signals, generating a microwave

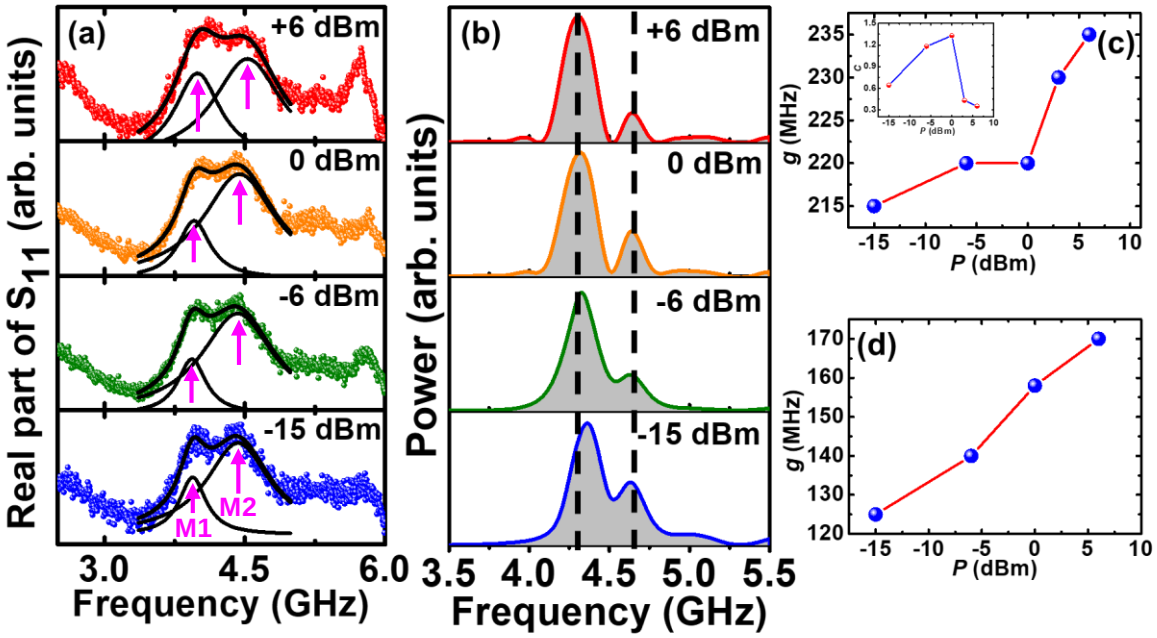

[32]**Figure 5.3.** (a) Real part of S_{11} parameters of lowest-frequency SW branch as a function of frequency at H = 200 Oe for different values of P showing the anticrossing. The solid black lines represent theoretical fits and SW modes are identified as M1, M2 by upward arrows. (b) Corresponding simulated SW spectra, where the black dotted lines help to visualize the shift in frequencies for clarity. (c) Experimental and (d) simulated values of g as a function of P for the anticrossing are shown by filled circular symbols. The inset of (c) represents variation of co-operativity (C) as a function of P. The solid lines are lines joining the symbols.

magnetic field h_{rf} along the y-axis of the nanocross array, are launched into the CPW structure using a G-S-G type probe through a high-frequency, low-noise coaxial cable (model no: N1501A-203). If the excitation frequency matches the resonance frequency of the sample at a given bias field, microwave power is absorbed in order to maintain the precessional motion of the magnetization and resonance occurs. From the resonance spectra, characteristic SW response of the sample is recorded. Here, the CPW is shorted at one end and the back-reflected signal is collected by the same probe to the analyzer via the same coaxial cable. We first calibrate the system using a commercially available calibration standard (CS-5 kit) to remove systematic errors from the measurement results, caused by non-ideal components in the VNA and test set-up. Next, the real and imaginary parts of the scattering parameters in reflection geometry (S_{11}) are measured at different magnetic fields and a reference spectrum obtained at the highest bias magnetic field (1.8 kOe) is subtracted from spectrum at each bias magnetic field. Here, we have systematically varied H from +600 Oe to 0 Oe at an interval of 10 Oe, microwave power from -15 dBm to +6 dBm, and bias-field angle from φ = 0° to 15° for this study. The schematic diagram of the experimental set-up is illustrated in Figure 5.1(a) and the whole measurement has been carried out under ambient conditions.

Table 5.1: Magnon-magnon coupling related parameters at different microwave powers

Microwave power (P in dBm)	Anticrossing strength (g in GHz)	Dissipation rate of M1 (k_1 in GHz)	Dissipation rate of M2 (k_2 in GHz)	Cooperativity $C = \frac{g^2}{k_1 k_2}$	Strong or weak coupling?
+6	0.235	0.39	0.40	0.35	Weak (as $g < k_1, k_2$)
+3	0.230	0.32	0.38	0.43	
0	0.220	0.13	0.28	1.33	Intermediate (as $k_1 < g < k_2$)
-6	0.220	0.12	0.34	1.18	
-15	0.215	0.19	0.38	0.64	

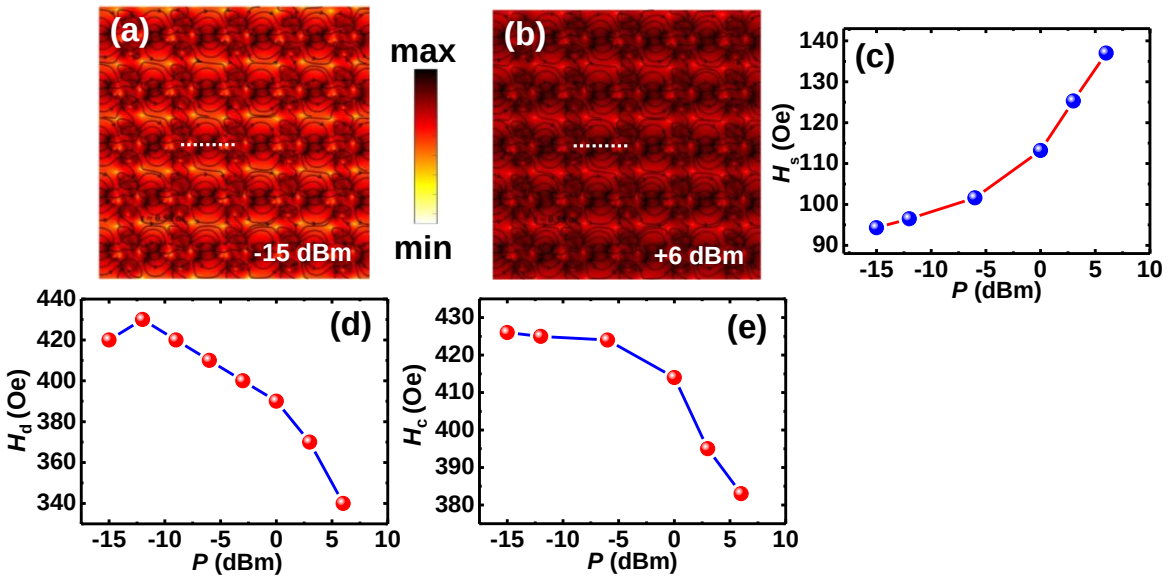

[33]**Figure 5.4.** Simulated magnetic stray-field distribution between the neighboring NCs at (a) P = −15 dBm and (b) P = +6 dBm, respectively, at H = 200 Oe. The color map is shown in between the images. The calculated magnetic stray field (H_s) at the between two NCs of the central region from the array as calculated from the linescans as shown by white dotted lines in (a), (b) and is plotted in (c). The mode-softening dip position (H_d) is plotted as a function of P in (d). (e) Simulated coercive field (H_c) values as a function of P.

5.2.3. Micromagnetic simulation

The experimentally obtained results have been elucidated with the help of micromagnetic simulations using OOMMF software[366] based on the finite difference method (FDM). The details of the simulations can be found in the literature.[367] Here, we have taken 5×5 nanocrosses and applied two-dimensional periodic boundary condition (2D-PBC) to mimic the large area of the experimentally measured sample. The entire array has been discretized

into identical rectangular parallelepiped-shaped cells with volume 4×4×20 nm^3. The lateral cell size is intentionally kept well below the exchange length of Py (~ 5.2 nm), to include the exchange interaction of the system. The material parameters used in the simulations are: gyromagnetic ratio, γ = 17.6 MHz/Oe, saturation magnetization, M_S = 800 emu/cm^3, anisotropy field, H_K = 0, exchange stiffness constant, A = 1.3×10^{-6} erg/cm,[330] and damping coefficient α = 0.008[331] for dynamic simulation. The value of M_S was extracted from the bias field-dependent precessional frequency of a Py thin film of identical thickness (Figure 5.2). The radio frequency (rf) excitation in the experiment is imitated by employing a two-step micromagnetic simulation. First, a static simulation is carried out to attain the ground state of the magnetization at the desired bias field by minimizing the total energy of the simulated magnetic volume from a high enough field to the bias field. Second, a dynamic simulation starting from the ground magnetization state is performed with an rf perturbation field h_{rf} applied perpendicular to the external bias field. The h_{rf} is adapted in the form of a "Sinc" function, $h_{rf}(t) = h_0 \sin(2\pi ft)/(2\pi ft)$.[312,368] Here, the amplitude $h_0 = \sqrt{\frac{P}{4Z_0 w^2}}$ is determined from the applied microwave power (P), Z_0, the characteristic impedance of the CPW, and w, the width of the central conductor of the CPW. The magnons with frequencies ranging from 0 to 20 GHz has been effectively excited by setting up the cut-off frequency of the "sinc" function to f = 20 GHz. During the dynamic simulation of 8 ns duration, the out-of-

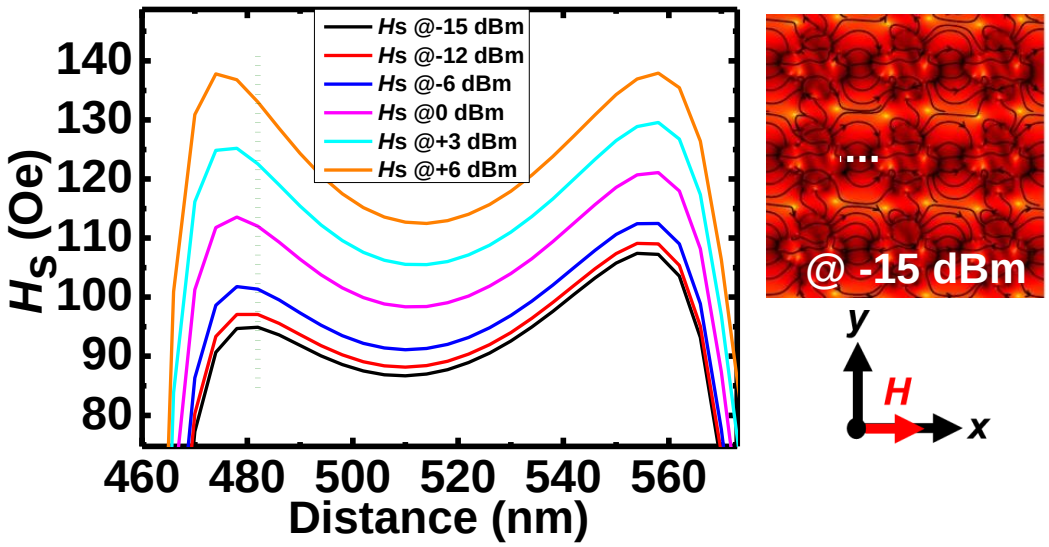

[34]**Figure 5.5.** Simulated magnetostatic field distribution between neighboring NCs for H = 200 Oe applied along φ = 0°, for different P values. The linescan has been taken from the white dotted line as shown on right hand side of the figure. The green dotted line represents the line from where the stray field values have been extracted to plot Figure 5.4(c).

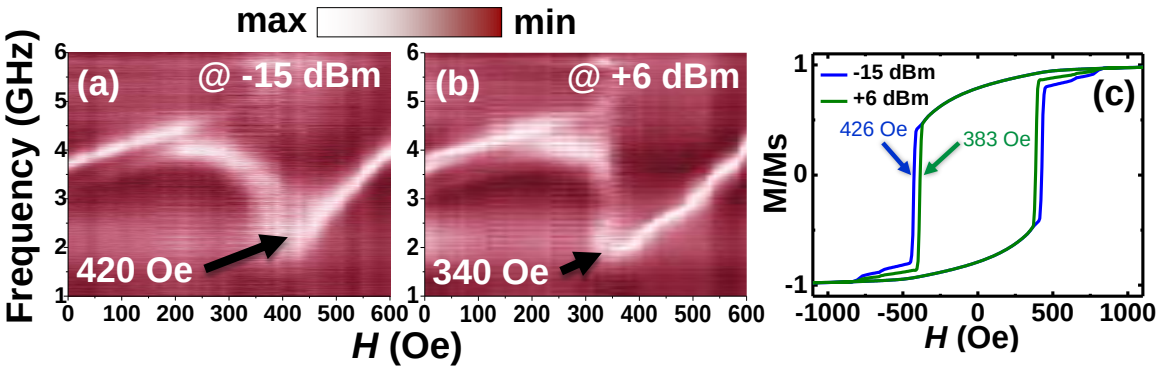

[36]**Figure 5.6.** Surface plots of the experimental bias-field-dependent SW mode frequencies at lower field regime for two different microwave powers (P) are shown in (a) P = -15 dBm and (b) P = +6 dBm, where mode-softening dip positions (H_d) are marked and written in each figure. (c) represents the simulated hysteresis loops with microwave powers applied perpendicular to the bias-field direction. Here, the coercive field (H_c) values are arrow-marked and written for both P values.

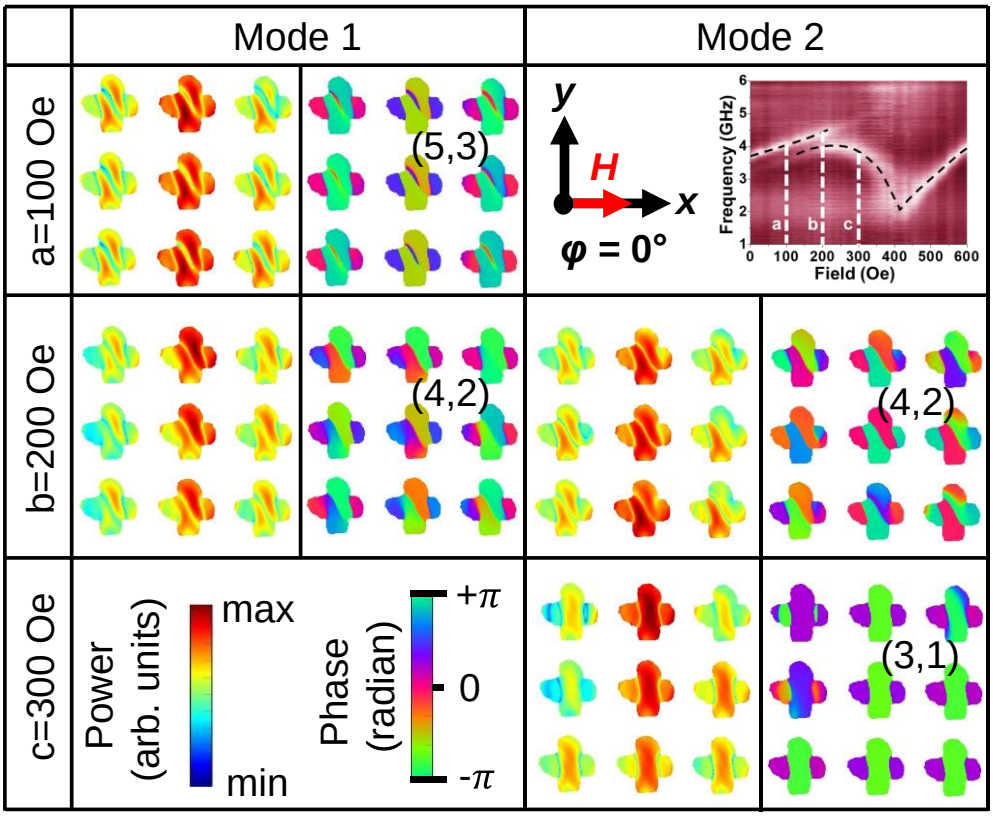

[35]**Figure 5.7.** Simulated spatial distribution of power and phase profiles of coupled SW modes at and away from the anticrossing region, where the two SW modes (marked as a, c) causing the anticrossing at b, which are shown in top right corner along with the bias-field orientation. The color maps of power and phase profiles are shown at the bottom left corner.

plane magnetization component (m_z) was saved at a time interval of 10 ps and the fast Fourier transform (FFT) of that yields the SW spectra at a specific bias magnetic field.

5.3. Results and discussion

5.3.1. External tuning of magnon-magnon coupling via microwave excitation power

The bias field dependence of the SW absorption spectra for the sample in the range of 1.6 kOe ≤ H ≤ 0 is plotted at an interval of 20 Oe in the form of a surface plot for a fixed azimuthal angle φ = 0° as presented in Figure 5.1(c). The real part of the forward scattering parameter S_{11}, i.e., the raw FMR spectra is shown for H = 800 Oe as illustrated in Figure 5.1(d), which reveals the presence of two SW modes marked by '*' and '#'. From Figure 5.1(c), a non-monotonic variation of frequencies of FMR modes with bias field are clearly observed. There also exists a transfer of mode power from one SW branch to another at lower bias field regime (around 200 Oe) as well as at higher field regime (around 1480 Oe), where both SW modes coexist for a certain field range. This corresponds to avoided crossing or anticrossing phenomenon. The magnified view of the first anticrossing region is presented in Figure 5.1(e). Additionally, this region includes a sharp minimum in the SW frequency at around 420 Oe, which is known as mode-softening phenomenon.[369,370] Here, we attempt to explore how various external factors such as amplitude of microwave excitation power and bias field angle affect or modulate two such remarkable observations.

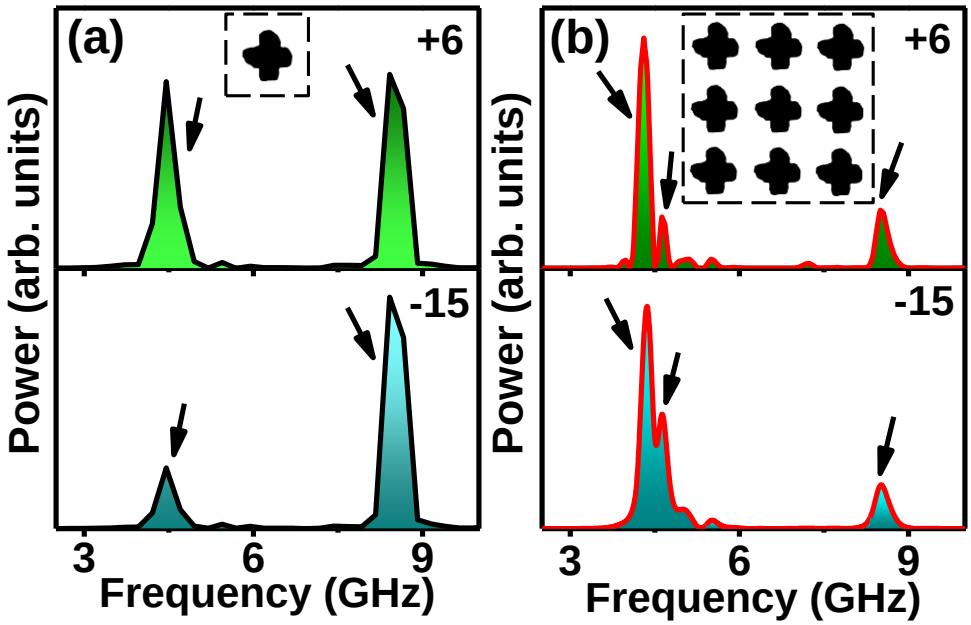

[37]**Figure 5.8.** Simulated SW spectra of a single Py NC at H = 200 Oe at two different values of P, where numbers represent P values in dBm. For comparison, the SW spectrum from the array is shown in (b). The downward arrows correspond to different SW frequencies. The image of the simulated sample is shown for each case.

We further explore the possible modulation of the anticrossing phenomenon by varying the amplitude of the excitation power. Figure 5.3(a) presents the experimentally observed anticrossing region with variable microwave power in the range -15 dBm ≤ P ≤ +6 dBm. The two coupled SW modes (M1 and M2) are fitted with double-peak lorentzian function to extract the SW frequency values of the individual mode. Subsequently, we define the coupling strength (g) as half the splitting between the two interacting SW modes at the anticrossing point i.e., $g = |M1 - M2|/2$,[360] where M1 and M2 are the frequencies of two interacting modes and plotted as a function of P in Figure 5.3(c). This clearly proclaims a gradual increment in g with the rise of P. Furthermore, we have extracted various other parameters from the fit as represented in Table 5.1, which indicates that this coupling falls in the weak or intermediate coupling regime. Figure 5.3(b) presents the corresponding simulated SW spectra for different values of P at H = 200 Oe. The g values are similarly calculated and plotted as a function of P as depicted in Figure 5.3(d). The incremental nature of g with P extracted via simulation agrees qualitatively with the experimental observations. Here, the magnon-magnon coupling in ferromagnetic nanocross (NC) structure has been obtained for a very low spin ensemble system.

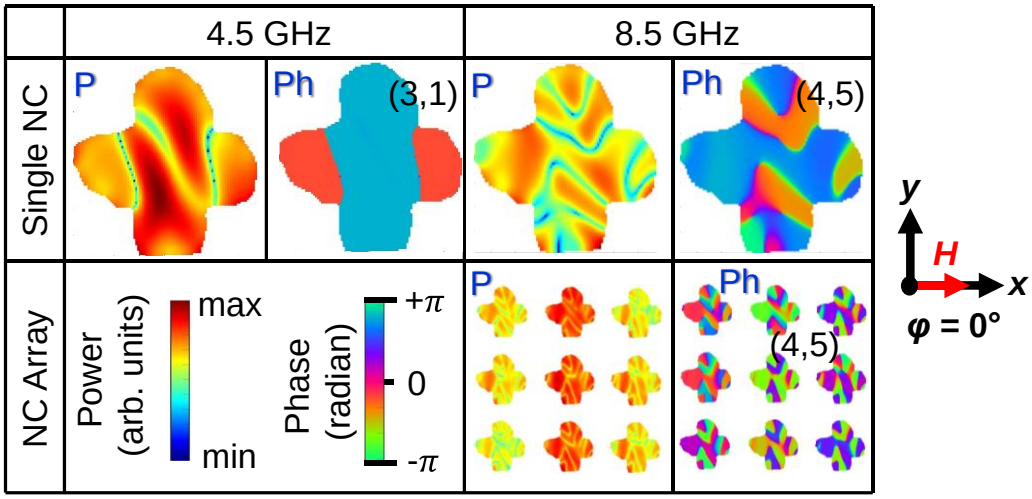

[38]**Figure 5.9.** Simulated spatial distribution of power (P) and phase (Ph) profiles of different SW modes from the single NC as well as arrays of NC (except the interacting modes of the array; which are discussed in the main article) for H applied along φ = 0°, as shown on right hand side of the figure. The color maps of power and phase profiles are shown at bottom left corner.

The number of spins in the entire system as well as individual NC element are calculated as follows:

$N = nN'$, n = total no. of NCs, and $N' = \frac{M_S V'}{\mu_B}$ represents the number of spins in the individual NC. Here, M_s = saturation magnetization = 800×10^3 A/m, μ_B = Bohr Magneton = 9.27×10^{-24} J/T, and V' = volume of the individual NC. Here, n = (total area/pitch of the array) = (25 μm × 250 μm)/(0.5 μm × 0.5 μm) = 25×10^3 and V' = area of a NC × thickness = $d\times(2L-d)\times t$; [d = width of each arm ≈ 130 nm, here]. Now, putting all the values, we found N' = 1.16×10^8 and N = 2.9×10^{12} for the entire system. However, this is slightly overestimated value, as it is clearly visible from the SEM images as shown in Figure 5.1(b) that the edges of each NC has rounded corners. Therefore, the actual value of magnetic volume and hence the value of N will be slightly less than the calculated value, i.e., $N \sim 10^{12}$.

To understand this incremental trend of g, we have simulated magneto-static field distribution of the sample at different values of P and illustrated in Figure 5.4(a) and (b) for lowest (-15 dBm) and highest (+6 dBm) values of P, respectively. It is clearly evident from the change in color contrast of the two figures that there is a significant decrease in uncompensated magnetic moments, when P is increased from -15 dBm to +6 dBm, due to the increment of dynamic dipolar interaction between the adjacent NCs as discussed in the article.[358] Nevertheless, we have calculated the stray-field values between two successive NCs from the line-scans (shown in white dashed lines in Figure 5.4(a) and (b)) at different values of P. Additionally, a comprehensive plot of stray-field distribution is presented in Figure 5.5. From there, we have extracted the values of H_s at different values of P and illustrated in Figure 5.4(c), which shows a drastic enhancement in H_s from ~94 Oe at -15 dBm to ~137 Oe at +6 dBm. Therefore, the interaction between the unsaturated spins at the edges of the neighboring NCs modifies the SW dynamics by an appreciable amount. Thus, this stray-field mediated dynamic dipolar interaction is likely the possible reason for the observed variation on magnon-magnon coupling in this system. On the other hand, Figure 5.4(d) presents the experimental mode-softening dip positions (H_d) at different values of P, which are extracted from the experimental bias-field dependent SW absorption spectra as shown in Figure 5.6(a),(b). It clearly shows that H_d decreases from ~420 Oe at -15 dBm to ~340 Oe at +6 dBm in a non-linear fashion. Hence, with an

increase in P, the SW mode softens at lower field values. This can easily be correlated with the coercive field (H_c) of the simulated hysteresis loops (by application of microwave power perpendicular to the external field), which is presented in Figure 5.6(c). The mode-softening dip position (H_d), i.e., magnetic field corresponding to the minimum in the SW

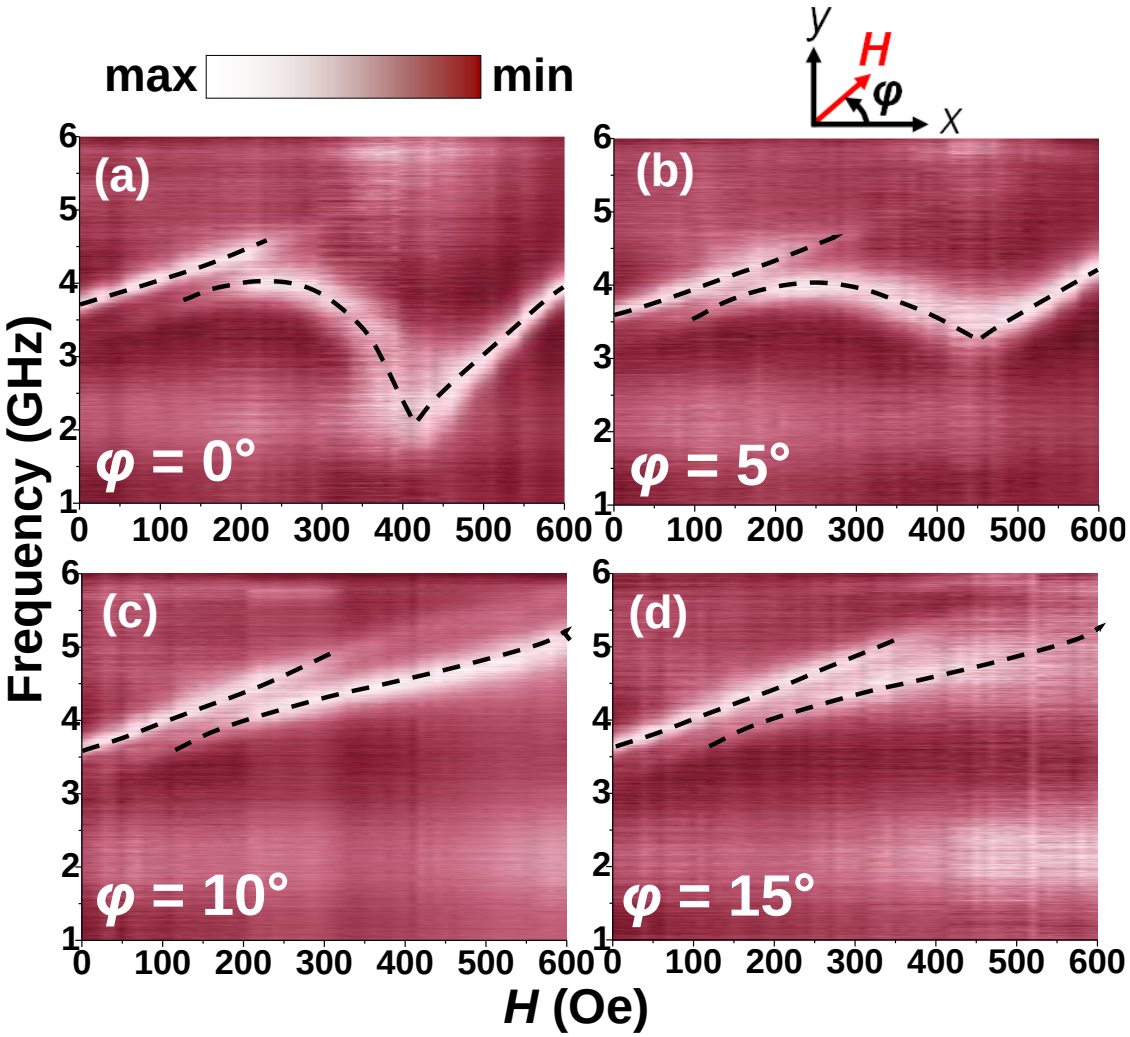

[39]**Figure 5.10.** Three-dimensional surface plots of the bias-field-dependent SW mode frequencies for different bias-field angles (φ) are shown in (a)-(d), where values of φ are written in each figure. The black dotted line is a guide to eye. The color map and the schematic of the orientation of H are shown at the top of the figure.

frequency for different values of P is extracted from the experimental SW absorption plots as shown by the arrows for two different values of P in Figure 5.6(a), (b). To understand what happens to the magnetic configuration when microwave power is varied, we have simulated hysteresis loops in presence of a rf field applied perpendicular to the external field. Figure 5.6(c) clearly reveals that with the increment of microwave excitation power, the coercive fields gradually decreases, i.e., samples becomes magnetically softer. This

decrement in coercive field with the rise in microwave power correlates with the shift in H_d qualitatively indicating a dynamic variation of magnetic configuration is responsible for this shift on mode softening field. On the other hand, Figure 5.4(e) shows that the variation of H_c with P follows similar trend as that of H_d. As coercive field indicates the ability of a ferromagnetic material to withstand an external magnetic field, this decremental trend of H_d signifies that the system is becoming magnetically softer with increment of P. This demonstrates that one can efficiently tune the mode-softening phenomena externally by precise control of excitation power.

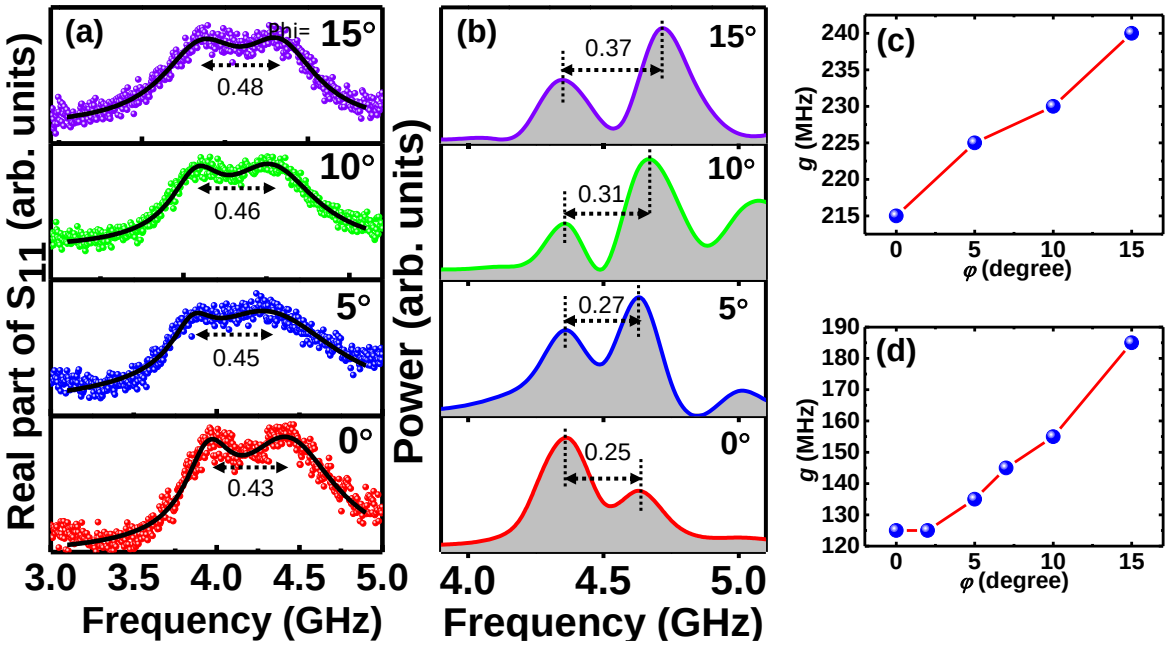

40Figure 5.11. (a) Real part of S_{11} parameters of interacting SW modes as a function of frequency at H = 200 Oe for different values of φ showing the anticrossing. (b) Simulated SW spectra for the same. The $2g$ value (in GHz) is shown in each case. (c) Experimental and (d) simulated values of g as a function of P for the anticrossing are plotted as filled circular symbols. The solid lines are lines joining the symbols.

Table 5.2: Magnon-magnon coupling related parameters at different bias field angles:

Angle (φ in °)	**Anticrossing strength (g in GHz)**	**Dissipation rate of M1 (k_1 in GHz)**	**Dissipation rate of M2 (k_2 in GHz)**	**Cooperativity $C = \frac{g^2}{k_1 k_2}$**	**Strong or weak coupling?**
0	0.215	0.17	0.35	0.77	Intermediate

5	0.225	0.15	0.53	0.63	(as $k_1 < g < k_2$)
10	0.230	0.19	0.33	0.84	
15	0.240	0.29	0.27	0.73	Weak (as $g < k_1, k_2$)

5.3.2. Mode profiles analysis

To understand the origin of the observed SW modes both experimentally and in the simulation, we have further analyzed the output files of the dynamic simulations to unlock the spatial power and phase maps of those SW modes by using a home-built code Dotmag.[285] The detailed procedure is discussed in the literature.[110] Power and phase maps of two interacting SW modes are shown in Figure 5.7 at three different field values, at the anticrossing field b = 200 Oe and away from the anticrossing fields a = 100 Oe and c = 300 Oe, which are presented at the inset of the top right corner of the figure for convenience. The SW modes are mixed standing wave (quantized) in nature and we assign quantization number as (n, m), where n, m are quantization numbers in the backward volume (BV) and Damon-Eshbach (DE) geometry, respectively. Mode 1 (at a = 100 Oe) and mode 2 (at c = 300 Oe) are mixed quantized SW modes with quantization numbers (5, 3), and (3, 1), respectively. Subsequently, these two SW modes interact with each other and transfer their energies, eventually showing identical behavior with the same quantization number (4, 2) at the anticrossing region b = 200 Oe. This sharp change in quantization number and consequent assumption of identical nature for a narrow field range manifests the magnon-magnon coupling in this system.

In order to understand the root cause of the anticrossing phenomena, we have further simulated the dynamics of a single Py NC and compared it with the NC arrays for two different microwave powers as presented in Figure 5.8(a)-(b), respectively. The SW modes are identified by a downward arrow in each case. The results clearly reveal the absence of any anticrossing gap at lower frequency regime even at higher microwave powers for a single Py NC as opposed to an array. Therefore, the anticrossing phenomenon must stems from the inter-NC interaction between neighbouring NCs, which is eventually getting modulated by the amplitude of external excitation. More precisely, the dynamic dipolar interaction between the neighbouring NCs boosts the observed anticrossing phenomenon, as it enhances the overall stray magnetic field in the arrays as indicated in Figure 5.4(c). The single NC element, the low

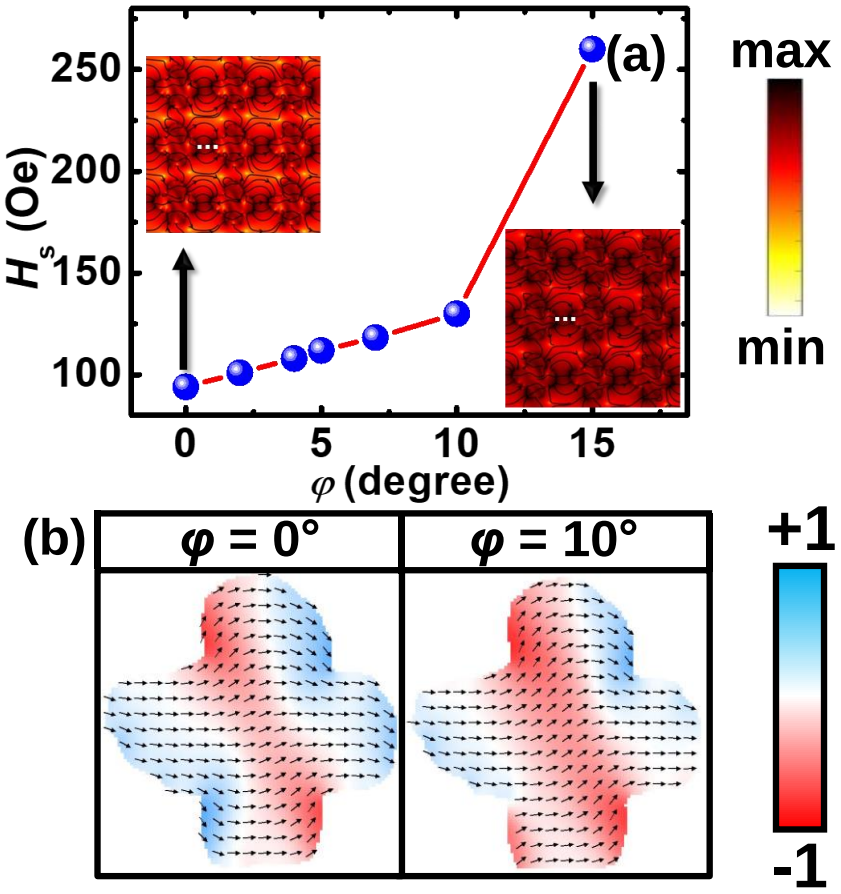

[41]**Figure 5.12.** Simulated magnetic stray-field (H_s) distribution as a function of φ at H = 200 Oe. The magnetic stray fields are calculated from the centre of the dotted lines as depicted for φ = 0° and 15°. (b) Simulated static magnetic configurations for Py NC at two different angles of bias magnetic-field H = 400 Oe. We have shown here a single NC from the center of the array for clarity in visualization of the spin configurations. The color maps of corresponding plots have been shown on right hand side.

frequency SW mode (~ 4.5 GHz) is mixed quantized in nature with quantization number (3,1). However, in case of an array of NC, an anticrossing gap occurs around that frequency regime. Additionally, the higher frequency SW mode at ~ 8.5 GHz in case of an array as well as a single NC have similar origin with identical quantization number (4, 5). It indicates that this mode is intrinsic to the NC structure as shown in Figure 5.9.

5.3.3. Role of azimuthal angle of bias field on the anticrossing phenomenon

Further, we investigate the role of azimuthal angle (φ) of the bias field on the mode-softening and mode anticrossing phenomena. Although we have systematically and precisely varied φ from 0° to 90°, the power of the SW modes diminishes significantly beyond φ = 15°, making it nontrivial to evaluate the anticrossing phenomenon beyond that angle. Hence, Figure

5.10(a)-(d) illustrates the surface plots of the anticrossing regions at four different φ values: 0°, 5°, 10°, and 15°. It is evident that the mode-softening feature, which is prevalent at φ = 0°, decreases rapidly by varying φ to only 5° and eventually disappears for $\varphi \geq 10°$. Additionally, we have analyzed the coupled SW modes to extract the magnon-magnon coupling strengths by fitting the spectra using dual-peak lorentzian function and present those in Figure 5.11(a) for different φ values. The peak-to-peak values of the coupled modes from the fits correspond to "2g" values (in GHz) in all cases. The extracted g values are then plotted as a function of φ in Figure 5.11(c). The plot reveals that the g increases from 215 MHz at 0° to 240 MHz at 15°. Furthermore, we have extracted various other parameters from the fits as presented in Table 5.2, which indicate the magnon-magnon coupling to be of intermediate strength.

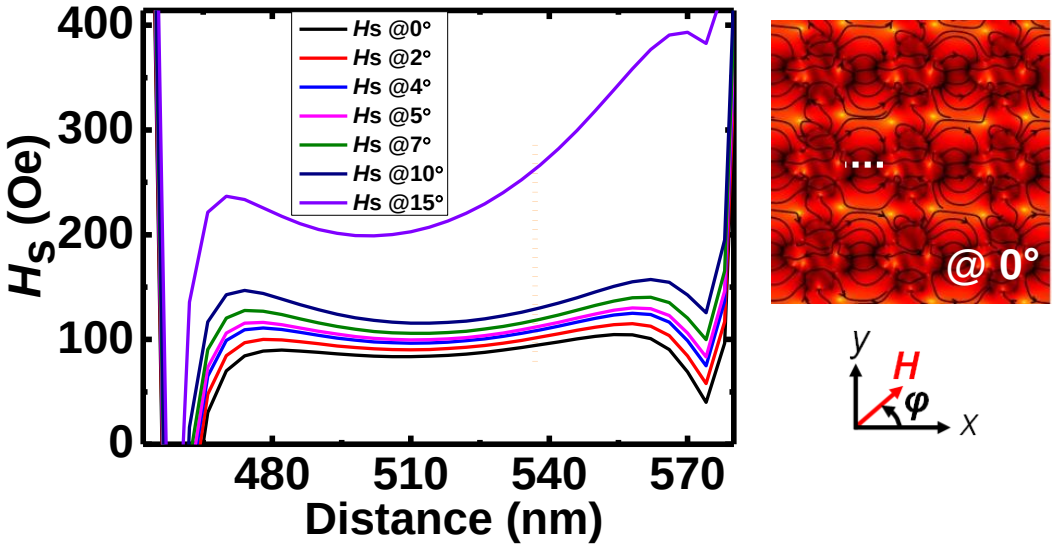

[42]**Figure 5.13.** Simulated magnetostatic stray-field distribution between the neighboring NCs at P = −15 dBm for H = 200 Oe, applied along different in-plane angles (φ). The linescan has been taken from the white dotted line as shown at right hand side of the figure. The orange dotted line represents the line from where the stray field values have been extracted to plot Figure 5.12(a).

Subsequently, we simulate the SW response from the sample for 0° ≤ φ ≤ 15°, out of which four SW power spectra are presented in Figure 5.11(b). This also manifests the incremental trend of peak-to-peak frequencies ("2g" in GHz) similar to the experiment. The simulated g values are also plotted at a function of φ in Figure 5.11(d), which reveals that g increases from 125 MHz at 0° to 185 MHz at 15°. Although the simulated g values qualitatively agree with the experimental ones, the quantitative agreement is relatively poor. This discrepancy can be attributed to the difficulties in incorporating the precise edge roughness and deformation as well as the surface textures in the FDM-based simulation as discussed in more detail in the literature.[110] Besides, other disagreements including the fact that simulations are

performed at T = 0 K, whereas experiments are carried out at room temperature also play important role.

To understand the upward trend of g with φ, we have post-processed the output files containing information about dynamic magnetization components at different φ and calculated the H_s values from the central region of the linescans as shown for φ = 0° and φ = 15° at the inset of Figure 5.12(a). From Figure 5.12(a), it is clear that H_s values increase almost linearly from ~94 Oe at 0° to ~125 Oe at 10° followed by a sudden jump to ~260 Oe at 15°. Additionally, we have also plotted the spatial distribution of stray fields at different φ values, from where the H_s values are extracted through the dotted lines as presented in Figure 5.13. This explains that with an increase in φ, the stray field increases drastically indicating an increase in the static dipolar interaction that eventually boosts the magnon-magnon coupling in the system as observed in Figure 5.11(c), (d). Furthermore, Figure 5.12(b) elucidates the ground state spin configurations of the system at two values of φ for H = 400 Oe. At φ = 0°, the ground state forms an onion-like spin configuration which transforms to S-like configuration for $\varphi \geq 10°$. This transition from onion to S-state is responsible for the drastic change in mode-softening phenomenon as observed in Figure 5.10(a)-(d). A similar phase transition has previously been reported in the literature.[170]

5.4. Conclusions

In summary, we have investigated the evolution of SW dynamics of $Ni_{80}Fe_{20}$ nanocross (NC) arrays of 330 ± 20 nm arm length, 170 ± 10 nm edge-to-edge separation, and 20 nm thickness by controlling the strength (H) and orientation (φ) of the external bias magnetic field using a broadband FMR technique. We have observed magnon-magnon coupling in the form of an anticrossing phenomenon in a very low spin-ensemble ($N \sim 10^{12}$) system. The anticrossing gap or coupling strength has been found to increase by increasing the microwave excitation power. We have qualitatively reproduced the experimental observations by micromagnetic simulations. Eventually, we have demonstrated that the inter-NC dynamic dipolar interaction results in the observed anticrossing feature. Subsequently, we have also contemplated that the dip position of mode-softening shifts its value with the rise of microwave excitation power and correlated it with the variation of coercive field. Subsequently, we have explored the crucial role of bias-field angle in modulating the anticrossing phenomenon, where we report an increment of coupling strength with bias-field angle for $0° \leq \varphi \leq 15°$, beyond which this phenomenon could not be resolved due to lower power of the SW modes. The observations are supported by simulated stray field distribution, where we observe the inter-element dipolar interaction between the NCs promoting the observed anticrossing phenomenon.

Furthermore, we have experimentally demonstrated angle-dependent appearance or disappearance of mode-softening and explained it from the ground-state spin configurations via static micromagnetic simulations. Finally, the findings regarding magnon-magnon coupling in ferromagnetic NC array hold enormous promise for applications in on-chip quantum transduction and coherent information transfer using magnons.[11]

Chapter 6

6. Control of Magnon-Magnon Coupling in $Ni_{80}Fe_{20}$ Nanocross Arrays through System Dimensions

Hybrid magnonics, founded on the coherent interplay between magnons and various quasiparticles, provides avenues for quantum transduction and the seamless transmission of coherent information. Magnon-magnon coupling, which exhibits remarkable coupling strength advantages over light-matter interactions, has emerged as a promising field. This research investigates magnon-magnon coupling in $Ni_{80}Fe_{20}$ nanocross arrays, with a focus on controlling the anticrossing phenomenon. Through a methodical adjustment of the nanocross arm length, it becomes possible to fine-tune the strength of coupling. The significance of the observed effect becomes evident when examining the power and phase profiles of distinct spin-wave modes in close proximity to and at a considerable distance from the anticrossing point. The research contributes to bridging the gap in hybrid quasi-particle interactions and offers insights into magnon-magnon coupling control. The findings open avenues for efficient magnon-based technologies and systems enabling efficient control of SW propagation characteristics and coupling, with implications for efficient quantum information processing architectures.

6.1. Introduction

In the past two decades, extensive research in the field of nanoscale magnonics has demonstrated great potential for energy-efficient and high-speed technologies[2]. Magnetic structures, patterned in nanoscale dimension, with unique characteristics, such as shorter spin-wave (SW) wavelengths, scalability, non-reciprocity, waveguiding, and hybridization, offer numerous advantages[11]. These structures hold promise for various applications, including SW filters[371], transistors[372,373], logic gates[326], memory devices[374], and wave-based computing[51]. However, a significant challenge lies in the modest conversion efficiencies[2] currently encountered in the excitation, manipulation, and detection of magnons. Consequently, there is an increasing need to integrate platforms and devices that demonstrate robust coupling between distinct quasiparticles. This coupling enables the manipulation of the system's response in one degree of freedom through controlled excitations in another, facilitating high-speed and energy-efficient operations. These burgeoning fields, known as hybrid magnonics[375] and quantum magnonics[62], emphasis is placed on the coherent interaction between fundamental matter excitations and magnons. They have harnessed considerable attention due to the potential for processing[82] and storing[343] quantum information with low-power dissipation. In this context, magnons can

interact coherently with various other platforms such as photons[376,377], phonons[378,379], plasmons[380,381], excitons[382,383], and superconducting qubits[65,384]. Furthermore, magnons can also engage in interactions with other magnons within the same system, giving rise to magnon-magnon coupling[385–390]. The remarkable advantage of magnon-magnon coupling lies in its superior coupling strength compared to light-matter interactions, due to the coexistence of two modes within a shared host medium, which eliminates the reduction in coupling strength caused by insufficient spatial mode overlap[79].

Over the years, the research field of magnon-magnon coupling has made significant advancements, with extensive research focused on fine-tuning this coupling phenomenon through various internal and external material and geometric parameters. Notably, breakthrough studies have emerged in the realm of synthetic antiferromagnetic (SAF) materials[79,391], where coupling phenomena are governed by interlayer exchange interactions between two ferromagnets (mediated by RKKY interactions), as well as out-of-plane tilt angles and dynamic dipolar interactions. The absence of stray fields in SAF[79,391] as well as natural antiferromagnets[72] have positioned them as a promising candidates for high-performance magnetic memory devices[392]. Recent notable works have probed the YIG/Py bilayer system using monochromatic laser beams[393] and ferromagnetic resonance[356] techniques respectively, highlighting the significant role played by strong interfacial exchange interactions between the two layers.

However, limited efforts have been dedicated to the study of localized SW modes in the form of tiny magnonic cavities, which can potentially replace conventional microwave cavities, thereby enabling device miniaturization and integration with complementary metal-oxide-semiconductor (CMOS) technology to process quantum information over extended distances. In light of these prevailing research gaps, recent literatures have successfully demonstrated the intriguing phenomenon of magnon-magnon coupling in irregular-shaped hexagonal dots[50], cross-shaped nanomagnets[111,358] and nanoring[159] arrays, which represent a significant stride towards addressing these limitations. Notably, this coupling is externally controllable by dynamic dipolar interactions between neighboring nanoelements, as elucidated in the notable study by Adhikari et al.[358]. The study revealed an absence of the anticrossing gap at lower microwave power; however, with the increase in power, a distinct gap emerged. Moreover, in systems characterized by smaller nanocross (NC) dimensions, the anticrossing gap was achieved and expanded through the implementation of distinct static and dynamic approaches, as detailed in the study conducted by Pal et al.[111]. Remarkably,

in this scenario, the anticrossing gap manifested even at the lowest power levels, further emphasizing the tunability and controllability of magnon-magnon interactions in nanoscale systems. Our study aims to bridge the gap between two significant findings in the field of hybrid magnon interactions. By systematically varying the NC dimensions, we seek to achieve and elucidate the observed phenomenon, shedding light on the underlying mechanisms driving magnon-magnon coupling in much more detailed fashion.

Herein, we have undertaken a systematic downsizing of the arm length of a NC structure, ranging from 720 nm to 250 nm, and successfully demonstrated the evolution of magnon-magnon coupling in the array of $Ni_{80}Fe_{20}$ (referred to as Permalloy or Py) NCs. To achieve this, we have employed a broadband ferromagnetic resonance (FMR) technique. Notably, the coupling between magnons is found to be reconfigurable by manipulating the dimensions of the NC devices as well as microwave excitation power. We have unraveled this captivating phenomenon through an examination of the simulated magnetic field distribution within the system. The observed outcome is grounded in the examination of power and phase maps of various SW modes, both in proximity to and at a distance from the anticrossing point. Our research reveals an innovative magnonic platform for facilitating the exchange of quantum information within highly correlated magnons, driving advancements in coupling strength, coherence, and enabling coherent information processing with exchange-coupled magnetic nanostructures.

6.2. Methods of Experimentation and Simulation

6.2.1. Method of sample fabrication

For this study, we have fabricated a series of samples comprising five sets with distinct NC arm lengths: 720 nm (L1), 600 nm (L2), 490 nm (L3), 380 nm (L4), and 250 nm (L5). These samples, characterized by an array dimension of 25 μm × 250 μm and a thickness (t) of approximately 20 nm, have been meticulously produced utilising a mix of electron beam lithography (EBL) and electron beam evaporation (EBE) techniques[111]. Figure 6.1(a) presents the scanning electron microscope (SEM) images of the samples for visual reference.

6.2.2. Measurement technique

The examination of the SW response from the samples was carried out using a broadband FMR spectrometer, which operates based on a vector network analyzer. To launch and detect radio frequency (rf) signals to and from the sample, a custom-made probe station equipped with a nonmagnetic ground-signal-ground (G-S-G) pico-probe and a high-frequency as well as low-noise coaxial cable was employed. This probe station features an integrated electromagnet positioned on a highly precise rotary stage, allowing for the generation of a

magnetic field (H) spanning from -1.8 kOe to +1.8 kOe and enabling azimuthal rotation within the range of 0° to 360°. For a detailed description of the measurement procedure and an illustration of the experimental setup, readers are referred to the literature[111]. In this study, we systematically varied the applied magnetic field (H) in increments of 10 Oe, ranging from +600 Oe to 0 Oe, while maintaining a constant experimental setup with fixed microwave powers (P) at -15 dBm and +6 dBm, as well as a bias-field angle (φ) of 0°. All measurements were conducted at room temperature.

6.2.3. Micromagnetic framework technique

Simulations at the micromagnetic scale were performed using the OOMMF software[366] package based on the finite difference method (FDM) as discussed in the literature[367] has been employed to provide insights into the experimentally obtained results. In the simulation, we replicated the rf excitation used in the experiment by applying a pulsed magnetic field. This magnetic field had a peak value of 20 Oe, a rise/fall time of 10 ps, and a pulse duration of 20 ps. Prior to reaching the desired bias field value, the sample was fully saturated using a high magnetic field. Subsequently, the magnetization was allowed to relax until it reached equilibrium, with the stopping criterion set at a maximum torque of $< 10^{-6}$ A/m. To simulate the extensive experimental sample area, we employed a 5×5 array of NCs under two-dimensional (2D) periodic boundary condition (PBC). Each unit cell within the array took the form of a rectangular parallelepiped, with a volume of 4×4×20 nm^3. The chosen cell size was deliberately smaller than the exchange length of Py to incorporate the exchange interaction into the simulation. The simulation utilized specific material parameters, including a gyromagnetic ratio (γ) of 17.6 MHz/Oe, a saturation magnetization (M_S) of 800 emu/cm^3, an anisotropy field (H_K) set to zero, an exchange stiffness constant (A) of 1.3×10^{-6} erg/cm[330], and a damping coefficient (α) of 0.008[331]. During the 8 ns dynamic simulation, m_z (out-of-plane magnetization) has been saved every 10 ps. The SW spectra at a particular bias magnetic field are provided by the FFT of the saved data.

6.3. Results and discussion

6.3.1. Examining the evolution of SW dynamics in various samples under the influence of external bias magnetic field strengths

The experimental measurement geometry, illustrated in the inset of Figure 6.1(a), demonstrates the sample's orientation situated within the x-y plane, with the applied bias magnetic field (H) aligned parallel to the x-axis. To precisely observe the emergence of the anticrossing phenomenon in relation to the NC dimensions, we have used a series of samples comprising five sets with progressively decreasing order of NC arm lengths from L1 to L5. The SW absorption spectra for each sample were measured with respect to the bias field

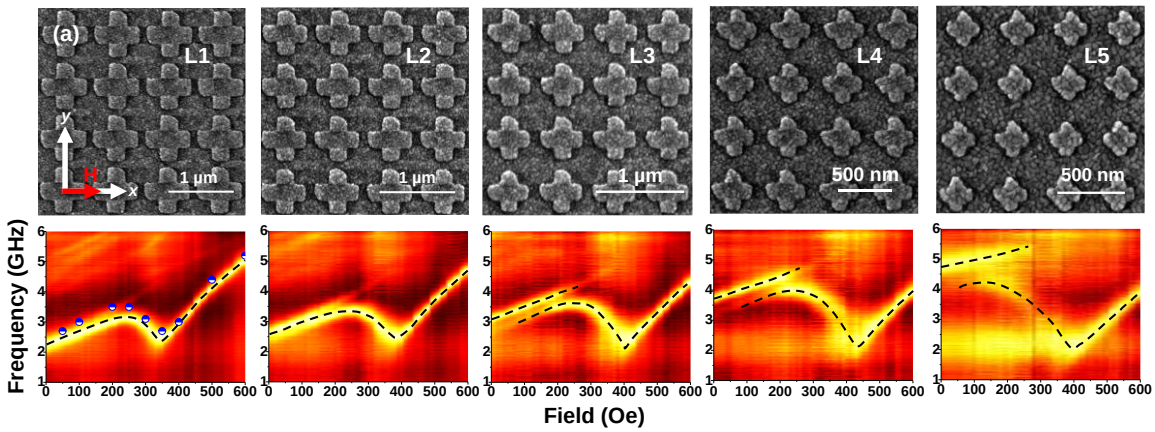

[43]**Figure 6.1.** (a) Scanning electron micrographs of Ni80Fe20 NC arrays with diminishing arm lengths ranging from L1 to L5. The inset illustrates the direction of the applied magnetic field. (b) Surface plots depicting the bias-field-dependent frequencies of SW modes for various NC arrays at $\varphi = 0°$ and $P = -15$ dBm. Black dashed lines have been added as visual aids. The half-filled circular dots represent simulated points for sample L1. The color map representing the surface plot is provided on the right-hand side of the figure.

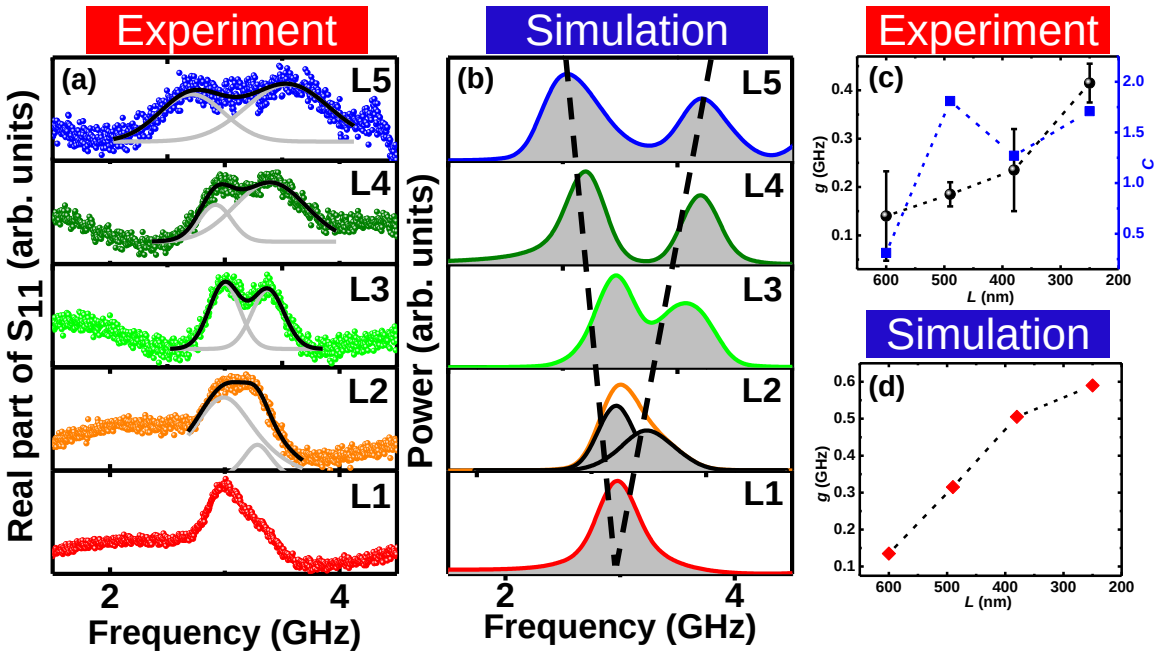

[44]**Figure 6.2.** (a) The real part of the S_{11} parameters at or near the anticrossing point, approximately $H \approx 200$ Oe, is displayed with respect to frequency for all the five samples (L1 to L5; arranged from bottom to top). This representation demonstrates the gradual increase in the anticrossing gap, with solid black lines indicating theoretical fits. (b) The corresponding simulated SW spectra, where dotted black lines aid in visualizing the evolution of the anticrossing gap with greater clarity. (c) Experimental values of g and C as a function of L, while (d) presents simulated g values as a function of L. The dashed lines connect the symbols for clarity.

dependence, covering the range from 600 Oe to 0 Oe, with data points being recorded at 10 Oe intervals. The gathered data is visualized through a surface plot, as shown in Figure 6.1(b). This plot illustrates the variation in SW frequency with respect to the bias field for each

sample, with the azimuthal angle being held constant at φ = 0°. Figure 6.1(b) notably exhibits a non-monotonic pattern in the frequencies of the FMR modes as the bias field varies, with a prominent dip in the SW frequency occurring within the range of 350-400 Oe, commonly referred to as the mode-softening phenomenon[369,370]. The half-filled circular dots in the surface plot of sample L1 represents simulated data points, reproducing the observed mode-softening phenomena quite well. The observed mode-softening phenomena occurs due to a drastic reconfiguration of internal spin structure of the complex NC system[365]. Intriguingly, sample L3 showcases a distinct power transfer between two SW branches around a field strength of ~150 Oe, resulting in the coexistence of the two SW modes within a specific field value. This phenomenon is in line with the concept of the avoided crossing or anticrossing effect[369]. Additionally, it is worth noting that the anticrossing gap increases as we transit from sample L2 to L5, i.e., with reduced sample dimension, indicating a possible correlation between sample dimensions and the observed phenomenon. In light of these significant findings, our investigation aims to explore deeper into the underlying mechanisms governing these observed phenomena and explore potential applications stemming from these observations.

In order to further investigate the potential modulation of the anticrossing phenomenon, we have systematically varied the NC arm length, L. Figure 6.2(a) showcases the experimentally observed SW spectra in the frequency domain at the field value where anticrossing is observed for some of the samples. Here, we have plotted real part of S_{11} parameters for five distinct samples under investigation, spanning the range of 250 nm ≤ L ≤ 720 nm. To precisely quantify the coupled SW modes, a double-peak Lorentzian function fitting is employed, allowing for the extraction of individual SW frequency values. Subsequently, the coupling strengths (g) are evaluated following the methodology discussed before[50] and subsequently, these values are graphically represented with respect to L in Figure 6.2(c). Notably, a gradual increase in g is clearly evident as L is decreased. Additionally, cooperativity factors (C) are calculated based on the extracted dissipation rates (k_1 and k_2) obtained from the expression $C = \frac{g^2}{k_1 k_2}$ and plotted against L. The resultant plot demonstrates that this coupling lies within the strong to intermediate coupling range. In conjunction with the experimental results, Figure 6.2(b) displays the simulated SW spectra for various samples at the anticrossing field, denoted as H = 150 Oe. Following a similar calculation methodology, the g values are determined and subsequently depicted as a function of L in Figure 6.2(d). Remarkably, the observed increase in g with L, as evaluated from the simulation, closely aligns

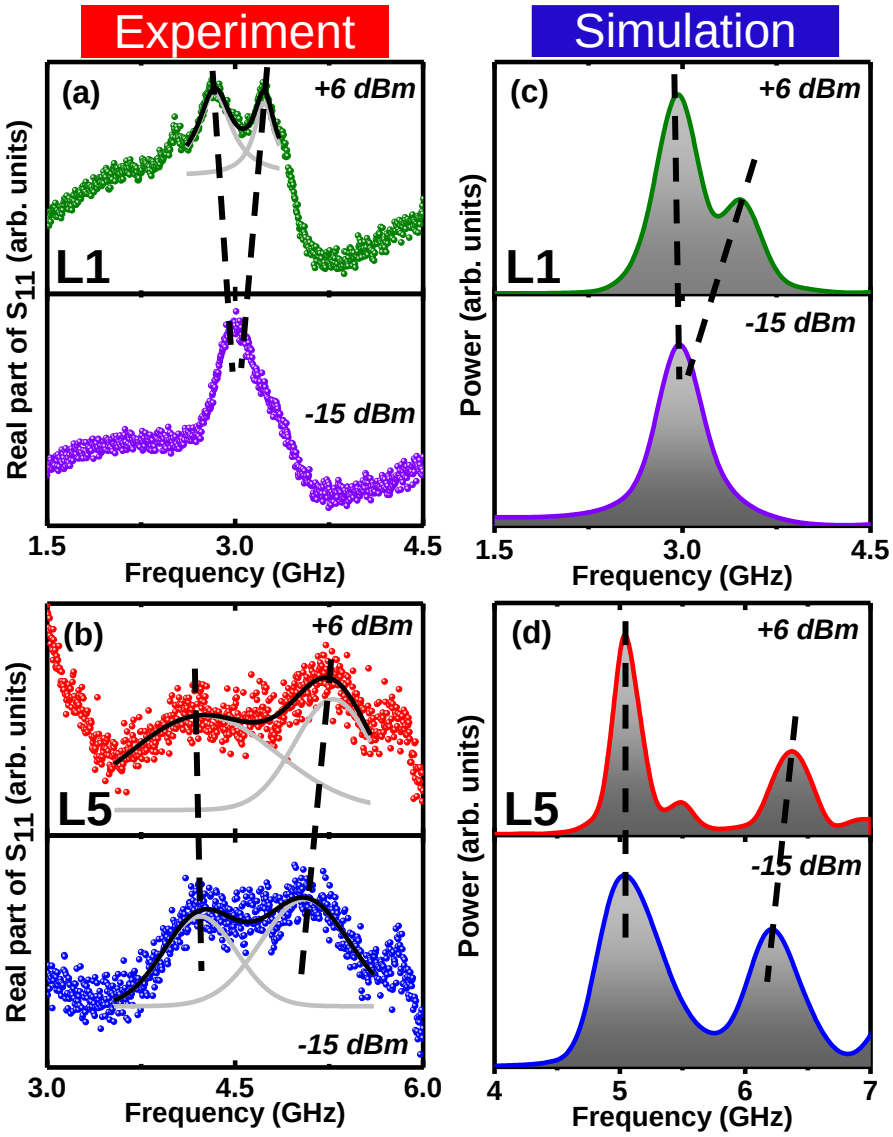

[45]**Figure 6.3.** The real part of the S_{11} parameters for the lowest-frequency SW branch is plotted against frequency in the vicinity of the anticrossing region for various values of *P*, specifically for (a) L1 and (b) L5. The theoretical fits are represented by the solid black lines. (c) and (d) represents the corresponding simulated SW spectra of L1 and L5, respectively. The dashed black lines aid in highlighting the frequency shifts for better clarity.

with the qualitative trends observed in the experimental data. This convergence enhances the overall consistency and validity of our findings.

In our continued investigation, we explore the potential control of the anticrossing phenomenon through microwave excitation power manipulation. Evidenced within Figure 6.3(a) and (b) are the depiction of the experimentally obtained anticrossing region, at highest (+6 dBm) and lowest (-15 dBm) microwave power. Notably, this endeavor reveals the confluence of two coupled SW modes, adeptly characterized through the utilization of a dual-peak Lorentzian function. The extracted parameters are presented in Table 6.1. This

analytical approach, meticulously employed, facilitates the extraction of discrete SW frequency values, thereby depicting the distinctiveness of each mode under investigation. This observation precisely signifies a progressive elevation in the parameter *g* as a direct consequence of the increasing magnitude of the variable *P*. It is significant to observe that the coupling strengths within the system can be effectively regulated not only by manipulating the dimensions of the device, but also by adjusting the amplitude of the microwave excitation power as reported previously[111]. It is noteworthy to mention that one can efficiently

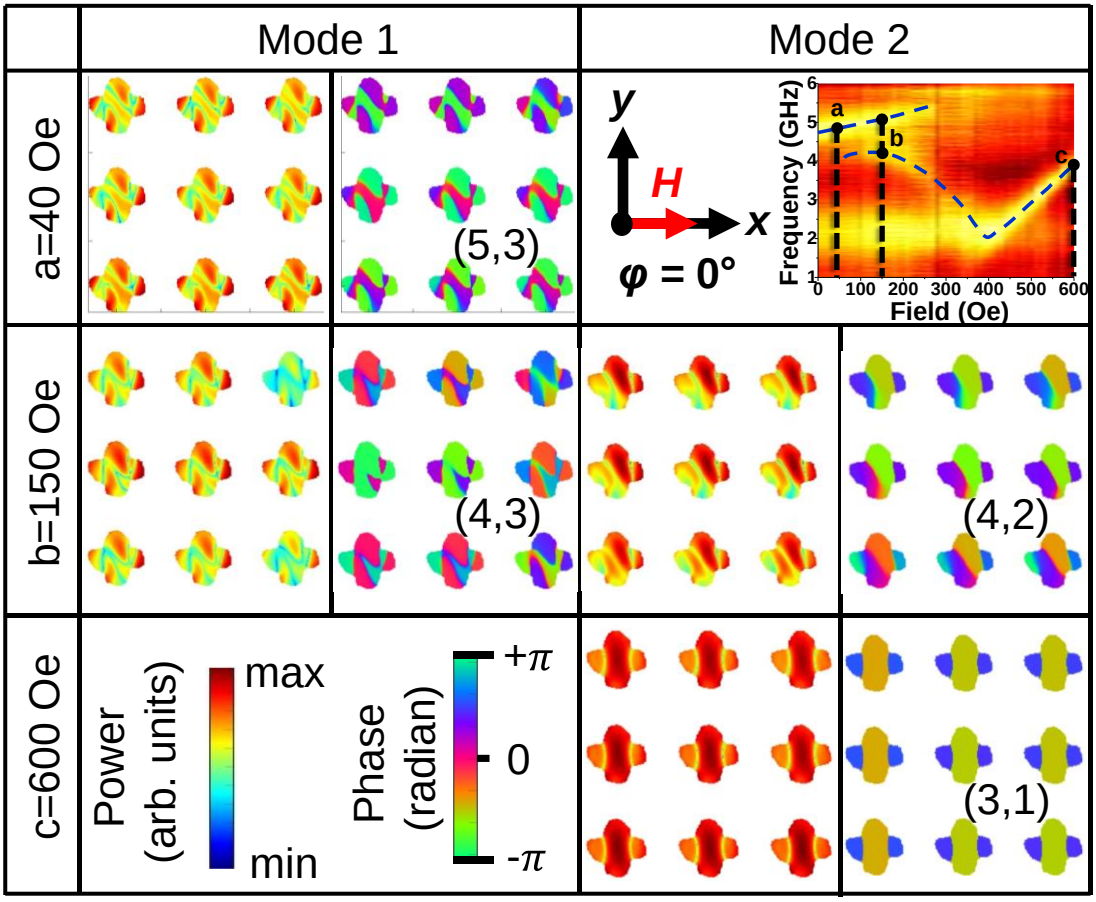

[46]**Figure 6.4.** The simulated power and phase profiles' spatial distribution of interacting SW modes is depicted, both at the anticrossing region and away from it. The two SW modes responsible for the anticrossing phenomenon at point b, as marked at a and c, are shown in the top right corner along with the bias field orientation. The color maps representing the power and phase profiles can be found in the bottom left corner for reference.

achieve *g* as high as 0.52 GHz through efficient control of microwave power as well as device size. Alongside, we have also reproduced the observed behaviour through micromagnetic simulations as shown in Figure 6.3(c) and (d) for sample L1 and L5, respectively. A substantial reduction in the uncompensated magnetic moments is observed with the increment of *P* from -15 dBm to +6 dBm. This phenomenon can be attributed to the enhanced dynamic dipolar interaction occurring between neighboring NCs as discussed in the literature[111,358]. This

characteristic fills the system with the ability to comprehensively address and manage the intricacies of coupling phenomena in a singular approach.

Table 6.1: Parameters obtained from the double-peak Lorentzian function fit of the coupled SW modes.

Sample	*P* (dBm)	*g* (GHz)	*k1* (GHz)	*k2* (GHz)	*C*	Nature of coupling
L1	+6	0.20	0.16	0.10	2.5	Strong
	-15	-	-	-	-	No coupling
L5	+6	0.520	0.585	0.305	1.51	Intermediate
	-15	0.415	0.29	0.35	1.71	Strong

6.3.2. Micromagnetic assessment of SW mode profiles

To gain a deeper understanding of the resonant magnonic modes, we employed a custom-developed code[369] for the analysis of the spatial profiles of the corresponding dynamic magnetization components. The dynamic simulations generated output files containing information about the spatial and temporal distribution of magnetization, represented as *M* (r, t). This dataset was organized into 4-D matrices, and we applied a discrete Fourier transform to each individual cell with respect to time. This process allowed us to extract the

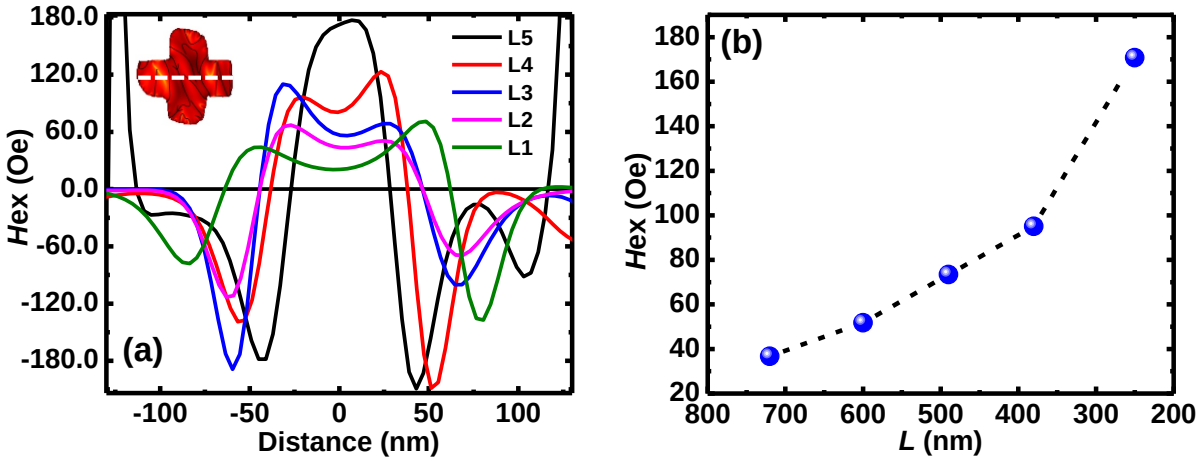

[47]**Figure 6.5.** (a) The simulated distribution of the exchange field within a NC at $P = -15$ dBm, with an applied magnetic field of approximately $H \approx 150$ Oe along $\varphi = 0°$. The line-scan was performed along the white dashed line, as indicated in the inset of (a). (b) Calculated average exchange field values (H_{ex}) at the center of the NC as a function of L, derived from the line-scan data. A black dashed line is included as a visual reference.

power value from the fast Fourier transform (FFT) spectrum associated with the desired frequency. By plotting these power values for all the cells, we constructed the power profile

of the system at that specific frequency. Additionally, phase information was extracted from the complex distribution of dynamic magnetization, facilitating the creation of phase plots. In Figure 6.4, we present the power and phase maps corresponding to two interacting SW modes at three distinct field values: the anticrossing field (b = 150 Oe), as well as points away from the anticrossing fields (a = 40 Oe and c = 600 Oe), as conveniently depicted in the inset at the top right-hand corner of the figure. The SW modes observed in this system exhibit a blended standing wave nature with quantization numbers assigned as (n, m) representing the quantization numbers in the backward volume (BV) and Damon-Eshbach (DE) geometries, respectively. Specifically, Mode 1 (at a = 40 Oe) and Mode 2 (at c = 600 Oe) are associated with mixed quantized SW modes having quantization numbers (5, 3) and (3, 1), respectively. Subsequently, these two SW modes interact, exchange energy, and eventually exhibit identical quantization numbers in the BV geometry (i.e., n = 4) with quantization numbers (4, 3) and (4, 2), respectively, at the anticrossing region (b = 150 Oe). This abrupt shift in quantization number and the subsequent adoption of a similar nature of the quantization number in the BV geometry over a narrow field range signify the presence of magnon-magnon coupling in this system[159].

As we strive to comprehend the significant increase in coupling strengths, we conducted additional simulations to investigate how the exchange field is distributed across the samples. We have performed a comprehensive analysis of the exchange field distribution, specifically from the central portion of the NC, as illustrated in Figure 6.5(a). The inset within the figure

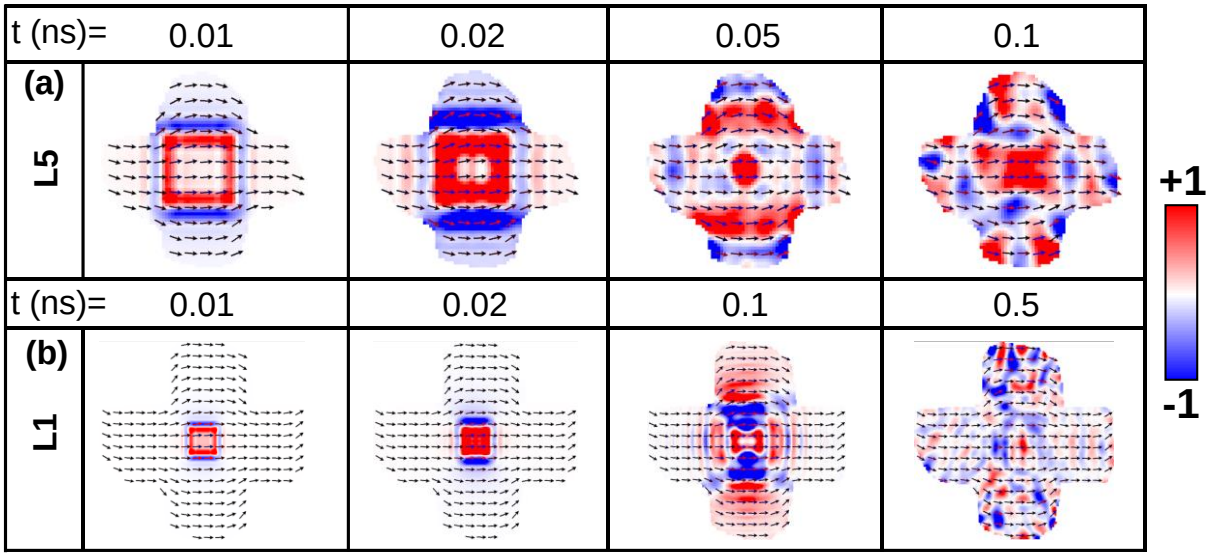

[48]**Figure 6.6.** The magnetization vector's z-component's spatial distribution of the extending SWs at different times within a single dot structure (t in ns) for sample (a) L5 and (b) L1 at *H* = 600 Oe oriented along the NC's length taken into account in simulation.

offers a magnified view of the exchange field distribution within a single NC element, with a dashed white line denoting the precise location from which the field values are extracted. Remarkably, our analysis has revealed a compelling pattern: as the NC arm length decreases from 720 nm to 250 nm, there is a salient and substantial increase in the exchange field values concentrated near-about the relative x-axis position of 0. To quantitatively assess this effect, we have precisely calculated the average field values extracted from this central region and plotted them as a function of *L*. The resulting plot, presented in Figure 6.5(b), provided unambiguous evidence of the incremental nature of the observed trend with reduction of sample size. Specifically, it showcases a remarkable rise in the exchange field value from ~35 Oe in the 720 nm system to ~170 Oe in the 250 nm system. This observation suggests that the incremental trend in coupling strength may be attributed to the exchange-field-mediated effects induced by the reduction in device size. As a result, the interconnection between these exchange field effects and the diminished device dimensions is likely to be the driving force behind the observed magnon-magnon coupling phenomenon.

6.3.3. Extension of SW response over isolated nanocross structure

We have conducted numerical investigations to further explore the extension characteristics of the SW modes within the single NC and to examine the influence of device size on these properties. To stimulate the SW, we have employed a locally launched sinc excitation with a cut-off frequency set at 30 GHz on the NC array's centre[110] covering an area of 100 nm × 100 nm with the help of OOMMF. Throughout the study, we applied an external bias field of *H* = 600 Oe in the desired in-plane angular orientation. Figure 6.6(a) and (b) visually illustrate the temporal evolution of SW modes within the NC. Notably, for the smallest NC structure (L5), SWs propagate within the structure in only 0.1 ns. In contrast, it takes approximately 0.5 ns for SWs to extend across the entire NC area in the case of the largest NC structure (L1). These findings emphasize the significant impact of device size on SW extension characteristics, with smaller structures exhibiting enhanced extensions. Importantly, our results indicate that reducing the device size leads to improved SW propagation profiles. These findings demonstrate that subtle adjustments in device size enable efficient control over SW extension, offering new possibilities for designing components in magnonic circuits and on-chip microwave communication devices.

6.4. Conclusions

In conclusion, our comprehensive investigation delves into the spin wave (SW) dynamics of $Ni_{80}Fe_{20}$ nanocross (NC) arrays through the precise manipulation of the external bias magnetic field strength using a broadband ferromagnetic resonance (FMR) technique.

Spanning a wide range of meticulously prepared samples featuring varying arm lengths, our study not only involves the observation and analysis of magnon-magnon coupling within the NC system but also demonstrates the efficient control over the emergence of the anticrossing phenomenon through carefully engineered sample dimensions. Additionally, we have demonstrated the augmentation of coupling strengths through external monitoring of microwave excitation power amplitudes. Remarkably, we achieved coupling strengths reaching as high as 0.52 GHz. Furthermore, our rigorous micromagnetic simulations faithfully reproduce the experimental findings, providing valuable insights into the evolution of SW dynamics and advancing the field of magnonics. Remarkably, the observed anticrossing phenomenon is governed by the exchange interaction within the NC system. Finally, our research highlights the efficient control of anticrossing phenomena through sample dimension adjustments and the potential for manipulation of SW extension characteristics, thus contributing to the advancement of quantum information processing[394,395].

Chapter 7

7. Resonant Amplification of Spin Waves by GHz-Frequency Spin-Orbit Torque in Cobalt Nanomagnets

This work explores the amplification of spin waves (SWs) within cobalt-based nanomagnet systems through alternating current spin-orbit torque (ac SOT). Leveraging the time-resolved magneto-optical Kerr effect (TR-MOKE) under field-free conditions, resonance conditions with intrinsic SW modes are achieved by applying radio frequency (rf) current at specific frequencies. The amplitudes are tunable with varying rf power values, resulting in an impressive ten-fold increment in the amplitude of a particular intrinsic mode. Notably, our findings reveal exceptional SW amplification, manifesting a versatile response across various frequencies. The study's significance is underscored by the revelation of heightened signal-to-noise ratios, enhancing the efficiency of information transmission, and the tunability of SW amplitudes. This establishes ac SOT as a pivotal tool for tailoring SW dynamics in nanoscale devices, promising advancements in the design and optimization of future spintronic applications. Our work contributes valuable insights, enriching the landscape of spintronics with the broader implications of amplified SWs.

7.1. Introduction

Within the dynamic arena of spintronics, a field revolutionizing information processing and storage devices through the dual manipulation of spin and charge, the intricate interplay between spin-orbit torque (SOT) and spin waves (SWs) is imperative for technological advancement[84]. Spintronics has not only spurred innovations in energy-efficient and high-performance technologies[396] but has also unravelled the complex synergy between SOT and magnetization. SOT, a phenomenon rooted in the relativistic coupling between electron's spin and orbital motion[397], has proven itself a powerful tool for manipulating magnetic moments within nanoscale structures. This torque induces substantial changes in the magnetization dynamics of materials, offering a versatile means of control in the realm of spintronic devices[398]. Concurrently, SWs, collective excitations of spins in magnonic crystals[42,301,399–401], have garnered significant attention as a promising avenue for information transfer and processing[8,402,403]. Their inherent properties, such as low energy consumption and high coherence, position them as compelling candidates for advancing the capabilities of information technologies. In the context of this study, a particular focus is directed towards the amplification of SWs through the application of alternating current SOT (ac-SOT). This avenue of investigation delves into the nuanced

relationship between SOT and SWs, aiming to uncover the underlying mechanisms that govern their interaction. The exploration of SW amplification through ac SOT not only deepens our comprehension of the underlying physics but also presents substantial promise for the development of advanced spintronic applications. As we navigate the intricate landscape of spintronics, the cooperative relationship between SOT and SWs emerges as a key focal point, where advancements have the potential to redefine the technological landscape. This research contributes to the broader scientific discourse by providing a comprehensive exploration of the interplay between these phenomena, shedding light on their synergistic effects and paving the way for the advancement of groundbreaking spintronic technologies.

Some important findings in this area of research includes the study by M. Endo et al.[404] that delves into the spin-orbit interaction-induced effective magnetic field in (Ga, Mn)As, unveiling changes in magnetic anisotropy through transport measurements. Another foundational work[405] showcases reversible manipulation of magnetization within a ferromagnetic material through spin-orbit magnetic fields. Theoretical insights[406] have been gained by systematically studying SOT and spin dynamics in ferromagnetic ultrathin films lacking inversion symmetry. Recently, another important investigation[407] explored the dynamics of current-induced angular momentum transfer in spin-orbit-coupled systems, focusing specifically on FM/W bilayers. They conducted theoretical calculations to determine the orbital and spin angular momentum in these systems, allowing to extract the effective spin Hall angle. Additionally, the transformative potential of SOTs is highlighted[408,409] demonstrating their powerful role in controlling magnetization and enriching device functionalities. The cutting-edge study by Wang et al.[410] unveiled SOT switching of magnetization and exchange bias in Pt/Co/IrMn heterostructures, showcasing partial magnetization switching by sub-nanosecond current pulses. It has been reported that the SOT, either within the bulk or at interfaces of material systems characterized by robust spin–orbit interaction, possess the capability to manipulate magnetic damping across expansive spatial domains in both conducting and insulating magnetic materials[411–413]. In another work, the propagation length of coherent SW has been increased by a factor of 10 and SW intensity has been amplified by a factor of 3 at the output terminal in 20-nm thick YIG film[414]. Subsequently, in a very recent work, researchers have observed an enhancement of SOT by a factor of 3 in the MHz frequency regime which has been attributed from the magnon excitation due to photon-magnon coupling[415] and pointed towards quasi-particle interaction in manipulating SOT. Despite the extensive body of research investigating SOT-induced modulation of magnetization dynamics in various systems, there remains a notable

gap in the literature concerning experimental demonstrations of SOT effects of the dynamics of nanoscale ferromagnetic systems. Our work may fill this critical gap, offering a unique development on the precise control of the magnonic bandgap, waveguiding characteristics, and the consequential potential for the creation of miniaturized and integrated devices, marking a significant advancement in the frontiers of magnon spintronics.

In this study, we embark upon an exploration of ac-SOT-induced spin dynamics within cobalt-based nanomagnet systems, providing unique insights into the amplification of SWs. Leveraging the time-resolved magneto-optical Kerr effect (TR-MOKE) technique, we introduce an alternating current of microwave frequency to induce SWs in the nanomagnets. Our distinctive experimental setup involves rectangular-shaped cobalt nanomagnets with specific ledge configurations. The absence of an external magnetic field unveils a compelling phenomenon—parametric amplification of SWs by ac-SOT when resonant with natural modes of the nanomagnet, offering a novel approach to control spin dynamics. These results not only contribute to the fundamental understanding of spin dynamics in the presence of ac-SOT but also hold promise for practical applications in spintronics. As we advance toward harnessing SWs for information processing and communication, our study propels the field forward by offering a nuanced perspective on the interplay between ac-SOT and natural SW modes. The findings presented here lay the groundwork for future investigations into the potential applications of ac-SOT-driven SW amplification, steering the trajectory of spintronics research toward innovative and efficient device architectures.

7.2. Experimental and Simulation Methods

7.2.1. Sample fabrication

The fabrication process for the cobalt nanomagnet with a ledge, featuring a thickness ~ 15 nm and a 2 nm Au capping layer, involves a series of meticulously controlled steps. The sample consists of Co square-shaped nanomagnets with sides of 450 nm, ledge length of 200 nm, ledge width of 50 nm, and ledge-to-ledge separation of 450 nm. Additionally, the edge-to-edge separation between the nanomagnets is maintained at 300 nm. To initiate the fabrication process, a bilayer resist consisting of MMA/PMMA was coated on a lithium niobate substrate. We utilized electron-beam lithography (EBL) with a beam current of 100 pA, to pattern the bilayer resist which serves as a template for subsequent steps. Cobalt thin film was then deposited onto the resist pattern at a base pressure of 2×10^{-8} Torr. A 2 nm Au layer, was then deposited on top of Co to protect the sample from environmental contamination. The last steps of fabrication involve lifting off sacrificial materials and using oxygen plasma cleaning

to eliminate any remaining resists, to finally obtain the nanomagnet structures. The Pt wire was patterned subsequently at 150 pA beam current on top of the ledges of the patterned nanomagnets.

7.2.2. Measurement technique

The study on ultrafast magnetization dynamics utilized a custom-built TR-MOKE microscope[172] in a collinear two-color pump-probe setup. For excitation, the second harmonic of a Ti-sapphire oscillator emitted at a wavelength of λ = 400 nm, with a spot size of about 1 µm, pulse width of approximately 100 fs, and fluence of around 12 mJ cm^{-2}, was used. Simultaneously, a time-delayed fundamental laser with a wavelength of λ = 800 nm, spot size of about 800 nm, pulse width of around 80 fs, and fluence of approximately 1 mJ cm^{-2} was employed as the probe beam. The pump-induced polar Kerr rotation in the probe beam,

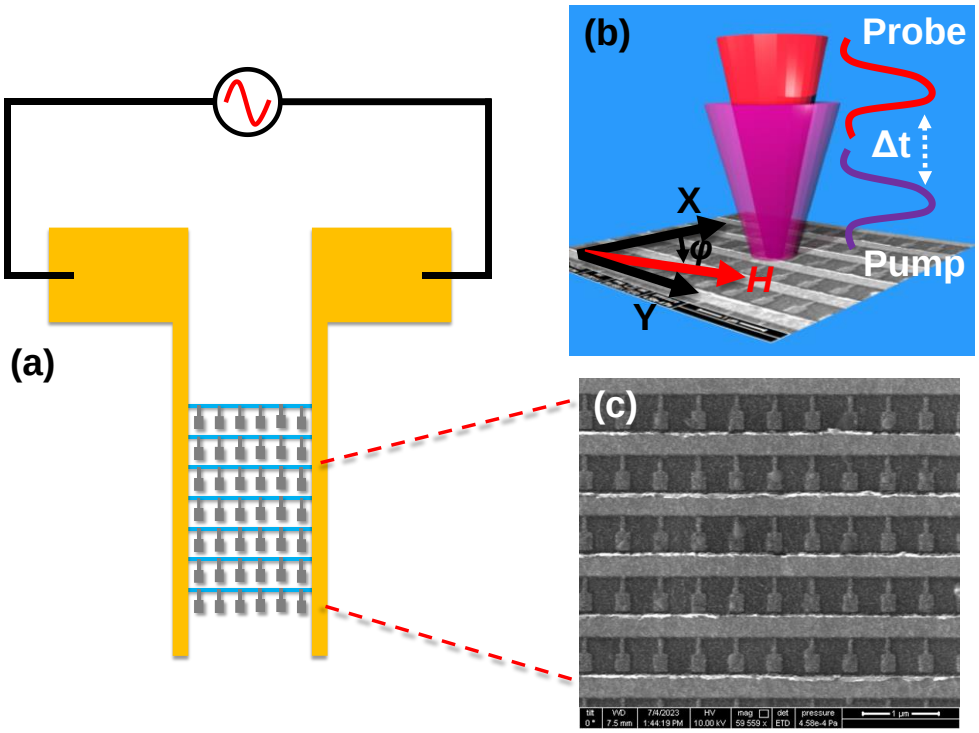

[49]**Figure 7.1.** (a) Schematic representation of the sample geometry, illustrating the pathway of the alternating current (ac) through the sample using the specified configuration. (b) Schematic diagram of the experimental setup for time-resolved magneto-optical Kerr effect (TR-MOKE) measurements. The sample is positioned in the x-y plane, and a two-color pump-probe beam is directed onto the sample from the z-direction. (c) Scanning electron micrographs showcasing array of Cobalt nanomagnets. The nanomagnets consist of a ledge designed for the application of ac-SOT to them by sending rf current through the Pt wires.

reflected from the sample, was measured using an optical bridge detector as the temporal delay between the pump and probe beams was varied. To initiate the measurements, a substantial magnetic field was initially applied to the sample, saturating its magnetization, followed by its removal setting the sample magnetization in its remanent state. The accurate

placement of the pump and probe beams at specific locations on the sample was accomplished by scanning a piezoelectric x-y-z stage. In tandem with the optical measurement, a radio frequency (RF) signal, generated by a Rohde & Schwarz SMB100A signal generator with a frequency range spanning from 100 kHz to 20 GHz, transmitted via a high-frequency, low-noise coaxial cable (model no. N1501A-203). This multifaceted experimental setup facilitated a comprehensive exploration of the ultrafast magnetization dynamics in the studied nanomagnet system, ensuring meticulous control and accurate measurement capabilities throughout the investigation.

7.2.3. Micromagnetic simulation

The analysis of experimental findings relies on micromagnetic simulations performed using the OOMMF software[26], a tool employing the finite difference method (FDM). The optical excitation in the experiment is mimicked in micromagnetic simulations using a pulsed magnetic field. The field, having a peak amplitude of 20 Oe, rise/fall time of 10 ps, and a pulse duration of 10 ps, is applied perpendicular to the sample plane. The simulation initiates with a bias magnetic field exceeding the saturating field value for sample saturation, followed by adjustment to the desired bias field value and magnetization relaxation until equilibrium is attained (criterion: maximum torque drops below 10^{-6} A/m). In the simulation, an array of ledged cobalt nanomagnets is considered with two-dimensional (2D) periodic boundary conditions (PBC) to replicate the large sample area in the sample used in the experiment. The array is divided into rectangular parallelepiped-shaped cells, each with a volume of3×3×15 nm^3. Material parameters for dynamic simulation include gyromagnetic ratio γ = 17.6 MHz/Oe, saturation magnetization M_S = 1400 emu/cc, anisotropy field H_K = 0, exchange stiffness constant A = 3×10^{-6} erg/cm)[27], and damping coefficient α = 0.01. The fast Fourier transform (FFT) of the simulated time-resolved out-of-plane magnetization component (m_z) is depicted in Figure 7.2(c), displaying the corresponding spin-wave (SW) spectra.

7.3. Results and discussion

7.3.1. Evolution of SW modes with application of external bias magnetic field

Figure 7.2(a) illustrates the FFT power spectra derived from the experimentally obtained time-resolved precessional data at three distinct bias magnetic field values: high, low, and intermediate. Despite a slightly compromised signal-to-noise ratio, a meticulous examination reveals the presence of four discernible SW modes, as indicated by arrowheads. To validate our experimental observations, we conducted simulations of the SW response using OOMMF software. Remarkably, the simulated SW modes exhibit a qualitatively similar trend to the

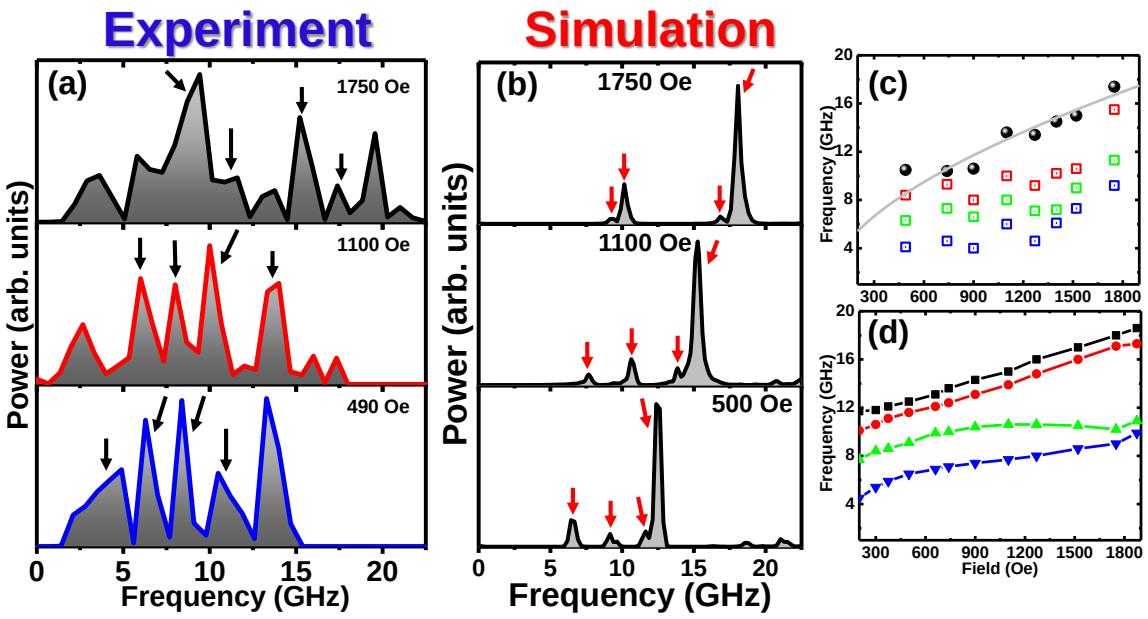

[50]**Figure 7.2.** (a) Experimentally obtained FFT power spectra at three distinct magnetic field values. Arrowheads indicate the SW modes present in the system. (b) FFT power spectra of simulated time-domain magnetization (m_z component) corresponding to the experimental configurations described in (a). (c) Bias field-dependent SW frequencies of cobalt nanomagnets as observed in the experiment. (d) Simulation-derived bias field-dependent SW frequencies for the cobalt nanomagnets. Filled circular symbols represent simulation data points, unfilled symbols represent experimental results, and the solid grey line indicates the Kittel fit.

experimentally observed modes, as depicted in Figure 7.2(b). The strong correlation between experimental and simulated results lends credibility to our characterization of the SW modes in the nanomagnet system. Moving forward, Figure 7.2(c) and (d) depicts the bias magnetic field-dependent SW frequencies from the sample, both experimental and simulated, respectively. Notably, four SW modes at approximately 17.4 GHz, 15.5 GHz, 11.3 GHz, and 9.2 GHz, observed at a bias magnetic field of 1750 Oe, exhibit a vibrant response to variation in the external field. As the bias magnetic field reduces to 490 Oe, the SW frequencies decrease to approximately 10.5 GHz, 8.4 GHz, 6.3 GHz, and 4.1 GHz. This pronounced bias-field dependence across all four modes underscores their magnetic origin. It is noteworthy to mention here that although the qualitative trend in bias field-dependent frequency is followed in the simulation, the frequencies are not exactly replicated. This discrepancy may occur due to various reasons: i) the simulations were conducted at T = 0 K, unlike the experiments which were carried out at room temperature,and ii) challenges in accurately incorporating edge roughness, deformation, and surface properties in the FDM-based simulation. However, since our primary focus was on the nature of the SW modes, the frequency mismatch does not affect the fundamental underlying physics. Furthermore, we conducted a detailed analysis of the highest frequency mode by fitting it with the Kittel formula[128]

$$f = \frac{\gamma}{2\pi}\sqrt{H(H + 4\pi M_{eff})} \quad (7.1)$$

The extracted effective saturation magnetization (M_{eff}) for the sample is approximately 1350 emu/cc. It is noteworthy that this value exhibits a slight discrepancy when compared with the literature values[416]. Possible factors contributing to this disparity include non-uniform magnetization profile within each nanomagnet specific to this mode.

7.3.2. Bias Field-Free SW Dynamics Without RF Excitation

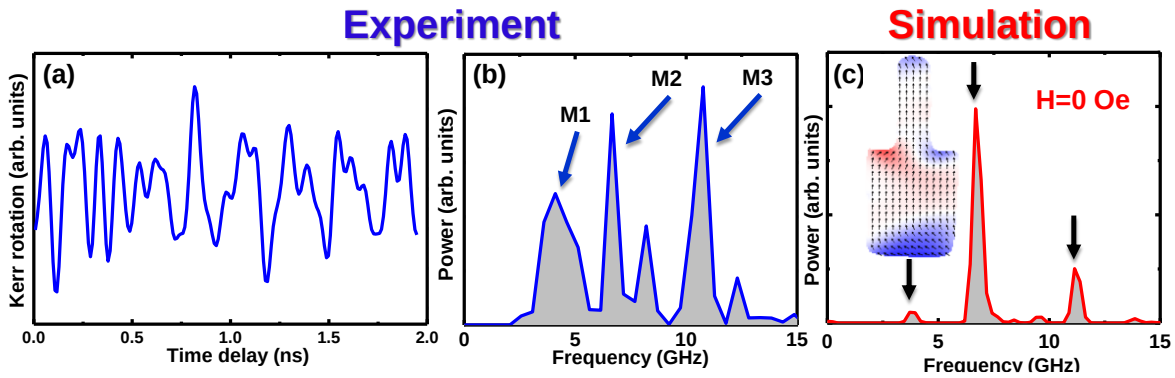

[51]**Figure 7.3.** (a) Experimental time-resolved Kerr rotation data captured in the absence of ac-SOT excitation and bias magnetic field. (b) Corresponding FFT power spectrum derived from the experimental data in (a). (c) Simulated FFT power spectrum under similar external variables, providing a comparative analysis with the experimental results. Arrowheads indicate the SW modes present in the system.

In the realm of bias field-free SW dynamics[417–419], we commence our investigation by scrutinizing the measured Kerr rotation signals without any external bias magnetic field or rf excitation, as depicted in Figure 7.3(a). This experimental setting offers a glimpse into the inherent or intrinsic behavior of SWs within the nanomagnet array. The subsequent analysis depicts a detailed examination of the FFT power spectra derived from both experimental and simulated time-domain magnetization data, as portrayed in Figure 7.3(b) and Figure 7.3(c), respectively. The inset of Figure 7.3(c) depicts the simulated static spin configuration within a single nanomagnet from the entire array at remanence (H = 0 Oe). However, the spin configuration does not adopt the typical 'S'-like or 'onion'-like nature; instead, it forms an unusual configuration between the two. Due to these unusual spin configurations, multiple SW modes emerge in the system. Without any externally applied magnetic field or rf excitation, the primary influencers of the magnetization dynamics include shape anisotropy, magnetostatic interactions between neighboring nanomagnets, etc. These factors collectively determine the optically excited precession of magnetization, giving rise to the intrinsic SW modes within the nanomagnet array. The intrinsic SW spectrum obtained from the Kerr oscillations in the experiment reveals three distinct modes at approximately 4.1 GHz (M1),

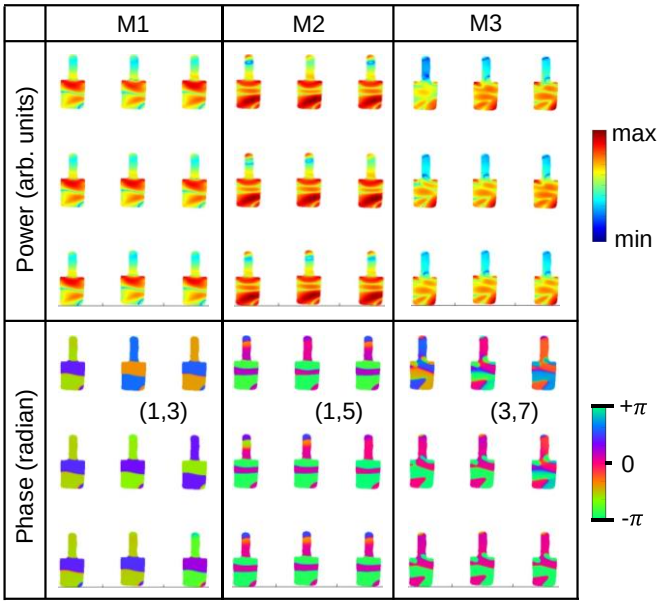

[52]**Figure 7.4.** Simulated spatial distribution of power and phase profiles for three distinct SW modes in absence of bias magnetic field and ac-SOT. Color maps illustrating the power and phase profiles are presented on the right-hand side of the figure. The quantization numbers corresponding to each mode are annotated within the figure.

6.6 GHz (M2), and 10.8 GHz (M3) in absence of bias field and rf excitation.

To unravel the origin of these observed SW modes, a comprehensive analysis of both experimental and simulated data was conducted. This involved an intricate examination of the output files from dynamic simulations and extracting spatial power and phase maps of the SW modes using a customized code, Dotmag[285]. The resultant power and phase maps, detailed in Figure 7.4, provide a spatial representation of the SW modes, shedding light on their distinct characteristics. To quantify each mode, we have assigned quantization numbers (n, m) to each mode, where n and m denote quantization numbers in the backward volume (BV) and Damon-Eshbach (DE) geometries, respectively. Mode 1 (M1) and Mode 2 (M2) are identified as mixed quantized SW modes with quantization numbers (1, 3) and (1, 5), respectively. In contrast, Mode 3 (M3) displays a substantial increase in quantization number in the BV geometry, indicative of a quantization number of (3, 7). This intriguing observation suggests a transition toward a more pronounced standing wave nature as SW frequencies escalate.

7.3.3. SOT Mechanism and Amplification of SWs

In the intricate landscape of spintronics, the advent of SOT has ushered in a transformative era, offering a versatile tool for manipulating magnetic moments in nanoscale structures. SOT

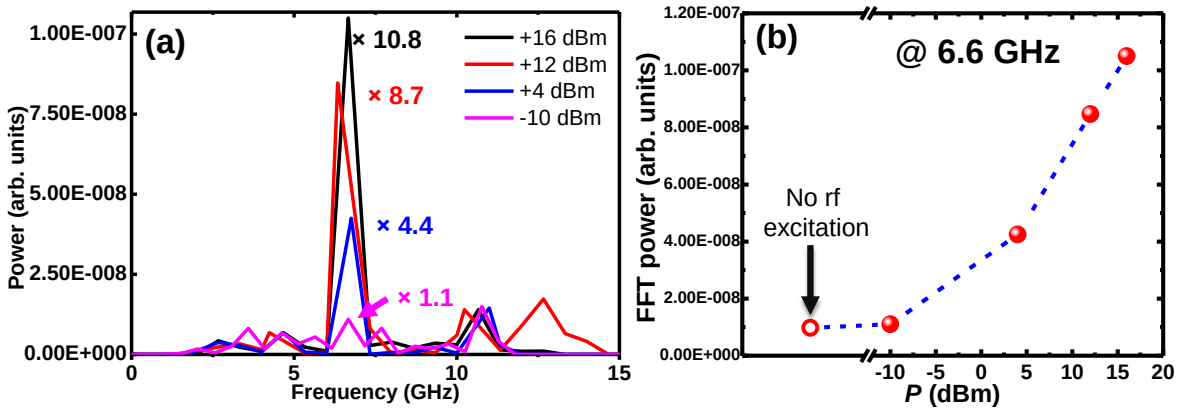

[53]**Figure 7.5.** (a) Experimental FFT spectra obtained at zero bias-field configuration under external rf excitation (ac-SOT) with a frequency of 6.6 GHz and variable rf power. SW power amplification factors are depicted for four different rf powers, comparing each to the SW spectra without any rf current. (b) The plot illustrates the variation of FFT power with changing rf power. The unfilled symbol represents the data point in the absence of any rf excitation. The dashed line is a guide to the eye.

arises from the relativistic coupling between electron spin and orbital motion, leading to torque generation and subsequent control over magnetization dynamics. Here we focus specifically on the amplification of SWs within a nanomagnet system, elucidating the underlying mechanisms of ac-SOT. The fundamental basis of SOT lies on spin-orbit coupling, spin current and transfer of angular momentum[420]. Two principal types of SOT are recognized: bulk SOT originated from the spin Hall effect (SHE)[60,421] and interface SOT originated from the Rashba-Edelstein effect (REE)[422,423]. In the SHE, a charge current flowing in a heavy metal induces transverse spin currents due to spin-orbit coupling, leading to the transfer of angular momentum to an adjacent ferromagnet. Conversely, the REE arises from the breaking of inversion symmetry at a heavy metal/ferromagnet interface, generating an effective magnetic field exerting a torque on the magnetization. The interaction of SOT with SWs in a nanomagnet system introduces a compelling avenue for the amplification of these collective excitations. The dynamics unfolds through the injection of spin currents into the ferromagnetic element, creating a torque that modifies the magnetization dynamics. In the context of ac-SOT, where an alternating current is applied, the torque oscillates at the frequency of the current. This resonance condition becomes pivotal when it aligns with the natural frequencies of the SW modes in the nanomagnet array. The ac-SOT-induced SW amplification operates on the principle of parametric resonance, akin to the well-known phenomenon in classical mechanics. When the frequency of the external driving force (ac-SOT) synchronizes with the intrinsic frequencies of the nanomagnet's natural SW modes, energy transfer becomes maximized, resulting in the amplification of these modes. In essence, ac-SOT acts as a modulator, fine-tuning the energy landscape of the nanomagnet array and

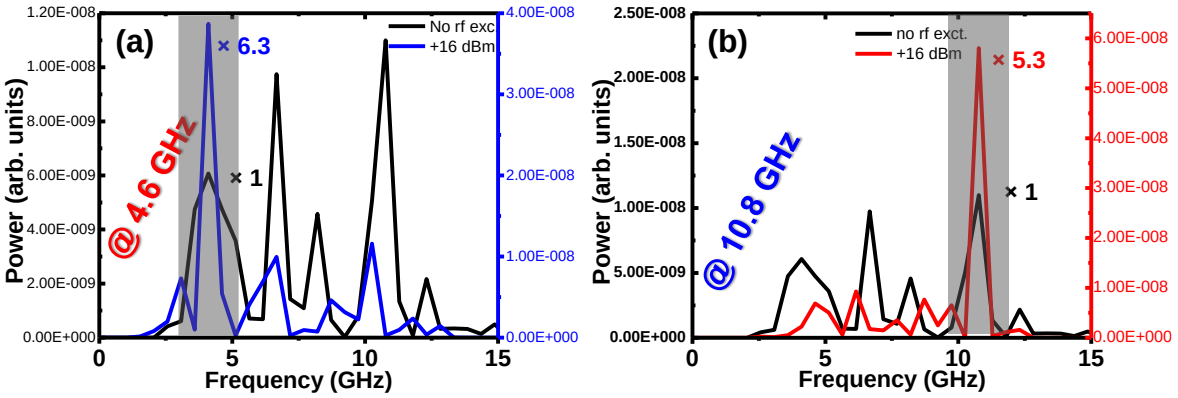

[54]**Figure 7.6.** (a) Experimental FFT power spectra obtained at zero bias-field configuration under external rf excitation with frequencies of (a) 4.6 GHz and (b) 10.8 GHz, respectively, at no rf and highest rf power conditions. Amplification factors are given for highest rf power, comparing each to the SW spectra without any rf excitation.

enabling the enhancement of specific SW modes. Understanding the intricate interplay between ac-SOT and SWs involves a delicate balance of resonant conditions, material parameters, and geometric considerations.

Under field-free conditions, three distinct intrinsic SW modes were observed within the system. Subsequently, the experiment involved the injection of rf current into the Pt wires, synchronized with the frequency of the second SW mode (M2) to resonate with the intrinsic mode. The experiment sought to unravel the nuanced relationship between microwave power of the rf excitation and the resultant SW power spectra. Varied microwave power levels, ranging from -10 dBm to +16 dBm, were applied, revealing a compelling narrative depicted in Figure 7.5(a). Four distinct SW power spectra were meticulously portrayed at different power values, each annotated with the corresponding amplification factor. The numerical annotations near the peak values signify the extent to which the SW power is amplified as opposed to no rf excitation. The results showcased a remarkable achievement where more than tenfold amplification of the SW amplitude was attained by applying rf power of +16 dBm. This observation underlines the tremendous potential of ac-SOT in dramatically enhancing the amplitude of SWs within the nanomagnet system. The ability to achieve such high levels of SW amplification will have profound applications in next-generation spintronic devices, promising to revolutionize the landscape of information processing technologies. Figure 7.5(b) further elucidates the variation of SW FFT power values and the amplitude of rf excitation power. The plot unveils a consistent incremental trend, underscoring the modulation of amplification by ac-SOT. The systematic increase in FFT power with the amplitude of rf excitation power corroborates the dynamic interplay between the applied rf current and the resultant amplification of SWs. This experimental endeavor not only unravels

the intricacies of ac-SOT-induced SW amplification but also sheds light on its broader implications.

Beyond the resonance with the second intrinsic SW mode (M2), our investigation extends to the amplification of SW responses at two other critical frequencies in the nanomagnet system. Notably, we targeted the SW frequencies at ~4.6 GHz (M1) and ~10.8 GHz (M3), initiating an exploration of the modulation of SW amplitudes at elevated rf power levels. In line with the mentioned protocol, the application of rf current at frequencies resonant with the specific SW modes enabled an in-depth investigation into the dynamics of SW amplification. Intriguingly, at the highest power level (+16 dBm), unprecedented levels of SW amplification were achieved, reaching approximately ~6.3 times for the 4.6 GHz frequency and ~5.3 times for the 10.8 GHz frequency. Figure 7.6(a) and Figure 7.6(b) portray the SW responses at +16 dBm for the 4.6 GHz and 10.8 GHz frequencies, respectively, from the level at the SW response without ac-SOT. While the observed amplifications at these frequencies are indeed substantial, the focus on the +16 dBm power level provides a clearer illustration of the upper limits of SW enhancement achievable with ac-SOT. This comprehensive exploration not only broadens our understanding of ac-SOT-induced SW amplification but also highlights the intricacies of modulating SW responses at multiple frequencies. The observed amplification levels, particularly at the highest rf power, signify the potential for versatile and controllable manipulation of SW dynamics within the nanomagnet system.

7.4. Conclusion

In this study of spin-wave (SW) dynamics within cobalt-based nanomagnet systems, we have unravelled the intriguing phenomenon of SW amplitude amplification facilitated by alternating current spin-orbit torque (ac-SOT). Under bias field-free condition without rf excitation, the intrinsic SW modes of the nanomagnet array were thoroughly characterized, setting the stage for the application of ac-SOT to modulate the SWs. Our experimental endeavor revealed a profound resonance between the applied rf current and specific intrinsic SW modes, exemplified by the resonant amplification of the second intrinsic SW mode (M2). Notably, at the highest rf power of +16 dBm, we achieved an unprecedented SW amplification, surpassing tenfold for the M2 mode. This exceptional amplification was also demonstrated across multiple SW frequencies, including 4.6 GHz and 10.8 GHz, reaching ~6.3 times and ~5.3 times, respectively, at the highest rf power of 16 dBm. The implications of such significant SW amplification extend far beyond the limitations of our experimental setup. This modulation capability, adapted by ac-SOT, introduces a versatile tool for tailoring the amplitude and efficiency of SWs within nanoscale devices. The observed higher SW

amplification not only enhances the fundamental properties of SWs but also paves the way for advanced spintronic applications. The benefits of this amplified SW response are multi-faceted. Firstly, it offers a substantial increase in the signal-to-noise ratio, ensuring reliable information transmission. Additionally, the tunability of SW amplitudes allows for the customization of device characteristics, fostering advancements in energy-efficient information transfer. Furthermore, the achievement of nonlinear dynamical effects and the potential for quantum information processing underscore the transformative impact of amplified SWs. Overall, our study not only contributes to the fundamental understanding of ac-SOT-driven SW amplification but also positions this phenomenon as a cornerstone for the next-generation spintronic devices. As we venture into the era of tunable and efficient SW manipulation, the implications of our findings resonate across diverse fields, promising innovative solutions for information processing technologies and quantum computing paradigms.

Chapter 8

8. Exploring Spin Pumping Effect and Giant Spin Transparency in $(Bi_{0.3}Sb_{0.7})_2Te_3/Co_{20}Fe_{60}B_{20}$ Heterostructures via an All-Optical Method

Topological insulators (TIs) exhibit unique electronic properties with metallic surface states and an insulating bulk, making them ideal candidate for spintronic applications. Here, we explore the spin pumping effects and interfacial spin transparency in $(Bi_{0.3}Sb_{0.7})_2Te_3$ (BST)/$Co_{20}Fe_{60}B_{20}$ (CoFeB) heterostructures using time-resolved magneto-optical Kerr effect (TR-MOKE) technique. BST thin films, deposited via pulsed laser deposition, demonstrate high crystallinity and surface state-dominated transport up to 90 K. We observe significant modulation of the Gilbert damping parameter with variations in both BST and CoFeB layer thicknesses, indicating efficient spin pumping. The intrinsic spin-mixing conductance and spin diffusion length are determined, showcasing effective spin current injection and propagation within the BST layer. Effective spin-mixing conductance and the contribution of two-magnon scattering are also analyzed. Control experiments with a Cu spacer layer confirm spin pumping as the primary damping modulation mechanism, with minimal influence from spin memory loss. The interfacial spin transparency is calculated to be approximately 0.94, emphasizing the potential of BST/CoFeB heterostructures for advanced spintronic devices due to their high spin transport efficiency and robust spin pumping capabilities.

8.1. Introduction

Recently, topological insulators (TIs) have garnered significant scientific interest owing to their intriguing properties. These quantum materials[35–37] possess an unconventional electronic structure, exhibiting metallic surface states in stark contrast to their insulating bulk[424,425]. This dichotomy arises from a complex interplay of quantum effects within the material, particularly strong spin-orbit coupling (SOC)[426]. A defining feature of TIs is spin-momentum locking, where the spin of an electron is tightly correlated with its linear momentum, leading to the formation of helical surface states in momentum space[38,39]. This coupling fosters electron travel along helical paths in momentum space as they traverse the Dirac cone[427,428], a characteristic feature of their dispersion relation. Consequently, these electrons flow in a specific direction without being impeded by backscattering (in the absence of magnetic disruptions), which is crucial for realizing time-reversal symmetry-protected topological states[429–433]. While no net charge current exists under equilibrium conditions, a pure spin current persists. Due to these unique surface states, TIs have become

central to spintronics research. They naturally facilitate the generation of highly spin-polarized currents, essential for devices like spin valves and spin-transfer torque MRAM, which rely on precise spin manipulation. Additionally, the robust SOC in TIs enables seamless conversion between spin and charge currents, underpinning functionalities such as spin current detection and injection into other materials. TIs also exhibit prolonged spin coherence lengths, allowing for long-distance transmission of spin information, crucial for various spintronic applications.

Spin pumping[187,434], where a precessing ferromagnet (FM) injects a pure spin current into an adjacent non-magnetic (NM) layer, holds immense potential for spintronics applications. While traditional FM/heavy metal (HM) bilayers use SOC for efficient spin pumping, FM/topological insulator (TI) heterostructures offer significant advantages. The unique band structure of TIs, with their insulating bulk and conducting surface states, allows for more efficient spin injection from the FM layer into the TI's surface states. The strong intrinsic SOC in TIs further enhances spin current transmission, resulting in superior spin pumping efficiency compared to HMs[435–437]. Moreover, FM/TI heterostructures exhibit superior interfacial transport phenomena. Studies in spin-orbitronics have shown that interfacial properties, such as spin conductance, play a crucial role in spin-related effects, including the spin Hall effect[60] and the Rashba-Edelstein effect[87,438]. FM/TI interfaces demonstrate high spin-mixing conductance, allowing for greater spin current diffusion across the interface, thereby enhancing spin pumping efficiency.

$(Bi_{1-x}Sb_x)_2Te_3$ emerges as a promising candidate for next-generation TI devices due to its superior properties compared to well-studied second-generation binary TIs like Bi_2Se_3, Bi_2Te_3, and Sb_2Te_3. A significant challenge in these second-generation TIs is the presence of parasitic crystalline defects within their bulk[36,37,439,440], which act as unwanted conductive pathways and hinder the isolation of the desired topological surface states crucial for device functionality. $(Bi_{1-x}Sb_x)_2Te_3$ addresses this limitation by exhibiting lower bulk conductivity, potentially due to a reduced concentration of such defects. This results in a weaker background signal from the bulk, making the intrinsic topological surface conduction in $(Bi_{1-x}Sb_x)_2Te_3$ more prominent and easier to exploit for technological applications.

In this study, we investigate spin pumping in $(Bi_{0.3}Sb_{0.7})_2Te_3$ (BST)/$Co_{20}Fe_{60}B_{20}$ (CoFeB) bilayer thin films using an all-optical technique. Our goal is to precisely determine parameters such as spin-mixing conductance, spin transparency at the interface, and spin diffusion length

within BST. Time-resolved magneto-optical Kerr effect (TR-MOKE) magnetometry[441] is employed as our primary measurement technique. This approach, which is local and non-

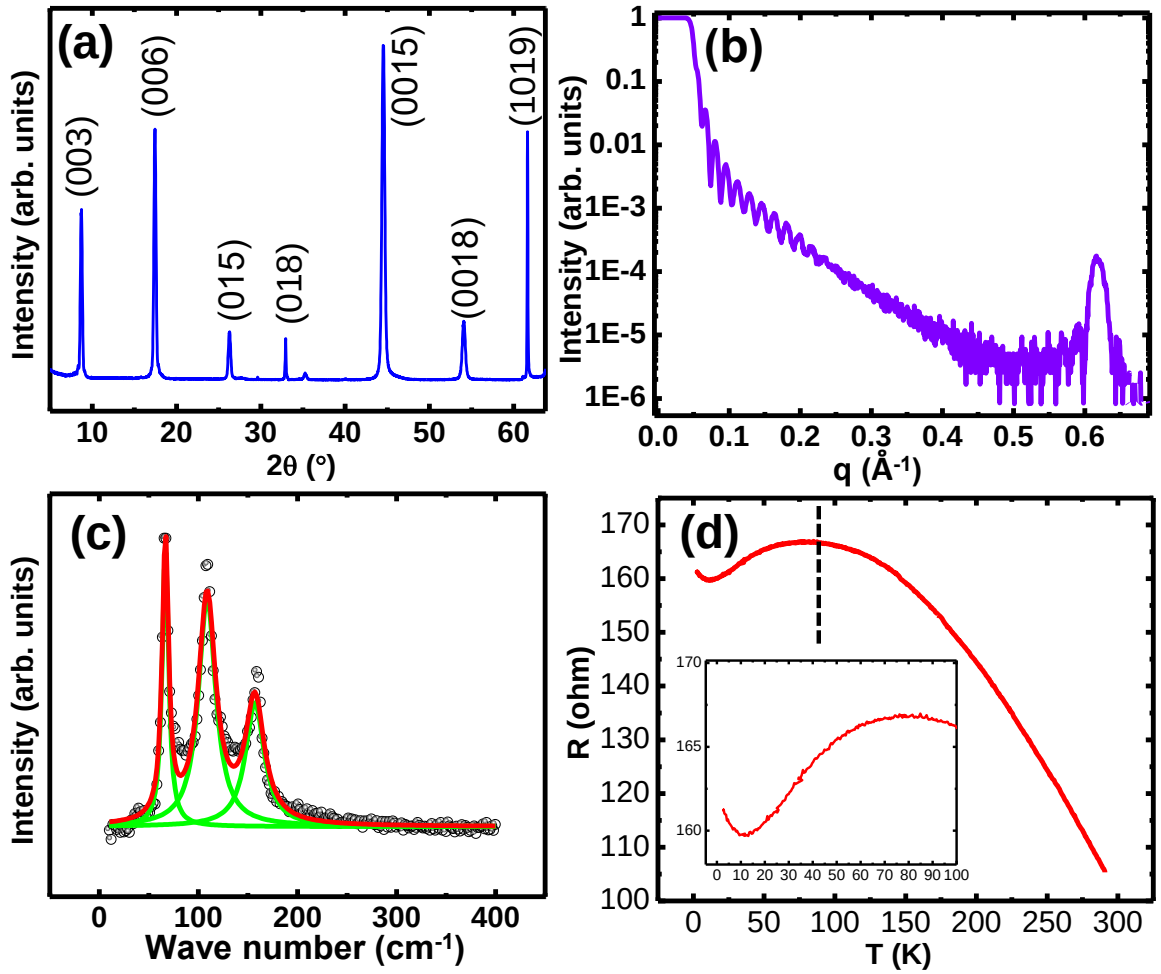

[55]**Figure 8.1.** Structural analysis and bulk insulating verification of the sample. (a) X-ray diffraction (XRD) pattern and (b) X-ray reflectivity (XRR) data of a 25 nm BST thin film. (c) Micro-Raman spectroscopy results for the 25 nm BST thin film. (d) A resistance measurement was performed on a 25 nm BST thin film, showing a temperature-dependent behavior. The dashed line represents the transition to surface-dominated transport. Inset: A zoomed-in view of the low-temperature regime.

invasive, offers a promising alternative to conventional electrical methods like spin-torque ferromagnetic resonance (ST-FMR) for studying spin pumping in HM/FM bilayers[442]. Unlike electrical techniques, TR-MOKE eliminates the need for complex microfabrication and overcomes limitations related to large-area averaging and inhomogeneous linewidth broadening inherent in those methods[443]. The decaying amplitude of the oscillatory Kerr signal enables clear extraction of damping without experimental artifacts from multimodal

oscillations or impurity/defect scattering. Our analysis focuses on studying damping modulation as a function of BST thickness to extract intrinsic spin-mixing conductance ($G_{\uparrow\downarrow}$) at the BST/CoFeB interface and estimate spin diffusion length (λ_s)[444] within BST. We also investigate the CoFeB thickness dependence of damping modulation to determine effective spin-mixing conductance (G_{eff}), which accounts for the backflow of spin angular momentum into the FM material and isolates the influence of two-magnon scattering (TMS) on damping modulation. Control experiments conducted by inserting a thin copper (Cu) spacer layer with varying thickness between BST and CoFeB. This is done to verify that spin pumping is the main mechanism responsible for the observed thickness-dependent damping modulation. The high SOC and intrinsic resistivity of the grown BST, which is a topological insulator, are anticipated to make a significant contribution to the observed efficient spin pumping. This underscores its potential as a spin current detector operating at room temperature.

8.2. Sample fabrication and measurement technique

8.2.1. Sample fabrication

We have employed pulsed laser deposition (PLD) to grow thin films of the topological insulator BST on SiO_2-coated Si substrates. While PLD may not achieve epitaxial growth, it retains the surface state topology due to the topological protection of Dirac electrons against non-magnetic defects like grain boundaries. We optimized the growth parameters, including pulse energy, deposition pressure, and substrate-to-target distance, based on established methods [432], controlling film thickness through laser pulse counts. The chamber was initially evacuated to a base pressure of 2.5×10^{-5} mbar. Deposition took place in an argon (Ar) atmosphere at 4.6×10^{-1} mbar pressure and a substrate temperature of 240 °C, with a laser fluence of 230 mJ/cm^2. Following deposition, samples underwent annealing in an Ar environment for 20 min. This annealing step facilitated the relocation of Sb and Te atoms to energetically favorable positions, reducing residual bulk carriers, akin to the behavior reported for Se and Te atoms [432]. The presence of Laue oscillations in the XRD pattern confirmed the high quality of the polycrystalline samples grown using PLD. This high quality was achieved through precise temperature control and an optimized in-situ annealing process during the deposition. Different thicknesses of ferromagnetic CoFeB layers of were sputter deposited onto the PLD-grown BST samples using DC magnetron sputtering. A 3 nm SiO_2 protective capping layer was subsequently added using RF sputtering to shield the samples during optical pump-probe measurements in ambient conditions. The deposition parameters included a DC voltage of approximately 360 V for CoFeB and an RF power of 50 W for SiO_2 deposition. For the Sub/BST (25 nm)/Cu (t_{Cu})/CoFeB (5 nm)/SiO_2 (3 nm) samples,

the Cu spacer layer was deposited at a DC voltage of about 340 V. All deposition processes were carried out at an Ar pressure of 0.5 mTorr, with a base pressure of 7.5×10^{-7} Torr. We ensured uniform deposition conditions for all samples, maintaining deposition rates of 0.2 Å/s for metallic films and 0.1 Å/s for the SiO_2 capping layer.

8.2.2. TR-MOKE Measurements

We utilized a customized TR-MOKE magnetometer based on a two-color, non-collinear pump-probe approach. A frequency-doubled femtosecond laser delivered 400 nm pulses with a pulse width exceeding 40 fs at 1 kHz repetition rate to excite the dynamics. A small portion of the fundamental 800 nm laser output (~40 fs pulse width, 1 kHz repetition rate; Libra regenerative amplifier system, Coherent) served as the probe to detect time-dependent polar Kerr rotation in the samples. The pump beam was focused to a spot size of ~300 μm and

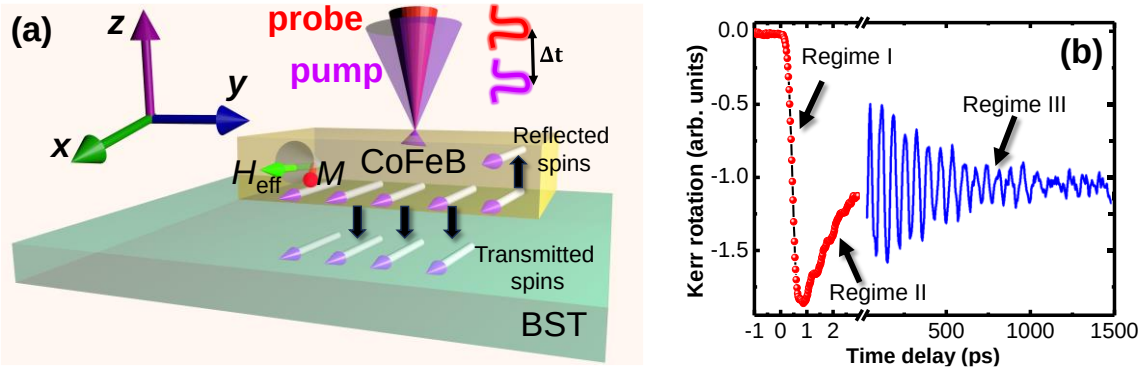

[56]**Figure 8.2.** Depiction of spin pumping phenomenon and TR-MOKE measurements. (a) Diagram of the sample configuration and the setup for TRMOKE measurements. (b) Time-resolved Kerr rotation data for the Sub/BST (25 nm)/CoFeB (10 nm)/SiO_2 (3 nm) heterostructure, identifying three distinct temporal regimes: Regime I indicates ultrafast demagnetization, Regime II represents rapid magnetization recovery, and Regime III demonstrates magnetization precession with characteristic Gilbert damping.

incident on the sample at an oblique angle (~30° from the surface normal). The probe beam, with a spot size of ~100 μm, was incident normally to the sample surface, ensuring perfect spatial overlap with the pump to eliminate spurious contributions to Gilbert damping arising from non-uniform precessional mode energy loss. A sufficiently strong magnetic field, tilted at ~25° relative to the sample plane, was applied to saturate the magnetization. This field was then reduced to a desired bias field value (H is the in-plane component) to maintain magnetization saturation along its direction. The tilted magnetization resulted in a non-zero demagnetizing field along the pump beam path. This field, further modulated by the pump pulse, initiated precessional dynamics within the sample. The pump was modulated at 373 Hz using an optical chopper, and the lock-in amplifier detected the dynamic Kerr rotation angle in the probe beam with phase sensitivity. Probe and pump fluences were maintained at

constant values of 1 mJ/cm^2 and 10 mJ/cm^2, respectively, throughout the measurements. All experiments were conducted at room temperature under ambient conditions.

8.3. Results and discussion

The crystallinity of BST thin films grown using pulsed laser deposition (PLD) was assessed via X-ray diffraction (XRD) analysis. Figure 1(a) illustrates the XRD pattern of a 25-nm-thick BST film. Analysis of the XRD data revealed distinct peaks at various positions, indicative of specific crystallographic phases and structural features. Notably, peaks observed at (003) and (006) planes are characteristic of the layered structure commonly found in topological insulators, reflecting the regular stacking of atomic layers along the crystal lattice's c-axis. Additionally, the presence of peaks at higher indices like (015), (018), (0015), and (0018) suggests potential complex crystal arrangements or the coexistence of multiple phases within the thin films. These findings hint at different crystallographic orientations or the presence of stacking faults, which can impact the overall crystallinity and structural characteristics of the material. The detection of a peak at (1019) raises the possibility of a secondary phase or distinct crystalline structure, possibly influenced by growth conditions, post-treatment processes, or the inclusion of dopants or impurities during thin film growth. Observation of such XRD spectra has already been reported previously[445]. The clear and distinct peaks seen in the single crystals demonstrate their uniform and precisely aligned characteristics. Conversely, in Fig. 1(b), the X-ray reflectivity (XRR) spectra of a BST/CoFeB sample, measured using a 1.54 Å Cu–Kα X-ray source, reveal distinct oscillations extending up to a scattering vector of 0.24 Å^{-1}, indicative of uniform deposition. Additionally, noticeable Laue oscillations corresponding to the film thickness were detected at approximately 0.62 Å^{-1}, confirming the high crystallinity and uniformity of these films.

To assess the quality and investigate the molecular structure of BST films, we conducted a micro-Raman scattering experiment using a LabRam HR Evolution micro-Raman spectrometer (HORIBA France SAS) with a 532 nm wavelength laser, a 10× objective, and a grating with 600 lines/mm, resulting in a spot size of ~100 μm with 1% ND filter. The Raman spectrum of a 25-nm-thick BST film, as depicted in Figure 1(c), displays three well-defined normal modes at 67.3 cm^{-1}, 107.7 cm^{-1}, and 158.9 cm^{-1}. Out-of-plane vibrations lead to smaller displacements of vibrating atoms, resulting in higher phonon frequencies compared to in-plane modes. Therefore, the three Raman modes in Figure 1(c) are designated as A_{1g}^1, E_g^2 and A_{1g}^2 modes, in accordance with previous studies on Se-based BST films [446].

In Fig. 1(d), we observe the resistance vs. temperature relationship in a 25-nm-thick BST film. The behavior of resistance mirrors the intrinsic bulk insulating properties characteristic of BST, a well-established trait in BST systems[447]. As temperature decreases, resistance rises until approximately 90 K, as depicted by the dashed line in Fig. 1(d). Below this temperature, a transition to surface-dominated metallic conduction occurs, evident from a sharp change in curvature and a drop in resistance. This qualitative transition signifies the weak antilocalization effect[448] observed in highly insulating topological insulators such as BST, highlighting the emergence of metallic characteristics in the topologically protected surface states[40] even at relatively high temperatures, such as 90 K. In contrast, the slight increase in resistance at much lower temperatures (≤ 11 K) is attributed to the freezing of bulk carriers within the material[432].

8.3.1. Variation in Gilbert Damping Induced by Spin Pumping

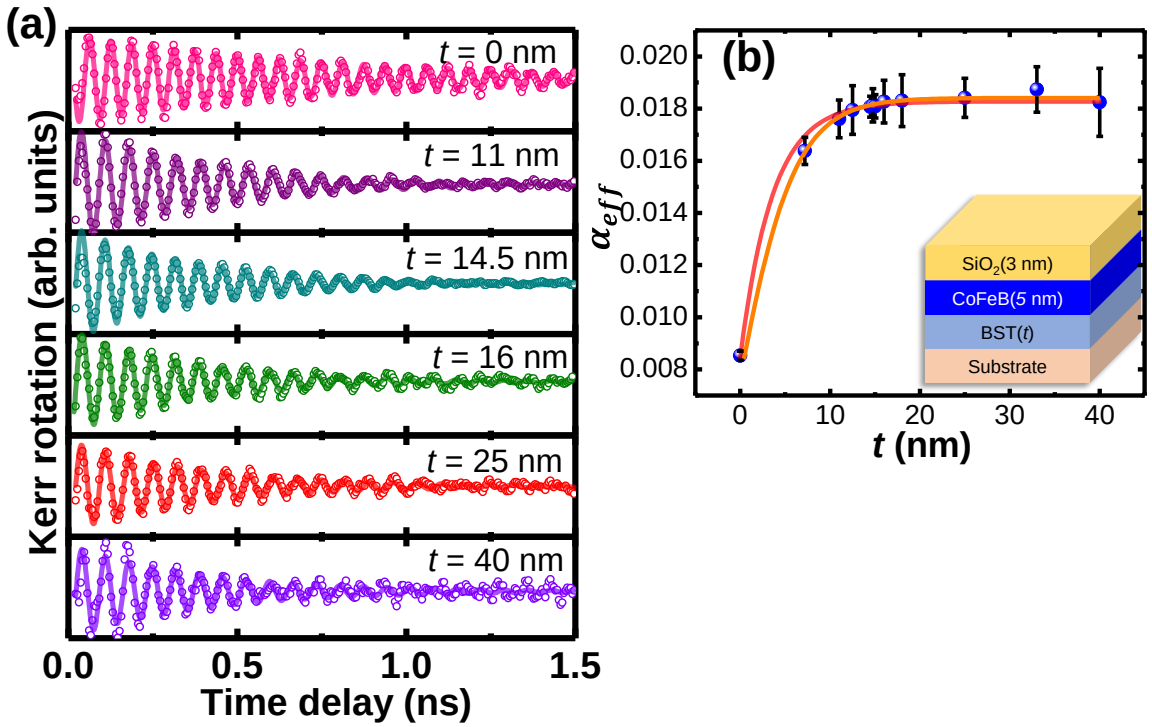

[57]**Figure 8.3.** Assessing the spin diffusion length and intrinsic spin-mixing conductance. (a) The precessional Kerr rotation data for Sub/BST(t)/CoFeB (5 nm)/SiO2 (3 nm) samples, measured with an external magnetic field of 1.72 kOe. (b) The damping parameter's dependence on the thickness of the BST layer. The solid line represents the theoretical fit using a spin pumping model to determine the intrinsic spin-mixing conductance and spin diffusion length (orange indicates the diffusive spin transport model, while red represents the ballistic spin transport model).

Besides intrinsic damping due to energy dissipation within electron and phonon subsystems, NM/FM systems can also show nonlocal damping. This type of damping occurs when

magnetic energy dissipates from the FM layer to the neighboring NM layer. Optically induced magnetization precession in the FM layer creates a spin current at the NM/FM interface. These spin currents transport angular momentum into the adjacent NM layer, serving as a sink for spins and absorbing the spin current over a specific distance known as the spin diffusion length. Consequently, this process results in an elevation of the Gilbert damping parameter[187,188,434], a phenomenon commonly known as spin pumping. The spin pumping mechanism can be explained using a modified form of the Landau-Lifshitz-Gilbert equation, which integrates the effects of spin current generation and absorption:

$$\frac{dm}{dt} = -\gamma(m \times H_{eff}) + \alpha_0 \left(m \times \frac{dm}{dt}\right) + \frac{\gamma I_S}{V M_S} \tag{8.1}$$

where $\gamma = \frac{g\mu_B}{\hbar}$ represents the gyromagnetic ratio, H_{eff} stands for the effective magnetic field, α_0 denotes the intrinsic Gilbert damping constant, V is the volume, and M_s signifies the saturation magnetization of the FM.

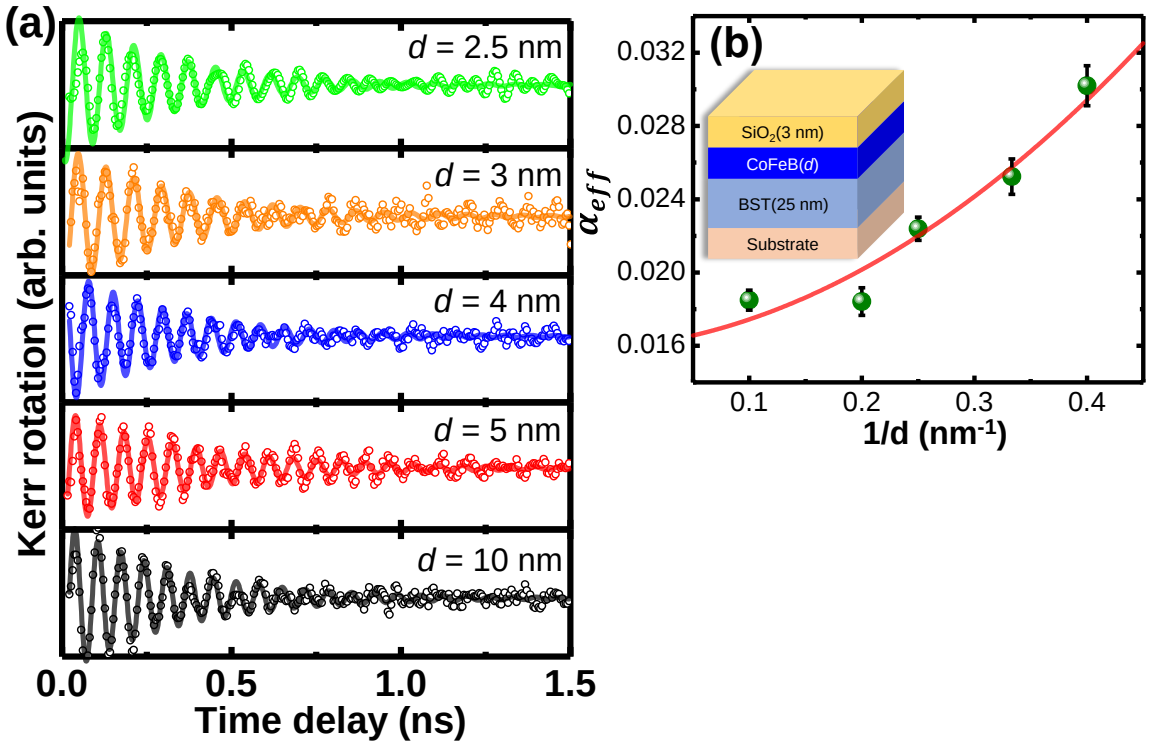

[58]**Figure 8.4.** Derivation of the intrinsic Gilbert damping parameter and effective spin-mixing conductance. (a) Precessional Kerr rotation data for Sub/BST (25 nm)/CoFeB (d)/SiO_2 (3 nm) samples. (b) Variation of the damping parameter with CoFeB layer thickness. The theoretical fit, represented by the solid line, integrates both spin pumping (SP) and two-magnon scattering (TMS) to ascertain the effective spin-mixing conductance.

The net spin current, denoted as I_s, comprises several components: the direct current I_S^0, which is absent in our scenario, the current resulting from pumped spins from the FM layer,

labeled as I_S^{pump}, and the current that returns back to the FM layer (backflow current), denoted as I_S^{back}.

$$I_S = I_S^0 + I_S^{pump} + I_S^{back} \tag{8.2}$$

The spins emitted can gather at the interface or experience relaxation via spin-flip scattering, leading to a transfer of angular momentum from the FM to the NM layer across the NM/FM interface. However, the NM layer doesn't always serve as an ideal spin reservoir due to the spin accumulation effect, mainly contributing to the reverse flow current known as I_S^{back}. This reversal of spin current towards the FM layer relies on the spin diffusion length within the adjacent NM layer. On the contrary, the transmission of spin angular momentum across the NM/FM interface is characterized by the spin-mixing conductance.

The backflow of spin current primarily stems from spin accumulation at the interface, leading to a reduction in spin transfer efficiency. The extent of spin accumulation can be measured using the backflow factor β [187,434]:

$$\beta = (G_{\uparrow\downarrow}\sqrt{\frac{4\varepsilon}{3}}\tanh\left(\frac{t}{\lambda_S}\right))^{-1} \tag{8.3}$$

Here, ε represents the ratio of spin-conserved to spin-flip scattering times, also known as the spin-flip probability, which is specific to the material and can be expressed as[59,449]:

$$\varepsilon = (\frac{Ze^2}{c})^4 = (Z\alpha_{fine})^4 \tag{8.4}$$

In this context, $\alpha_{\text{fine}} = 1/137$ represents the fine structure constant, and Z denotes the atomic number of the NM material. The intensity of ε is more evident for elements with greater mass, preventing the disappearance of the backflow effect when the ratio t/λ_s is significantly greater than 1. Nonetheless, the intrinsic spin-mixing conductance $G_{\uparrow\downarrow}$ provides a straightforward measurement of pure spin current transfer without accounting for spin backflow. In the context of diffusive spin transport, an extra parameter called the effective spin-mixing conductance G_{eff} can be obtained from $G_{\uparrow\downarrow}$ by incorporating the backflow factor, formulated as [188]:

$$G_{eff} = \frac{G_{\uparrow\downarrow}}{(\sqrt{\frac{4\varepsilon}{3}}\tanh\left(\frac{t}{\lambda_S}\right))^{-1}+1} \tag{8.5}$$

The efficient transfer of angular momentum across the NM/FM interface relies on achieving a balance between the forward and backflow currents. The forward current is affected by the intrinsic spin-mixing conductance $G_{\uparrow\downarrow}$[450], which indicates the effectiveness of spin transfer

across the interface. In the ballistic approximation, which is applicable for film thicknesses smaller than the momentum mean free path[451], $G_{\uparrow\downarrow}$ can be determined by analysing the dependence of the effective Gilbert damping α_{eff} with the NM layer thickness t, based on this corelation [59,451]:

$$\alpha_{eff} = \alpha_0 + \frac{g\mu_B G_{\uparrow\downarrow}}{4\pi M_S d}\left(1 - e^{-\frac{2t}{\lambda_S}}\right) \tag{8.6}$$

where d and λ_s denote the FM layer thickness and spin diffusion length within the NM, respectively.

Incorporating the backflow factor introduces variability specific to each element and relies on the thickness of the NM layer, rendering G_{eff} dependent on both these factors. G_{eff} can also be determined experimentally by investigating the relationship between damping and the thickness d of the FM layer, given by[188,443]:

$$\alpha_{eff} = \alpha_0 + \frac{g\mu_B G_{eff}}{4\pi M_S d} = \alpha_0 + \frac{g\mu_B}{4\pi M_S d}\frac{G_{\uparrow\downarrow}}{\left(\sqrt{\frac{4\varepsilon}{3}}\tanh\left(\frac{t}{\lambda_S}\right)\right)^{-1}+1} \tag{8.7}$$

By substituting the result from Eq. (6) into the latter half of the provided equation, a diffusive approximation can be employed to model the dependence of spin pumping on the thickness of the NM layer for a constant FM layer thickness d.

Besides spin pumping, factors like magnetic disorder and intermixing at the NM/FM interface can lead to spin information loss and reduced spin transmission efficiency due to specific interfacial effects beyond spin pumping. One such effect is spin memory loss (SML), where interfacial spin-orbit coupling (SOC) enables spin-flip scattering events at the interface, diminishing spin transmission to the NM layer [452,453]. Further losses may arise from the two-magnon scattering (TMS) effect [454,455], which occurs when defects and non-uniformities are present at the interface, leading to the dephasing of the uniform ferromagnetic resonance (FMR) mode and its scattering into degenerate magnons. The presence of SML or TMS can significantly modulate effective damping more than pure spin pumping. While the damping modulation caused by SML decreases linearly with increasing FM thickness, similar to spin pumping, the modulation due to TMS increases quadratically. This distinct behavior enables the straightforward isolation of the TMS contribution from FM-thickness-dependent damping measurements. The overall modulation in total damping, arising from the combined effects of spin pumping and TMS, can be represented as mathematically as [442,456–458]:

$$\Delta\alpha = \alpha_{eff} - \alpha_0 = \frac{g\mu_B G_{eff}}{4\pi M_S d} + \frac{\beta_{TMS}}{d^2} \tag{8.8}$$

Together, these interfacial effects contribute as a whole to a parameter referred to as the interfacial spin transparency, denoted by T, expressed as[459,460]:

$$T = \frac{G_{eff}\ \tanh\left(\frac{t}{2\lambda_S}\right)}{G_{eff}\coth\left(\frac{t}{\lambda_S}\right)+\frac{h}{2\rho\lambda_S e^2}} \tag{8.9}$$

where ρ is the resistivity and λ_S is the spin diffusion length of the NM layer.

The effective spin-mixing conductance, denoted by G_{eff}, is directly linked to the interfacial spin transparency, regulating the transfer of spin angular momentum across the NM/FM interface. Variations in spin transparency affect the observed spin-Hall angle independently of the SML effect. Identifying and optimizing highly transparent interfaces are essential steps in improving spin transfer efficiency for real-world device implementations.

8.3.2. All-optical Evaluation of Damping Characteristics

We utilized time-resolved magneto-optic Kerr effect (TR-MOKE) magnetometry to optically study magnetization dynamics in Sub/BST(t)/CoFeB(d)/SiO_2(3 nm) samples. Employing a non-collinear pump-probe geometry within a two-color setup, as shown in Fig. 2(a), allowed us to examine the temporal phases of laser-induced magnetization dynamics. Figure 2(b) presents typical time-resolved Kerr rotation data, depicting various stages of the dynamics. In Regime I, we observed ultrafast demagnetization, characterized by a rapid reduction in magnetization at the picosecond timescale due to laser excitation. Regime II showcases the rapid magnetization recovery process. In Regime III, the oscillatory Kerr signal indicates magnetization precession with characteristic Gilbert damping, superimposed on a background signal due to slow relaxation caused by heat dissipation into the substrate. In order to determine the Gilbert damping parameter α_{eff}, we start by fitting the background-subtracted oscillatory Kerr signal with a damped sinusoidal function:

$$M_{eff} = M(0)e^{-\frac{t}{\tau}}\sin(2\pi f_{FFT}t + \varphi) \tag{8.10}$$

where the precessional frequency is represented as f_{FFT}, with τ indicating the relaxation time and φ representing the initial phase of precession. Additionally, to determine the effective saturation magnetization M_{eff} of the samples, we conducted a fitting analysis of the bias magnetic field dependence of f_{FFT} using the Kittel formula [128], which is applicable to ferromagnetic systems:

$$f_{FFT} = \frac{\gamma}{2\pi}\sqrt{(H + H_k)(H + H_k + 4\pi M_{eff})} \quad (8.11)$$

where $\gamma = \frac{g\mu_B}{\hbar}$ is the gyromagnetic ratio and H is the bias magnetic field. The Kittel fitting analysis conducted on the Sub/BST (25 nm)/CoFeB(d)/SiO_2(3 nm) samples demonstrate that the effective saturation magnetization M_{eff} decrease with increasing CoFeB thickness d, indicating a linear correlation with 1/d. By fitting this dataset with the conventional equation $M_{eff} = M_S - \frac{2K_S}{4\pi M_S d}$, we were able to extract the saturation magnetization M_s from the intercept and the interfacial anisotropy K_s from the slope. The interfacial anisotropy K_s holds significant importance as it reflects the strength of the interfacial SOC. The saturation magnetization M_s decrease from 1547 ± 54 emu/cc in the reference CoFeB films to 1354 ± 25 emu/cc in the BST/CoFeB bilayers. In contrast, K_s slightly increases from 1.11 ± 0.22 erg/cm^2 in the reference films to 1.41 ± 0.10 erg/cm^2 in the bilayers. The reduction in Ms seen in the TI/FM bilayers could be due to the magnetic proximity effect at the BST/CoFeB interface. This effect involves orbital hybridization between the 3d electrons in CoFe and the topological surface states of BST, potentially causing a perpendicular magnetic anisotropy that results in decreased M_s at lower temperatures. However, under ambient conditions, the more likely explanation is the presence of atomic intermixing at the BST/CoFeB interface. Lastly, we calculated the effective Gilbert damping parameter α_{eff} using the extracted values of τ and M_{eff}:

$$\alpha_{eff} = \frac{1}{\gamma\tau(H+2\pi M_{eff})} \quad (8.12)$$

8.3.3. Thickness-dependent modulation of damping

In this investigation, we analyze precessional Kerr rotation data that has been background-subtracted, as obtained from Sub/BST(t)/CoFeB(5 nm)/SiO_2(3 nm) samples under a saturating magnetic field of approximately 1.72 kOe (Fig. 3(a)). The thickness of the BST layer (t) was systematically varied within the range of 7.2 nm to 40 nm. Setting this lower thickness limit ensures it surpasses twice the estimated surface state thickness. This precaution is taken to eliminate the potential influence of quantum tunnelling between opposing surfaces, a phenomenon that could lead to a transition from a topological phase to a trivial gapped insulator in ultrathin films.

Our experiments reveal a significant increase in the effective damping (α_{eff}) of the 5 nm CoFeB thin film upon the inclusion of a BST underlayer (Fig. 3(b)). Without the underlayer, the intrinsic damping value (α_0) is found to be 0.0085. Interestingly, α_{eff} displays a non-monotonic

trend with increasing BST thickness (t). It rises sharply from the intrinsic value to a saturation point of 0.0183 at higher *t*. This observed dependence corresponds to the typical behavior of spin pumping observed in FM/NM thin film systems. However, such behavior is unexpected in TIs where spin-to-charge conversion is primarily associated with the topologically protected surface states[40], whose thickness remains unaffected by the overall film thickness. In TIs, the strength of SOC differs between bulk and surface states. Spin pumping can facilitate the inverse Edelstein effect (IEE) within the spin-momentum-locked surface states. The spin current injected from the ferromagnet creates a spin imbalance in the surface states, and due to spin-momentum locking, this results in a two-dimensional confined charge current (J_c). This mechanism contrasts with the inverse spin Hall effect (ISHE)[436], where a bulk spin current converts into a three-dimensional charge current. Distinguishing between ISHE and IEE of the surface state in room-temperature spin-pumping experiments is highly challenging, with ISHE typically dominating. Although an enhanced spin-orbit coupling of the surface states has been reported to enhance the pure spin current injected into the TI, any contribution from these states to spin pumping should remain consistent across the investigated thickness range. Therefore, the observed variation in α_{eff} (Fig. 3(b)) cannot be solely attributed to the surface states.

Our observations suggest that the variation in α_{eff} with BST thickness may stem from the robust bulk SOC within the bismuth-based alloy, resembling that of a traditional heavy metal. This insight, derived under room temperature conditions, hints at possible scattering events

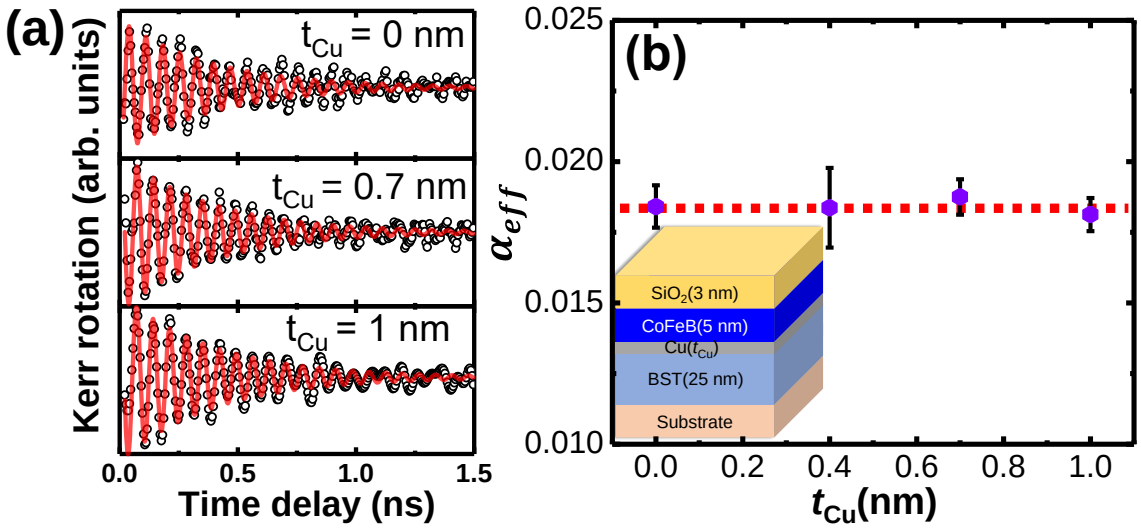

[59]**Figure 8.5.** Variation of damping with spacer layer thickness. (a) Time-resolved Kerr rotation data for spacer layer thicknesses of t_{Cu} = 0, 0.7, and 1.0 nm. (b) Dependence of the damping parameter on spacer layer thickness. The dashed line provides a visual guide.

between surface and bulk states. Such scattering mechanisms could lead to the redirection of injected carriers into the material's bulk. Temperature-dependent investigations of α_{eff} could provide further insights into the surface states' involvement in spin pumping. Specifically, studies at temperatures below 90 K, where the resistance-temperature (R-T) characteristics demonstrate a transition to surface-dominated transport, could be enlightening. By fitting the data in Fig. 3(b) to the latter part of Eq. (7), we derived an intrinsic $G_{\uparrow\downarrow}$ value of (3.105 ± 0.441) × 10^{16} cm^{-2} and a corresponding spin diffusion length (λ_s) of 6.9 nm. The notable $G_{\uparrow\downarrow}$ value and the non-monotonic behavior of the damping parameter both support the notion of spin current injection into the BST layer. For a comprehensive analysis, we also applied the ballistic transport model represented by Eq. (6). This approach yielded a $G_{\uparrow\downarrow}$ value of (4.516 ± 0.125) × 10^{15} cm^{-2} and a λ_s of 7.3 nm. Using Eq. (4), In these heterostructures, the spin-flip probability (ε) was calculated to be 2.68%, indicating a strong SOC of the heavy metal bismuth and its efficacy as a spin sink[461]. From the extracted values of ε, $G_{\uparrow\downarrow}$, and λ_s, the value of β for the 25-nm-thick BST layer is determined to be 5.39 × 10^{-17} cm^2 using Eq. (7). As expected, β tends to be higher for thinner films and approaches a lower limit as the thickness significantly exceeds the spin diffusion length ($t >> \lambda_s$). However, even at substantial thicknesses, β persists due to the material property reflected in ε. On the other hand, the exponential dependence of the backflow factor in Eq. (6) is relevant in the ballistic regime, where the film thickness is less than the mean free path. The calculated G_{eff}, incorporating the effect of spin backflow using Eq. (5), is (4.932 ± 0.700) × 10^{15} cm^{-2} for the 25 nm BST layer, approximately three times lower than $G_{\uparrow\downarrow}$. Notably, considering a non-negligible spin backflow leads to a higher G_{eff} value compared to estimates obtained from spin diffusion and ballistic models.

To experimentally measure G_{eff} directly, we varied the thickness (d) of the CoFeB layer while maintaining a constant thickness (25 nm) for the BST layer, ensuring it exceeds the spin diffusion length (λ_s). This method effectively removes the influence of BST thickness variations, allowing us to focus solely on the impact of CoFeB thickness on damping. Figure 4(a) illustrates the precessional data obtained under a saturating field of 1.72 kOe for Sub/BST (25 nm)/CoFeB(d)/SiO_2(3 nm) samples, where d ranges from 2.5 to 10 nm. The damping parameter shows a significant increase with the inverse of CoFeB thickness, indicating a robust spin pumping effect in our system. We fitted this observed dependence using Eq. (8), which incorporates both linear and quadratic scaling with the inverse thickness, representing contributions from spin pumping and TMS effects, respectively. The fit yields values of (7.38 ± 0.514) × 10^{14} cm^{-2} for G_{eff}, (6.37 ± 1.097) × 10^{-16} cm^2 for the TMS coefficient

(β_{TMS}), and 0.016 for the intrinsic Gilbert damping (α_0). Equation (8) allows us to separate the contributions of spin pumping and TMS to the total damping modulation. As anticipated, the TMS contribution increases as CoFeB thickness decreases, corresponding to the higher surface roughness observed for thinner films using AFM measurements. The non-zero β_{TMS} value in these heterostructures likely results from the PLD growth process employed for BST. Improved interfacial quality could enhance spin transmission efficiency and reduce the TMS contribution. Finally, we sought to investigate T of the BST/CoFeB interface using the experimentally determined values of $G_{\uparrow\downarrow}$ and G_{eff}. However, T shows a complex dependence on multiple factors, such as the spin-mixing conductance of the interface, spin diffusion length, and the resistivity of the NM layer.

Within the spin-Hall magnetoresistance framework[460], we integrated the finite thickness of the BST layer. By employing the experimentally determined G_{eff} value of $(4.932 \pm 0.700) \times 10^{15}$ cm^{-2}, alongside the derived resistivity and spin diffusion length (λ_s = 6.9 nm), Eq. (9) yields a remarkably high spin transparency (T) of 0.94. This value corresponds to the "perfect spin-sink" regime ($t >> \lambda_s$), where the effect of BST thickness on damping modulation saturates, leading to the observed high G_{eff} at the BST/CoFeB interface. These outcomes showcase the potential for achieving elevated T values in BST/CoFeB systems, presenting a novel perspective for their utilization in spintronic devices reliant on pure spin currents. The robust bulk SOC characteristic of the BST topological insulator aids in spin current dissipation, contributing to the high G_{eff} and T values. Furthermore, the surface SOC likely amplifies the pumped spin current, further enhancing the G_{eff}. Beyond the high G_{eff}, the substantial resistivity of BST also plays a role in augmenting the interfacial transparency. Optimizing spin transfer efficiency in such systems will necessitate strategic choices regarding BST layer thickness and exploring methods to manipulate its resistivity. These aspects warrant further exploration and will serve as the focal point of future investigations.

To examine the specific impact of spin pumping, we have isolated the BST and CoFeB interfaces by introducing a thin Cu spacer layer in between our heterostructures. This spacer layer was designed to minimize spin-flip scattering at the Cu interfaces due to its weak spin-orbit coupling. Additionally, the long spin diffusion length of copper[444] allows the injected spin current from spin pumping to traverse the entire spacer layer without significant loss. We conducted TR-MOKE measurements on these new samples as a control experiment. Figure 5(a) displays the time-resolved Kerr rotation data for Sub/BST (25 nm)/Cu (t_{Cu})/CoFeB (5 nm)/SiO_2 (3 nm) thin films, where t_{Cu} is varied from 0 to 1 nm. The results, as shown in Fig. 5(b), reveals that introducing and varying the Cu spacer thickness leads to

minimal modulation of the damping parameter. These findings strongly suggest that the observed thickness-dependent damping modulation is primarily attributed to the spin pumping mechanism, while ruling out any significant contribution from the spin memory loss (SML) effect in our heterostructures.

8.4. Conclusions

In our investigation, we have utilized a time-resolved magneto-optical Kerr effect (TR-MOKE) technique to delve into the pronounced spin pumping effects and interfacial spin transparency within $(Bi_{0.3}Sb_{0.7})_2Te_3/Co_{20}Fe_{60}B_{20}$ (BST/CoFeB) heterostructures. The high-quality BST thin films, deposited through pulsed laser deposition, exhibits distinctive structural characteristics and displays a bulk insulating behavior. The resistance versus temperature profile indicates prevalent surface transport dominance up to 90 K. The discerned modulation of Gilbert damping in relation to the thicknesses of the CoFeB and BST layers unveils a robust spin-pumping mechanism within these heterostructures. This efficacy is further affirmed through a meticulous analysis of Gilbert damping variations concerning the BST and CoFeB layer thicknesses. Our study pinpoints the intrinsic spin-mixing conductance $G_{\uparrow\downarrow}$ of the interface at $(3.105 \pm 0.441) \times 10^{16}$ cm^{-2} and identifies the spin-diffusion length λ_s in BST as 6.9 nm at room temperature, indicating the optical detection of pure spin current injection into the BST layer. Through a thorough examination of the thickness-dependent fluctuations in Gilbert damping within the CoFeB layer, we derive an effective spin-mixing conductance G_{eff} of $(4.932 \pm 0.700) \times 10^{15}$ cm^{-2} and isolate the two-magnon scattering parameter β_{TMS}, calculated at $(6.37 \pm 1.097) \times 10^{-16}$ cm^2. This highlights the prominent role of spin pumping as the primary contributor to the observed damping modulation. Other interfacial losses, such as spin memory loss, are deemed negligible, as evidenced by the minimal damping modulation observed when a Cu spacer layer is introduced at the BST/CoFeB interface. Additionally, we have calculated the interfacial spin transparency T to be approximately 0.94 (94%) for a BST thickness of 25 nm, emphasizing the critical significance of high interfacial spin transparency in augmenting spin transport efficiency. The distinct characteristics of topological insulators coupled with the near-ideal spin transparency observed in BST/CoFeB heterostructures present substantial promise for propelling advancements in spin-orbitronic device applications.

Chapter 9

9. Optimizing the Polarization and Antireflection Characteristics of Metallic Wire Grid Structures in the Terahertz Frequency Range

The ever-increasing demand for high-quality quasi-optic components, such as phase shifters, filters, and polarizers, has led to the exploration of new paradigms for structuring and patterning existing materials, as well as the search for novel materials. In this work, we have found a simple yet efficient way to boost the polarization efficiency of metallic wire grid polarizers made of gold by reducing the period of the wire grid structures. The thus fabricated metallic wire grids offer a degree of polarization as high as 94.3% and an extinction ratio ~ 22.1 dB over a broad frequency range of 0.2-2.5 THz. Simultaneously, the thus prepared metallic wire grid structures also perform efficiently as anti-reflection coating materials, showcasing their versatility and multifunctionality. We believe that these durable, long-lasting, and low-maintenance metallic wire grid structures will meet the ever-lasting need for efficient THz polarizers.

9.1. Introduction

Terahertz (THz) technology is a delicate trade-off between electronics and photonics as it spans a rather elusive frequency window in the electromagnetic spectrum between microwave and infrared. This spectral range (0.1 to 10 THz (3.3 cm^{-1}-333 cm^{-1})) hosts the fingerprint modes of low frequency dielectric relaxation, rotational and vibrational motions of molecules. This frequency domain possesses unique properties which promote it for diverse applications, including telecommunications, pharmaceuticals as well as chemical analysis.[92,462,463] Its non-ionizing nature makes it safe for the usage in medical imaging[90] and other fields. Furthermore, THz frequency allows the imaging of opaque materials, enabling non-destructive testing and security screening.[91] Such unique potentialities make bridging of the so-called THz gap[88] essential, offering significant impetus for research and innovation across various sectors.[89] Over the last few decades, this research field has been witnessing remarkable expansion and a paradigm shift due to the development of novel THz sources and detectors.[93] In spite of all the advancements the development of efficient and cost effective THz optical components, such as lenses,[464] beam splitters,[465] absorbers,[466] wave plates,[467] and polarizers is still in its early phase. In this regard fabricating a high-performance, reliable, and long-lasting THz polarizer still remains as a challenging task.[98]

THz polarizers can be divided into two main categories: free-standing and substrate-supported. While free-standing polarizers exhibit high power extinction ratios and low insertion losses, they tend to be expensive and delicate.[468] In contrast, substrate-supported polarizers offer moderate polarization performance and are relatively robust and long-lasting, making them highly demanding. Among the existing substrate-supported polarizers, metallic wire grid (MWG) polarizers, due to their ease of fabrication, low cost, and high polarization efficiency over a broad frequency range stand out among the various types of polarizers used in the THz frequency range. An MWG is an optical device composed of a series of wire grids. When transverse electric (TE) polarized light is incident on the wire-grid(s) with an electric field parallel to the wire-grids, it induces a conduction current along the length of each wire. The flow of electrons, in turn, collides with the lattice atoms, transferring energy to them and thus raising the temperature of the wires, leading to joule heating within the wire-grids or a re-radiation in the backward direction, resulting in either absorption or reflection. In contrast, transverse magnetic (TM) polarized light can travel through the wire-grids, resulting in highly polarized transmitted or reflected light.[469] The performance of an MWG, including its extinction ratio, is primarily governed by a set of key parameters that are instrumental in defining its optical properties. These parameters include the period, which is the centre-to-centre distance between the adjacent grid elements, as well as the linewidth and thickness of the individual grid element(s). These factors are critical determinants of the MWG's performance and play a pivotal role in shaping its optical response in different operational contexts. Till date several efforts have been made to construct and optimize the performance of different THz polarizers. Wang et al.[470] have shown that a highly aligned aluminium nanowire grid structure on a silica wafer offers efficient optical polarization in ultraviolet wavelength down to ~250 nm. Later studies report that by utilizing carbon nanotube polarizers as both substrate back-up[101] and reel wound,[100] an exceptionally elevated polarization degree has been attained across the entire frequency spectrum, rendering them superior as high-performance polarizers for THz applications. In a recent development, substantial advancements have been achieved through the utilization of MXenes, a novel category of solution-processable two-dimensional materials, patterned in the form of grid-wires on quartz substrates to investigate their polarization efficacy across a broad frequency spectrum.[105] In a separate study,[471] an innovative approach to optimize THz polarization performance involved the construction of bilayer metal wire-grid structures, comprising of aluminium, with highly adaptable properties was achieved by fine-tuning of various geometric parameters. The resulting

structures represent a significant advancement in the field by mitigating the multireflection effects that can adversely affect their performance. In spite of all these efforts a significant gap in the literature still remains in the area of fine-tuning the THz polarization performance of MWG structures through precise adjustment of the array period on a micron scale. This gap highlights the need for further exploration and investigation to address the lack of comprehensive understanding in this critical aspect of THz polarization performance optimization.

In this study we report the fabrication of MWG structures using gold (Au) on high-resistive silicon (HR-Si) wafers with varying array periods, thereby achieving effective regulation of performance across a wide frequency range. We have evaluated the THz response of the MWGs in transmission geometry using THz-time domain spectroscopy (THz-TDS) measurements. By carefully altering the in-plane orientation of the samples while maintaining all other parameters constant, we have determined several polarization-related properties. Our experimental findings have revealed an excellent extinction ratio of 22.1 dB spanning over a frequency range of 0.2 to 2.5 THz, accompanied by a degree of polarization up to 94.3%. We posit that this superior performance across broad THz frequency range renders the thus fabricated MWG to evolve as an excellent testbed for THz polarizers.

9.2. Experimental and Simulation Methods

9.2.1. Sample fabrication

We have successfully fabricated Au MWG structures on HR-Si (100) wafers with varying array periods using maskless photolithography technique. Specifically, we have employed a direct laser writer (LW405-MICROTECH), electron-beam evaporation (EBE), and lift-off processes to obtain our desired structures. Scanning electron micrograph (SEM) images of the samples are depicted in Figure 9.1(a)-(e). Initially, an AZ-1512 resist pattern has been developed on the HR-Si (100) substrate using a laser writer. Following this step, we have deposited an 8 nm Cr/62 nm Au layer on the substrate at a very slow deposition rate under a base pressure of 2×10^{-7} Torr using EBE. Our selection of Au as the material of choice is based upon its exceptional electrical conductivity, which enables superior performance as polarizer. Additionally, Au is highly resistant to oxidation, making it an ideal choice for maintaining stable and consistent performance over time. We have prepared five sets of samples with different periods: P1 (200 μm), P2 (100 μm), P3 (40 μm), P4 (20 μm), and P5 (10 μm). The width of each wire is half the period value, resulting in a constant fill factor of 0.5, which is required to achieve higher THz performance.[472] A fill factor of 0.5 is optimal for THz polarizers because it balances polarization efficiency and transmission. A high fill factor

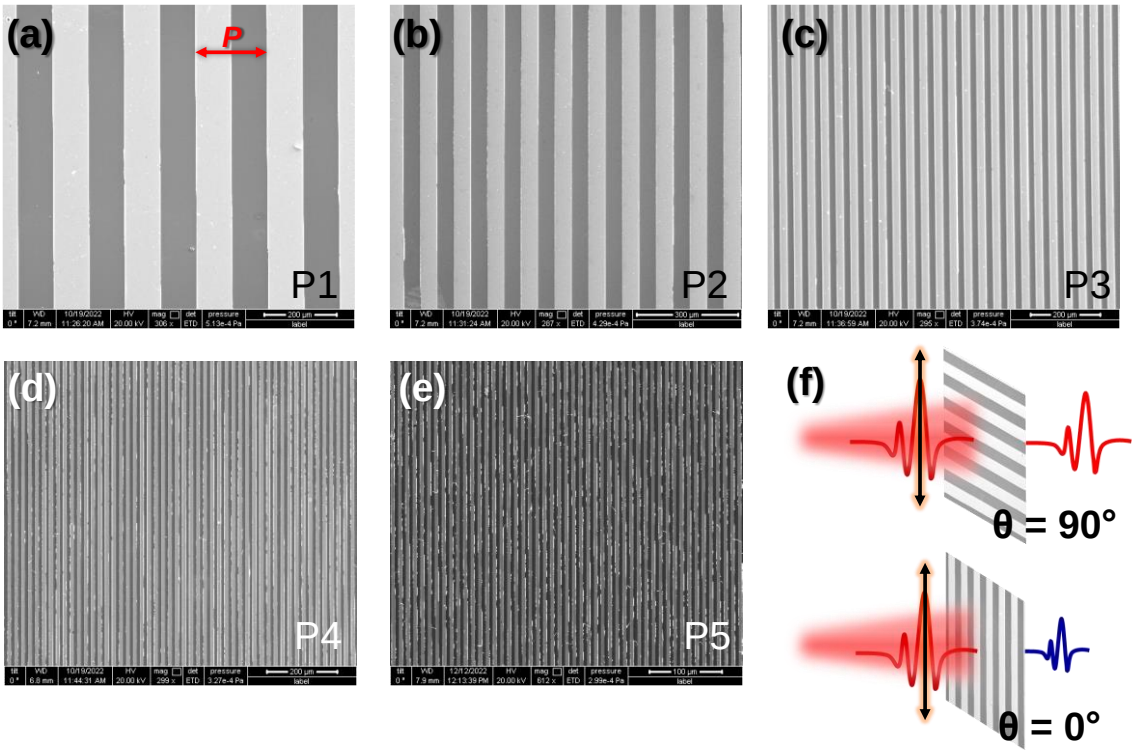

[60]**Figure 9.1.** Scanning electron microscope (SEM) images of the MWG structures with periods (a) 200 µm (P1), (b) 100 µm (P2), (c) 40 µm (P3), (d) 20 µm (P4) and (e) 10 µm (P5). The value of width of each sample is half the period value. (f) Schematic representation of the THz electric field amplitude after the interaction with samples at parallel and perpendicular configurations.

reduces transmission because the wires block much of the radiation, whereas a low fill factor reduces polarization efficiency. A fill factor of 0.5 achieves high polarization efficiency while maintaining high transmission. It is pertinent to mention that our choice of HR-Si wafers is motivated by their exceptionally low absorbance of THz radiation across a wide frequency spectrum.[473]

9.2.2. Measurement technique

In this study, we have conducted THz time-domain measurements utilizing a commercially available THz spectrophotometer, the TeraSmart by Menlo Systems. To generate THz radiation with a bandwidth of up to 6 THz (>100 dB), we have employed a 780 nm, Er-doped fiber laser (ELMO by Menlo Systems) characterized by a pulse width of <100 fs and a repetition rate of ~100 MHz. This laser is used to excite a 100 V gated THz emitter antenna (TERA 15-TX-FC), which, in turn, focuses the THz radiation onto the sample with the help of a couple of parabolic metal mirrors. The transmitted THz radiation is then focused on a THz detector antenna (TERA 15-RX-FC), which is gated by the probe laser beam itself. The emitter and the receiver antennas are composed of Fe:InGaAs/InAlAs and low temperature grown LT-

InGaAs/InAlAs, respectively due to their very high electron mobility and low loss. To prevent water vapor absorption, all measurements are conducted in a dry nitrogen atmosphere with a controlled humidity of <10% at 20°C. The samples are mounted on a high-precision rotary mount with a circular hole to allow the THz beam to pass through. The mount can be rotated over 360° angles within the sample-plane. The amplitude and phase of the THz electric field are measured as a function of time by varying the time delay between the probe and the pump beam. To ensure accuracy of our results, each experiment is triplicated.

9.2.3. Comsol simulation

The electric field distribution on this MWG systems is investigated by finite element method (FEM) based simulations using COMSOL Multiphysics 6.0 (radio frequency module) software. In this module, we have considered the incident plane wave to be polarized along the x-axis and travelling along y-axis with a very high normalized electric field amplitude of 10^5 V/m. The light matter interaction of the system is studied by simulating the MWG structures over the entire experimental frequency span of 0.2-2.5 THz. The propagation parameter satisfies the electromagnetic wave equation:

$$\nabla \times \frac{1}{\mu_r}(\nabla \times E) - k_0^2(\varepsilon_r - \frac{j\sigma}{\varepsilon\omega})E = 0 \qquad (9.1)$$

where, μ_r is the permeability (taken to be 1), ε_r is the relative permittivity (taken to be infinite) of the material (gold) and k_0 (equals to $\frac{\omega}{c}$) is the wave number in free space.

9.3. Results and discussion

Figure 9.2(a) illustrates the time-domain THz signal transmitted through the P3 sample and a bare HR-Si substrate, which serves as the reference signal (indicated by the black dotted line). The longitudinal axis of the aligned MWG system was systematically rotated at angles of 0° (parallel), 30°, 60°, and 90° (perpendicular) relative to the polarization axis of the THz electric field. The waveform of the time-domain THz signal exhibits a high degree of similarity to that of the reference signal in the perpendicular orientation (90°), indicating minimal THz absorption in this configuration. On the contrary THz transmission through the sample is found to be strikingly reduced when the polarization is oriented at 0°. Similar observation is apparent from the frequency domain measurements also (Figure 9.2b). This result can be explained taking into consideration that the conduction electrons within the wire-like structures can interact with the THz photons when the polarization is parallel to the

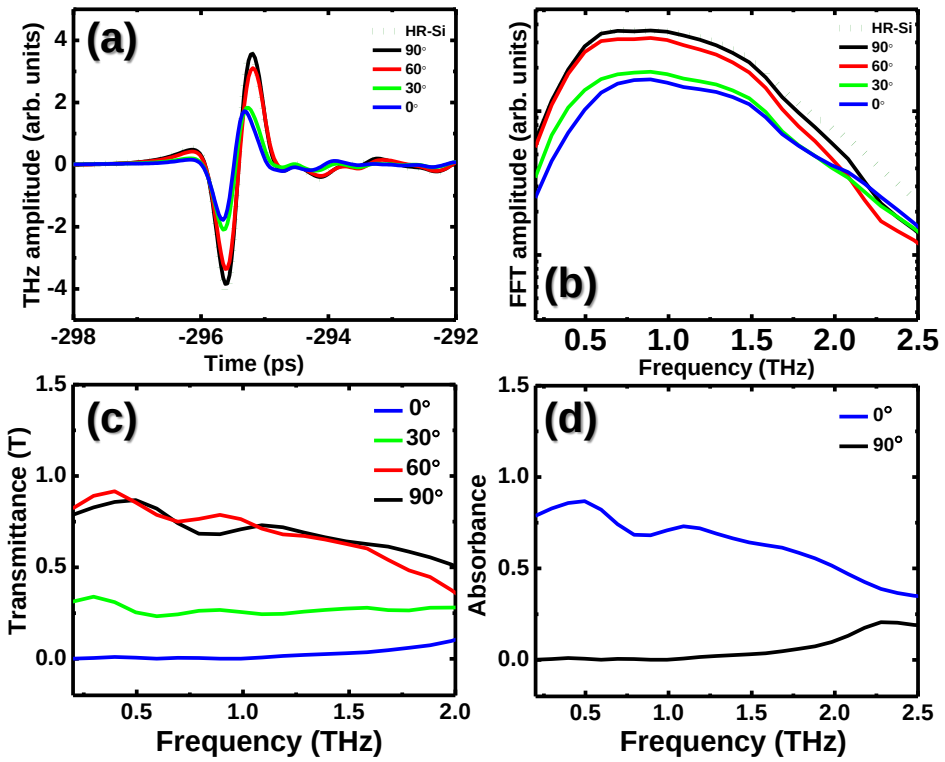

[61]**Figure 9.2.** (a) Time-domain THz electric field amplitude passing through bare HR-Si substrate (reference) and MWG sample having period of 40 μm, i.e., P3, at 0° (parallel), 30°, 60°, and 90° (perpendicular) configurations with respect to the THz pulse. (b) The corresponding FFT amplitude spectra are shown. The obtained transmittance profiles of the sample in all these configurations are shown in (c). Whereas, (d) represents the absorbance profile at 0° and 90° orientation.

symmetry axis of the structure, thereby preventing the passage of the THz radiation through the polarizer, resulting in a minimum transmission. In contrast, since the interaction is minimal in the perpendicular orientation, transmission is maximized. For a quantitative insight into this, we measure the transmittance, $T = \left|\frac{E_S}{E_R}\right|^2$ as a function of frequency for all the orientations (Figure 9.2c). E_S and E_R are the complex THz electric fields of the sample and the reference, respectively. The observed increase in the transmittance with increasing orientation angle is consistent with prior findings[99] and strongly supports our argument. For 0° and 30°, the non-monotonic variation of transmittance is not prominent in this frequency domain. However, the observed consistent variation of transmittance at 60° and 90° is likely due to the imperfections in the MWG structure and/or presence of defect states in the system. The one-dimensional nature of the confined carriers and phonons within a possible minor misaligned MWG structures explains the observed anisotropic transmittance. $A = -\log_{10} T$ represents the corresponding absorbance as shown in Fig. 2(d) at two

different in-plane angles, which also exhibits very high attenuation at 0° angular orientation due to the interaction of THz photons with conduction electrons as discussed earlier.

To further quantify the polarization performance of the system, we estimate the following parameters: degree of polarization (DOP), extinction ratio (ER), linear dichroism (LD) and reduced LD (LD^r). The quantification of DOP serves as a potential tool for comprehending the intricate interplay between spatial orientation and electric field intensity within the THz frequency domain, illuminating the nuanced characteristics embedded within the electric field of a given material. Specifically, it provides a quantitative measure of the extent to which the electric field is oriented in a particular direction by the polarizer material, thereby reflecting the directionality of the polarization. It is defined as the ratio of the difference in the intensities of the electric field between two perpendicular directions to the total intensity of the field, i.e., $DOP = \frac{A_{\parallel}-A_{\perp}}{A_{\parallel}+A_{\perp}}$,[474] where $A_{\parallel}$ is the absorbance for $\theta = 0°$ and $A_{\perp}$ is that for $\theta = 90°$. An ideal polarizer should offer a DOP = 1, manifesting that the electric field of the THz wave is completely oriented in a specific direction. We found that the average DOP value for the sample with period 40 μm (P3) in the frequency range 0.2-2.5 THz is ~81.3% (Figure

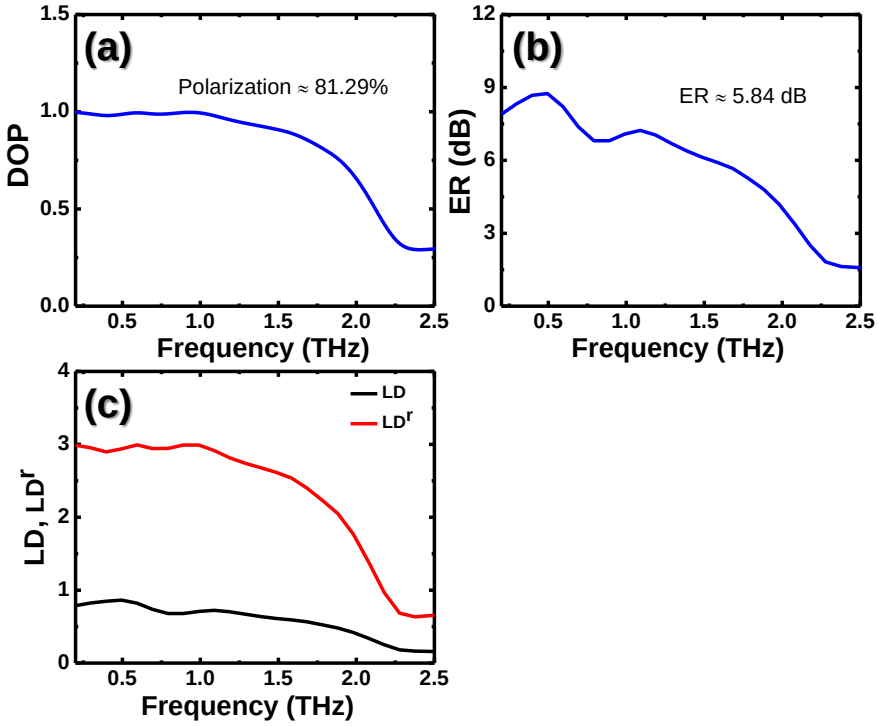

[62]**Figure 9.3.** (a) DOP of the sample as a function of frequency between 0.2-2.5 THz and (b) shows the corresponding ER profile. (c) Linear dichroism (LD) and reduced linear dichroism (LD^r) of the sample as a function of frequency.

9.3a). Interesting to note that while we observe a high DOP value (~90%) between 0.2-2.0 THz, it diminishes substantially beyond 2.0 THz. Such a decrease perhaps results from the concept of wavelength's critical limit to be polarized beyond 2.0 THz (150 μm wavelength) according to which for a good polarizing performance, the period must be approximately three times less than the wavelength of the light to be polarized.[470] We also verify that a 40 μm array period-MWG polarizer works efficiently up to 2.0 THz frequency. It is noteworthy here that single-walled and multi-walled carbon nanotube (SWNT and MWNT) type polarizers sometimes offer a higher DOP;[100,101] however, the mechanical winding process being tricky, such materials are of limited interest. On the other hand, highly aligned Ni nanowire arrays provide better performance as broadband polarizer based on layer number.[475] The other critical parameter for a good polarizer is its ER, which is defined as the ratio of optical powers of perpendicular polarizations, usually called TE (transverse electric) and TM (transverse magnetic), i.e., $ER = -\log_{10}(\frac{T_{max}}{T_{min}})$. As represented in Figure 9.3(b), it shows a plateau in the low frequency range, however, a downward trend is noticed in the region beyond the critical frequency limit. The ER value decreases from ~8 dB at lower frequency regime to ~1.5 dB at 2.5 THz frequency with average ER value to be ~5.8 dB in the entire frequency regime. With increasing frequency, the ability of the polarizer to block or transmit the polarization of THz radiation decreases, resulting in the observed decrease in the ER. Also at higher frequency, the polarizer's capacity to differentiate between distinct polarization states diminishes, leading to this observed effect. Another important parameter LD^r, defined as $LD^r = \frac{LD}{A_0}$, where LD = $(A_{\parallel} - A_{\perp})$ and $A_0 = \frac{(A_{\parallel}+2A_{\perp})}{3}$ [476] measures the difference in the absorption of THz radiation that is polarized parallel and perpendicular to the orientation of the conduction electrons of the system. Reduced LD^r provides a normalized measure of absorbance of the system, which is independent of other external parameters. Figure 9.3(c) shows the variation of LD and LD^r for sample P3, manifesting a decremental trend with increase in frequency. Upon evaluating all the provided parameters, it is evident that the wire grid structures offer an improved THz polarization performance up to 2 THz.

To optimize the polarizing ability of the structures, we check the DOP as a function of frequency for different array periods of a set of samples (Fig. 4(a)). We found that the DOP of the system having 200 μm period (P1) is relatively poor, with an average DOP of ~12.66%, which is not at per for a good THz polarizer over this frequency range. The polarization performance, however, improves significantly as the array period is decreased (Figure 9.4(a)). It can be noted here that although the sample having 20 μm array period (P4) exhibits a very

high DOP value in the frequency range 0.2-2.5 THz, its performance drops significantly beyond 2.0 THz frequency, reaching only ~55% at 2.5 THz. Therefore, P4 is not a suitable polarizer for application beyond 2.0 THz frequency. On the other hand, the MWG structure having 10 μm array period (P5) exhibits consistent performance up to 2.5 THz frequency, making it a perfect candidate as a polarizer over a broad range of frequencies. Our findings demonstrate a significant impact of array period on the DOP performance and the importance of careful selection of the array period to achieve optimal THz polarization performance. In Figure 9.4(b), the variation of ER with respect to frequency is presented for all the samples examined. A consistent trend is observed, where ER value decreases as the frequency

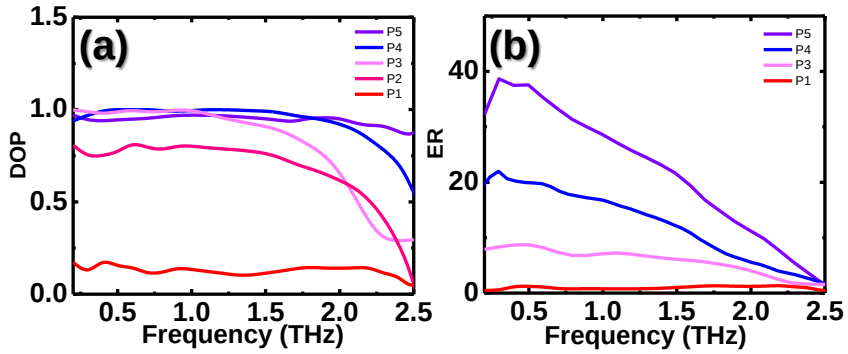

[63]**Figure 9.4.** (a) DOP and (b) corresponding ER profile of the samples having different periods as a function of frequency between 0.2-2.5 THz.

increases across all the samples. Moreover, as the period of the MWG structures decreases, the ER values increase, indicating that the polarization performance of the samples is enhanced with a reduction in the period. These findings suggest that the polarization properties of the samples can be effectively manipulated simply by controlling the period of the MWG structures. We extract the mean values of all the parameters within the frequency range of 0.2-2.5 THz. A comprehensive summary of the results (DOP, ER, and LD^r values of all samples) as a function of the array period is shown in Figure 9.5a-c. We observe a remarkable improvement in the DOP with a reduction in the array period (Figure 9.5a). Specifically, the DOP value displays a substantial rise from ~12.5% at 200 μm to ~ 94.3% at 10 μm period. Correspondingly, the ER value shows a prominent escalation from ~1 dB at 200 μm to ~22.1 dB at 10 μm period. The LD^r value also increases from ~0.27 at 200 μm to ~2.75 at 10 μm period. These results unambiguously proves that the fabricated MWG structures serve as efficient polarizers, where the efficiency can be tuned simply by manipulating the geometrical period of the wire grids.

For a deeper insight into the period dependent polarization performance, we investigate the electric field distribution into the wire grid structures using COMSOL Multiphysics simulation framework (see the experimental section for simulation details). Two such representative distributions for 200 and 20 μm at 1 THz for 0º polarization angle are shown in figures 9.5(d

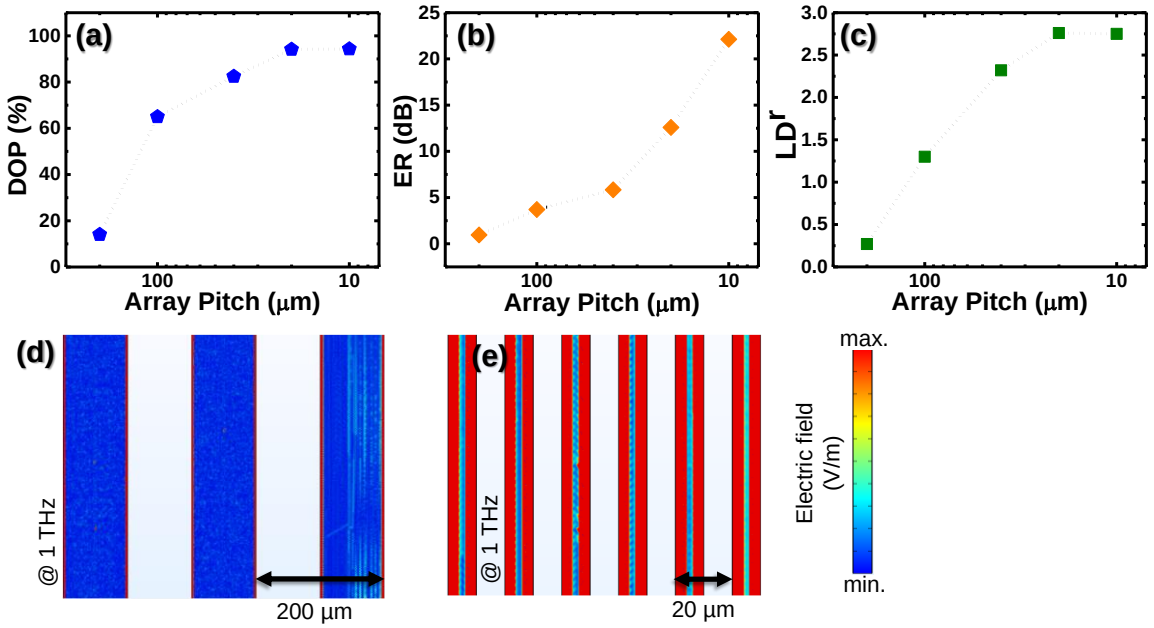

[64]**Figure 9.5.** (a), (b), (c) represent the DOP, ER and LD^r, respectively, as a function of array period. Here, the average values of all parameters are taken from the frequency range between 0.2-2.5 THz. (d), (e) represents the simulated electric field distribution of sample P1 and P4 respectively, for applied electric field along the direction parallel to the length of MWGs. The color map of the electric field distribution is shown on lower right side.

and e). The simulation results show that when the period is 200 μm, the electric field along the direction parallel to the length of MWGs is very small; interestingly, when the period length is decreased to 20 μm the simulation result shows a drastic increase in the electric field distribution. This expansion causes the electric field to be absorbed more deeply into the sample as the array period decreases. The simulation results thus explain the rationale behind the observed period dependent DOP. Gold is known for its excellent plasmonic properties over a wide range of the electromagnetic spectrum. Electromagnetic wave interacting with gold MWG structures induces localized surface plasmon resonances, which actually emantes from the collective oscillations of conduction electrons in response to the incident electromagnetic field. For a larger period of 200 μm the spacing between the adjacent MWGs is large compared to the wavelength of the incident light. As a result, the plasmonic coupling between the neighboring MWGs is rather weak producing a smaller electric field along the direction parallel to the length of the MWGs (Figure 9.5d). As the

period is reduced to 20 μm, the spacing between MWGs becomes comparable to or smaller than the incident light's wavelength and thereby promotes stronger plasmonic coupling between the neighboring MWGs, resulting in an enhanced electric field distribution along the length of the MWGs (Figure 9.5e).

Finally we examine the anti-reflection (AR) performance of the same set of samples at an angle of 90° by analysing the amplitude of the Fabry-Perot (FP) peak.[477] The relative amplitude of the FP peak (the second peak of the multi-reflection pattern, normalized by the FP peak amplitude in HR-Si) is illustrated in Figure 9.6(a). We observe that the normalized FP peak increases as the array period decreases from 200 μm to 10 μm and almost approaches the value obtained for bare HR-Si. In addition to the wire-grids, we also fabricated two additional samples: a square dot and a connected dot structure, for better understanding of the structural dependence of the AR performance of the system. Such fabrication is in line of our intension to study the impact of structural changes on the system's AR performance at a fixed period length (in this case 200 μm). The highlighted portion in Figure 9.6(a) represents

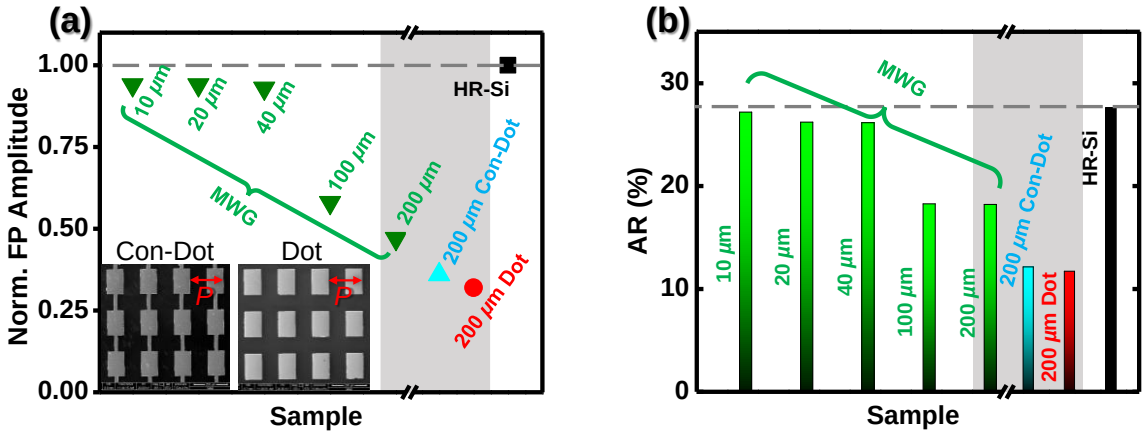

[65]**Figure 9.6**. (a) FP peak amplitude (normalized with the FP peak in HR-Si) for all MWG structures as well as two additional samples, one square-shaped dots and another connected dot structures. The inset shows SEM images of connected and square dot structures having period P = 200 μm. (b) AR, in %, of the FP peak/primary THz peak (AR) for the bare substrate (HR-Si) and for all the samples.

the normalized FP peak variation with the dotted structures. The result demonstrates that the normalized FP peak intensity increases in the order dot structure < connected-dot structure <1D wire-like structure (MWG). We calculate the AR performance (ratio of the amplitude of the FP peak and the main THz peak multiplied by 100) which is a metric to determine the efficiently of the system to restrict reflection from the device (Figure 9.6b). It is evident that decreasing the array period significantly improved the system's AR performance from ~18.2% for 200 μm to ~27.2% for the 10 μm MWG structure. Notably, the performance also improves significantly from the dot structure to the connected-dot

structure and finally to the MWG structure, as shown in the highlighted portion of the Figure. These results provide a comprehensive understanding of the structural dependence of the AR performance of the system, highlighting the potential of MWG structures in enhancing the AR properties of THz devices. Our experimental findings make it unambiguously apparent that MWG with low array period lengths are the most optimum candidates to serve as THz polarizers and ARC materials in the THz frequency range.

9.4. Conclusion

In this study we report the fabrication of aligned metallic wire grid (MWG) structures made up of gold on a high-resistive silicon substrate, which are found to be highly efficient optical polarizer operative in the THz frequency range. These MWG structures are easy to fabricate, highly robust, long-lasting, and require minimal maintenance, which ensure them to becoming a useful and popular THz polarizer. We further demonstrate that the polarizing performance of these devices can systematically be modulated by changing the array period of the MWG structures. In addition, the MWG structures also exhibit excellent performance as anti-reflection coating (ARC) material exhibiting their unique multifunctional character. With such high polarizing efficiency over a wide frequency range and multifunctionality, these MWGs pave a new avenue towards the search for efficient THz opto-electronic components.

Chapter 10

10. Summary and Future Perspective

10.1. Summary

Throughout this thesis, a comprehensive investigation into the quasistatic and dynamic properties of thin films and micro- and nanostructured magnetic and non-magnetic materials has been conducted. The primary objective is to advance the potential of spin-based devices for future applications in information processing and data storage. Specifically, we focused on patterned magnetic structures in the form of magnonic crystals (MCs) with enhanced functionalities and novel heterostructures to gain insights into their fundamental spin-wave (SW) properties, which are crucial for the development of future magnonic circuits. The samples were meticulously prepared using advanced lithography techniques including photo- and electron-beam lithography, along with various ultrahigh vacuum deposition methods such as magnetron sputtering, electron beam evaporation, and pulsed laser deposition. Initial characterizations involved scanning electron microscopy (SEM), X-ray diffraction (XRD), energy dispersive X-ray spectroscopy (EDXS), and micro-Raman spectroscopy. To explore the static magnetic parameters, magneto-optical Kerr effect magnetometry (MOKE) and vibrating sample magnetometry (VSM) were employed. Dynamic magnetization behavior was probed using innovative techniques such as home-built time-resolved magneto-optical Kerr effect (TR-MOKE), a broadband ferromagnetic resonance spectrometer, and THz-time domain spectroscopy. The experimental findings were analyzed to elucidate the underlying physics of the systems using micromagnetic simulations and COMSOL multi-physics software, providing a comprehensive understanding of the observed phenomena.

At first, the reconfigurable nature of SW dynamics in ferromagnetic nanostripe arrays (1D MCs) was thoroughly studied by employing a combined experimental and micromagnetic simulation approach, the study explored how variations in stripe thickness and external magnetic field (both strength and orientation) influence the spectrum of SW modes observed (uniform, localized, and standing waves). The analysis of these variations, including instances of mode-merging phenomenon, was enriched by examining simulated spin configurations, magnetostatic field maps, and SW mode profile analysis. Notably, the simulations revealed the potential to manipulate SW propagation by strategically controlling both the thickness of the nanostripes and the geometry of the external magnetic field. This opens doors for the design of reconfigurable magnonic circuit components, such as waveguides and omni-

directional emitters. These promote the applications of the ferromagnetic nanostripes as omnidirectional SW emitters and reconfigurable magnonic waveguide.

Next, we shifted our focus a bit from magnonics to hybrid magnonics. By strategically selecting a nanoscale magnonic cavity in the form of a ferromagnetic nanocross elements with lateral dimensions down to 300 nm i.e., with a record lowest number of spins $\sim 10^{12}$ (an order of magnitude lower than the lowest number of spins showing hybrid magnonic so far). The strength of this coupling has been effectively tuned by varying the microwave excitation power and the orientation of the external magnetic field. Simulations revealed that both static and dynamic dipolar interactions between the magnetic dipoles (magnons) were responsible for the observed phenomenon. Hence, the magnon-magnon coupling phenomenon is exhibited due to the magnons present within the nanocross structures only. So, the nanocross structure serves as a magnonic cavity and the coupling is boosted by dynamic dipolar interaction in the array. Additionally, the study observed a "mode-softening" effect of SWs that could be controlled by subtle adjustments to the field orientation. These findings hold great promise for enriching various hybrid phenomena utilizing magnons as information carriers, potentially leading to on-chip magnonic devices for quantum information processing and communication.

In our follow-up work, we emphasize our ability to control the intriguing anticrossing phenomenon by systematically varying the nanocross arm length. We achieve this by precisely manipulating the external bias magnetic field strength and employing the broadband ferromagnetic resonance technique. Going beyond observation, we investigate magnon-magnon coupling within the nanocross system, showcasing precise control over the emergence of the anticrossing phenomenon through engineered sample dimensions. This manipulation results in a significant enhancement of coupling strengths, reaching values as high as 0.52 GHz, underscoring the importance of our findings. Our rigorous micromagnetic simulations faithfully replicate the experimental results, providing crucial insights into the evolution of SW dynamics and shedding light on the underlying mechanisms of the anticrossing phenomenon. This work bridges the gap in understanding hybrid quasiparticle interactions and offers a path toward efficient magnon-based technologies.

Next, we have taken the spin-orbit torque route to modulate the SW response of cobalt-based ledge-shaped 2D magnonic crystals. We have been able to measure the dynamics in bias-field-free condition and we were able to achieve a breakthrough in amplifying SWs within cobalt-based nanometer-scale magnets by applying current. By virtue of alternating current spin-

orbit torque (ac-SOT), we have observed a tenfold increase in the amplitude of specific SW modes. This amplification effect was tunable across various frequencies, significantly boosting signal-to-noise ratios. These findings open doors for designing future spintronic devices with efficient information transmission and tailored SW characteristics. The ability to manipulate SWs in this way has potential applications in energy-efficient information processing, exploring non-linear SW dynamics. Overall, the study establishes ac-SOT as a powerful tool for controlling SWs in nanoscale devices, paving the way for a new generation of spintronic technologies.

In our next work, we have investigated spin pumping effects and interfacial spin transparency in the topological insulator (TI), e.g., BST/FM heterostructures using TR-MOKE techniques. High-quality BST thin films, deposited via pulsed laser deposition, exhibit characteristic crystallographic features and bulk insulating behavior, with dominant surface transport below 90 K. By analyzing the Gilbert damping parameter across different BST and CoFeB thicknesses, we identify efficient spin pumping mechanisms. We determine the intrinsic spin-mixing conductance and spin diffusion length in BST, confirming robust spin current injection. Effective spin-mixing conductance and two-magnon scattering contributions to damping modulation are also characterized, with two-magnon scattering increasing at thinner CoFeB layers. Control experiments with a Cu spacer layer between BST and CoFeB show negligible spin memory loss effects, verifying that spin pumping primarily influences damping modulation. The interfacial spin transparency of approximately 0.94 highlights the efficient spin transport at the BST/CoFeB interface. These results demonstrate the potential of BST/CoFeB heterostructures in spintronic applications, emphasizing the importance of high interfacial spin transparency for optimal device performance.

Finally, we have systematically improved the polarization efficiency of metallic wire grid (MWG) polarizers made of gold by simply altering the pitch of the wire grid structures. Our investigation has successfully demonstrated that through a reduction in the pitch of MWG structures, we have achieved a remarkable polarization level of up to 94.3% alongside an extinction ratio approaching 22.1 dB. These notable results position the MWG structures as a fitting candidate for serving as optimal THz polarizers. Nonetheless, this exceptional enhancement in polarization efficiency significantly broadens the application potential of these MWG structures, allowing their utilization across the extensive frequency range of 0.2-2.5 THz. Consequently, these results distinguish themselves from other published findings, setting a new benchmark in the field. Furthermore, we have determined that the prepared MWG structures also exhibit excellent anti-reflection properties, highlighting their versatility

and multifunctionality. The significance of our findings lies in the potential impact they can have on the development of THz polarizers. The durable, long-lasting, and low-maintenance nature of the MWG structures, combined with their exceptional performance characteristics, positions them as strong contenders for THz polarizers in various applications.

10.2. Future Perspective

The comprehensive investigations into spin dynamics, hybrid quasi-particle interactions, and SOT-driven modulation of spin dynamics presented in the aforementioned studies offer promising avenues for future developments in materials science and condensed matter physics. These investigations lay the groundwork for potential future directions, such as the design of reconfigurable devices leveraging 1D magnonic crystals. Simulation-based demonstrations, like the proposed omni-directional emitter and SW waveguide, exemplify the possibilities in this domain. Utilizing low-damping materials like YIG or Heusler alloys could further enhance the efficacy of magnonic devices. Additionally, the creation of ferromagnetic nanocross structures using different materials holds promise as a hybrid quantum device, enabling efficient, coherent, and long-distance information propagation. SOT-driven

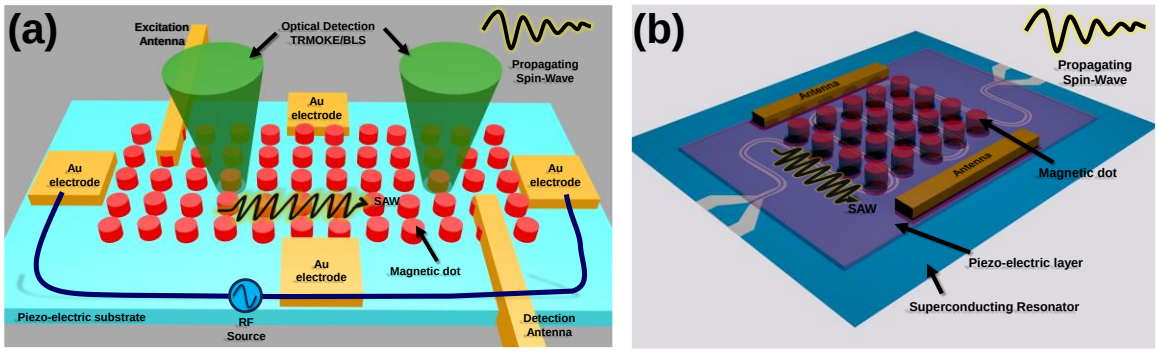

[66]**Figure 10.1.** (a) and (b) Futuristic magnonics devices for multi-quasi particle interactions along with multiple tunable parameters.

magnonics present another groundbreaking opportunity, potentially leading to the development of spin torque nano oscillators with minimal damping. Future studies may delve into various device types to deepen our understanding of these systems, with materials such as CoFeB being of interest due to their low damping characteristics.

In summary, the investigations conducted in these studies offer a promising outlook for advancements in magnonics and spintronics. These findings not only deepen our fundamental understanding of condensed matter physics but also set the stage for innovative technologies with wide-ranging applications in information processing, energy harvesting, and beyond. A proposed device structure, as illustrated in Figure 10.1, has the potential to manipulate multi-quasi-particle hybrid interactions involving magnons, photons, phonons,

and superconducting qubits through the adjustment of multiple external parameters, showcasing the potential for sophisticated control and manipulation in future research endeavors.

Bibliography:

[1] S.K. Kim et al., Ferrimagnetic spintronics, Nat. Mater. 21 (2022) 24–34.

[2] A. V. Chumak et al., Magnon spintronics, Nat. Phys. 11 (2015) 453–461.

[3] A. Hirohata et al., Review on spintronics: Principles and device applications, J. Magn. Magn. Mater. 509 (2020) 166711.

[4] L.A. Benítez et al., Tunable room-temperature spin galvanic and spin Hall effects in van der Waals heterostructures, Nat. Mater. 19 (2020) 170–175.

[5] S. Choudhury et al., Voltage controlled on-demand magnonic nanochannels, Sci. Adv. 6 (2020) eaba5457.

[6] J. VAN KRANENDONK et al., Errata: Spin Waves, Rev. Mod. Phys. 31 (1959) 839–839.

[7] B. Dieny et al., Opportunities and challenges for spintronics in the microelectronics industry, Nat. Electron. 3 (2020) 446–459.

[8] B. Lenk et al., The building blocks of magnonics, Phys. Rep. 507 (2011) 107–136.

[9] D. Grundler, Reconfigurable magnonics heats up, Nat. Phys. 11 (2015) 438–441.

[10] S.A. Wolf et al., Spintronics: A Spin-Based Electronics Vision for the Future, Science (80-.). 294 (2001) 1488–1495.

[11] A. Barman et al., The 2021 Magnonics Roadmap, J. Phys. Condens. Matter. 33 (2021) 413001.

[12] D.D. Awschalom et al., Quantum Spintronics: Engineering and Manipulating Atom-Like Spins in Semiconductors, Science (80-.). 339 (2013) 1174–1179.

[13] Q. Wang et al., Inverse-design magnonic devices, Nat. Commun. 12 (2021) 2636.

[14] M. Romera et al., Vowel recognition with four coupled spin-torque nano-oscillators, Nature. 563 (2018) 230–234.

[15] M. Zahedinejad et al., Two-dimensional mutually synchronized spin Hall nano-oscillator arrays for neuromorphic computing, Nat. Nanotechnol. 15 (2020) 47–52.

[16] M.N. Baibich et al., Giant Magnetoresistance of (001)Fe/(001)Cr Magnetic Superlattices, Phys. Rev. Lett. 61 (1988) 2472–2475.

[17] G. Binasch et al., Enhanced magnetoresistance in layered magnetic structures with antiferromagnetic interlayer exchange, Phys. Rev. B. 39 (1989) 4828–4830.

[18] K. Prachumrasee et al., Crosstalk Suppression in High Data Rate and High Density Hard Disk Drive Interconnects Using Magnetic Composites, Frequenz. 67 (2013) 223–228.

[19] R. Sellmann et al., Growth of thin Co films on W() and Au() layers prepared on Al2O3(), Surf. Sci. 495 (2001) 185–194.

[20] D. Makarov et al., Nanopatterned CoPt alloys with perpendicular magnetic anisotropy, Appl. Phys. Lett. 93 (2008) 153112.

[21] J.-M. Beaujour et al., Anomalous Enhancement of the Magnetic Anisotropy of CoCrPt Alloy Thin Film With Ultrathin Pt Interface, IEEE Trans. Magn. 52 (2016) 1–4.

[22] M. Albrecht et al., Recording performance of high-density patterned perpendicular magnetic media, Appl. Phys. Lett. 81 (2002) 2875–2877.

[23] S. Iwasaki et al., Co-Cr recording films with perpendicular magnetic anisotropy, IEEE Trans. Magn. 14 (1978) 849–851.

[24] H. Yamada et al., A study of perpendicular magnetic recording characteristics with magnetoresistive head, J. Magn. Magn. Mater. 176 (1997) 56–60.

[25] T. June et al., 2007 Index IEEE Transactions on Magnetics, 43 (2007) 4123–4263.

[26] D. Wu et al., Understanding the dense stripe domains in soft magnetic film, Appl. Surf. Sci. 346 (2015) 567–573.

[27] N. Amos et al., Magnetic force microscopy study of magnetic stripe domains in sputter deposited Permalloy thin films, J. Appl. Phys. 103 (2008) 1–4.

[28] A. Moser et al., Magnetic recording: advancing into the future, J. Phys. D. Appl. Phys. 35 (2002) R157–R167.

[29] Z. Liu et al., Systematic Evaluation of Microwave-Assisted Magnetic Recording, IEEE Trans. Magn. 54 (2018) 1–5.

[30] S. Okamoto et al., Microwave assisted magnetic recording technologies and related physics, J. Phys. D. Appl. Phys. 48 (2015) 353001.

[31] S. Tehrani et al., High density submicron magnetoresistive random access memory (invited), J. Appl. Phys. 85 (1999) 5822–5827.

[32] A.J. Princep et al., The full magnon spectrum of yttrium iron garnet, Npj Quantum Mater. 2 (2017) 63.

[33] C. Liu et al., Origin of low Gilbert damping in half metals, Appl. Phys. Lett. 95 (2009) 14–17.

[34] M. Oogane et al., Gilbert magnetic damping constant of epitaxially grown Co-based Heusler alloy thin films, Appl. Phys. Lett. 96 (2010) 1–4.

[35] J.E. Moore, The birth of topological insulators, Nature. 464 (2010) 194–198.

[36] M.Z. Hasan et al., Colloquium : Topological insulators, Rev. Mod. Phys. 82 (2010) 3045–3067.

[37] Y. Ando, Topological Insulator Materials, J. Phys. Soc. Japan. 82 (2013) 102001.

[38] D. Hsieh et al., Observation of Unconventional Quantum Spin Textures in Topological Insulators, Science (80-.). 323 (2009) 919–922.

[39] D. Hsieh et al., Observation of Time-Reversal-Protected Single-Dirac-Cone Topological-Insulator States in Bi2Te3 and Sb2Te3, Phys. Rev. Lett. 103 (2009) 146401.

[40] Y. Wang et al., Topological Surface States Originated Spin-Orbit Torques in Bi2Se3, Phys. Rev. Lett. 114 (2015) 257202.

[41] A. V. Chumak et al., Magnonic crystals for data processing, J. Phys. D. Appl. Phys. 50 (2017) 244001.

[42] Z.K. Wang et al., Nanostructured Magnonic Crystals with Size-Tunable Bandgaps, ACS Nano. 4 (2010) 643–648.

[43] M. Kostylev et al., Partial frequency band gap in one-dimensional magnonic crystals, Appl. Phys. Lett. 92 (2008).

[44] B. RANA et al., MAGNETO-OPTICAL MEASUREMENTS OF COLLECTIVE SPIN DYNAMICS OF TWO-DIMENSIONAL ARRAYS OF FERROMAGNETIC NANOELEMENTS, SPIN. 03 (2013) 1330001.

[45] V. V. Kruglyak et al., Precessional dynamics in microarrays of nanomagnets, J. Appl. Phys. 97 (2005) 1–4.

[46] S. Sahoo et al., Observation of Coherent Spin Waves in a Three-Dimensional Artificial Spin Ice Structure, Nano Lett. 21 (2021) 4629–4635.

[47] S. Sahoo et al., Ultrafast magnetization dynamics in a nanoscale three-dimensional cobalt tetrapod structure, Nanoscale. 10 (2018) 9981–9986.

[48] R. Mandal et al., Effects of antidot shape on the spin wave spectra of two-dimensional Ni80Fe20 antidot lattices, Appl. Phys. Lett. 103 (2013) 262410.

[49] R. Mandal et al., Optically Induced Tunable Magnetization Dynamics in Nanoscale Co Antidot Lattices, ACS Nano. 6 (2012) 3397–3403.

[50] C. Dai et al., Strong coupling between magnons confined in a single magnonic cavity, J. Appl. Phys. 127 (2020) 203902.

[51] A. V. Chumak et al., Advances in Magnetics Roadmap on Spin-Wave Computing, IEEE Trans. Magn. 58 (2022) 1–72.

[52] S.S.P. Parkin et al., Magnetic Domain-Wall Racetrack Memory, Science (80-.). 320 (2008) 190–194.

[53] V. V. Kruglyak et al., Dynamic configurational anisotropy in nanomagnets, Phys. Rev. B. 75 (2007) 024407.

[54] R. Dreyer et al., Spin-wave localization and guiding by magnon band structure engineering in yttrium iron garnet, Phys. Rev. Mater. 5 (2021) 064411.

[55] C. Banerjee et al., Pseudo-One-Dimensional Magnonic Crystals for High-Frequency Nanoscale Devices, Phys. Rev. Appl. 8 (2017) 014036.

[56] G. Gubbiotti et al., Spin wave dispersion and intensity correlation in width-modulated nanowire arrays: A Brillouin light scattering study, J. Appl. Phys. 124 (2018) 083903.

[57] Z.K. Wang et al., Observation of frequency band gaps in a one-dimensional nanostructured magnonic crystal, Appl. Phys. Lett. 94 (2009) 1–4.

[58] B. Heinz et al., Propagation of Spin-Wave Packets in Individual Nanosized Yttrium Iron Garnet Magnonic Conduits, Nano Lett. 20 (2020) 4220–4227.

[59] A. Kumar et al., Spin transfer torque ferromagnetic resonance induced spin pumping in the Fe/Pd bilayer system, Phys. Rev. B. 95 (2017) 064406.

[60] J. Sinova et al., Spin Hall effects, Rev. Mod. Phys. 87 (2015) 1213–1260.

[61] Y. Li et al., Hybrid magnonics: Physics, circuits, and applications for coherent information processing, J. Appl. Phys. 128 (2020).

[62] H.Y. Yuan et al., Quantum magnonics: When magnon spintronics meets quantum information science, Phys. Rep. 965 (2022) 1–74.

[63] Y. Tabuchi et al., Coherent coupling between a ferromagnetic magnon and a superconducting qubit, Science (80-.). 349 (2015) 405–408.

[64] B. Zare Rameshti et al., Cavity magnonics, Phys. Rep. 979 (2022) 1–61.

[65] J.T. Hou et al., Strong Coupling between Microwave Photons and Nanomagnet Magnons, Phys. Rev. Lett. 123 (2019) 107702.

[66] Y. Tabuchi et al., Hybridizing Ferromagnetic Magnons and Microwave Photons in the

Quantum Limit, Phys. Rev. Lett. 113 (2014) 083603.

[67] X. Zhang et al., Strongly Coupled Magnons and Cavity Microwave Photons, Phys. Rev. Lett. 113 (2014) 156401.

[68] Y. Li et al., Coherent Coupling of Two Remote Magnonic Resonators Mediated by Superconducting Circuits, Phys. Rev. Lett. 128 (2022) 047701.

[69] D.I. Schuster et al., High-Cooperativity Coupling of Electron-Spin Ensembles to Superconducting Cavities, Phys. Rev. Lett. 105 (2010) 140501.

[70] Y. Makhlin et al., Quantum-state engineering with Josephson-junction devices, Rev. Mod. Phys. 73 (2001) 357–400.

[71] J.M. Martinis et al., Rabi Oscillations in a Large Josephson-Junction Qubit, Phys. Rev. Lett. 89 (2002) 117901.

[72] D. MacNeill et al., Gigahertz Frequency Antiferromagnetic Resonance and Strong Magnon-Magnon Coupling in the Layered Crystal CrCl3, Phys. Rev. Lett. 123 (2019) 047204.

[73] C. Dai et al., Strong magnon–magnon coupling in synthetic antiferromagnets, Appl. Phys. Lett. 118 (2021) 1–7.

[74] T. Makihara et al., Ultrastrong magnon–magnon coupling dominated by antiresonant interactions, Nat. Commun. 12 (2021) 3115.

[75] H.Y. Yuan et al., Enhancement of magnon-magnon entanglement inside a cavity, Phys. Rev. B. 101 (2020) 014419.

[76] L. Liensberger et al., Exchange-Enhanced Ultrastrong Magnon-Magnon Coupling in a Compensated Ferrimagnet, Phys. Rev. Lett. 123 (2019) 117204.

[77] Q. Zhang et al., Distant Magnon-Magnon Coupling Mediated by Nonresonant Photon, Symmetry (Basel). 15 (2023) 518.

[78] X. Chen et al., Manipulation of Time- and Frequency-Domain Dynamics by Magnon-Magnon Coupling in Synthetic Antiferromagnets, Magnetochemistry. 8 (2021) 7.

[79] A. Sud et al., Tunable magnon-magnon coupling in synthetic antiferromagnets, Phys. Rev. B. 102 (2020) 100403.

[80] L. Trifunovic et al., Long-Distance Entanglement of Spin Qubits via Ferromagnet, Phys. Rev. X. 3 (2013) 041023.

[81] F. Heussner et al., Frequency-Division Multiplexing in Magnonic Logic Networks Based on Caustic-Like Spin-Wave Beams, Phys. Status Solidi – Rapid Res. Lett. 12 (2018) 1–6.

[82] H.J. Kimble, The quantum internet, Nature. 453 (2008) 1023–1030.

[83] C.L. Degen et al., Quantum sensing, Rev. Mod. Phys. 89 (2017) 035002.

[84] J. Ryu et al., Current-Induced Spin–Orbit Torques for Spintronic Applications, Adv. Mater. 32 (2020) 1907148.

[85] A. Soumyanarayanan et al., Emergent phenomena induced by spin–orbit coupling at surfaces and interfaces, Nature. 539 (2016) 509–517.

[86] B. Divinskiy et al., Excitation and Amplification of Spin Waves by Spin–Orbit Torque, Adv. Mater. 30 (2018) 1–6.

[87] J.C.R. Sánchez et al., Spin-to-charge conversion using Rashba coupling at the interface between non-magnetic materials, Nat. Commun. 4 (2013) 2944.

[88] G.P. Williams, Filling the THz gap—high power sources and applications, Reports Prog. Phys. 69 (2006) 301–326.

[89] J. Neu et al., Tutorial: An introduction to terahertz time domain spectroscopy (THz-TDS), J. Appl. Phys. 124 (2018) 231101.

[90] E.P.J. Parrott et al., Terahertz spectroscopy: Its future role in medical diagnoses, J. Mol. Struct. 1006 (2011) 66–76.

[91] J. Ma et al., Security and eavesdropping in terahertz wireless links, Nature. 563 (2018) 89–93.

[92] J.D.B. Bradley et al., Erbium-doped integrated waveguide amplifiers and lasers, Laser Photon. Rev. 5 (2011) 368–403.

[93] H. Park et al., Accurate photoconductive antenna characterization using a thin film polarizer, Appl. Phys. Lett. 101 (2012).

[94] S. Li et al., Super terahertz phase shifter achieving high transmission and large modulation depth, Opt. Lett. 45 (2020) 2834.

[95] O. Paul et al., Highly selective terahertz bandpass filters based on trapped mode excitation, Opt. Express. 17 (2009) 18590.

[96] B.R. Sangala et al., Single and multiband THz metamaterial polarisers, Pramana. 94 (2020) 2.

[97] H. Wong et al., Active meta polarizer for terahertz frequencies, Sci. Rep. 10 (2020) 15382.

[98] F. Yan et al., Advances in Polarizer Technology for Terahertz Frequency Applications, J. Infrared, Millimeter, Terahertz Waves. 34 (2013) 489–499.

[99] D. Polley et al., Polarizing effect of aligned nanoparticles in terahertz frequency region, Opt. Lett. 38 (2013) 2754.

[100] J. Kyoung et al., A Reel-Wound Carbon Nanotube Polarizer for Terahertz Frequencies, Nano Lett. 11 (2011) 4227–4231.

[101] L. Ren et al., Carbon Nanotube Terahertz Polarizer, Nano Lett. 9 (2009) 2610–2613.

[102] I. Yamada et al., Terahertz wire-grid polarizers with micrometer-pitch Al gratings, Opt. Lett. 34 (2009) 274.

[103] N.K. Grady et al., Terahertz Metamaterials for Linear Polarization Conversion and Anomalous Refraction, Science (80-.). 340 (2013) 1304–1307.

[104] W.A. Challener et al., Grid polarizers for infrared fourier spectrometers, Infrared Phys. 20 (1980) 215–222.

[105] G. Li et al., Terahertz Polarizers Based on 2D Ti3C2Tz MXene: Spin Cast from Aqueous Suspensions, Adv. Photonics Res. 1 (2020) 2000084.

[106] T. Nagashima et al., Measurement of complex optical constants of a highly doped Si wafer using terahertz ellipsometry, Appl. Phys. Lett. 79 (2001) 3917–3919.

[107] T. Hofmann et al., Variable-wavelength frequency-domain terahertz ellipsometry, Rev. Sci. Instrum. 81 (2010).

[108] A.E. Costley et al., Free-standing fine-wire grids: Their manufacture, performance, and use at millimeter and submillimeter wavelengths, J. Opt. Soc. Am. 67 (1977) 979.

[109] P.K. Pal et al., Optimizing the polarization and antireflection characteristics of metallic wire

grid structures in the Terahertz frequency range, Opt. Mater. (Amst). 146 (2023) 114553.

[110] P.K. Pal et al., Thickness-Dependent Reconfigurable Spin-Wave Dynamics in Ni80Fe20 Nanostripe Arrays, Adv. Mater. Interfaces. 9 (2022) 2201333.

[111] P.K. Pal et al., Bias-Field Tunable Magnon-Magnon Coupling in Ni80Fe20 Nanocross Array, Adv. Quantum Technol. 6 (2023) 2300003.

[112] P. Kumar Pal et al., Control of magnon-magnon coupling in Ni80Fe20 nanocross arrays through system dimensions, J. Magn. Magn. Mater. 588 (2023) 171431.

[113] A. Barman et al., Magnetization dynamics of nanoscale magnetic materials: A perspective, J. Appl. Phys. 128 (2020) 170901.

[114] D. Aurélio et al., Understanding Magnetization Dynamics of a Magnetic Nanoparticle with a Disordered Shell Using Micromagnetic Simulations, Nanomaterials. 10 (2020) 1149.

[115] A. Aharoni, Introduction to the Theory of Ferromagnetism (International Series of Monographs on Physics), Oxford University Press, 1996.

[116] P. Yu et al., Curie temperatures of fcc and bcc nickel and permalloy: Supercell and Green's function methods, Phys. Rev. B. 77 (2008) 054431.

[117] G. Dumpich et al., Structural and magnetic properties of NixFe1-x evaporated thin films, J. Magn. Magn. Mater. 67 (1987) 55–64.

[118] K.-M. Lee et al., Temperature dependence of the interfacial magnetic anisotropy in W/CoFeB/MgO, AIP Adv. 7 (2017) 1–8.

[119] J.A. Betancourt-Cantera et al., Magnetic properties and crystal structure of elemental cobalt powder modified by high-energy ball milling, J. Mater. Res. Technol. 8 (2019) 4995–5003.

[120] L. LANDAU et al., On the theory of the dispersion of magnetic permeability in ferromagnetic bodies, in: Perspect. Theor. Phys., Elsevier, 1992: pp. 51–65.

[121] T.L. Gilbert, Classics in Magnetics A Phenomenological Theory of Damping in Ferromagnetic Materials, IEEE Trans. Magn. 40 (2004) 3443–3449.

[122] J.K. Galt, Motion of a Ferromagnetic Domain Wall in Fe3O4, Phys. Rev. 85 (1952) 664–669.

[123] A. V. Khvalkovskiy et al., High Domain Wall Velocities due to Spin Currents Perpendicular to the Plane, Phys. Rev. Lett. 102 (2009) 067206.

[124] R. Medapalli et al., Multiscale dynamics of helicity-dependent all-optical magnetization reversal in ferromagnetic Co/Pt multilayers, Phys. Rev. B. 96 (2017) 224421.

[125] P.P.J. Haazen et al., Domain wall depinning governed by the spin Hall effect, Nat. Mater. 12 (2013) 299–303.

[126] T.A. Moore et al., High domain wall velocities induced by current in ultrathin Pt/Co/AlOx wires with perpendicular magnetic anisotropy, Appl. Phys. Lett. 93 (2008) 262504.

[127] D. Kumar et al., Domain wall memory: Physics, materials, and devices, Phys. Rep. 958 (2022) 1–35.

[128] C. Kittel, On the Theory of Ferromagnetic Resonance Absorption, Phys. Rev. 73 (1948) 155–161.

[129] E.Y. Tsymbal et al., Spin-dependent tunnelling in magnetic tunnel junctions, J. Phys. Condens. Matter. 15 (2003) R109–R142.

[130] X.H. Xiang et al., Recent developments in magnetic tunnel junctions, IEEE Trans. Magn. 39

(2003) 2770–2775.

[131] N. Maciel et al., Magnetic Tunnel Junction Applications, Sensors. 20 (2019) 121.

[132] D.E. Heim et al., Design and operation of spin valve sensors, IEEE Trans. Magn. 30 (1994) 316–321.

[133] M. Jamali et al., Spin wave nonreciprocity for logic device applications, Sci. Rep. 3 (2013) 3160.

[134] M.P. Kostylev et al., Spin-wave logical gates, Appl. Phys. Lett. 87 (2005) 1–3.

[135] B.A. Kalinikos et al., Theory of dipole-exchange spin wave spectrum for ferromagnetic films with mixed exchange boundary conditions, J. Phys. C Solid State Phys. 19 (1986) 7013–7033.

[136] J.S. Harms et al., Theory of the dipole-exchange spin wave spectrum in ferromagnetic films with in-plane magnetization revisited, J. Magn. Magn. Mater. 557 (2022) 169426.

[137] Y. Jin et al., Excitation and modulation of exchange spin waves in CoFeB films, Appl. Phys. Lett. 123 (2023).

[138] B. Rana et al., Excitation of coherent propagating spin waves in ultrathin CoFeB film by voltage-controlled magnetic anisotropy, Appl. Phys. Lett. 111 (2017).

[139] Q. Wang et al., Voltage-controlled nanoscale reconfigurable magnonic crystal, Phys. Rev. B. 95 (2017) 134433.

[140] T. Nozaki et al., Magnetization switching assisted by high-frequency-voltage-induced ferromagnetic resonance, Appl. Phys. Express. 7 (2014) 073002.

[141] B. Rana et al., Voltage-Controlled Reconfigurable Spin-Wave Nanochannels and Logic Devices, Phys. Rev. Appl. 9 (2018) 014033.

[142] A.G. Gurevich et al., Magnetization Oscillations and Waves, CRC Press, 2020.

[143] D.D. Stancil, Theory of Magnetostatic Waves, Springer New York, New York, NY, 1993.

[144] D.D. Stancil et al., Spin Waves: Theory and Applications, Springer US, Boston, MA, 2009.

[145] D.J.L. Michael G. Cottam, Light Scattering in Magnetic Solids, Wiley-Interscience, 1986.

[146] R.W. Damon et al., Magnetostatic modes of a ferromagnet slab, J. Phys. Chem. Solids. 19 (1961) 308–320.

[147] V.E. Demidov et al., Excitation of microwaveguide modes by a stripe antenna, Appl. Phys. Lett. 95 (2009) 10–13.

[148] K. Ounadjela et al., Spin Dynamics in Confined Magnetic Structures II, Springer Berlin Heidelberg, 2003.

[149] B. Hillebrands et al., Spin Dynamics in Confined Magnetic Structures I, Springer, 2002.

[150] B. Rana et al., Detection of Picosecond Magnetization Dynamics of 50 nm Magnetic Dots down to the Single Dot Regime, ACS Nano. 5 (2011) 9559–9565.

[151] B. Rana et al., Anisotropy in collective precessional dynamics in arrays of Ni80Fe20 nanoelements, J. Appl. Phys. 111 (2012) 1–4.

[152] B. Rana et al., All-Optical Excitation and Detection of Picosecond Dynamics of Ordered Arrays of Nanomagnets with Varying Areal Density, Appl. Phys. Express. 4 (2011) 113003.

[153] S. Sahoo et al., Nanochannels for spin-wave manipulation in Ni80Fe20 nanodot arrays, J. Magn. Magn. Mater. 522 (2021) 167550.

[154] A.K. Mondal et al., Spin-texture driven reconfigurable magnonics in chains of connected Ni80Fe20 submicron dots, Phys. Rev. B. 101 (2020) 224426.

[155] R. Mandal et al., Tunable spin wave spectra in two-dimensional Ni80Fe20 antidot lattices with varying lattice symmetry, J. Appl. Phys. 118 (2015) 053910.

[156] K. Dutta et al., Dynamic configurational anisotropy in Ni80Fe20 antidot lattice with complex geometry, J. Alloys Compd. 884 (2021) 161105.

[157] S. Mallick et al., Tunability of Domain Structure and Magnonic Spectra in Antidot Arrays of Heusler Alloy, Phys. Rev. Appl. 12 (2019) 014043.

[158] C. Banerjee et al., Width dependent transition of quantized spin-wave modes in Ni80Fe20 square nanorings, J. Appl. Phys. 116 (2014) 163912.

[159] K. Adhikari et al., Observation of magnon–magnon coupling with high cooperativity in Ni80Fe20 cross-shaped nanoring array, Nanotechnology. 32 (2021) 395706.

[160] S. Choudhury et al., Anisotropic spin waves in two-dimensional triangular shaped bi-component magnonic crystal, J. Magn. Magn. Mater. 490 (2019) 165484.

[161] S. Choudhury et al., Shape- and Interface-Induced Control of Spin Dynamics of Two-Dimensional Bicomponent Magnonic Crystals, ACS Appl. Mater. Interfaces. 8 (2016) 18339–18346.

[162] C. Kumar et al., Spin-wave mode reversal and anisotropy in bicomponent magnonic crystals, Phys. Rev. B. 109 (2024) 075407.

[163] B.K. Mahato et al., Tunable configurational anisotropy in collective magnetization dynamics of Ni80Fe20 nanodot arrays with varying dot shapes, J. Appl. Phys. 117 (2015) 213909.

[164] B.K. Mahato et al., Tunable spin wave dynamics in two-dimensional Ni80Fe20 nanodot lattices by varying dot shape, Appl. Phys. Lett. 105 (2014) 012406.

[165] S. Choudhury et al., Efficient Modulation of Spin Waves in Two-Dimensional Octagonal Magnonic Crystal, ACS Nano. 11 (2017) 8814–8821.

[166] S. Choudhury et al., Active Control of Mode Crossover and Mode Hopping of Spin Waves in a Ferromagnetic Antidot Lattice, Phys. Rev. Appl. 10 (2018) 064044.

[167] S. Choudhury et al., Controlled evolution of spin waves in unconventional defective honeycomb antidot lattices, J. Magn. Magn. Mater. 489 (2019) 165408.

[168] S. Mondal et al., Influence of anisotropic dipolar interaction on the spin dynamics of Ni 80 Fe 20 nanodot arrays arranged in honeycomb and octagonal lattices, J. Magn. Magn. Mater. 458 (2018) 95–104.

[169] S. Mondal et al., Transition from strongly collective to completely isolated ultrafast magnetization dynamics in two-dimensional hexagonal arrays of nanodots with varying inter-dot separation, RSC Adv. 6 (2016) 110393–110399.

[170] K. Adhikari et al., Tunable Angle-Dependent Magnetization Dynamics in Ni80Fe20 Nanocross Structures of Varying Size, Phys. Rev. Appl. 10 (2018) 044010.

[171] A. Barman et al., Dynamic dephasing of magnetization precession in arrays of thin magnetic elements, Phys. Rev. B. 79 (2009) 144415.

[172] A. Barman et al., Spin Dynamics and Damping in Ferromagnetic Thin Films and Nanostructures, Springer International Publishing, Cham, 2018.

[173] V. Kamberský, On ferromagnetic resonance damping in metals, Czechoslov. J. Phys. 26 (1976) 1366–1383.

[174] B. Heinrich et al., FMR linebroadening in metals due to two-magnon scattering, J. Appl. Phys. 57 (1985) 3690–3692.

[175] J. Lindner et al., Non-Gilbert-type damping of the magnetic relaxation in ultrathin ferromagnets: Importance of magnon-magnon scattering, Phys. Rev. B. 68 (2003) 060102.

[176] S. Manipatruni et al., Material Targets for Scaling All-Spin Logic, Phys. Rev. Appl. 5 (2016) 014002.

[177] W. Yu et al., Magnetic Logic Gate Based on Polarized Spin Waves, Phys. Rev. Appl. 13 (2020) 024055.

[178] B. Rakesh et al., Magnetic Thin Films used for Memory Devices: A Scientometric Analysis, J. Scientometr. Res. 11 (2022) 235–245.

[179] S. Stricker, The Hall Effect and its Applications, in: Adv. Electron. Electron Phys., 1968: pp. 97–143.

[180] G. Vignale, Ten Years of Spin Hall Effect, J. Supercond. Nov. Magn. 23 (2010) 3–10.

[181] L. Berger, Side-Jump Mechanism for the Hall Effect of Ferromagnets, Phys. Rev. B. 2 (1970) 4559–4566.

[182] D. Bhowmik et al., Spin Hall effect clocking of nanomagnetic logic without a magnetic field, Nat. Nanotechnol. 9 (2014) 59–63.

[183] S.O. Valenzuela et al., Direct electronic measurement of the spin Hall effect, Nature. 442 (2006) 176–179.

[184] J. Kim et al., Spin-Hall effect MRAM based cache memory: A feasibility study, in: 2015 73rd Annu. Device Res. Conf., IEEE, 2015: pp. 117–118.

[185] T. Giamarchi et al., Theory of spin-anisotropic electron-electron interactions in quasi-one-dimensional metals, J. Phys. 49 (1988) 819–835.

[186] L. Berger, Emission of spin waves by a magnetic multilayer traversed by a current, Phys. Rev. B. 54 (1996) 9353–9358.

[187] Y. Tserkovnyak et al., Spin pumping and magnetization dynamics in metallic multilayers, Phys. Rev. B. 66 (2002) 224403.

[188] Y. Tserkovnyak et al., Nonlocal magnetization dynamics in ferromagnetic heterostructures, Rev. Mod. Phys. 77 (2005) 1375–1421.

[189] C. Song et al., Spin-orbit torques: Materials, mechanisms, performances, and potential applications, Prog. Mater. Sci. 118 (2021) 100761.

[190] X.-Y. Feng et al., A review of current research on spin currents and spin–orbit torques*, Chinese Phys. B. 28 (2019) 107105.

[191] D.C. Ralph et al., Spin transfer torques, J. Magn. Magn. Mater. 320 (2008) 1190–1216.

[192] T. Kawahara et al., Spin-transfer torque RAM technology: Review and prospect, Microelectron. Reliab. 52 (2012) 613–627.

[193] D. Go et al., Intrinsic Spin and Orbital Hall Effects from Orbital Texture, Phys. Rev. Lett. 121

(2018) 086602.

[194] T. Tanaka et al., Intrinsic spin Hall effect and orbital Hall effect in 4d and 5d transition metals, Phys. Rev. B. 77 (2008) 165117.

[195] Y. Zhuo et al., Mechanism of field-like torque in spin-orbit torque switching of perpendicular magnetic tunnel junction, Sci. China Physics, Mech. Astron. 65 (2022) 107511.

[196] Z. Wang et al., Modulation of field-like spin orbit torque in heavy metal/ferromagnet heterostructures, Nanoscale. 12 (2020) 15246–15251.

[197] L.J. Zhu et al., Irrelevance of magnetic proximity effect to spin-orbit torques in heavy-metal/ferromagnet bilayers, Phys. Rev. B. 98 (2018) 134406.

[198] J. Kim et al., Layer thickness dependence of the current-induced effective field vector in Ta|CoFeB|MgO, Nat. Mater. 12 (2013) 240–245.

[199] K. Garello et al., Symmetry and magnitude of spin–orbit torques in ferromagnetic heterostructures, Nat. Nanotechnol. 8 (2013) 587–593.

[200] C.-F. Pai et al., Dependence of the efficiency of spin Hall torque on the transparency of Pt/ferromagnetic layer interfaces, Phys. Rev. B. 92 (2015) 064426.

[201] R. Saha et al., Comparative analysis of STT and SOT based MRAMs for last level caches, J. Magn. Magn. Mater. 551 (2022) 169161.

[202] H. Wu et al., Magnetic memory driven by topological insulators, Nat. Commun. 12 (2021) 6251.

[203] J. Yang et al., Neuromorphic Engineering: From Biological to Spike-Based Hardware Nervous Systems, Adv. Mater. 32 (2020) 2003610.

[204] Y. Zhang et al., Ring-shaped Racetrack memory based on spin orbit torque driven chiral domain wall motions, Sci. Rep. 6 (2016) 35062.

[205] A. Shukla et al., Spin-Torque-Driven Terahertz Auto-Oscillations in Noncollinear Coplanar Antiferromagnets, Phys. Rev. Appl. 17 (2022) 034037.

[206] Z.Q. Qiu et al., Surface magneto-optic Kerr effect, Rev. Sci. Instrum. 71 (2000) 1243–1255.

[207] Z.. Qiu et al., Surface magneto-optic Kerr effect (SMOKE), J. Magn. Magn. Mater. 200 (1999) 664–678.

[208] P. Bruno et al., Magneto-optical Kerr effect in a paramagnetic overlayer on a ferromagnetic substrate: A spin-polarized quantum size effect, Phys. Rev. B. 53 (1996) 9214–9220.

[209] R. Kubo, A GENERAL EXPRESSION FOR THE CONDUCTIVITY TENSOR, Can. J. Phys. 34 (1956) 1274–1277.

[210] M. Freiser, A survey of magnetooptic effects, IEEE Trans. Magn. 4 (1968) 152–161.

[211] C.-Y. You et al., Generalized analytic formulae for magneto-optical Kerr effects, J. Appl. Phys. 84 (1998) 541–546.

[212] P.N. Argyres, Theory of the Faraday and Kerr Effects in Ferromagnetics, Phys. Rev. 97 (1955) 334–345.

[213] R.P. Hunt, Magneto-Optic Scattering from Thin Solid Films, J. Appl. Phys. 38 (1967) 1652–1671.

[214] D. Weller et al., Orientation dependence of the polar Kerr effect in fcc and hcp Co, Phys.

Rev. Lett. 72 (1994) 2097–2100.

[215] E. Beaurepaire et al., Ultrafast Spin Dynamics in Ferromagnetic Nickel, Phys. Rev. Lett. 76 (1996) 4250–4253.

[216] V.I. Belotelov et al., Extraordinary transmission and giant magneto-optical transverse Kerr effect in plasmonic nanostructured films, J. Opt. Soc. Am. B. 26 (2009) 1594.

[217] The Basics of Microlithography, (n.d.). https://www.lithoguru.com/scientist/lithobasics.html.

[218] C. Vieu et al., Electron beam lithography: resolution limits and applications, Appl. Surf. Sci. 164 (2000) 111–117.

[219] Y. Chen, Nanofabrication by electron beam lithography and its applications: A review, Microelectron. Eng. 135 (2015) 57–72.

[220] P.M. Winter et al., Photolithography, in: B. Bhushan (Ed.), Encycl. Nanotechnol., Springer Netherlands, Dordrecht, 2012: pp. 2051–2060.

[221] M.S. Oh et al., Development of Photolithography Process for Printed Circuit Board Using Liquid Crystal Mask in Place of Photomask, Jpn. J. Appl. Phys. 51 (2012) 09MF16.

[222] A. Pimpin et al., Review on Micro- and Nanolithography Techniques and their Applications, Eng. J. 16 (2012) 37–56.

[223] J.E. Mahan, Physical vapor deposition of thin films, John Wiley & Sons, Inc., 2000.

[224] E. Marenkov et al., Angular and velocity distributions of tungsten sputtered by low energy argon ions, J. Nucl. Mater. 496 (2017) 18–23.

[225] T. Schenkel et al., Electronic Sputtering of Thin Conductors by Neutralization of Slow Highly Charged Ions, 1 (1997) 2481–2484.

[226] K. Strijckmans et al., Modeling target erosion during reactive sputtering, Appl. Surf. Sci. 331 (2015) 185–192.

[227] Y. Ohtsu et al., Plasma characteristics and target erosion profile of racetrack-shaped RF magnetron plasma with weak rubber magnets for full circular target utilization, Surf. Coatings Technol. 307 (2016) 1134–1138.

[228] R.A. Scholl, Power systems for reactive sputtering of insulating films, Surf. Coatings Technol. 93 (1997) 7–13.

[229] J. Sinha et al., Enhanced interface perpendicular magnetic anisotropy in Ta|CoFeB|MgO using nitrogen doped Ta underlayers, Appl. Phys. Lett. 102 (2013).

[230] A.K. Chaurasiya et al., Dependence of Interfacial Dzyaloshinskii-Moriya Interaction on Layer Thicknesses in Ta/Co-Fe-B/TaOx Heterostructures from Brillouin Light Scattering, Phys. Rev. Appl. 9 (2018) 014008.

[231] M.W. Pyun et al., Oblique angle deposition of TiO2 thin films prepared by electron-beam evaporation, Appl. Surf. Sci. 257 (2010) 1149–1153.

[232] K. Masood et al., Emission characteristics of the thermionic electron beam sources developed at EBSDL, Nucl. Instruments Methods Phys. Res. Sect. A Accel. Spectrometers, Detect. Assoc. Equip. 584 (2008) 9–24.

[233] O.C. Olawole et al., Progress in the experimental and computational methods of work function evaluation of materials: A review, Heliyon. 8 (2022) e11030.

[234] Z.X. Yang et al., Novel nanostructures of β-Ga2O3 synthesized by thermal evaporation, Phys. E Low-Dimensional Syst. Nanostructures. 30 (2005) 93–95.

[235] M.J. Aziz, Film growth mechanisms in pulsed laser deposition, Appl. Phys. A. 93 (2008) 579–587.

[236] A. Pandey et al., Pulsed laser deposition of highly c-axis oriented thin films of BSTS topological insulator, ArXiv. (2019) 1–11.

[237] S. Roy et al., Photothermal Control of Helicity-Dependent Current in Epitaxial Sb2Te2Se Topological Insulator Thin-Films at Ambient Temperature, ACS Appl. Mater. Interfaces. 14 (2022) 9909–9916.

[238] S. Choudhury, Investigation and Control of Gigahertz Frequency Spin Wave Dynamics in Magnonic Crystals, 2019.

[239] D. Porschke, Time-Resolved Analysis of Macromolecular Structures During Reactions by Stopped-Flow Electrooptics, Biophys. J. 75 (1998) 528–537.

[240] S.J. George et al., Time-Resolved Binding of Carbon Monoxide to Nitrogenase Monitored by Stopped-Flow Infrared Spectroscopy, J. Am. Chem. Soc. 119 (1997) 6450–6451.

[241] C.J. Shields et al., Photochemistry of aryl azides: detection and characterization of a dehydroazepine by time-resolved infrared spectroscopy and flash photolysis at room temperature, J. Am. Chem. Soc. 109 (1987) 4723–4726.

[242] M.C. Fischer et al., Invited Review Article: Pump-probe microscopy, Rev. Sci. Instrum. 87 (2016) 031101.

[243] A. Schmidt et al., An optical pump-probe technique for measuring the thermal conductivity of liquids, Rev. Sci. Instrum. 79 (2008) 064902.

[244] S. Yoshida et al., Probing ultrafast spin dynamics with optical pump–probe scanning tunnelling microscopy, Nat. Nanotechnol. 9 (2014) 588–593.

[245] H.A. Haus, Mode-locking of lasers, IEEE J. Sel. Top. Quantum Electron. 6 (2000) 1173–1185.

[246] M.J. Ablowitz et al., Pulse dynamics and solitons in mode-locked lasers, Phys. Rev. A. 78 (2008) 011802.

[247] J.N. Kutz, Mode-Locked Soliton Lasers, SIAM Rev. 48 (2006) 629–678.

[248] J. Kim et al., All-fiber acousto-optic modulator based on a cladding-etched optical fiber for active mode-locking, Photonics Res. 5 (2017) 391.

[249] R. Liu et al., Composite acousto-optical modulation, Opt. Express. 30 (2022) 27780.

[250] J.J. Degnan, Optimization of passively Q-switched lasers, IEEE J. Quantum Electron. 31 (1995) 1890–1901.

[251] Y. Wang et al., Actively Q-switched fiber lasers: Switching dynamics and nonlinear processes, Prog. Quantum Electron. 31 (2007) 131–216.

[252] wikipedia, Streak camera, (n.d.). https://en.wikipedia.org/wiki/Streak_camera.

[253] T. Moriyama et al., Ferromagnetic resonance measurement using stroboscopic magneto-optical Kerr effect, J. Appl. Phys. 117 (2015) 213908.

[254] K.M. Aamir et al., On Cooley-Tukey FFT method for zero padded signals, in: Proc. IEEE Symp. Emerg. Technol. 2005., IEEE, 2005: pp. 41–45.

[255] wikipedia, Window function, (n.d.).

[256] B. Lojek, Reflectivity of the silicon semiconductor substrate and its dependence on the doping concentration and intensity of the irradiation, in: 11th IEEE Int. Conf. Adv. Therm. Process. Semicond. RTP 2003, IEEE, 2003: pp. 215–220.

[257] T.-M. Winkel et al., An Accurate Determination of the Characteristic Impedance Matrix of Coupled Symmetrical Lines on Chips Baser on High Frequency S-Parameter Measurements, in: 49th ARFTG Conf. Dig., IEEE, 1997: pp. 223–226.

[258] V.P. Denysenkov et al., Broadband ferromagnetic resonance spectrometer, Rev. Sci. Instrum. 74 (2003) 3400–3405.

[259] S. Tamaru et al., Vector network analyzer ferromagnetic resonance spectrometer with field differential detection, Rev. Sci. Instrum. 89 (2018) 053901.

[260] I. Neudecker et al., Comparison of frequency, field, and time domain ferromagnetic resonance methods, J. Magn. Magn. Mater. 307 (2006) 148–156.

[261] E. Montoya et al., Broadband ferromagnetic resonance system and methods for ultrathin magnetic films, J. Magn. Magn. Mater. 356 (2014) 12–20.

[262] C.P. Wen, Coplanar Waveguide: A Surface Strip Transmission Line Suitable for Nonreciprocal Gyromagnetic Device Applications, IEEE Trans. Microw. Theory Tech. 17 (1969) 1087–1090.

[263] C. Gonzalez-Fuentes et al., Systematic errors in the determination of the spectroscopic g-factor in broadband ferromagnetic resonance spectroscopy: A proposed solution, J. Appl. Phys. 123 (2018).

[264] C. Grech et al., Error characterization and calibration of real-time magnetic field measurement systems, Nucl. Instruments Methods Phys. Res. Sect. A Accel. Spectrometers, Detect. Assoc. Equip. 990 (2021) 164979.

[265] L.F. Tiemeijer et al., Comparison of the “pad-open-short” and “open-short-load” deembedding techniques for accurate on-wafer RF characterization of high-quality passives, IEEE Trans. Microw. Theory Tech. 53 (2005) 723–729.

[266] J.A. Jargon et al., Robust SOLT and alternative calibrations for four-sampler vector network analyzers, IEEE Trans. Microw. Theory Tech. 47 (1999) 2008–2013.

[267] L.A. Hayden et al., Calibration methods for time domain network analysis, IEEE Trans. Microw. Theory Tech. 41 (1993) 415–420.

[268] W.L. Chan et al., Imaging with terahertz radiation, Reports Prog. Phys. 70 (2007) 1325–1379.

[269] B. Ferguson et al., Materials for terahertz science and technology, Nat. Mater. 1 (2002) 26–33.

[270] T. Wogan, Filling the terahertz gap, Phys. World. 32 (2019) 6–6.

[271] S. Kono et al., Detection of up to 20 THz with a low-temperature-grown GaAs photoconductive antenna gated with 15 fs light pulses, Appl. Phys. Lett. 77 (2000) 4104–4106.

[272] S. Matsuura et al., Generation of coherent terahertz radiation by photomixing in dipole photoconductive antennas, Appl. Phys. Lett. 70 (1997) 559–561.

[273] User Manual TeraSmart, in: Data Base, MenloSystems, 2012: pp. 1–148.

[274] T. Schrefl, Finite elements in numerical micromagnetics, J. Magn. Magn. Mater. 207 (1999)

45–65.

[275] M.J. Donahue et al., OOMMF user's guide, version 1.0, in: Oommf User's Guid. Version 1.0, Interag. Rep. NISTIR 6376, NIST, 1999.

[276] LLG Micromagnetics Simulator, (n.d.). http://llgmicro.home.mindspring.com.

[277] MicroMagus, (n.d.). http://www.micromagus.de/home.html.

[278] A. Vansteenkiste et al., MuMax: A new high-performance micromagnetic simulation tool, J. Magn. Magn. Mater. 323 (2011) 2585–2591.

[279] Boris, (n.d.). http://www.boris-spintronics.uk/.

[280] T. Fischbacher et al., A Systematic Approach to Multiphysics Extensions of Finite-Element-Based Micromagnetic Simulations: Nmag, IEEE Trans. Magn. 43 (2007) 2896–2898.

[281] C. Lee et al., Micromagnetic study of magnetization reversal in patterned DyFeCo thin films, Phys. Status Solidi. 204 (2007) 4049–4052.

[282] C. Abert et al., Numerical methods for the stray-field calculation: A comparison of recently developed algorithms, J. Magn. Magn. Mater. 326 (2013) 176–185.

[283] A. Kakay et al., Speedup of FEM Micromagnetic Simulations With Graphical Processing Units, IEEE Trans. Magn. 46 (2010) 2303–2306.

[284] J. Wang et al., Magnetic domain wall engineering in a nanoscale permalloy junction, Appl. Phys. Lett. 111 (2017) 072401.

[285] D. Kumar et al., Numerical calculation of spin wave dispersions in magnetic nanostructures, J. Phys. D. Appl. Phys. 45 (2012) 015001.

[286] G. Venkat et al., Proposal for a Standard Micromagnetic Problem: Spin Wave Dispersion in a Magnonic Waveguide, IEEE Trans. Magn. 49 (2013) 524–529.

[287] R. Skomski, Nanomagnetics, J. Phys. Condens. Matter. 15 (2003) R841–R896.

[288] M. Krawczyk et al., Review and prospects of magnonic crystals and devices with reprogrammable band structure, J. Phys. Condens. Matter. 26 (2014) 123202.

[289] C.M. Lieber et al., Understanding and Manipulating Inorganic Materials with Scanning Probe Microscopes, Angew. Chemie (International Ed. English). 35 (1996) 687–704.

[290] C.M. Lieber et al., Scanning Tunneling Microscopy Studies of Low-Dimensional Materials: Probing the Effects of Chemical Substitution at the Atomic Level, Acc. Chem. Res. 24 (1991) 170–177.

[291] V.F. Puntes et al., Colloidal nanocrystal shape and size control: The case of cobalt, Science (80-.). 291 (2001) 2115–2117.

[292] Y. Zhen et al., Carbon nanotube intramolecular junctions, Nature. 402 (1999) 273–276.

[293] M. Franchin et al., Current driven dynamics of domain walls constrained in ferromagnetic nanopillars, Phys. Rev. B - Condens. Matter Mater. Phys. 78 (2008) 054447.

[294] J.D. Holmes et al., Control of thickness and orientation of solution-grown silicon nanowires, Science (80-.). 287 (2000) 1471–1473.

[295] Z.K. Wang et al., Spin-Wave Quantization in Ferromagnetic Nickel Nanowires, Phys. Rev. Lett. 89 (2002) 027201.

[296] M.P. Kostylev et al., Collective magnetostatic modes on a one-dimensional array of

ferromagnetic stripes, Phys. Rev. B - Condens. Matter Mater. Phys. 69 (2004) 064408.

[297] S. Saha et al., All-optical investigation of tunable picosecond magnetization dynamics in ferromagnetic nanostripes with a width down to 50 nm, Nanoscale. 7 (2015) 18312–18319.

[298] T. Pradeep, Nano: The Essentials, Understanding Nanoscience and Nanotechnology, Tata McGraw-Hill Publishing Company Limited, 2007.

[299] P.M. Yarbrough et al., Parallel pumping of a ferromagnetic nanostripe : Confinement quantization and off-resonant driving, J. Appl. Phys. 123 (2018) 043904-1-043904–10.

[300] A. Barman et al., Magnetization dynamics of nanoscale magnetic materials: A perspective, J. Appl. Phys. 128 (2020) 170901.

[301] S.A. Nikitov et al., Spin waves in periodic magnetic structures—magnonic crystals, J. Magn. Magn. Mater. 236 (2001) 320–330.

[302] R. Arias et al., Magnetostatic modes in ferromagnetic nanowires. II. A method for cross sections with very large aspect ratio, Phys. Rev. B - Condens. Matter Mater. Phys. 72 (2005) 104418.

[303] G. Gubbiotti et al., Spin wave dispersion and intensity correlation in width-modulated nanowire arrays: A Brillouin light scattering study, J. Appl. Phys. 124 (2018) 083903.

[304] Z.K. Wang et al., Observation of frequency band gaps in a one-dimensional nanostructured magnonic crystal, Appl. Phys. Lett. 94 (2009) 083112.

[305] Q. Wang et al., Spin Pinning and Spin-Wave Dispersion in Nanoscopic Ferromagnetic Waveguides, Phys. Rev. Lett. 122 (2019) 247202.

[306] B. Heinz et al., Propagation of Spin-Wave Packets in Individual Nanosized Yttrium Iron Garnet Magnonic Conduits, Nano Lett. 20 (2020) 4220–4227.

[307] C. Mathieu et al., Lateral quantization of spin waves in micron size magnetic wires, Phys. Rev. Lett. 81 (1998) 3968–3971.

[308] J.P. Park et al., Spatially Resolved Dynamics of Localized Spin-Wave Modes in Ferromagnetic Wires, Phys. Rev. Lett. 89 (2002) 277201.

[309] C. Bayer et al., Spin-wave excitations in finite rectangular elements of Ni80Fe20, Phys. Rev. B - Condens. Matter Mater. Phys. 72 (2005) 064427.

[310] C. Schoeppner et al., Angular dependent ferromagnetic resonance analysis in a single micron sized cobalt stripe, J. Appl. Phys. 116 (2014) 033913.

[311] V.E. Demidov et al., Mode interference and periodic self-focusing of spin waves in permalloy microstripes, Phys. Rev. B - Condens. Matter Mater. Phys. 77 (2008) 064406.

[312] K.S. Lee et al., Physical origin and generic control of magnonic band gaps of dipole-exchange spin waves in width-modulated nanostrip waveguides, Phys. Rev. Lett. 102 (2009) 127202.

[313] Z.K. Wang et al., Nanostructured magnonic crystals with size-tunable bandgaps, ACS Nano. 4 (2010) 643–648.

[314] B. Obry et al., A micro-structured ion-implanted magnonic crystal, Appl. Phys. Lett. 102 (2013) 202403.

[315] L. Bai et al., Observation of spin wave modes depending on a tunable periodic magnetic field, Appl. Phys. Lett. 98 (2011) 172508.

[316] C. Banerjee et al., Pseudo-One-Dimensional Magnonic Crystals for High-Frequency Nanoscale Devices, Phys. Rev. Appl. 8 (2017) 014036.

[317] A. Adhikari et al., Anisotropic spin-wave propagation in asymmetric width modulated $Ni_{80}Fe_{20}$ nanostripes, Mater. Sci. Eng. B Solid-State Mater. Adv. Technol. 272 (2021) 115385.

[318] K. Zakeri, Magnonic crystals: Towards terahertz frequencies, J. Phys. Condens. Matter. 32 (2020) 363001.

[319] V.E. Demidov et al., Transformation of propagating spin-wave modes in microscopic waveguides with variable width, Phys. Rev. B - Condens. Matter Mater. Phys. 79 (2009) 054417.

[320] V.E. Demidov et al., Nano-optics with spin waves at microwave frequencies, Appl. Phys. Lett. 92 (2008) 232503.

[321] V.E. Demidov et al., Nonlinear propagation of spin waves in microscopic magnetic stripes, Phys. Rev. Lett. 102 (2009) 177207.

[322] S. Choi et al., Strong radiation of spin waves by core reversal of a magnetic vortex and their wave behaviors in magnetic nanowire waveguides, Phys. Rev. Lett. 98 (2007) 087205.

[323] S. Zhang et al., High-sensitivity ferromagnetic resonance measurements on micrometer-sized samples, Appl. Phys. Lett. 70 (1997) 2756–2758.

[324] S.S.P. Parkin et al., Magnetic domain-wall racetrack memory, Science (80-.). 320 (2008) 190–194.

[325] S. Tehrani et al., High density submicron magnetoresistive random access memory (invited), J. Appl. Phys. 85 (1999) 5822–5827.

[326] X. Zhu et al., Spatially resolved observation of domain-wall propagation in a submicron ferromagnetic NOT-gate, Appl. Phys. Lett. 87 (2005) 062503.

[327] W.C. Uhlig et al., Direct imaging of current-driven domain walls in ferromagnetic nanostripes, J. Appl. Phys. 105 (2009) 103902.

[328] C. Jin et al., Control of morphology and formation of highly geometrically confined magnetic skyrmions, Nat. Commun. 8 (2017) 15569.

[329] Z. Hou et al., Creation of Single Chain of Nanoscale Skyrmion Bubbles with Record-High Temperature Stability in a Geometrically Confined Nanostripe, Nano Lett. 18 (2018) 1274–1279.

[330] K.H.J. Buschow, Handbook of Magnetic Materials, 2009.

[331] J. Fassbender et al., Structural and magnetic modifications of Cr-implanted Permalloy, Phys. Rev. B. 73 (2006) 184410.

[332] T. Roth et al., Temperature dependence of laser-induced demagnetization in Ni: A key for identifying the underlying mechanism, Phys. Rev. X. 2 (2012) 1–7.

[333] Y.P. Ivanov et al., Magnetic configurations of Co(111) nanostripes with competing shape and crystalline anisotropies, Phys. Rev. B - Condens. Matter Mater. Phys. 87 (2013) 184410.

[334] R.C. O'handley, Modern Magnetic Materials, A Wiley-lnterscience Publication, 2000.

[335] P. Bruno, Dipolar magnetic surface anisotropy in ferromagnetic thin films with interfacial roughness, J. Appl. Phys. 64 (1988) 3153–3156.

[336] C.A.F. Vaz et al., Roughness-induced variation of magnetic anisotropy in ultrathin epitaxial films: The undulating limit, Phys. Rev. B. 75 (2007) 132402.

[337] S. Sahoo et al., Nanochannels for spin-wave manipulation in Ni80Fe20 nanodot arrays, J. Magn. Magn. Mater. 522 (2021) 167550.

[338] S. Saha et al., Time-domain study of spin-wave dynamics in two-dimensional arrays of bi-component magnetic structures, Appl. Phys. Lett. 102 (2013) 242409.

[339] J.A. Osborn, Demagnetizing Factors of the General Ellipsoid, Phys. Rev. 67 (1945) 351–357.

[340] LLG micromagnetics simulator, (2003). http://llgmicro.home.mindspring.com.

[341] A. Barman et al., The 2021 Magnonics Roadmap, J. Phys. Condens. Matter. 33 (2021) 413001.

[342] Y. Li et al., Hybrid magnonics: Physics, circuits, and applications for coherent information processing, J. Appl. Phys. 128 (2020) 130902.

[343] G. Kurizki et al., Quantum technologies with hybrid systems, Proc. Natl. Acad. Sci. 112 (2015) 3866–3873.

[344] Y. Kubo et al., Strong Coupling of a Spin Ensemble to a Superconducting Resonator, Phys. Rev. Lett. 105 (2010) 140502.

[345] R.H. Dicke, Coherence in Spontaneous Radiation Processes, Phys. Rev. 93 (1954) 99–110.

[346] N. Kostylev et al., Superstrong coupling of a microwave cavity to yttrium iron garnet magnons, Appl. Phys. Lett. 108 (2016) 062402.

[347] N.J. Lambert et al., Identification of spin wave modes in yttrium iron garnet strongly coupled to a co-axial cavity, J. Appl. Phys. 117 (2015) 053910.

[348] D. Zhang et al., Cavity quantum electrodynamics with ferromagnetic magnons in a small yttrium-iron-garnet sphere, Npj Quantum Inf. 1 (2015) 15014.

[349] M. Goryachev et al., High-Cooperativity Cavity QED with Magnons at Microwave Frequencies, Phys. Rev. Appl. 2 (2014) 054002.

[350] X. Zhang et al., Magnon dark modes and gradient memory, Nat. Commun. 6 (2015) 8914.

[351] Y.-P. Wang et al., Dissipative couplings in cavity magnonics, J. Appl. Phys. 127 (2020) 130901.

[352] C. Dai et al., Strong magnon–magnon coupling in synthetic antiferromagnets, Appl. Phys. Lett. 118 (2021) 112405.

[353] Y. Shiota et al., Tunable Magnon-Magnon Coupling Mediated by Dynamic Dipolar Interaction in Synthetic Antiferromagnets, Phys. Rev. Lett. 125 (2020) 017203.

[354] J. Chen et al., Strong Interlayer Magnon-Magnon Coupling in Magnetic Metal-Insulator Hybrid Nanostructures, Phys. Rev. Lett. 120 (2018) 217202.

[355] S. Klingler et al., Spin-Torque Excitation of Perpendicular Standing Spin Waves in Coupled YIG/Co Heterostructures, Phys. Rev. Lett. 120 (2018) 127201.

[356] Y. Li et al., Coherent Spin Pumping in a Strongly Coupled Magnon-Magnon Hybrid System, Phys. Rev. Lett. 124 (2020) 117202.

[357] A. Barman et al., Magnetization dynamics of nanoscale magnetic materials: A perspective, J. Appl. Phys. 128 (2020) 170901.

[358] K. Adhikari et al., Large nonlinear ferromagnetic resonance shift and strong magnon-magnon coupling in Ni80Fe20, Phys. Rev. B. 101 (2020) 054406.

[359] K. Adhikari et al., Observation of magnon-magnon coupling with high cooperativity in Ni80Fe20 cross-shaped nanoring array, Nanotechnology. 32 (2021) 395706.

[360] C. Dai et al., Strong coupling between magnons confined in a single magnonic cavity, J. Appl. Phys. 127 (2020) 203902.

[361] K. Machida et al., Magnetic structure of cross-shaped permalloy arrays embedded in silicon wafers, J. Magn. Magn. Mater. 290–291 (2005) 779–782.

[362] K. Nanayakkara et al., Spin wave scattering and interference in ferromagnetic cross, J. Appl. Phys. 118 (2015) 163904.

[363] K. Machida et al., Magnetic structure of cross-shaped permalloy arrays embedded in silicon wafers, J. Magn. Magn. Mater. 290–291 (2005) 779–782.

[364] B.K. Mahato et al., Configurational anisotropic spin waves in cross-shaped Ni80Fe20 nanoelements, Appl. Phys. Lett. 102 (2013) 192402.

[365] K. Adhikari et al., Bias field tunable magnetic configuration and magnetization dynamics in Ni80Fe20 nano-cross structures with varying arm length, J. Appl. Phys. 121 (2017) 043909.

[366] M. Donahue et al., OOMMF User's Guide, Version 1.0, NIST Interagency Report No. 6376, National Institute of Standard and Technology, Gaithersburg, MD, National Institute of Standard and Technology, Gaithersburg, MD, 1999. http://math.nist.gov/oommf.

[367] A. Barman et al., Dynamic dephasing of magnetization precession in arrays of thin magnetic elements, Phys. Rev. B - Condens. Matter Mater. Phys. 79 (2009) 144415.

[368] F. Ma et al., Skyrmion-Based Dynamic Magnonic Crystal, Nano Lett. 15 (2015) 4029–4036.

[369] F. Montoncello et al., Soft spin waves and magnetization reversal in elliptical Permalloy nanodots: Experiments and dynamical matrix results, Phys. Rev. B. 76 (2007) 024426.

[370] G. Zhang et al., Shape-tuned dynamic properties of magnetic nanoelements during magnetization reversal, J. Magn. Magn. Mater. 385 (2015) 402–406.

[371] S.-K. Kim et al., A gigahertz-range spin-wave filter composed of width-modulated nanostrip magnonic-crystal waveguides, Appl. Phys. Lett. 95 (2009) 082507-1–3.

[372] A. V. Chumak et al., Magnon transistor for all-magnon data processing, Nat. Commun. 5 (2014) 4700.

[373] D. Kumar et al., Magnetic Vortex Based Transistor Operations, Sci. Rep. 4 (2014) 4108.

[374] A. Kozhevnikov et al., Pattern recognition with magnonic holographic memory device, Appl. Phys. Lett. 106 (2015).

[375] Y. Li et al., Hybrid magnonics: Physics, circuits, and applications for coherent information processing, J. Appl. Phys. 128 (2020) 130902.

[376] H. Maier-Flaig et al., Tunable magnon-photon coupling in a compensating ferrimagnet—from weak to strong coupling, Appl. Phys. Lett. 110 (2017).

[377] L. Bai et al., Control of the Magnon–Photon Coupling, IEEE Trans. Magn. 52 (2016) 1–7.

[378] K. Shen et al., Laser-Induced Spatiotemporal Dynamics of Magnetic Films, Phys. Rev. Lett. 115 (2015) 197201.

[379] D.A. Bozhko et al., Bottleneck Accumulation of Hybrid Magnetoelastic Bosons, Phys. Rev. Lett. 118 (2017) 237201.

[380] A.T. Costa et al., Strongly Coupled Magnon–Plasmon Polaritons in Graphene-Two-Dimensional Ferromagnet Heterostructures, Nano Lett. 23 (2023) 4510–4515.

[381] S. Pal et al., Acousto-Plasmo-Magnonics: Coupling Spin Waves with Hybridized Phonon-Plasmon Waves in a 2D Artificial Magnonic Crystal Deposited on a Plasmonic Material, Adv. Funct. Mater. (2023).

[382] S. Freeman et al., Exciton-Magnon Interaction in Magnetic Insulators, Phys. Rev. Lett. 21 (1968) 910–913.

[383] A. Gloppe et al., Magnon-exciton proximity coupling at a van der Waals heterointerface, Phys. Rev. B. 105 (2022) L121403.

[384] Y. Li et al., Strong Coupling between Magnons and Microwave Photons in On-Chip Ferromagnet-Superconductor Thin-Film Devices, Phys. Rev. Lett. 123 (2019) 107701.

[385] R.J. Elliott et al., The effects of magnon-magnon interaction on the two-magnon spectra of antiferromagnets, J. Phys. C Solid State Phys. 2 (1969) 312.

[386] C. Dai et al., Strong magnon–magnon coupling in synthetic antiferromagnets, Appl. Phys. Lett. 118 (2021) 112405.

[387] A. Kumar Mondal et al., Bias field orientation driven reconfigurable magnonics and magnon–magnon coupling in triangular shaped Ni80Fe20 nanodot arrays, Nanotechnology. 34 (2023) 135701.

[388] S. Majumder et al., Tunable Strong Magnon-Magnon Coupling in Two- Dimensional Array of Diamond Shaped Ferromagnetic Nanodots, Arxiv. (2023).

[389] F. Mazzola et al., Tuneable electron–magnon coupling of ferromagnetic surface states in PdCoO2, Npj Quantum Mater. 7 (2022) 20.

[390] S. Memarzadeh et al., Effect of magnon-magnon interaction on ferromagnetism in hexagonal manganese pnictide monolayers, Phys. Rev. B. 107 (2023) 144409.

[391] W. He et al., Anisotropic Magnon–Magnon Coupling in Synthetic Antiferromagnets, Chinese Phys. Lett. 38 (2021) 057502.

[392] T. Jungwirth et al., Antiferromagnetic spintronics, Nat. Nanotechnol. 11 (2016) 231–241.

[393] Y. Xiong et al., Probing magnon–magnon coupling in exchange coupled Y3Fe5O12/Permalloy bilayers with magneto-optical effects, Sci. Rep. 10 (2020) 12548.

[394] V. Giovannetti et al., Advances in quantum metrology, Nat. Photonics. 5 (2011) 222–229.

[395] V. Giovannetti et al., Quantum-Enhanced Measurements: Beating the Standard Quantum Limit, Science (80-.). 306 (2004) 1330–1336.

[396] S.D. Bader et al., Spintronics, Annu. Rev. Condens. Matter Phys. 1 (2010) 71–88.

[397] A. Manchon et al., Theory of spin torque due to spin-orbit coupling, Phys. Rev. B. 79 (2009) 094422.

[398] R. Mondal et al., Unified theory of magnetization dynamics with relativistic and nonrelativistic spin torques, Phys. Rev. B. 98 (2018) 214429.

[399] S. Saha et al., Tunable Magnonic Spectra in Two-Dimensional Magnonic Crystals with Variable Lattice Symmetry, Adv. Funct. Mater. 23 (2013) 2378–2386.

[400] A. V. Chumak et al., Scattering of backward spin waves in a one-dimensional magnonic crystal, Appl. Phys. Lett. 93 (2008).

[401] V V Kruglyak et al., Magnonics, J. Phys. D. Appl. Phys. 43 (2010) 260301.

[402] A.A. Serga et al., YIG magnonics, J. Phys. D. Appl. Phys. 43 (2010) 264002.

[403] M. Krawczyk et al., Review and prospects of magnonic crystals and devices with reprogrammable band structure, J. Phys. Condens. Matter. 26 (2014) 123202.

[404] M. Endo et al., Current induced effective magnetic field and magnetization reversal in uniaxial anisotropy (Ga,Mn)As, Appl. Phys. Lett. 97 (2010) 222501.

[405] A. Chernyshov et al., Evidence for reversible control of magnetization in a ferromagnetic material by means of spin–orbit magnetic field, Nat. Phys. 5 (2009) 656–659.

[406] X. Wang et al., Spin-orbit-coupled transport and spin torque in a ferromagnetic heterostructure, Phys. Rev. B. 89 (2014) 054405.

[407] D. Go et al., Theory of current-induced angular momentum transfer dynamics in spin-orbit coupled systems, Phys. Rev. Res. 2 (2020) 033401.

[408] X. Qiu et al., Spin–orbit-torque engineering via oxygen manipulation, Nat. Nanotechnol. 10 (2015) 333–338.

[409] M. Baumgartner et al., Spatially and time-resolved magnetization dynamics driven by spin–orbit torques, Nat. Nanotechnol. 12 (2017) 980–986.

[410] Y. Wang et al., Time-resolved detection of spin–orbit torque switching of magnetization and exchange bias, Nat. Electron. 5 (2022) 840–848.

[411] V.E. Demidov et al., Magnetization oscillations and waves driven by pure spin currents, Phys. Rep. 673 (2017) 1–31.

[412] Y. Kajiwara et al., Transmission of electrical signals by spin-wave interconversion in a magnetic insulator, Nature. 464 (2010) 262–266.

[413] K. Ando et al., Electric Manipulation of Spin Relaxation Using the Spin Hall Effect, Phys. Rev. Lett. 101 (2008) 036601.

[414] M. Evelt et al., High-efficiency control of spin-wave propagation in ultra-thin yttrium iron garnet by the spin-orbit torque, Appl. Phys. Lett. 108 (2016).

[415] H. Zhang et al., Large enhancement of spin–orbit torques under a MHz modulation due to phonon–magnon coupling, Appl. Phys. Lett. 123 (2023) 252402.

[416] V.A. Bautin et al., Magnetic properties of polycrystalline cobalt nanoparticles, AIP Adv. 7 (2017).

[417] A. Haldar et al., Reconfigurable and self-biased magnonic metamaterials, J. Appl. Phys. 128 (2020).

[418] A. De et al., Resonant amplification of intrinsic magnon modes and generation of new extrinsic modes in a two-dimensional array of interacting multiferroic nanomagnets by surface acoustic waves, Nanoscale. 13 (2021) 10016–10023.

[419] D. Meng et al., Field-Free Spin-Orbit Torque Driven Perpendicular Magnetization Switching of Ferrimagnetic Layer Based on Noncollinear Antiferromagnetic Spin Source, Adv. Electron. Mater. (2023) 2300665.

[420] Q. Shao et al., Roadmap of Spin–Orbit Torques, IEEE Trans. Magn. 57 (2021) 1–39.

[421] T. Jungwirth et al., Spin Hall effect devices, Nat. Mater. 11 (2012) 382–390.

[422] C. Zhou et al., Broadband Terahertz Generation via the Interface Inverse Rashba-Edelstein Effect, Phys. Rev. Lett. 121 (2018) 086801.

[423] T.S. Ghiasi et al., Charge-to-Spin Conversion by the Rashba–Edelstein Effect in Two-Dimensional van der Waals Heterostructures up to Room Temperature, Nano Lett. 19 (2019) 5959–5966.

[424] Y. Xia et al., Observation of a large-gap topological-insulator class with a single Dirac cone on the surface, Nat. Phys. 5 (2009) 398–402.

[425] Y.L. Chen et al., Experimental Realization of a Three-Dimensional Topological Insulator, Bi 2 Te 3, Science (80-.). 325 (2009) 178–181.

[426] U. Mukhopadhyay et al., Surface optical and bulk acoustic phonons in the topological insulator, Bi2Se2Te, Appl. Phys. Lett. 106 (2015) 0–4.

[427] H. Zhang et al., Topological insulators in Bi2Se3, Bi2Te3 and Sb2Te3 with a single Dirac cone on the surface, Nat. Phys. 5 (2009) 438–442.

[428] T. Arakane et al., Tunable Dirac cone in the topological insulator Bi2-xSbxTe3-ySey, Nat. Commun. 3 (2012) 636.

[429] A. Banerjee et al., Granular topological insulators, Nanoscale. 9 (2017) 6755–6764.

[430] H.B. Zhang et al., Weak localization bulk state in a topological insulator Bi2Te3 film, Phys. Rev. B. 86 (2012) 075102.

[431] H.B. Zhang et al., Experimental evidence of the nanoscaled topological metallic surface state of Bi 2 Te 3 and Sb 2 Te 3 films, EPL (Europhysics Lett. 95 (2011) 56002.

[432] R.K. Gopal et al., Topological delocalization and tuning of surface channel separation in Bi2Se2Te Topological Insulator Thin films, Sci. Rep. 7 (2017) 4924.

[433] J.D. Yao et al., Polarization dependent photocurrent in the Bi2Te3 topological insulator film for multifunctional photodetection, Sci. Rep. 5 (2015) 14184.

[434] Y. Tserkovnyak et al., Enhanced Gilbert Damping in Thin Ferromagnetic Films, Phys. Rev. Lett. 88 (2002) 117601.

[435] L. Liu et al., Spin-polarized tunneling study of spin-momentum locking in topological insulators, Phys. Rev. B. 91 (2015) 235437.

[436] M. Jamali et al., Giant Spin Pumping and Inverse Spin Hall Effect in the Presence of Surface and Bulk Spin−Orbit Coupling of Topological Insulator Bi 2 Se 3, Nano Lett. 15 (2015) 7126–7132.

[437] A.R. Mellnik et al., Spin-transfer torque generated by a topological insulator, Nature. 511 (2014) 449–451.

[438] Y.A. Bychkov et al., Properties of a 2D electron gas with lifted spectral degeneracy, JETP Lett. 39 (1984) 78–81.

[439] Z. Ren et al., Optimizing Bi2-xSbxTe3- ySey solid solutions to approach the intrinsic topological insulator regime, Phys. Rev. B. 84 (2011) 165311.

[440] N. Bansal et al., Thickness-Independent Transport Channels in Topological Insulator Bi2Se3 Thin Films, Phys. Rev. Lett. 109 (2012) 116804.

[441] M. van Kampen et al., All-Optical Probe of Coherent Spin Waves, Phys. Rev. Lett. 88 (2002)

227201.

[442] S.N. Panda et al., All-optical detection of interfacial spin transparency from spin pumping in β-Ta/CoFeB thin films, Sci. Adv. 5 (2019) 1–7.

[443] O. Mosendz et al., Detection and quantification of inverse spin Hall effect from spin pumping in permalloy/normal metal bilayers, Phys. Rev. B. 82 (2010) 214403.

[444] J. Bass et al., Spin-diffusion lengths in metals and alloys, and spin-flipping at metal/metal interfaces: an experimentalist's critical review, J. Phys. Condens. Matter. 19 (2007) 183201.

[445] M.D. Anoop et al., Effect of isovalent substitution on the structural and electrical properties of BixSb2-xTe3 topological insulator single crystals, Mater. Today Proc. 31 (2020) 616–621.

[446] J. Yuan et al., Raman Spectroscopy of Two-Dimensional Bi2TexSe3 − x Platelets Produced by Solvothermal Method, Materials (Basel). 8 (2015) 5007–5017.

[447] F. Yang et al., Top gating of epitaxial (Bi1−x Sbx)2Te3 topological insulator thin films, Appl. Phys. Lett. 104 (2014) 161614.

[448] S. Hikami et al., Spin-Orbit Interaction and Magnetoresistance in the Two Dimensional Random System, Prog. Theor. Phys. 63 (1980) 707–710.

[449] H. Nakayama et al., Geometry dependence on inverse spin Hall effect induced by spin pumping in Ni81Fe19/Pt film, Phys. Rev. B. 85 (2012) 144408.

[450] A. Brataas et al., Finite-Element Theory of Transport in Ferromagnet–Normal Metal Systems, Phys. Rev. Lett. 84 (2000) 2481–2484.

[451] J. Foros et al., Scattering of spin current injected in Pd(001), J. Appl. Phys. 97 (2005) 10A714.

[452] K. Chen et al., Spin Pumping in the Presence of Spin-Orbit Coupling, Phys. Rev. Lett. 114 (2015) 126602.

[453] J.-C. Rojas-Sánchez et al., Spin Pumping and Inverse Spin Hall Effect in Platinum: The Essential Role of Spin-Memory Loss at Metallic Interfaces, Phys. Rev. Lett. 112 (2014) 106602.

[454] M.J. Hurben et al., Theory of two magnon scattering microwave relaxation and ferromagnetic resonance linewidth in magnetic thin films, J. Appl. Phys. 83 (1998) 4344–4365.

[455] R. Arias et al., Extrinsic contributions to the ferromagnetic resonance response of ultrathin films, Phys. Rev. B. 60 (1999) 7395–7409.

[456] S. Mukhopadhyay et al., All-optical observation of giant spin transparency at the topological insulator BiSbTe1.5Se1.5/Co20Fe60B20 interface, NPG Asia Mater. 15 (2023) 57.

[457] K. Dutta et al., All-Optical Detection of Spin Pumping and Giant Interfacial Spin Transparency in Co2Fe0.4Mn0.6Si/Pt Heterostructure, Adv. Quantum Technol. 5 (2022) 1–10.

[458] S.N. Panda et al., Femtosecond laser-induced spin dynamics in single-layer graphene/CoFeB thin films, Nanoscale. 13 (2021) 13709–13718.

[459] W. Zhang et al., Role of transparency of platinum–ferromagnet interfaces in determining

the intrinsic magnitude of the spin Hall effect, Nat. Phys. 11 (2015) 496–502.

[460] Y.-T. Chen et al., Theory of spin Hall magnetoresistance, Phys. Rev. B. 87 (2013) 144411.

[461] V.E. Demidov et al., Excitation of coherent propagating spin waves by pure spin currents, Nat. Commun. 7 (2016) 10446.

[462] M. Tonouchi, Cutting-edge terahertz technology, Nat. Photonics. 1 (2007) 97–105.

[463] D.M. Mittleman, Frontiers in terahertz sources and plasmonics, Nat. Photonics. 7 (2013) 666–669.

[464] B. Scherger et al., Variable-focus terahertz lens, Opt. Express. 19 (2011) 4528.

[465] B.S.-Y. Ung et al., Inkjet printed conductive polymer-based beam-splitters for terahertz applications, Opt. Mater. Express. 3 (2013) 1242.

[466] H. Tao et al., Highly flexible wide angle of incidence terahertz metamaterial absorber: Design, fabrication, and characterization, Phys. Rev. B. 78 (2008) 241103.

[467] S.C. Saha et al., Imprinted terahertz artificial dielectric quarter wave plates, Opt. Express. 18 (2010) 12168.

[468] A.E. Costley et al., Free-standing fine-wire grids: Their manufacture, performance, and use at millimeter and submillimeter wavelengths, J. Opt. Soc. Am. 67 (1977) 979.

[469] E. Hecht, Optics, Pearson, 2017.

[470] J.J. Wang et al., High-performance, large area, deep ultraviolet to infrared polarizers based on 40 nm line/78 nm space nanowire grids, Appl. Phys. Lett. 90 (2007) 061104.

[471] Z. Huang et al., High extinction ratio and low transmission loss thin-film terahertz polarizer with a tunable bilayer metal wire-grid structure, Opt. Lett. 39 (2014) 793.

[472] I. Yamada et al., Terahertz wire-grid polarizers with micrometer-pitch Al gratings, 2009.

[473] D. Grischkowsky et al., Far-infrared time-domain spectroscopy with terahertz beams of dielectrics and semiconductors, 1990.

[474] G.R. Fowles, Introduction to Modern Optics, Dover Publications, I. C., Newyork, 1975.

[475] W. Xiang et al., High extinction ratio terahertz broadband polarizer based on the aligned Ni nanowire arrays, Opt. Lett. 45 (2020) 1978.

[476] E.W. Thulstrup, Linear and magnetic circular dichroism of conjugated molecules, J. Mol. Struct. 47 (1978) 359–364.

[477] K. Neeraj et al., Efficient terahertz anti-reflection properties of metallic anti-dot structures, Opt. Lett. 42 (2017) 1764.